UNIVERSITÀ DEGLI STUDI DI PAVIA

DOTTORATO IN SCIENZE CHIMICHE E FARMACEUTICHE E INNOVAZIONE INDUSTRIALE (XXXVIII Ciclo)

Coordinatore: Chiar.mo Prof. Giorgio Colombo

Development of Chiral Metal Halides for Chiroptical Applications

Tesi di Dottorato di
Clarissa Coccia

AA 2024/2025

Tutor
Chiar.mo Prof. Lorenzo Malavasi

Co-tutor
Prof. Alessio Porta

Contents

CHAPTER 1 1

Introduction 1

1.1 General Overview 1

1.2 Perovskites 2

1.3 Hybrid Organic-Inorganic Perovskites 5

1.4 Chirality 8

1.5 Chiral Perovskites 13

Aim of the Project 23

References 24

CHAPTER 2 29

Ligand-Induced Chirality in Cl-MBA$_2$SnI$_4$ 2D Perovskites 29

1. Introduction 32

2. Results and Discussion 33

3. Conclusions 42

References 44

SUPPLEMENTARY INFORMATION 47

CHAPTER 3 63

Unraveling the Role of Structural Topology on Chirality Transfer and Chiroptical Properties in Chiral Germanium Iodides 63

1. Introduction 66

2. Results and Discussion 69

3. Conclusions 85

References 87

SUPPLEMENTARY INFORMATION 93

CHAPTER 4 109

Engineering the Electronic Structure and Optoelectronic Properties of Chiral Metal Halides through Cation Design 109

1. Introduction 112

2. Results and Discussion 113

3. Conclusions 124

References 127

SUPPLEMENTARY INFORMATION 132

CHAPTER 5 143

3D Chiral Metal Halide Semiconductors 143

1. Introduction 146
2. Results and Discussion 147
3. Conclusion 154
References 156
SUPPLEMENTARY INFORMATION 161
CHAPTER 6 175
Conclusion and Outlook 175

To my sister Arianna

CHAPTER 1

Introduction

1.1 General Overview

In recent years, hybrid organic-inorganic perovskites (HOIPs) have emerged as promising materials for solar cells, light-emitting diodes, photodetectors, and devices for optoelectronics and energy harvesting [1–6], thanks to the outstanding quantum yields and easy emission tunability. Further expansion of these applications may be achieved through chirality, i.e., the property of an object not being superimposable to its mirror image.[7] In this context, HOIPs can be imparted with chiroptical properties by the employment of chiral organic cations, generating compounds that combine the advantages of both the chiral molecules and the halide perovskites. Indeed, while the asymmetric ligand induces nonlinear optical (NLO) properties in the final materials, the HOIPs skeleton shifts the asymmetric absorption and emission maxima in the UV-Vis-IR region, through a mechanism known as Chirality Transfer Mechanism, which is currently being investigated.[8] Although a pioneering work on chiral perovskites was carried out in 2003 [9], characterizing the crystal structure of a 1D HOIP, the first 2D HOIP appeared in 2006.[10] The chiroptical properties of these materials started being deeply investigated only in 2017[11], with the first characterization of the dichroic behaviour of various HOIPs through circular dichroism (CD).

Immediately after, the field started growing significantly, as the chemical and structural tuning of HOIPs offered a unique playground for developing novel and more efficient materials featuring higher spin selectivity, superior circular dichroism, improved stability, and so on. Although the field is still at an early stage, it is clear that a number of functional properties, such as CD, Rashba-Dresselhaus (RD) spin splitting[12], conductivity, ferroelectricity or piezoelectricity, strictly depends on the chemical nature, stoichiometry, network dimensionality (0D, 1D, or 2D), hydrogen bonding, and other structural parameters, such as the octahedral distortions.[12]

1.2 Perovskites

Originally, the concept of perovskite was introduced for the $CaTiO_3$ mineral in 1839 by Gustav Rose and its name was subsequently derived from the Russian mineralogist Count Lev Alekseyevich von Perovski. Later, the perovskite term was extended to all the families of materials with the same formula ABX_3. In general, perovskite minerals are found in nature as oxides, mainly silicates, but they can also occur as fluorides, chlorides, hydroxides, arsenides, and intermetallic compounds.[13] After a century since the first identification of natural oxide perovskite, a class of artificial inorganic metal trihalide perovskite with general stoichiometry ABX_3 (X = Cl, Br, I) was reported in literature, synthetized through a simple reaction between two salts.[14] The importance of these materials became rather relevant along with the discovery of intriguing electronic properties, as well as of interesting ferro- and antiferromagnetic, ferroelectric and piezoelectric characteristics. The turning point occurred when the introduction of hybrid organic-inorganic systems revealed several advantages in terms of exciton binding energy, lifetimes, and electronic tunability of these novel compounds.[14]

1.2.1 Crystal Structure

The ideal perovskite crystal lattice can be described by a primitive cubic structure with $Pm\bar{3}m$ space group, presenting the general formula ABX_3, where B is a metallic cation, X is oxygen or a halogen, (Br, Cl,or I) and A is a voluminous cation which can be metallic (totally inorganic perovskite) or an organic cation (hybrid organic-inorganic perovskite). This structure can be visualized as a three-dimensional network of BX_6 octahedra sharing all the corners, while A cations are located among them [15] (Figure 1).

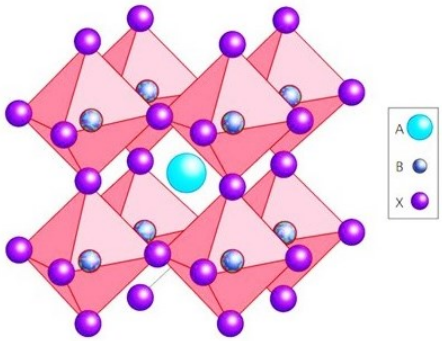

Figure 1: Schematic representation of ABX_3 perovskite structure[15]

1.2.2 Dimensionalities

Metal halide perovskites (MHPs), characterized by the presence of an halong as X exhibit a variety of crystal structures depending on how the B-site cation coordination octahedra [BX_6] connect with each other. These different connectivities lead to four distinct dimensionalities of perovskite structures (Figure 2), which are three-dimensional (3D), two-dimensional (2D), one-dimensional (1D), and zero-dimensional (0D). Each of these configurations are characterized by unique properties. [16]

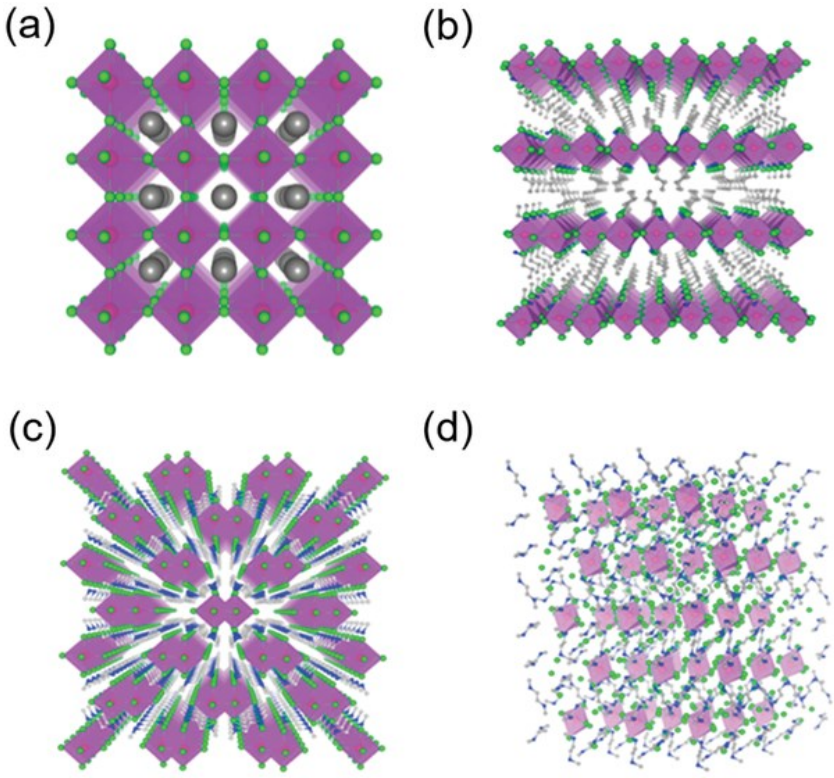

Figure 2: General representation of crystal structure of a a) 3D, b) 2D, c) 1D, d) 0D perovskites [16]

The classic 3D perovskites have the general formula ABX_3 and consist of corner-sharing $[BX_6]^{4-}$ octahedra forming a continuous three-dimensional network. In this structure, the A^+ cations occupy the voids formed by four connected octahedra. A variation of this is the double perovskite, where the B site is replaced by one monovalent and one trivalent cation, resulting in the formula $A_2B^+B^{3+}X_6$.

Two-dimensional perovskites (2D), often referred to as layered perovskites, are composed of alternating layers of corner-sharing $[BX_6]^{4-}$ octahedra and A^+ cation layers. Their stoichiometries include also AB_2X_5 and $A_3M_2X_9$, the latter is

characterized by $[M_2X_9]^{3-}$ isolated cluster made of two face-sharing octahedra with A^+ cations as bridge between the cluster.

In one-dimensional perovskites (1D), BX_5 octahedra connect by sharing two opposite corners, forming isolated infinite chains with a general stoichiometry of A_3BX_5 .[17]

Zero-dimensional perovskites (0D) are featured by an A_4BX_6 stoichiometry, which is characterized by completely isolated $[BX_6]^{4-}$ octahedra that do not share corners or edges. However, examples include also stoichiometries as A_2BX_6, where the unit cell contains four decoupled octahedra surrounded by A^+ cations in the interstitial.

The original perovskite structure is quite simple, however due to the several possibilities of including elements with different ionic radius, the structure can be subjected to slight distortion of the unit cell. In 1920s Goldschmidt introduced an experimental factor, called “tolerance factor” (t), which allows to predict the stability of the perovskite structure.

For the ABX_3 perovskite the t factor is defined as:

$$t = \frac{r_A + r_x}{\sqrt{2}(r_b + r_x)} \qquad \text{(eq. 1)}$$

where r_A, r_B, and r_X represent the ionic radii of the A cation, B cation, and anion X, respectively. This value helps to understand which ions size the structure can tolerate without giving a phase transition and the accepted value of t varies from 0.76 to 1.13, when the values is 1 corresponds to a perfectly packed cubic structure. Higher or lower numbers of t lead to a deviation from the idealist. The distortions from the ideal cubic structure can derive from several parameters, as different size of cations and anions or the displacement of the B cation in the octahedra. The occurrence of these phenomena leads to the formation of various perovskite and non-perovskite structures. Specifically, distorted structures caused by the tilting of octahedra are formed when the tolerance factor ranges between 0.7 and 0.9, resulting in orthorhombic and rhombohedral variants. In contrast, tolerance factors outside this range produce non-perovskite structures, such as hexagonal forms when $t > 1$, or corundum/ilmenite-type structures when $t < 0.7$.

An additional subsequent parameter is the “octahedral factor” (μ), which describes the stability of the $[BX_6]$ octahdera.

$$\mu = \frac{r_b}{r_x} \qquad \text{(eq. 2)}$$

Where r_b and r_x are the radii of the B cation and the X anion. This value ranges from 0.44 to 0.89. These two factors are used to predict the stability of low-dimensional perovskites as well. Specifically, the tolerance factor (*t*) threshold can be relaxed when the compound is expected to form a 2D structure instead of a 3D one. [18] This effect is likely due to the strain caused by larger A-cations being relieved by the separation of flexible organic layers. Spacer cations serve as buffers, reducing the compression experienced by the inorganic layers. [19]

1.3 Hybrid Organic-Inorganic Perovskites

In the landscape of 2D materials, it is possible to focus the attention into a specific class, known as “Hybrid Organic-Inorganic Perovskites” (HOIPs). The structure of the HOIPs can be described starting from a simple yet fundamental modification of the fully inorganic perovskite structure. In HOIPs, the inorganic A-site cation is replaced by an organic molecule of varying size and characteristics, while still preserving the stability condition of the perovskite, indicated by a Goldschmidt tolerance factor value close to 1. This approach allows the combination of the typical properties of both inorganic and organic components within a single material. Generally, high electronic mobility, a wide range of band gaps, and interesting dielectric and magnetic properties can be combined with the large polarizability and unique mechanical characteristics of the organic part. Moreover, the possibility of specifically designing organic ligands ensures a high degree of control and tunability over the resulting properties.

A particularly important class of hybrid perovskites for optoelectronic applications, known as hybrid metal halide perovskites (HMHs), feature a halogen as the anion and a group 14 metal (Ge, Sn, Pb) at the B-site. The importance of a halogen as X site lies in the possibility of tuning the optoelectronic properties. [20]

The presence of an organic molecule, which is generally characterized by a smaller symmetry than the inorganic cation it replaces, inevitably affects the distortion of the inorganic framework. Additionally, the symmetry of the structure is influenced by the

coordinated organic molecule within the BX_6 octahedra (where B = Ge, Sn, Pb; X = Cl, Br, I). The octahedral lattice is influenced both by the orientational order of the organic molecules and the inorganic framework. As a result, each phase in these perovskites is characterized by a specific system of octahedral tilting and the orientational order of the organic component.

Two-dimensional layered hybrid perovskites are made up of alternating inorganic BX_6 octahedral sheets and double layers of organic cations. The regularity of the inorganic octahedra depends not only on the metal cation occupying the B site but also on the nature of the organic spacer molecules, including their chain length, functionalization, and potential aromatic conjugation. The phase transition temperature in these materials often correlates with the length of the organic chain spacers, as strong hydrogen bonding forms between the groups of the organic cations and the halide ions at the octahedral vertices. This interaction influences the distortion of the inorganic framework, demonstrating the tightly concerted relationship between the organic and inorganic layers. Consequently, the mechanical and electronic properties of these composite materials can be finely tuned by altering either the bonding strength within the inorganic layer or the characteristics of the organic ligands. [21]

Most applications of hybrid perovskites, such as materials for solar cells, LEDs, or photodetectors, involve interaction with electromagnetic radiation, which depends on the characteristics of the perovskite's electronic structure. Therefore, it is essential to understand what determines this structure to rationally design the material and tailor its properties according to the intended application.

The primary property to interpret is the semiconducting nature of hybrid perovskites, which depends on the value of the band gap. Specifically, this corresponds to the energy difference between the conduction band minimum (CBM) and the valence band maximum (VBM); the projected density of states (PDOS) diagrams for various hybrid show that, despite the differences among the systems, the energy levels closest to the valence band maximum (VBM) and conduction band minimum (CBM) are predominantly composed of orbitals from the metal and halogen atoms. Indeed, some studies reveals that the limits of the bands are determined by the octahedra' s connection, while the orbitals of the organic molecules are too low in the VB or too high in the CB. Moreover, the layered structure of these materials plays an important role in the electronic structure. Indeed, the alternating layers exhibiting a strong

electronic and dielectric mismatch result in a very distinctive electronic structure, where insulating organic layers act as potential barriers, and inorganic layers enable the promotion of electrons to conduction energy states, thereby imparting semiconducting properties to layered perovskites as well. This separation causes charge carriers (holes or electrons) to experience strong quantum confinement within a very thin layer and the repeated organic barrier/inorganic well structure leads to the formation of a characteristic quantum well system. [22]

The second factor influencing the electronic structure of HOIPs, in particular as 2D and quasi-2D perovskites, is anything that can cause distortion of the inorganic layer. As previously mentioned, the electronic properties depend on the connectivity characteristics of the B–X bonds; however, interactions at the organic–inorganic interface can lead to octahedral distortions and, consequently, indirectly modulate these electronic properties. From this perspective, it becomes clear why, although the energy levels defining the valence and conduction bands, and thus the band gap (*Eg*) arise from linear combinations of orbitals of the inorganic atoms, changes in both the dimensionality and the organic component are crucial for band gap control. [23-26]

While the ability to tune the band gap by varying the organic cation is rather limited and mainly linked to the distortion it induces in the inorganic octahedra, the optoelectronic properties of 2D perovskites are much more strongly dependent on the nature of the organic spacer. These properties manifest in the material's interaction with radiation and depend not only on the energy gap but also on the distribution of the exciton energy levels. An exciton forms as a result of the photoinduced promotion of an electron from the valence band to a higher energy state, leaving behind an electron hole in the valence band. The stability of the exciton, which tend to undergo electron-hole recombination, is determined by its binding energy (Eb), which is the difference between the conduction band minimum and the energy of the exciton's 1s level.

Optoelectronic applications of perovskites are closely linked to the binding energy: stable excitons tend to recombine easily and are ideal for LED applications, whereas excitons with low Eb favor the promotion of photoelectrons to the conduction band, making them more suitable for photovoltaic devices. [27]

1.4 Chirality

By definition, chirality, from Greek “Chiro” meaning hand, is the property of an object of not being superimposable to its specular counterpart (Figure 3). Practically, this means that chiral materials must not contain S_n symmetry elements, such as mirror planes or inversion centers, condition achieved only if they crystallize in one of the 65 Shohncke space groups. [28] From a functional perspective, chiral materials feature an intriguing behavior upon irradiation with polarized light, preferentially interacting with the left- or right-handed component. This property can be investigated by several characterization methods, of which the most widely employed are the Circular Dichroism (CD) and Circular Photoluminescence (CPL), related to the chirality in the ground and excited states, respectively. Indeed, CD refers to the preferential absorption of Left-handed circularly polarized light (LCP) and right-handed circularly polarized light (RCP), while CPL is related to its preferential emission.

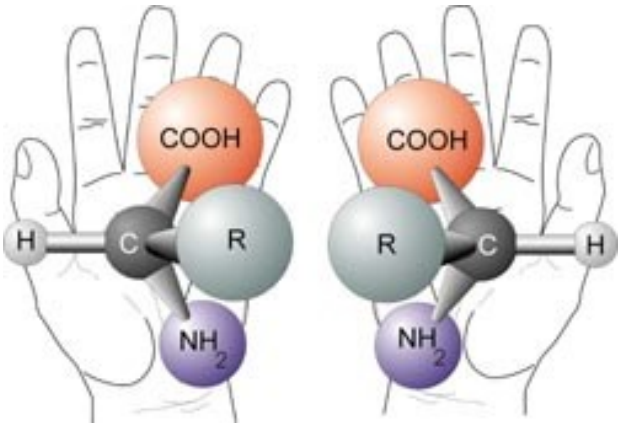

Figure 3: Representation of a chiral object

Chirality can be defined more rigorously by referring to the symmetry properties of an object. There are two enantiomorphic symmetry operations, which are reflection with respect to a plane and inversion with respect to a point and these two can change the chirality of an object. If an object possesses at least one mirror plane or an inversion center as symmetry elements, it is achiral. From a geometric perspective, symmetry is defined as the invariance of an object under a given transformation. For instance, if an object has a center of inversion, it means that every point of the object can be swapped with its opposite relative to this center without altering the object itself. Moreover, if an object has a plane of reflection, it means the object can be divided into two mirror-image parts by that plane. Every point on one side of the plane

has a corresponding mirror point on the other side, at the same distance from the plane. These two definitions are the opposite compared to the definition of “chirality”.

1.4.1 Polarization of the Electromagnetic radiation

Electromagnetic radiation is composed of electromagnetic waves, which consist of the coordinated oscillation of an electric field and a magnetic field. These waves propagate in a direction that is orthogonal to the direction of oscillation. A key characteristic of an electromagnetic wave is its polarization. The electric field vector (as well as the magnetic field vector) of the wave always oscillates in the same direction. The plane defined by the direction of the electric field's oscillation and the direction of wave propagation is known as the plane of polarization. Besides linear polarization, electromagnetic radiation can also exhibit circular polarization, where the electric field vector rotates around the direction of propagation. This form of polarization carries a well-defined optical handedness, making it intrinsically chiral. As a result, when circularly polarized light interacts with a chiral medium, it can give rise to circular dichroism, which will be discussed in the following section. [28]

1.4.2 Circular Dichroism (CD)

In chiral photonics, circularly polarized light, LCP (σ^+) or RCP (σ^-) (Figure 4) provides a chiral optical excitation. When such light interacts with a chiral material, the two polarizations couple differently to its electronic or excitonic transitions, leading to differential absorption. This asymmetric interaction constitutes the basis of CD. For instance, chiral materials preferentially absorb LCP or RCP light based on the redistribution of helical electron clouds for a particular transition. This differentia absorption of LCP and RCP lights is often referred to as the Cotton effect or CD intensity (ΔA) which is defined as follows:

$$\Delta A = A^L - A^R \qquad \text{(eq. 3)}$$

Where A^L and A^R are the absorbance of LCP and RCP lights. The CD spectrum provides important information about the configuration of materials and properties of electronic transition.

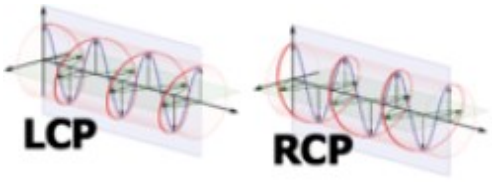

Figure 4: Left-handed circularly polarized light and right-handed circularly polarized light

It provides direct information about the electronic structure and stereochemistry of molecules in their ground state and is therefore one of the most widely employed spectroscopic tools for probing molecular chirality, conformational dynamics, and supramolecular organization. In contrast to circularly polarized photoluminescence, which probes the emissive excited state, CD focuses on the absorptive properties of the ground-to-excited-state transition, making the two techniques highly complementary.

The extent of circular dichroism is expressed by the absorption dissymmetry factor, g_{abs}, which quantifies the normalized difference between the molar absorption coefficients of left- and right-circularly polarized light. It is defined as

$$g_{abs} = \frac{\Delta A}{A} \qquad \text{(eq.4)}$$

where ΔA represent the difference of the molar absorption coefficients for left- and right-circularly polarized light, respectively.

Experimentally, CD is typically measured using a spectropolarimeter, in which polarized monochromatic light is modulated between left and right circular polarization before being transmitted through the sample. The difference in absorption is recorded as a function of wavelength, yielding a CD spectrum. Since the CD signal is usually very weak compared to total absorption, careful optical alignment, baseline correction, and control of sample scattering are critical to obtaining reliable spectra.

On a theoretical level, CD arises from the interaction between electric dipole and magnetic dipole transition moments. The sign and magnitude of a CD band depend on the relative orientation and coupling of these transition moments, which are strongly influenced by molecular geometry and conformation.

1.4.3 Circular Polarized Photoluminescence (CPL)

CPL spectroscopy relies on the differential spontaneous emission of LCP or RCP light from luminescent systems, upon relaxation from an excited electronic state. This difference is defined by the expression given by Equation 5, which is similar Equation 3.

$$\Delta l = l^L - l^R \qquad \text{(eq.5)}$$

Where I^L and I^R are luminescence intensities of LCP and RCP lights, respectively. As CPL and CD are based on opposite optical phenomena, which are emission and absorption of light, the CD spectrum reflects the structural properties of the excited state, whereas CPL provides information of ground states. [29] CPL provides direct insight into the chiral nature of excited states and the associated electronic transitions and is therefore considered a powerful probe in the study of molecular chirality.

The degree of circular polarization in luminescence is quantified by the luminescence dissymmetry factor, g_{lum}, which expresses the relative difference between the intensities of left- and right-circularly polarized emission. It is defined as:

$$g_{lum} = \frac{\Delta I}{I} \qquad \text{(eq.6)}$$

Even small dissymmetry factors can be technologically significant when combined with high photoluminescence quantum yields, since the overall fraction of circularly polarized photons can be enhanced at the device level.

Experimentally, CPL is measured using dedicated spectrofluorometers equipped with optical components such as circular polarizers or photoelastic modulators, which separate the left and right-handed components of the emitted light. Because the signals are intrinsically weak, minimizing experimental artifacts is essential, particularly those arising from birefringence, scattering, or instrumental asymmetry. Proper calibration and background correction are therefore critical for obtaining reliable spectra.

On a theoretical level, CPL originates from the interplay between electric dipole and magnetic dipole transition moments. The relative orientation and magnitude of these two contributions determine both the sign and amplitude of g_{lum} This dependence

makes CPL highly sensitive to subtle conformational and electronic factors and complements absorption-based chiroptical methods such as circular dichroism (CD). Importantly, CPL probes the emissive excited state, whereas CD is restricted to ground-state absorption; thus, comparison of the two techniques often reveals dynamic information about structural relaxation, aggregation, or excited-state reorganization that would otherwise remain inaccessible.[30]

1.5 Chiral Perovskites

In the last decades the research interest towards hybrid organic inorganic perovskites (HOIPs) has widely increased due to their promising applications in many fields, such as photovoltaics, photodetection, optoelectronics, technologies based on light-emitting diodes (LEDs), energy harvesting and photocatalysis. Indeed, these materials do possess outstanding light absorption in the UV, visible and even infrared spectral regions, as well as tunable emission with remarkable quantum yields.[7] In addition to these advantages, it is possible to employ chiral molecules as organic cations imparting chirality to the perovskite itself, by virtue of a mechanism known as chirality transfer, whose fundamentals are currently being examined. Therefore, chiral HOIPs combine the above-described optical properties with the capability of discriminating the polarized light, thus displaying superior circular dichroism (CD) or circularly polarized luminescence (CPL) as well as an intrinsically generated spin selectivity. [1-6]

Despite the above listed promising characteristics, the field of chiral perovskites is still at an early stage. Indeed, the first example appeared in 2003, when Billing and Lemmerer reported the crystal structure of the 1D (*S*-MBA)$PbBr_3$ (MBA = α-methylbenzylamine), followed in 2006 by the 2D (*R*/*S*-MBA)$_2PbI_4$ However, their chiroptical properties started being deeply investigated only in 2017 with the groundbreaking work of Ahn and co-workers, pioneering a field which is in continuous growth. Indeed, up to date, chiral HOIPs have been investigated for different purposes spanning from the optical properties, the spin-related features such as the Rashba-Dresselhaus (RD) spin-splitting or the chirality induced spin selectivity (CISS), and the ferroelectric and piezoelectric properties. So far, the research on chiral HOIPs has mainly centred on 2D and quasi-2D materials, employing a number of different commercial chiral cations (Figure 5) and also tuning the halogen and, more rarely, the metal center, to evaluate the impact on the functional properties. On the contrary, investigations on 1D and 0D perovskite derivatives are scarce, and, in addition, lead has been the most investigated metal center despite its well-known toxicity, the latter highlighting the need for prompting the research field toward less toxic and more sustainable metal cations.[31-32]

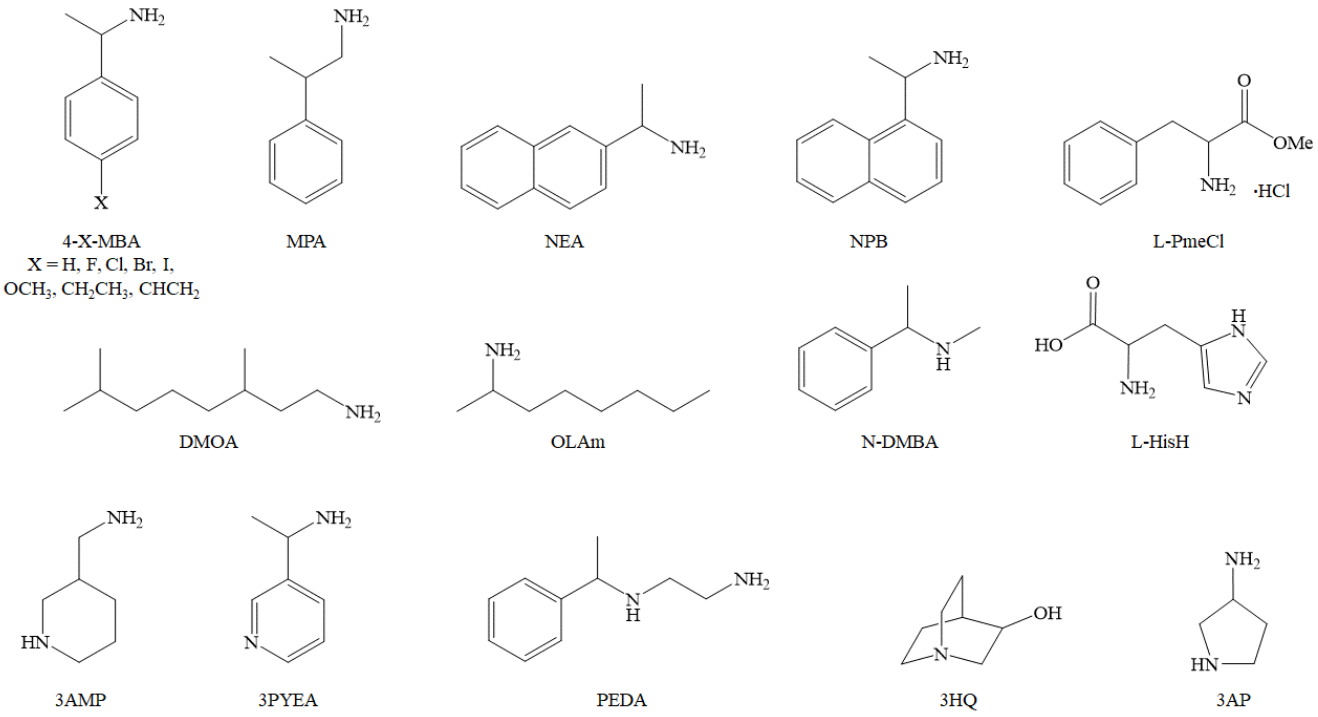

Figure 5: Different chiral commercial cations [32]

The general chemical formula for 3D HOIPs is ABX_3, where A represents a monovalent cation, B is a metallic bivalent cation, and X is a halogen anion. From a structural point of view, as already explained in the previous chapters, 3D perovskites display corner-shared $[MX_6]$ octahedrons, which since the optical and physical properties can easily be tuned by changing n and chemical composition, theoretical calculations revealed that the generation of stable compounds requires that the A cation is small enough to fit within the inorganic framework cavities. Due to this constraint, 3D chiral HOIPs remain in the theoretical development stage, as their instability hinders their practical optoelectronic applicability. To overcome these problems, 2D chiral HOIPs have been introduced and developed. Compared to the 3D counterparts, these can be regarded as a horizontal slicing of the 3D frameworks with the incorporation of a bigger organic cation. 2D HOIPs exhibit the generic chemical formula of $(R\text{-}NH_3)_2A_{n-1}MX_{3n+1}$, where n denotes the number of inorganic layers between two layers of organic cations, and $R\text{-}NH_3$ represents the chiral ligand inserted between two inorganic layers. At the state of the art, this family of chiral HOIPs is the most widely investigated since the optical and physical properties can easily be tuned by changing n and chemical composition.

In contrast to 2D chiral HOIPs, studies on 1D and 0D HOIPs are scarce. 1D chiral HOIPs, featuring the generic chemical formula of R-NH_3MX_3, can be created when chiral organic cations and metallic cations are present in a 1:1 ratio. 0D HOIPs, instead, can be produced when the geometric sizes of 3D, 2D and 1D chiral HOIPs shrink to a few nanometres. These low-dimensional structures are more correctly defined as perovskite derivatives of perovskite-hybrid halides since, in general, they do not feature any corner sharing network where n denotes the number of inorganic layers between two layers of organic cations, and R-NH_3 represents the chiral ligand inserted between two inorganic layers.

Despite the promise, this is a relatively young field and the fundamental challenge for these materials remains how to effectively transfer molecular chirality into the extended inorganic lattice to influence bulk physical behavior, a mechanism still under intense study. Furthermore, toxicity concerns associated with lead-based systems have prompted the exploration of lead-free analogues, focusing on elements like bismuth, tin, and silver. These developments have paved the way for a broader exploration of dimensionality-dependent phenomena, from molecular 0D, to extended layered 2D architectures.[32]

1.5.1 0D Chiral Metal Halides

Zero-dimensional chiral metal halides (CMH) represent the molecular limit of perovskite chemistry, typically comprising discrete [MX_6] octahedra surrounded by organic cations. Unlike extended frameworks, these systems lack connectivity through corner, edge, or face-sharing octahedra, and as such are better described as perovskite-like derivatives. The absence of extended structure does not preclude functional utility; in fact, 0D chiral MH have shown exceptional nonlinear optical (NLO) responses, as the lack of inversion symmetry at the molecular level facilitates strong SHG signals. In the state of the art are reported some 0D CMH which can help the understanding of chirality transfer.

In 2021, Zhao et al. reported a lead-free 0D CMH system based on tin and the chiral amine β-methylphenethylamine (MPEA), forming the compound (*R*/*S*-MPEA)$_2$SnBr$_6$. The materials crystallized in the chiral space group $P2_1$, exhibiting pronounced CD and SHG responses, these are key indicators of chirality transfer and symmetry breaking at the molecular level. Their optical bandgap of 2.69 eV and high laser-induced damage threshold (LDT) highlighted their potential for stable, high-intensity optical applications.[33]

Only a year later, Rajput and co-workers extended this concept using bismuth to synthesize (*R*/*S*-MBA)$_4$Bi$_2$I$_{10}$, again leveraging solution-phase crystallization to obtain 0D systems with distinct chiral and racemic forms. Notably, the enantiopure compounds displayed unique CD signals and photoluminescence behavior distinct from the racemic analogue, supporting the conclusion that even in the absence of long-range inorganic networks, chirality can strongly modulate optical properties.

The trend continued with Jiang et al., who compared 0D and 1D chiral bismuth CMH differing only in the alkyl chain length of the organic cation. Their analysis revealed that the 0D system (*R*/*S*-MBA)$_4$Bi$_2$Br$_{10}$ displayed lower CD intensity than its 1D counterpart, underscoring the influence of dimensionality and the packing arrangement of organic cations on the transfer and amplification of chiroptical effects. The latter example shows how the different dimensionality of these materials plays and important role for the NLO. Indeed, the 1D system (*R*/*S*-MPA)$_2$BiBr$_5$ shows higher values of CD, mainly due to the connection between the anisotropic coefficient and the magnetic dipole moment, related to the disposition of the octahedra.[34-35]

1.5.2 1D Chiral Metal Halides

Recent advances in the design of low-dimensional hybrid perovskites have emphasized the delicate interplay between structural configuration and chiroptical functionality. In 1D CMH, corner-sharing octahedra form linear chains separated by bulky organic cations. These structures provide a useful compromise between electronic coupling and structural flexibility. They also represent an intermediate in which chirality can start influencing collective properties such as exciton transport, spin dynamics, and ferroelectric polarization.

Li et al. (2021) synthesized the first reported lead-free 1D chiral double MH [(*R*/*S*-)-β-MPA]$_4$AgBiI$_8$. This compound featured alternating AgI_6 and BiI_6 octahedra arranged along a single axis, stabilized by β-methylphenethylammonium cations. Beyond structural novelty, this system demonstrated both CD and CPL activity. The measured CPL anisotropy factors confirmed direct chirality transfer, a non-trivial result given the spatial separation between the chiral moieties and the emitting inorganic core. This behavior speaks to the crucial role of the organic-inorganic interface in mediating symmetry breaking.[36]

Jiang et al. also showed that 1D structures possess superior chiroptical responses compared to their 0D analogues, likely due to improved directional alignment of the chiral ligands and the inorganic motifs. The increased rigidity and anisotropy of 1D chains seem to amplify the coupling between molecular chirality and inorganic optical transitions. Moreover, the dimensional confinement of excitons in these chains enhances spin-orbit interactions, further favoring chiroptical effects.

A particularly illuminating example is also provided by Liu et al., who synthesized and compared two classes of one-dimensional chiral MH to investigate the role of achiral species in modulating chiroptical properties. Their work is highly relevant to this research as it provides insight into how supramolecular interactions, especially those involving non-chiral components, can significantly influence chirality transfer and optoelectronic behavior in low-dimensional systems.

The study involved the preparation of two structurally analogous MH systems:

A mono-cation system, (*R*/*S*-AMP)$_2$Pb$_3$Br$_{10}$, incorporating only a single type of chiral cation (AMP = *R*/*S*-2-aminomethylpyrrolidine).

A mixed-cation system, *R*/*S*-AMP(DMA)PbBr$_5$, in which the chiral cation is co-assembled with an achiral organic species, dimethylammonium (DMA).

Both compounds were synthesized using a solution-phase method, with single-crystal X-ray diffraction (SC-XRD) revealing that all four enantiomeric variants crystallize in the chiral orthorhombic space group $P2_12_12_1$. Notably, the mixed-cation compounds exhibit reduced interchain spacing, suggesting stronger intermolecular interactions between the chiral and achiral building blocks.

From a structural standpoint, this difference in interchain organization is crucial: the inclusion of DMA leads to a greater degree of octahedral distortion in the inorganic framework, quantified by a higher distortion index (D). This increased distortion has a direct effect on the photophysical properties. Photoluminescence (PL) spectra revealed two emission peaks for the mono-cation system, while the mixed-cation system exhibited a broader emission. Despite this, the PL quantum yield (PLQY) was found to be higher in the mono-cation system, consistent with the lower distortion of its inorganic framework.

Chiroptical measurements further underscored the influence of structural modulation. Circular dichroism spectra exhibited opposite signals for the two enantiomers in both systems, confirming symmetry breaking. However, the CD intensity in the mixed-cation perovskites was nearly double that of the mono-cation counterparts, indicating an enhanced magnetic transition dipole moment. This enhancement is attributed to the stronger hydrogen bonding network established by the incorporation of DMA, which facilitates more efficient chirality transfer from the molecular to the extended structure.

Additionally, circularly polarized luminescence (CPL) data demonstrated that the anisotropy factor was significantly higher in the mixed-cation systems. This again supports the conclusion that the supramolecular arrangement, in particular the nature and strength of hydrogen bonding, plays a critical role in amplifying structural chirality and its optical manifestations. [37]

Overall, this case study exemplifies how even small changes in molecular composition, such as the introduction of an achiral cation, can have substantial effects on both the structural distortion and the chiroptical properties of 1D chiral MH.

1.5.3 2D and quasi 2D Chiral Perovskites

Two-dimensional chiral perovskites represent the most thoroughly explored class, both structurally and functionally. Their architecture, composed by sheets of corner-sharing octahedra interleaved with organic cations, permits effective integration of bulky chiral molecules while retaining excellent quantum confinement and exciton transport properties. Most importantly, 2D chiral perovskites are readily processable into thin films, making them ideal candidates for device integration.

The seminal example, (*R/S*-MBA)$_2$PbI$_4$, was first structurally reported in 2006 and later became the workhorse for chiroptical investigations. Ahn et al., instead in 2017 measured strong CD signals for thin films of (*R*/*S*-MBA)$_2$PbI$_4$, observing dissymmetry factors g_{cd} nearly one order of magnitude larger than prior chiral quantum dot systems. These studies not only confirmed efficient chirality transfer but also revealed structural chirality amplification, whereby supramolecular assembly reinforced chiral signals beyond molecular contributions.

Quasi-2D systems have further expanded the design space, offering a tunable dimensionality parameter "n" that governs the number of inorganic layers between organic bilayers. These systems bridge the gap between 2D and 3D structures, allowing tailored control over carrier confinement, exciton dissociation, and stability. Recent reports show that varying n or introducing halogen substitutions can modulate both optical and chiroptical properties. This has led to optimization strategies for CPL and CD output via compositional tuning, defect passivation, and polymerized organic layers.

The dimensionality reduction to two-dimensional systems, introduces new structure, property relationships that are crucial to both fundamental understanding and potential applications in photonics, spintronics, and quantum technologies.

To be more detailed in the case of 2D chiral perovskites, the inorganic layer usually adopts the Ruddlesden–Popper (RP) or Dion–Jacobson (DJ) type framework, and the chiral cations are typically placed between the perovskite layers, where they not only act as structural spacers but also mediate chiral interactions. These organic spacers can break the centrosymmetry of the crystal and thus induce chiroptical activity. Notably, Zhang et al. in 2019 demonstrated that such materials exhibit enhanced circular dichroism and circularly polarized luminescence owing to the anisotropic and confined environment of the chiral organic inorganic interfaces [3]

Another significant example of structure property correlation is provided by Liu et al., who explored a family of 2D chiral halide perovskites and observed that the nature of the organic spacer, especially its chirality and length, significantly influenced the excitonic behavior, charge mobility, and spin polarization. These variations were directly linked to the distortions induced in the inorganic framework and to the degree of spatial confinement.[38]

In quasi-2D chiral perovskites, where, as explained before multiple perovskite layers are stacked between the organic spacers, so there is a possibility of playing with n, the degree of structural anisotropy can be finely tuned. Duan and Zhou proposed a hierarchy of chirality that includes both the molecular chirality of organic cations and the structural chirality arising from asymmetric distortions in the inorganic lattice. Their work emphasized that quasi-2D architectures can better balance electronic delocalization with chiroptical performance, providing materials with both high photoluminescence quantum yields and robust chiral response .[39]

Moreover, Ding et al. employed structure guided design to enhance Rashba spin-splitting in 2D chiral perovskites, a property intimately connected to symmetry-breaking at the atomic scale. They showed that specific organic inorganic pairings could be used to amplify spin-dependent phenomena through cooperative orbital alignment and lattice strain. [40]

Interestingly, the incorporation of achiral or mixed cations into 2D chiral perovskites can lead to hybrid systems where supramolecular interactions such as hydrogen bonding and steric hindrance govern the final symmetry and photophysical behavior. Revanakar et al., emphasized that such systems challenge the traditional structure–function paradigms by introducing emergent chiral responses in materials that do not possess chirality in every constituent. [41]

Overall, these examples underline the crucial importance of understanding how molecular design and structural dimensionality affect electronic structure, exciton behavior, and chiroptical properties. The fine tuning of chirality transfer from molecular to macroscopic scales in 2D and quasi-2D systems reveals a versatile platform for engineering new functionalities.

Future investigations into the role of layer thickness, interlayer spacing, and the orientation of chiral cations are expected to offer further insights into tailoring material behavior. As such, 2D and quasi-2D chiral perovskites not only expand the

fundamental understanding of chirality in solid-state materials but also provide a strategic blueprint for developing next-generation chiral optoelectronic devices.

1.5.4 3D Chiral Perovskites: Theoretical Aspirations

Unlike their low-dimensional analogues, 3D chiral perovskites remain largely theoretical or structurally unstable. The challenge lies in incorporating bulky, chiral organic cations into the perovskite lattice without disrupting the corner-sharing octahedral framework. This difficulty is compounded by Goldschmidt tolerance factor limitations, which restrict the size and shape of A-site cations compatible with stable 3D perovskite geometry.

Nevertheless, recent computational studies and synthetic strategies aim to overcome these constraints via double perovskites, mixed-metal systems, or co-crystallization approaches. These systems are of significant interest for fundamental studies of chirality-induced spin splitting and ferroelectricity in extended 3D frameworks. Although experimentally elusive, the realization of a stable 3D chiral perovskite could open new horizons in nonlinear optics, topological materials, and spin-based quantum devices.[32]

Aim of the Project

Despite the above listed promising characteristics, the field of chiral perovskites is still at an early stage. So far, the research on chiral HOIPs has mainly centred on 2D and quasi-2D materials, employing a number of different commercial chiral cations. On the contrary, investigation on 1D and 0D perovskite derivatives are scarce,[16] and, in addition, lead has been the most investigated metal center despite its well-known toxicity, the latter highlighting the need for prompting the research field toward less toxic and more sustainable metal cations.

The aim of the Ph.D. work is to study and to investigate structure-property correlations in these materials. Thanks to the systematic tuning of different parameters, it has been possible to understand what the most impactful factors are for improving the linear and the non-linear optical properties in chiral metal halids. During this research four different systems have been studied and characterized, each of them provide a structural detailed characterization as fundamental for the exploitation of the optical properties. All the experimental parts have been also sustained by computational modelling. One of the main goals was also the replacement of the lead, and its toxicity.

References

(1) Wu, Z.Y.; Jian, B.-L.; Hsu, H.-C. Photoluminescence Characterizations of Highly Ambient-Air-Stable CH 3 NH 3 PbI 3 /PbI 2 Heterostructure. *Opt. Mater. Express* **2019**, *9*, 1882.

(2) Liang, W.-Y.; Liu, F.; Lu, Y.-J.; Popović, J.; Djurišić, A.; Ahn, H. High Optical Nonlinearity in Low-Dimensional Halide Perovskite Polycrystalline Films. *Opt. Express* **2020**, *28*, 24919.

(3) Fu, Q.; Wang, X.; Liu, F.; Dong, Y.; Liu, Z.; Zheng, S.; Chaturvedi, A.; Zhou, J.; Hu, P.; Zhu, Z.; et al. Ultrathin Ruddlesden–Popper Perovskite Heterojunction for Sensitive Photodetection. *Small* **2019**, *15*, 1902890.

(4) Ma, J.; Wang, H.; Li, D. Recent Progress of Chiral Perovskites: Materials, Synthesis, and Properties. *Adv. Mater.* **2021**, *33*, 2008785.

(5) Wu, X.; Trinh, M.T.; Niesner, D.; Zhu, H.; Norman, Z.; Owen, J.S.; Yaffe, O.; Kudisch, B.J.; Zhu, X.-Y. Trap States in Lead Iodide Perovskites. *J. Am. Chem. Soc.* **2015**, *137*, 2089–2096.

(6) Li, J.; Wang, J.; Ma, J.; Shen, H.; Li, L.; Duan, X.; Li, D. Self-Trapped State Enabled Filterless Narrowband Photodetections in 2D Layered Perovskite Single Crystals. *Nat Commun* **2019**, *10*, 806.

(7) Wang, Y.; Xu, J.; Wang, Y.; Chen, H. Emerging Chirality in Nanoscience. *Chem. Soc. Rev.* **2013**, *42*, 2930–2962.

(8) Ma, S.; Ahn, J.; Moon, J. Chiral Perovskites for Next-Generation Photonics: From Chirality Transfer to Chiroptical Activity. *Adv. Mater.* **2021**, *33*, 2005760.

(9) Billing, D.G.; Lemmerer, A. Bis[(*S*)-β-Phenethylammonium] Tribromoplumbate(II). *Acta Crystallogr E Struct Rep Online* **2003**, *59*.

(10) Billing, D.G.; Lemmerer, A. Synthesis and Crystal Structures of Inorganic–Organic Hybrids Incorporating an Aromatic Amine with a Chiral Functional Group. *CrystEngComm* **2006**, *8*, 686–695.

(11) Ahn, J.; Lee, E.; Tan, J.; Yang, W.; Kim, B.; Moon, J. A New Class of Chiral Semiconductors: Chiral-Organic-Molecule-Incorporating Organic–Inorganic Hybrid Perovskites. *Mater. Horiz.* **2017**, *4*, 851–856.

(12) Schlipf, M.; Giustino, F. Dynamic Rashba-Dresselhaus Effect. *Phys. Rev. Lett.* **2021**, *127*, 237601.

(13) Akkerman, Q.A.; Manna, L. What Defines a Halide Perovskite? *ACS Energy Lett*. **2020**, 5, 604–610.

(14) Manser, J.S.; Christians, J.A.; Kamat, P.V. Intriguing Optoelectronic Properties of Metal Halide Perovskites. *Chem. Rev*. **2016**, 116, 12956–13008.

(15) Bello, S., Urwick, A., Bastianini, F., Nedoma, A. J. & Dunbar, A. An introduction to perovskites for solar cells and their characterisation., *Energy Reports 8*. **2022**, 89-106.

(16) Shamsi, J.; Urban, A.S.; Imran, M.; De Trizio, L.; Manna, L. Metal Halide Perovskite Nanocrystals: Synthesis, Post-Synthesis Modifications, and Their Optical Properties. *Chem. Rev.* **2019**, 119, 3296–3348

(17) Sum, T.C.; Mathews, N. Advancements in Perovskite Solar Cells:Photophysics behind the Photovoltaics. *Energy Env. Sci* **2014**, 7, 2518–2534.

(18) Liang, M.; Lin, W.; Lan, Z.; Meng, J.; Zhao, Q.; Zou, X.; Castelli, I.E.; Pullerits, T.; Canton, S.E.; Zheng, K. Electronic Structure and Trap States of Two-Dimensional Ruddlesden–Popper Perovskites with the Relaxed Goldschmidt Tolerance Factor. *ACS Appl. Electron. Mater*. **2020**, 2, 5, 1402-1412.

(19) Fu, Y.; Hautzinger, M.P.; Luo, Z.; Wang, F.; Pan, D.; Aristov, M.M.;Guzei, I.A.; Pan, A.; Zhu, X.; Jin, S. Incorporating Large A Cations into Lead Iodide Perovskite Cages: Relaxed Goldschmidt Tolerance Factor and Impact on Exciton–Phonon Interaction. *ACS Cent. Sci*. **2019**, 5, 8, 1377-1386.

(20) Møller, C. K. Crystal Structure and Photoconductivity of Caesium Plumbohalides. *Nature* **1958**, 182.

(21) Stoumpos, C. C. et al. Ruddlesden-Popper Hybrid Lead Iodide Perovskite 2D Homologous Semiconductors. *Chem. Mater*.**2016** ,28, 2852–2867

(22) Liang, M. et al. Electronic Structure and Trap States of Two-Dimensional Ruddlesden- Popper Perovskites with the Relaxed Goldschmidt Tolerance Factor. *ACS Appl. Electron. Mater. 2*, **2020**, 1402–1412.

(23) Feng, J. & Xiao, B. Effective masses and electronic and optical properties of nontoxic MASnX3 (X = Cl, Br, and I) perovskite structures as solar cell absorber: A theoretical study using HSE06. *J. Phys. Chem. C* **2014**, 118, 19655–19660.

(24) Qiu, D., Huang, F., Li, S. & Mi, Q. General trends for the effect of ionic substitution on the band gap of MAPbX3. *Solid State Commun***. 2017**, 264, 35–38.

(25) Sun, P. P., Li, Q. S., Yang, L. N. & Li, Z. S. Theoretical insights into a potential lead-free hybrid perovskite: Substituting Pb2+ with Ge2+. *Nanoscale* **2016**, 8, 1503–1512.

(26) Pedesseau, L. et al. Electronic properties of 2D and 3D hybrid organic/inorganic perovskites for optoelectronic and photovoltaic applications., *Opt. Quantum Electron*. 46 **2014**, 1225–1232.

(27) Chakraborty, R. & Nag, A. Dielectric confinement for designing compositions and optoelectronic properties of 2D layered hybrid perovskites. *Phys. Chem. Chem. Phys*. **2021**, 23, 82– 93.

(28) G. H. Fecher, J. Kübler and C. Felser, *Materials*, **2022**, 15, 5812.

(29) Winald R. Kitzmann, John Freudenthal, Antti-Pekka M. Reponen, Zachary A. VanOrman, and Sascha Feldmann *Adv. Mater*. **2023**, 2302279

(30) Sunihl Ma, Jihoon Ahn, and Jooho Moon, *Adv. Mater*. **2021**, 33, 2005760

(31) D. G. Billing and A. Lemmerer, *Acta Crystallogr E Struct Rep Online*, **2003**, 59.

(32) Marco Moroni, Clarissa Coccia and Lorenzo Malavasi * Chiral 2D and quasi-2D hybrid organic inorganic perovskites: from fundamentals to applications, *Chem. Commun.*, **2024**, 60, 9310

(33) Zhao, L.; Han, X.; Zheng, Y.; Yu, M.-H.; Xu, J. Tin-Based Chiral Perovskites with Second-Order Nonlinear Optical Properties. *Adv Photo Res* **2021**, *2*, 2100056.

(34) Rajput, P.K.; Poonia, A.K.; Mukherjee, S.; Sheikh, T.; Shrivastava, M.; Adarsh, K.V.; Nag, A. Chiral Methylbenzylammonium Bismuth Iodide with Zero-Dimensional Perovskite Derivative Structure. *J. Phys. Chem. C* **2022**, *126*, 9889–9897.

(35) Jiang, S.; Zhao, P.; Xing, G.; Kang, H.; Li, X.; Zhao, T.; Li, B.; Zhang, T. Bismuth-Based Chiral Perovskite with Different Dimensions for Second-Order Nonlinear Optical Properties. *Advanced Optical Materials* **2023**, 2203078.

(36) Li, D.; Liu, X.; Wu, W.; Peng, Y.; Zhao, S.; Li, L.; Hong, M.; Luo, J. Chiral Lead-Free Hybrid Perovskites for Self-Powered Circularly Polarized Light Detection. *Angew. Chem. Int. Ed.* **2021**, *60*, 8415–8418.

(37) Liu, H.-L.; Ru, H.-Y.; Sun, M.-E.; Wang, Z.-Y.; Zang, S.-Q. Mixed-Cation Chiral Perovskites Displaying Warm-White Circularly Polarized Luminescence. *Sci. China Chem.* **2023**, *66*, 1425–1434.

(38) L. Zhang, S. Hu, M. Guo, Y. Ren, L. Wei, W. Li, F. Lin, Z. Yang, Z. Yang, C. Liu and B. Liu, *Advanced Materials*, **2023**, 35, 2302059.

(39) T. Duan, Y. Zhou, Leveraging Hierarchical Chirality in Perovskite(-Inspired) Halides for Transformative Device Applications, *Adv. Energy Mater*. **2023**, 33

(40) J. Yao, Z. Wang, Y. Huang, J. Xue, D. Zhang, J. Chen, X. Chen, S.-C. Dong and H. Lu, *J. Am. Chem. Soc.*, **2024**, 146, 14157–14165.

(41) S. Revanakar, S. Jena, H. Krishnaiah, S. Rondiya, *Langmuir* **2025**, 41, 29, 18935-18964.

CHAPTER 2

Ligand-Induced Chirality in Cl-MBA$_2$SnI$_4$ 2D Perovskites

Clarissa Coccia,[a] Marta Morana,[b] Arup Mahata,*[c,d] Waldemar Kaiser,[c] Marco Moroni,[a] Benedetta Albini,[e] Pietro Galinetto,[e] Giulia Folpini,[f] Chiara Milanese,[a] Alessio Porta,[a] Edoardo Mosconi,[c] Annamaria Petrozza,[f] Filippo De Angelis,[c,g,h] and Lorenzo Malavasi*[a]

[a] Department of Chemistry, University of Pavia, Via Taramelli 12, Pavia 27100, Italy

[b] Department of Earth Science, University of Firenze, Via G. La Pira 4, Firenze 50121, Italy

[c] Computational Laboratory for Hybrid/Organic Photovoltaics (CLHYO), Istituto CNR di Scienze e Tecnologie Chimiche „Giulio Natta“ (CRN-SCITEC), Perugia 06123, Italy

[d] Department of Chemistry, Indian Institute of Technology Hyderabad, Knadi, Sangareddy, Telangana 502285, India

[e] Department of Physics, University of Pavia, Via Bassi 6, Pavia 27100, Italy

[f] Center for Nano Science and Technology, Istituto Italiano di Tecnologia, Milan 20133, Italy

[g] Department of Chemistry, Biology and Biotechnology, University of Perugia and INSTM, Perugia 06123, Italy

[h] SKKU Insitute of Energy Science and Technology (SIEST) Sungkyunkwan University, Suwon, Korea 440-746

Corrisponding Authors

Lorenzo Malavasi, email: lorenzo.malavasi@unipv.it

ToC

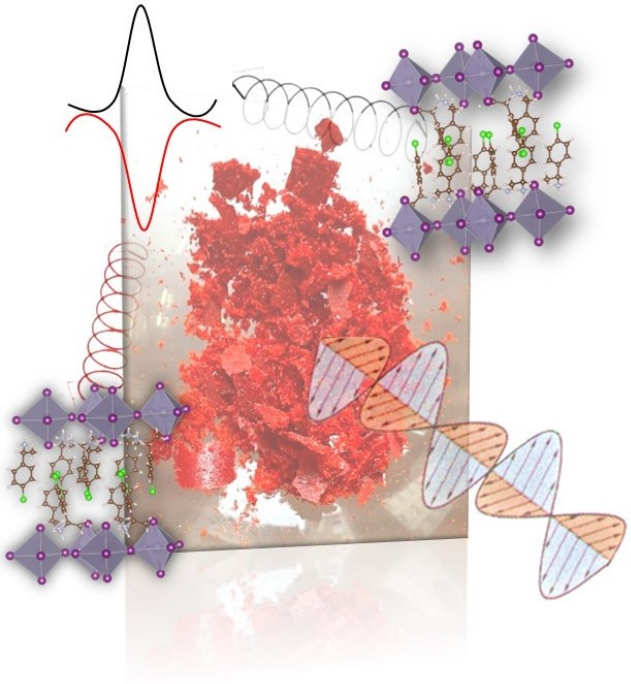

Abstract

Chiral perovskites possess a huge applicative potential in several areas of optoelectronics and spintronics. The development of novel lead-free perovskites with tunable properties is a key topic of current research. Herein, we report a novel lead-free chiral perovskite, namely (*R*/*S*-)ClMBA$_2$SnI$_4$ (ClMBA = 1-(4-chlorophenyl)ethanamine) and the corresponding racemic system. The reported ClMBA$_2$SnI$_4$ samples exhibit a low band gap (2.12 eV) together with broad emission extending in the red region of the spectrum (~1.7 eV). Chirality transfer from the organic ligand induces chiroptical activity in the 465-530 nm range. Density function theory calculations show a Rashba type band splitting for the chiral samples and no band splitting for the racemic isomer. Self-trapped exciton formation is origin of the large Stokes shift in the emission. Careful correlation with analogous lead and lead-free chiral perovskites confirms the role of the symmetry-breaking distortions in the inorganic layers associated with the ligands as the source of the observed chiroptical properties providing also preliminary structure-property correlation in 2D chiral perovskites.

1. Introduction

Chiral metal halide perovskites (MHPs) are emerging as one of the most appealing classes of chiral materials due to their potential use for chiroptoelectronics, spintronics, and ferroelectrics.[1–4] One of the most common strategies used to induce chirality-dependent properties in MHPs, such as circular dichroism (CD), circular polarized luminescence (CPL), chiro-induced spin selectivity (CISS) effect and ferroelectricity, is based on the introduction of a chiral ligand in low-dimensional MHPs. This approach, coupled with their rich structural tunability, made the preparation of 2D, 1D, and 0D chiral MHPs possible. Some of these effects could also be induced by breaking the centrosymmetry by bulky achiral ligands, but the use of chiral pairs not only assures such symmetry break but also allows to better scrutinize the impact of chirality on optoelectronic properties.

Most of the chiral perovskites reported so far are based on the few available chiral ligands on the market such as methylbenzylammonium (MBA), *β*- methylphenethylammonium (MPEA), 1-(naphthyl)ethylammonium (NEA), *R*-3- aminopiperidine (3APD), 3-ammonioquinuclidinium (3AQ), and 2- octylamine (2OA).[5–18] In terms of structural motifs, 2D chiral perovskites are those most commonly reported together with 1D systems, while 3D systems have been predicted but not yet realized.[16,19] This directly correlates to the fact that a chiral center requires organic ligands that are too big to be accommodated into a 3D lattice of interconnected octahedra but are easily inserted in layered systems. In terms of metal ion , analogously to MHPs for photovoltaics, lead has been used to prepare the vast majority of chiral perovskites, with copper being the second most common metal found in currently available chiral perovskites and with just one Sn-containing system reported to date.[1,2,20–25]

In their three dimensional form, in-based perovskites have similar or superior electronic and optical properties to lead-containing systems, such as higher charge carrier mobilities and long-lived hot carriers.[26] In the field of chiral perovskites, except for the (*R*-/*S*-MBA)$_2$SnI$_4$ system (MBA= methylbenzylammonium), no other tin-based materials have been reported so far. However, in view of potential future applications in chiral optoelectronic devices, the use of tin could guarantee a reduced environmental impact and provide the degree of optical properties tunability required. In addition, the design of novel chiral perovskites should be based on solid structure-property correlations, which are the basis of the actual engineering

of perovskites for optoelectronic applications. There are only few structure-property correlations works on chiral perovskite, mainly as a consequence of the limited number of phases with solved crystal structures reported, and few rational series of materials where, for example, the impact of organic ligand, central atom, or halide has been progressively and rationally changed to unveil the respective roles on the chiro-optical response. This is even more dramatic when considering tin-based perovskites.

The performance of chiral perovskites is usually estimated by taking into account the anisotropy factor, g_{CD}, which is the CD normalized to absorption, and it is generally recognized as a quantitative figure-of-merit of chiro-optical activity. In general, higher values of the g_{CD} correlates to higher levels of spin polarizations which are achieved in chiral perovskites without applying an external field. It is imperative to widen the number of available chiral perovskites, particularly lead-free systems, to design MHPs with enhanced anisotropy factor and identify relevant compositional and structural parameters.
With this aim, we designed the $ClMBA_2SnI_4$ chiral perovskites (ClMBA = 1-(4-chlorophenyl)ethanamine) and investigated its crystal structure by room temperature single-crystal x-ray diffraction (SCXRD) together with optical spectroscopy and computational modelling. With respect to the use of MBA cation, introducing Cl on the benzene ring in *para* position with respect to the amine group may introduce further weak bond interactions with the inorganic framework as it has been shown on lead-based similar systems.[27]

2. Results and Discussion

Single crystals of the *R*/*S*- enantiomers and racemic (*rac*) form of $ClMBA_2SnI_4$ have been prepared by solution chemistry (see Supporting Information, SI) and the respective crystal structures are solved by SCXRD. The crystallographic data and selected structural parameters are reported in Table 1. Figure 1 reports a sketch of the respective structures and the appearance of the red crystals of $(R\text{-ClMBA})_2SnI_4$.

The structural arrangement is typical of 2D perovskites with a slab of corner-sharing octahedra separated by two molecules of the ClMBA ligand. The two chiral compositions, *i.e*. $(R\text{-ClMBA})_2SnI_4$ and $(S\text{-ClMBA})_2SnI_4$, crystallize into the triclinic *P*1 chiral space group,

while the racemic form in the centro-symmetric orthorhombic *Pnma*. ClMBA ligand introduces a further reduction of symmetry compared to MBA, where the chiral (*R*-MBA)$_2$SnI$_4$ and (*S*-MBA)$_2$SnI$_4$ crystallize in the orthorhombic $P2_12_12_1$ space group.[25]

Table 1. Crystal structure data for (*R*-ClMBA)$_2$SnI$_4$, (*S*-ClMBA)$_2$SnI$_4$, and (*rac*-ClMBA)$_2$SnI$_4$.

	(*R*-ClMBA)$_2$SnI$_4$	**(*S*-ClMBA)$_2$SnI$_4$**	**(*rac*-ClMBA)$_2$SnI$_4$**
Empirical formula	$C_{16}H_{22}N_2Cl_2I_4Sn$	$C_{16}H_{22}N_2Cl_2I_4Sn$	$C_{16}H_{22}N_2Cl_2I_4Sn$
Formula weight	939.54	939.54	939.54
Temperature	273.5 K	273.5 K	273.5 K
Wavelength	0.71073	0.71073	0.71073
Crystal system	Triclinic	Triclinic	Orthorhombic
Space group	*P1*	*P1*	*Pnma*
Lattice parameters	a = 8.9234(6) Å	a = 8.9085(15) Å	a = = 8.6242(5) Å
	b = 9.0822(8) Å	b = 9.0993(16) Å	b = 9.2932(4) Å
	c = 16.2963(13) Å	c = 16.295(3) Å	c = 32.1932(17) Å
Volume	1306.33(18) Å^3	1306.3(4) Å^3	2580.2(2) Å^3
Z	2	2	4

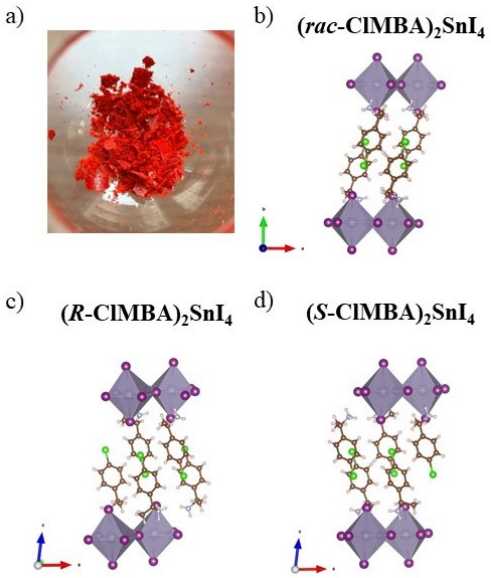

Figure 1. a) Appearance of the crystal of (*R*-ClMBA)$_2$SnI$_4$; sketch of the crystal structures of (*rac*-ClMBA)$_2$SnI$_4$ (b), (*R*-ClMBA)$_2$SnI$_4$ (c), and (S-ClMBA)$_2$SnI$_4$ (d).

The octahedra of (*R*-ClMBA)$_2$SnI$_4$ and (*S*-ClMBA)$_2$SnI$_4$ are distorted, presenting six different bond lengths and an in-plane Sn-I-Sn angle significantly lower than the ideal value of 180°

(around 155°). Such effects are closely related to the hydrogen bond formation and the penetration of the protonated amine group.[25,28,29]
The level of octahedral distortion has been quantified in terms of the octahedral quadratic elongation (λ_{oct}), and their bond angle variance (σ_{oct}^2), as defined by Robison *et al*., as well as by calculating the distortion index, *D*.[30,31] The respective values for these parameters are reported in Table S1 of SI for (*R*-ClMBA)$_2$SnI$_4$, (*S*-ClMBA)$_2$SnI$_4$, and (*rac*-ClMBA)$_2$SnI$_4$.

While the quadratic elongation shows a slight difference among the three perovskites, the racemic compound is characterized by a higher value of both the bond angle variance and the distortion index. Together with the data for the actual perovskites, we added in Table S1, SI, the structural parameters for the other Sn-based chiral system known to date, as well as for the Pb analogues (ClMBA)$_2$PbI$_4$ and (MBA)$_2$PbI$_4$, to identify possible correlations as a function of central metal and organic ligand. The variation of quadratic elongation *vs*. bond angle variance and of these two parameters as a function of NH_3 penetration is reported in Figure S1, SI. As a general trend, lead-containing systems show smaller values of quadratic elongation and of the distortion index for the same organic cation, and slightly higher values of the bond angle variance.
For comparison, the *D* value for (*R*-ClMBA)$_2$SnI$_4$ and (*S*-ClMBA)$_2$SnI$_4$ is about half of that reported by Lu and co-workers for (*R*-MBA)$_2$SnI$_4$ and (*S*-MBA)$_2$SnI$_4$, namely ~0.004 and ~0.008, respectively.[25] On the other hand, by keeping the same central metal (Pb or Sn) and moving from MBA to ClMBA, a general reduction of the distortion index and of the quadratic elongation is observed. However, we realize that the number of chiral 2D perovskites (with solved crystal structure) available and suitable to extract more solid structural correlations is limited. Still, we may, with these preliminary results, suggest a possible route to tune the distortion parameters.

Structural stability of the three 2D perovskites reported here has been determined by means of differential scanning calorimetry (DSC). The respective DSC traces in the range -80-140°C are reported in Figure S2, and do not show any peak indicating the presence of structural phase transitions. Further stability test was related to the air stability of (*R*-ClMBA)$_2$SnI$_4$, (*S*-ClMBA)$_2$SnI$_4$ which, containing Sn(II), may be susceptible of air-degradation. For this purpose, the two perovskites were left in contact with laboratory air (21°C, Relative Humidity 40%) for a varying time from 24 to 156 hours. Figures S3 reports the diffraction patterns as a function of time. After 24 hours some extra peaks in the X-ray

diffraction data start to appear and increase with time even though the main perovskite phase remains present in the whole time interval. Such additional peaks are not related to SnI4 but, possibly, to some unknown mixed oxidized phase.

The optical properties of (*R*-ClMBA)$_2$SnI$_4$, (*S*-ClMBA)$_2$SnI$_4$, and (*rac*-ClMBA)$_2$SnI$_4$ have been determined by UV-Vis, micro-photoluminescence (μPL), CD and CPL spectra. Figure 2a-d shows the corresponding results.

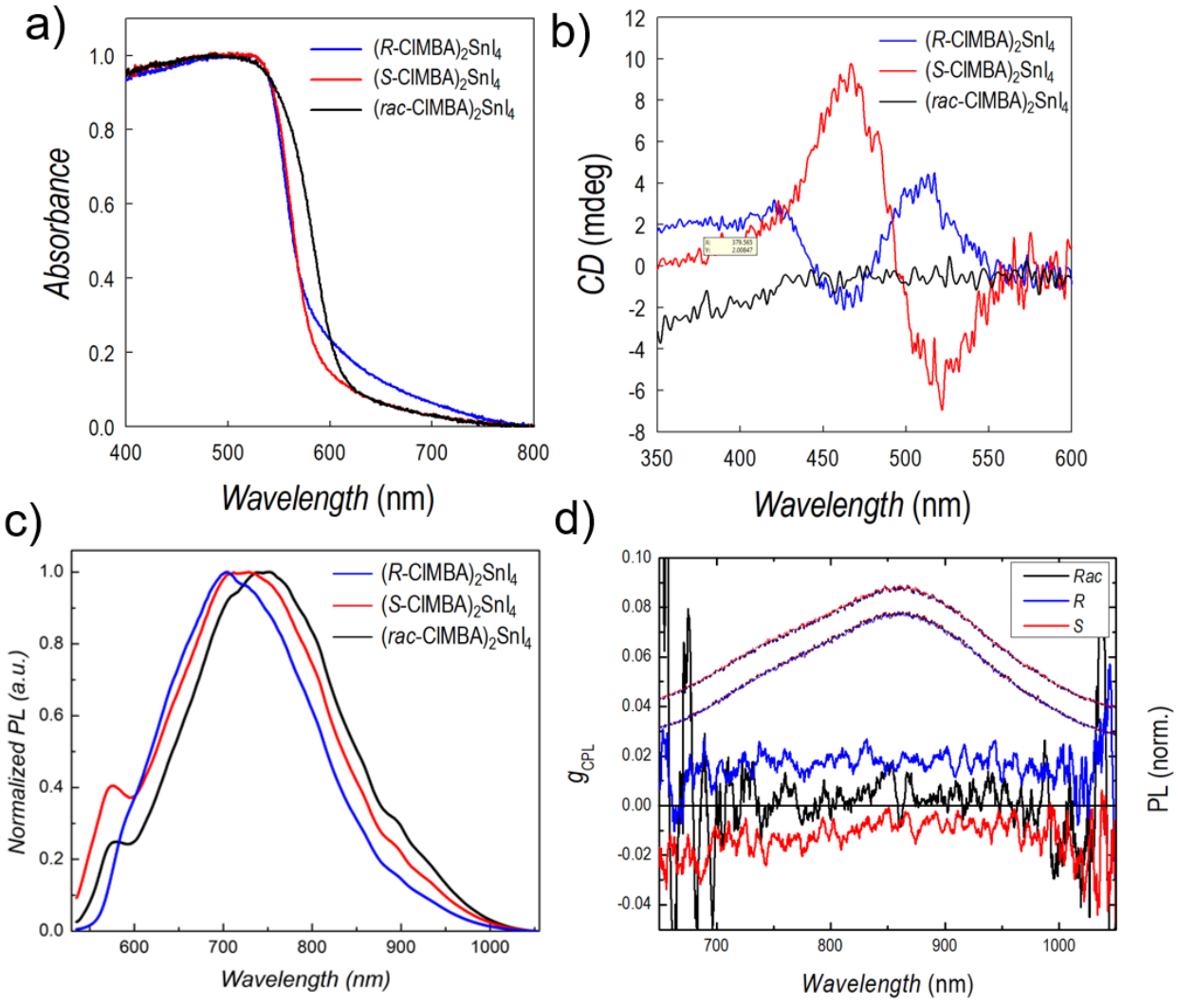

Figure 2. a) Absorbance; b) CD, and c) μPL of (*R*-ClMBA)$_2$SnI$_4$, (*S*-ClMBA)$_2$SnI$_4$, and (*rac*-ClMBA)$_2$SnI$_4$. measured at room temperature. d) g_{CPL} (left axis) and static PL (right axis) measured at 90 K.

Absorption spectra show steep optical band edges around 600 nm with a slight red-shift for (*rac*-ClMBA)$_2$SnI$_4$ compared to the two chiral perovskites. The corresponding optical band gap values have been extracted from the Tauc plots for direct transition (Figure S4) and correspond to about 2.12 eV for the two chiral perovskites and 2.08 for the racemic compound. The band gap of the present samples is among the lowest band gap reported so far for a 2D chiral perovskite, being that of lead-containing materials around 2.3-2.8 eV and ~2.55 for the only other tin-based 2D chiral perovskite, namely (*R/S*-MBA)$_2$SnI$_4$.[1,4,25]

The circular dichroism, carried out on thin films (Figure 2b) of (*R/S*-ClMBA)$_2$SnI$_4$, presents signal in the 400-550 nm spectral range, while (*rac*-ClMBA)$_2$SnI$_4$ does not show any CD. The CD spectra of the two chiral materials have opposite peaks at the same wavelengths, *i.e.* ~465 and ~520 nm, with the last one correlating very well with the linear absorption shown in Figure 2a, interpreted as the Cotton effect, indicating that the chiroptical properties arise from the Sn-I inorganic framework (the chiral group has CD signals around 250 nm, see Figure S5).[32,33] From the CD data we calculated the asymmetry factor, g_{CD}, which resulted to be around 1×10^{-4} for both enantiomers, in line with the values usually found in 2D chiral perovskites. This value is close to the value we extracted from ref. 25 for (*R/S*-MBA)$_2$SnI$_4$, where the asymmetry factor is not reported, and corresponding to about 3×10^{-4}.

The PL spectra of the three 2D perovskites shown in Figure 2c presents a minor emission tail close to the optical absorption edge and broad peaks (Full Width at Half Maximum, FWHM, of about 200 nm) with a significant Stokes shift and emission centered around 720-740 nm (1.72-1.67 eV). Such broad emission is not found in the corresponding Pb-containing perovskites where, in addition, the Stokes shift is of only 15-20 nm.[33] This difference in the emission properties may be related to the degree of distortion of the octahedra. As a matter of fact, by comparing Table S1, it can be seen that the distortion index, as well as the bond-angle variance values of the present samples, is significantly higher than the corresponding Pb-analogues.[28,34–36] We remark that achieving chiral perovskites with emission in the red part of the visible spectrum may be of interest for future applications and the present samples are among the first examples of chiral lead-free 2D perovskites possessing such characteristic.

The origin of the broadband emission observed in ClMBA$_2$SnI$_4$ is investigated by measuring the fluence dependence of the integrated PL signal of *R*-, *S*- and racemic samples (Fig. S6).

It indicates that the broadband emission can be fit with a power law $I_{PL} = I_0 P_{laser}^k$ with k ≈ 0.8 for all samples. While free excitonic recombination is characterized by *k* =1, a value of *k* <≈ 1 indicates contributions from trap-assisted recombination. However, considering that the broadband emission completely overwhelms any excitonic contribution to the material luminescence as well as the power dependence not too far from linearity, we expect distortion of the crystal lattice to also play a role in the observed broadband emission, resulting in significant contributions from STEs. In addition, as we recently demonstrated, the presence of Stokes-shifted broad emission in the absence of a STE would require an enormous defect density and, considering the relatively sharp absorption edges (cfr. Fig 2a), halide vacancies alone may not cause the observed Stoke shift and broad emission.[37] This is further supported by the significant increase in luminescence observed at cryogenic temperatures (Fig. S7) particularly of the 800 nm spectral component compared to the region closer the absorption edge. We have also characterized the PL lifetime of the materials (Fig. S8), finding that the broadband emission for all samples extends up to tens of nanoseconds, with a fast 55 ps decay component and a longer lived 500 ps decay. Interestingly, at very early times for the racemic compound it is possible to observe a small PL contribution from a free exciton, with a much faster lifetime of 6.5 ps: as the excitonic emission quickly disappears, a small corresponding increase is observed in the broadband emission (Fig. S8b), suggesting a transfer to a localized state over 10 ps.

From a computational point of view, we have attempted to find out the underlying reason for the broad emission by investigating the energetics of the self-trapped excitons (STE) emission pathway. For a ready comparison, we have studied our Sn-based (*R*-isomer) system and the corresponding Pb counterpart, where such broad emission is found to be absent.[34] STE emission energy has been calculated, following the approach of our previous studies, by considering the energy difference between the energies of the triplet and singlet states (at the equilibrium geometry of triplet state) as schematically described by point 3 and point 4, respectively in the Figure 3d.[37,38] We have found an excellent agreement of emission energy of 1.70 eV compared to that of experiment, where the emission peak appears around 720-740 nm (1.72-1.67 eV). Furthermore, as shown in Figure 3e, the Kohn-Sham (KS) orbitals of the relaxed excited triplet state show the different spatial localization of the electron and hole charge density along with substantial Sn-I bond length lengthening (average 3.54 Å) and shortening (average 3.06 Å), thus indicating the formation of STE. On the other hand, the Pb-counterpart shows a delocalized electron and hole charge density as

shown in Figure S9 in SI. Furthermore, the calculated triplet and singlet relaxation energies, as depicted in Figure 3d, for the Sn-system are 277 and 565 meV, respectively, compared to that of 88 and 56 meV for Pb-system. Therefore, the broad *vs*. sharp emission in Sn- and Pb-systems can be assigned for localized (STE formation) and delocalized (band-to-band transition) exited states, respectively. It is noteworthy to mention that halide vacancies may also open emission channels, which may contribute to the broad emission. Nevertheless, our high-level calculations provide a vis-à-vis comparison of the excited state behavior of the Sn- and Pb-systems, reasonably explaining the experimental emission characteristic.

Finally, we characterized the chirality of the PL emission of crystalline samples, as shown in Fig. 2d. In order to enhance the strength of the chiral luminescence response, these measurements were conducted at cryogenic temperatures, *i.e.* 90K. The PL intensity is strongly increased, particularly the broad component around 800 nm (Fig. S7). Comparing the left hand and right hand circularly polarized component of the photoluminescence (Fig. 2d, right *y*-axis), we calculate the $g_{CPL} = 2(I_{RH} - I_{LH})/I_{RH} + I_{LH}$, obtaining a PL dichroism of the order of 0.02 with opposite sign for the *R*- and *S*-ClMBA$_2$SnI$_4$, while the racemic material show no sign of circular dichroism in its emission.

To gain insight into the electronic structure of the ClMBA$_2$SnI$_4$ compounds, Density Functional Theory (DFT) calculations have been carried out for the *R*- and *S*- and racemic configurations. As expected, the three enantiomers show very similar electronic properties with the band gap of 2.50, 2.51 and 2.39 eV for the *R*- and *S*- and racemic configurations, respectively, which is consistent with the experimental band gap trend showing a little lower band gap for the racemic isomer compared to the chiral samples. Figure 3a shows the projected densities of states (DOS) with the contributions of different atomic species for the *R*-isomers (see Figure S10 in SI for *S*- and Racemic isomers). As can be seen, the band edges are dominated by I and Sn contributions, while the Cl contributions lie far from the band edges as also evidenced by the band edge wave functions (Figure S11). Further, we have calculated the electronic band structure of the three systems, and the results (Figure 3b-c and Figure S12) show that all the structures have a direct band gap, which is consistent with the experimental optical results.

To investigate the spin characteristics, we have calculated the spin splitting of the electronic band structures for chiral and racemic isomers by calculating the Rashba spin–orbit splitting.

Typically, a specific conformational characteristic of organic cations with chiral space group can exert inorganic layer distortion in such a way that breaks the inversion symmetry of the system, leading to Rashba spin–orbit splitting. Such spin splitting, in principle, should be absent in racemic isomer due to presence of centro-symmetric space group in the structure. As happens in typical Rashba spin–orbit splitting, both valence and conduction band split away from the Γ point, leading to valence band maximum (VBM) and conduction band minimum (CBM) which are shifted in k-space by Δk, with the band energy splitting ($\varepsilon^{\neq}$).[39–41] The Rashba interaction parameter is defined as $\alpha=\varepsilon^{\neq}/2\Delta k$. The band structure of chiral (*R*-isomer) and racemic isomers have been shown in Figure 3b-c, whereas the *S*-isomer has been shown in Figure S12. As can be seen from Figure 3b-c, and Table 1, the frontier bands (both VB and CB) show a Rashba type band splitting, with the highest spin splitting values of 17.8 and 16.4 meV for the conduction and valence band, respectively for the *R*-isomer. *S*-isomer also shows almost similar types of splitting values of 16.9 and 18.7 meV for the frontier conduction and valence band, respectively. As expected, no band splitting has been found for the racemic isomer. While looking at the Rashba parameter, the *R*- and *S*-isomer show the maximum values of 1.06 and 1.03 eV Å, respectively.

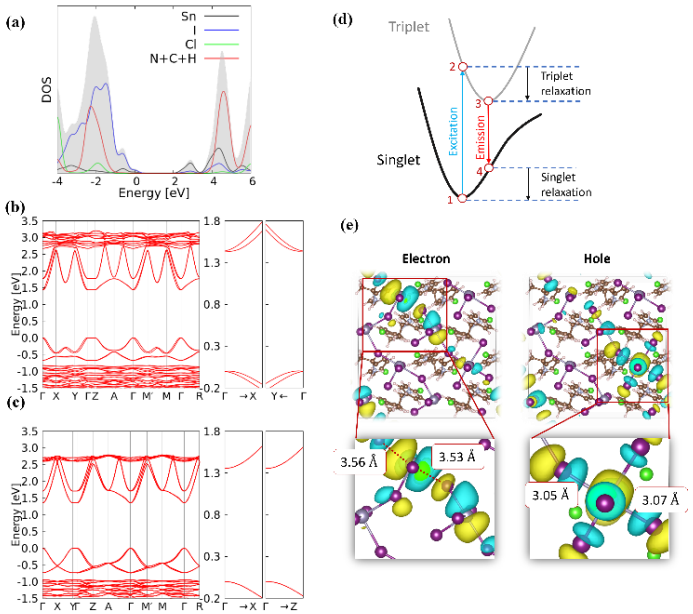

Figure 3. (a) Projected density of states (HSE06-SOC level) of *R*-isomer. Band structure (PBE-SOC level) of (b) *R*- and (c) Racemic isomers. Right panel of the (b) and (c) represents the zoomed figure considering the four frontier bands. The VBM has been set to zero in both the band structure and DOS figures. The *z*- and *y*-direction represent the stacking direction for the chiral and Racemic isomers, respectively. (d) Schematic Jablonski diagram describing the formation mechanism of STEs and the red-shifted PL emission from the STE to the ground state potential energy surface. (e) Kohn-Sham (KS) orbitals of the electron and hole in triplet state.

Table 2. Calculated spin splitting and Rashba parameter for the *R*- and *S*-isomers at the frontier valence and conduction bands in various directions.

		CBM				VBM			
		Γ → X	Γ → Y	Γ→M′	Γ→M	Γ → X	Γ → Y	Γ→M′	Γ→M
Splitting Energy (meV)	R	17.8	11.1	11.1	17.8	10.4	16.3	16.4	10.2
	S	16.8	11.0	11.0	16.9	6.8	18.6	18.7	6.68
Rashba Parameter (α)	R	1.06	0.83	0.74	0.99	0.68	0.86	0.77	0.63
	S	1.03	0.82	0.73	0.96	0.55	0.92	0.82	0.51

Computational results confirm the ability of the ClMBA chiral ligands to induce a band splitting which correlates to the emergence of chiroptical properties. Based on the present evidence, the origin of such an effect can be related to the symmetry-breaking distortions in the inorganic layers associated with the ligands. For (*R/S*-ClMBA)$_2$SnI$_4$, this occurs at the level of the average structure and not to possible local asymmetry within the inorganic framework. Indeed, Mitzi and co-workers highlighted the role of structural descriptor in 2D hybrid perovskites suggesting that spin-splitting could be related to a specific in-plane component of the disparity in adjacent M-X-M bond angles, namely the distortion level of the inter-octahedral bond angles (defined as ($\Delta\beta_{in}$).[42] Such parameter scales linearly with the effective α value (calculated from DFT) for a series of chiral and achiral 2D perovskites.

Interestingly, this correlation does not hold for the present chiral 2D perovskites where the $\Delta\beta_{in}$ parameter is even greater for the racemic sample (not presenting any spin-splitting). It should be noted, however, that the model proposed in ref. 42 refers only to lead-based 2D perovskites. The present results, being the first where the Rashba parameter has been calculated for a Sn-containing 2D chiral perovskite, further point out the strong need to further widen the number and type of chiral perovskites available. Many open questions still hold, such as the role of spin-orbit coupling related to the nature of the metal ion, the role of local and average inversion symmetry breaking on the emergence of Rashba splitting, the influence of hydrogen bonding, etc. The present paper, while reporting novel chiral lead-free perovskites with one of the lowest band gaps to date, has also highlighted the strong need

for further materials chemistry efforts in order to provide solid and reliable structure-property correlations in these appealing materials to pave the way for an effective materials design.

3. Conclusions

Herein we reported novel lead-free 2D chiral perovskites, namely (*R*/*S*-ClMBA)$_2$SnI$_4$. The crystal structure investigation confirmed the crystallization in non-centrosymmetric space groups for the *R*- and *S*- enantiomers, opposite to the racemic compound. The presence of chiral ligands effectively induces the emergence of chiroptical properties, as demonstrated by the CD spectra. The optical properties determination by UV-vis spectroscopy and PL shows a direct band gap of about 2.12 eV for the two chiral perovskites and 2.08 for the racemic compound with a broad emission centered around 1.70 eV. DFT calculation confirms Rashba band splitting, with the highest spin splitting values of 17.8 and 18.7 meV for the *R*- and *S*-isomer, respectively, and without any splitting for the racemic composition, thus confirming the structural distortion induced by chiral organic cations. Such structural distortions eventually lead to the formation of STEs and concomitant red-shifted emission highlighting the impact of local environment on the electronic properties.[43] Thanks to the reported data on this new system, some preliminary attempts to correlate chiroptical properties to structural distortions and the nature of the central metal are proposed. By comparing the present chiral 2D perovskites with the analogue Pb-based compositions, namely (*R*/*S*-ClMBA)$_2$PbI$_4$, it can be seen that replacing lead with tin lead to a further reduction of the crystal symmetry, to a variation of the octahedral distortion parameters, to a reduction of the band gap from 2.55 eV (Pb) to 2.12 eV (Sn) and a strong variation from a narrow emission to a broad emission centered in the red region of the visible spectrum.

Overall, this work reported a novel low band gap Sn-based 2D chiral perovskite which allowed tuning the chiroptical properties through the inclusion of Cl-MBA ligand and provided novel clues to extend the actual comprehension of the structure-property correlations in chiral perovskites.

Acknowledgements

LM acknowledges support from the Ministero dell'Università e della Ricerca (MUR) and the University of Pavia through the program "Dipartimenti di Eccellenza 2023–2027" and through PRIN2022 projects "MIRROR" and "REVOLUTION". W.K, E.M, and F.D.A. acknowledge funding from the European Union's Horizon Europe research and innovation programme under grant agreement No. 101082176 – VALHALLA and from the European UnionNextGenerationEU under the Italian Ministry of University and Research (MUR) National Innovation Ecosystem grant ECS00000041 - VITALITY. Views and opinions expressed are, however, those of the author(s) only and do not necessarily reflect those of the European Union or CINEA. Neither the European Union nor the granting authority can be held responsible for them.

The first-author Clarissa Coccia, author of the present Ph.D. work, carried out the synthesis of all the materials and part of the optical characterization: Absorption spectra, CD Spectra and the connected part of the revision of the paper.

References

(1) Y. Dang, X. Liu, B. Cao, X. Tao, *Matter* **2021**, *4*, 794–820.

(2) G. Long, R. Sabatini, M. I. Saidaminov, G. Lakhwani, A. Rasmita, X. Liu, E. H. Sargent, W. Gao, *Nat Rev Mater* **2020**, *5*, 423–439.

(3) Y. Dong, Y. Zhang, X. Li, Y. Feng, H. Zhang, J. Xu, *Small* 2019, *15*, 1902237.

(4) J. Ma, H. Wang, D. Li, *Adv. Mater.* **2021**, *33*, 2008785.

(5) D. G. Billing, A. Lemmerer, *CrystEngComm* **2006**, *8*, 686–695.

(6) J. Ma, C. Fang, C. Chen, L. Jin, J. Wang, S. Wang, J. Tang, D. Li, *ACS Nano* **2019**, *13*, 3659–3665.

(7) C. Yang, W. Chen, Y. Ding, J. Wang, Y. Rao, W. Liao, Y. Tang, P. Li, Z. Wang, R. Xiong, *Adv. Mater.* **2019**, *31*, 1808088.

(8) M. K. Jana, R. Song, H. Liu, D. R. Khanal, S. M. Janke, R. Zhao, C. Liu, Z. Valy Vardeny, V. Blum, D. B. Mitzi, *Nat Commun* **2020**, *11*, 4699.

(9) T. Liu, W. Shi, W. Tang, Z. Liu, B. C. Schroeder, O. Fenwick, M. J. Fuchter, *ACS Nano* **2022**, *16*, 2682–2689.

(10) G. Long, C. Jiang, R. Sabatini, Z. Yang, M. Wei, L. N. Quan, Q. Liang, A. Rasmita, M. Askerka, G. Walters, X. Gong, J. Xing, X. Wen, R. Quintero-Bermudez, H. Yuan, G. Xing, X. R. Wang, D. Song, O. Voznyy, M. Zhang, S. Hoogland, W. Gao, Q. Xiong, E. H. Sargent, *Nature Photon* **2018**, *12*, 528–533.

(11) Y. Peng, Y. Yao, L. Li, Z. Wu, S. Wang, J. Luo, *J. Mater. Chem. C* **2018**, *6*, 6033–6037.

(12) C. Yuan, X. Li, S. Semin, Y. Feng, T. Rasing, J. Xu, *Nano Lett.* **2018**, *18*, 5411–5417.

(13) C. Chen, L. Gao, W. Gao, C. Ge, X. Du, Z. Li, Y. Yang, G. Niu, J. Tang, *Nat Commun* **2019**, *10*, 1927.

(14) J. Ahn, S. Ma, J.-Y. Kim, J. Kyhm, W. Yang, J. A. Lim, N. A. Kotov, J. Moon, *J. Am. Chem. Soc.* **2020**, *142*, 4206–4212.

(15) D. Fu, J. Xin, Y. He, S. Wu, X. Zhang, X. Zhang, J. Luo, *Angew Chem Int Ed* **2021**, *60*, 20021–20026.

(16) Y. Dang, X. Liu, Y. Sun, J. Song, W. Hu, X. Tao, *J. Phys. Chem. Lett.* **2020**, *11*, 1689–1696.

(17) H. Lu, J. Wang, C. Xiao, X. Pan, X. Chen, R. Brunecky, J. J. Berry, K. Zhu, M. C. Beard, Z. V. Vardeny, *Sci. Adv.* **2019**, *5*, eaay0571.

(18) J. Ahn, E. Lee, J. Tan, W. Yang, B. Kim, J. Moon, *Mater. Horiz.* 2017, *4*, 851–856.

(19) G. Long, Y. Zhou, M. Zhang, R. Sabatini, A. Rasmita, L. Huang, G. Lakhwani, W. Gao, *Adv. Mater.* **2019**, *31*, 1807628.

(20) Z. Guo, J. Li, C. Wang, R. Liu, J. Liang, Y. Gao, J. Cheng, W. Zhang, X. Zhu, R. Pan, T. He, *Angew. Chem. Int. Ed.* **2021**, *60*, 8441–8445.

(21) J. Hao, H. Lu, L. Mao, X. Chen, M. C. Beard, J. L. Blackburn, *ACS Nano* **2021**, *15*, 7608–7617.

(22) B. Li, Y. Yu, M. Xin, J. Xu, T. Zhao, H. Kang, G. Xing, P. Zhao, T. Zhang, S. Jiang, *Nanoscale* **2023**, *15*, 1595–1601.

(23) Y. Lu, Q. Wang, R. He, F. Zhou, X. Yang, D. Wang, H. Cao, W. He, F. Pan, Z. Yang, C. Song, *Angew. Chem. Int. Ed.* **2021**, *60*, 23578–23583.

(24) R. Das, M. Hossain, A. Mahata, D. Swain, F. De Angelis, P. K. Santra, D. D. Sarma, *ACS Materials Lett.* **2023**, 1556–1564.

(25) H. Lu, C. Xiao, R. Song, T. Li, A. E. Maughan, A. Levin, R. Brunecky, J. J. Berry, D. B. Mitzi, V. Blum, M. C. Beard, *J. Am. Chem. Soc.* **2020**, *142*, 13030–13040.

(26) M. Pitaro, E. K. Tekelenburg, S. Shao, M. A. Loi, *Advanced Materials* **2022**, *34*, 2105844.

(27) Z. Zhang, Z. Wang, H. H.-Y. Sung, I. D. Williams, Z.-G. Yu, H. Lu, *J. Am. Chem. Soc.* **2022**, *144*, 22242–22250.

(28) R. Chiara, M. Morana, G. Folpini, A. Olivati, B. Albini, P. Galinetto, L. Chelazzi, S. Ciattini, E. Fantechi, S. A. Serapian, A. Petrozza, L. Malavasi, *J. Mater. Chem. C* **2022**, *10*, 12367–12376.

(29) R. Chiara, M. Morana, M. Boiocchi, M. Coduri, M. Striccoli, F. Fracassi, A. Listorti, A. Mahata, P. Quadrelli, M. Gaboardi, C. Milanese, L. Bindi, F. De Angelis, L. Malavasi, *J. Mater. Chem. C* **2021**, *9*, 9899–9906.

(30) K. Robinson, G. V. Gibbs, P. H. Ribbe, *Science* **1971**, *172*, 567–570.

(31) W. H. Baur, *Acta Crystallogr B Struct Sci* **1974**, *30*, 1195–1215.

(32) A. Ben-Moshe, A. Teitelboim, D. Oron, G. Markovich, *Nano Lett.* **2016**, *16*, 7467–7473.

(33) J. Lin, D. Chen, L. Yang, T. Lin, Y. Liu, Y. Chao, P. Chou, C. Chiu, *Angew Chem Int Ed* **2021**, *60*, 21434–21440.

(34) X. Li, J. M. Hoffman, M. G. Kanatzidis, *Chem. Rev.* **2021**, *121*, 2230–2291.

(35) D. Cortecchia, J. Yin, A. Petrozza, C. Soci, *J. Mater. Chem. C* **2019**, *7*, 4956–4969.

(36) D. Cortecchia, S. Neutzner, A. R. Srimath Kandada, E. Mosconi, D. Meggiolaro, F. De Angelis, C. Soci, A. Petrozza, *J. Am. Chem. Soc.* **2017**, *139*, 39–42.

(37) L. Malavasi, W. Kaiser, F. De Angelis, E. Mosconi, M. Morana, R. Chiara, D. Meggiolaro, P. Galinetto, B. Albini, *Origin of Broad Emission Induced by Rigid Aromatic Ditopic Cations in Low-Dimensional Metal Halide Perovskites*, Chemistry, **2023**.

(38) S. Kahmann, D. Meggiolaro, L. Gregori, E. K. Tekelenburg, M. Pitaro, S. D. Stranks, F. De Angelis, M. A. Loi, *ACS Energy Lett.* **2022**, *7*, 4232–4241.

(39) T. Etienne, E. Mosconi, F. De Angelis, *J. Phys. Chem. Lett.* **2016**, *7*, 1638–1645.

(40) Abd. R. B. Mohd Yusoff, A. Mahata, M. Vasilopoulou, H. Ullah, B. Hu, W. Jose Da Silva, F. Kurt Schneider, P. Gao, A. V. Ievlev, Y. Liu, O. S. Ovchinnikova, F. De Angelis, M. Khaja Nazeeruddin, *Materials Today* **2021**, *46*, 18–27.

(41) A. Bernasconi, A. Rizzo, A. Listorti, A. Mahata, E. Mosconi, F. De Angelis, L. Malavasi, *Chem. Mater.* **2019**, *31*, 3527–3533.

(42) M. K. Jana, R. Song, Y. Xie, R. Zhao, P. C. Sercel, V. Blum, D. B. Mitzi, *Nat Commun* **2021**, *12*, 4982.

(43) A. Pisanu, A. Mahata, E. Mosconi, M. Patrini, P. Quadrelli, C. Milanese, F. De Angelis, L. Malavasi, *ACS Energy Lett.* **2018**, *3*, 1353–1359

SUPPLEMENTARY INFORMATION

Ligand-Induced Chirality in Cl-MABA$_2$SnI$_4$ 2D Perovskites

Clarissa Coccia,[a] Marta Morana,[b] Arup Mahata,*[c,d] Waldemar Kaiser,[c] Marco Moroni,[a] Benedetta Albini,[e] Pietro Galinetto,[e] Giulia Folpini,[f] Chiara Milanese,[a] Alessio Porta,[a] Edoardo Mosconi,[c] Annamaria Petrozza,[f] Filippo De Angelis,[c,g,h] and Lorenzo Malavasi*[a]

[a] Department of Chemistry, University of Pavia, Via Taramelli 12, Pavia 27100, Italy

[b] Department of Earth Science, University of Firenze, Via G. La Pira4, Firenze 50121, Italy

[c] Computational Laboratory for Hybrid/Organic Photovoltaics (CLHYO), Istituto CNR di Scienze e Tecnologie Chimiche „Giulio Natta“ (CRN-SCITEC), Perugia 06123, Italy

[d] Department of Chemistry, Indian Institute of Technology Hyderabad, Knadi, Sangareddy, Telangana 502285, India

[e] Department of Physics, University of Pavia, Via Bassi 6, Pavia 27100, Italy

[f] Center for Nano Science and Technology, Istituto Italiano di Tecnologia, Milan 20133, Italy

[g] Department of Chemistry, Biology and Biotechnologu, University of Perugia and INSTM, Perugia 06123, Italy

[h] SKKU Insitute of Energy Science and Technology (SIEST) Sungkyunkwan University, Suwon, Korea 440-746

Corrisponding Authors

Lorenzo Malavasi, email: lorenzo.malavasi@unipv.it

Table S1. Octahedral distortion parameters, bond angles, and asymmetry factor for selected chiral 2D perovskites.

Compound	Distortion Index (10^{-3})	Bond angle variance (deg^2)	Quadratic elongation	g_{CD}	NH_3 penetration (Å)	M-X-M
(*R*-ClMBA)$_2$SnI$_4$	41	10.2286	1.0062	$1 * 10^{-4}$	0.412	155.95(4)
(*S*-ClMBA)$_2$SnI$_4$	42	10.4871	1.0062	$-1 * 10^{-4}$	0.404	155.79(5)
(*rac*-ClMBA)$_2$SnI$_4$	51	14.4544	1.0081		0.425	151.03(2)
(*R*-MBA)$_2$SnI$_4$	79	10.3754	1.0112	$2.4 * 10^{-4}$	0.495	153.52(1)
(*S*-MBA)$_2$SnI$_4$	79	10.3515	1.0113		0.450	153.24(1)
(*rac*-MBA)$_2$SnI$_4$	76	13.0348	1.0115		0.446	154.69(1)
(*R*-ClMBA)$_2$PbI$_4$	14	11.2159	1.0036	$3.1 * 10^{-3}$	0.417	154.51(2)
(*S*-ClMBA)$_2$PbI$_4$	15	10.9071	1.0035	$-3.1 * 10^{-3}$	0.440	154.11(1)
(*rac*-ClMBA)$_2$PbI$_4$	10	12.8567	1.0039		0.442	152.72(2)
(*R*-MBA)$_2$PbI$_4$	22	18.5367	1.0060	$-1 * 10^{-3}$		
(*S*-MBA)$_2$PbI$_4$	22	18.9285	1.0061	$1 * 10^{-3}$		
(*rac*-MBA)$_2$PbI$_4$	14	14.5563	1.0046		0.477	155.40(1)

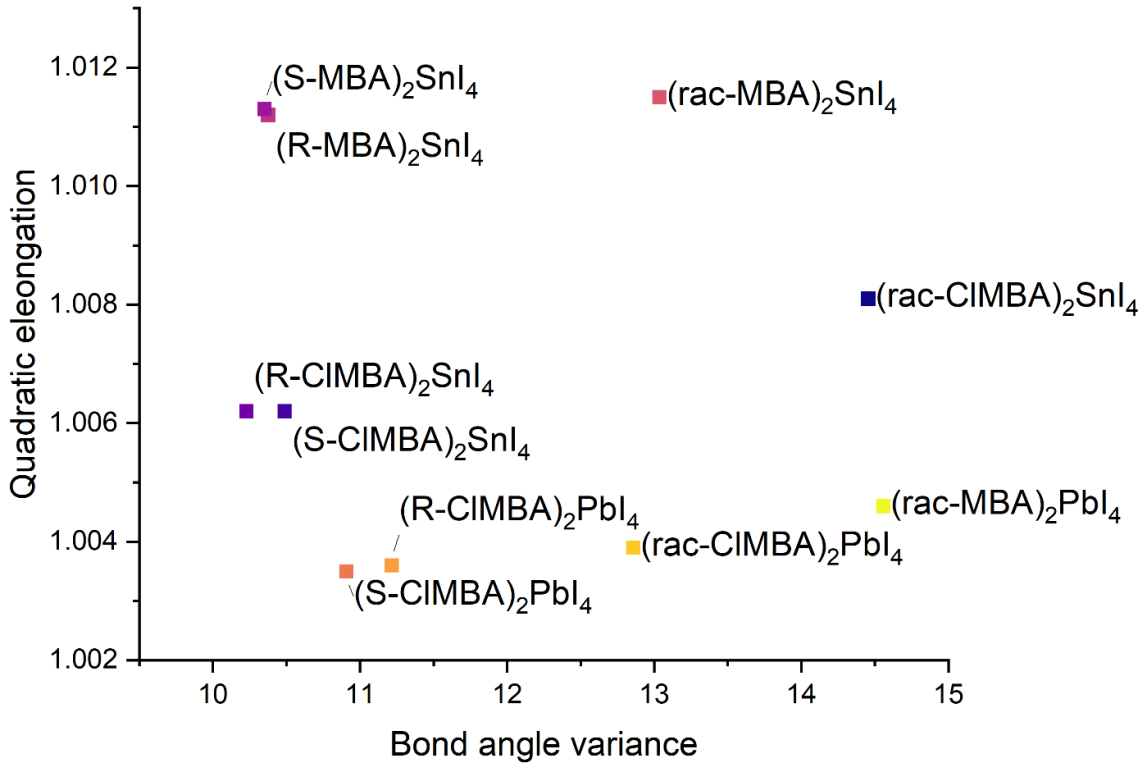

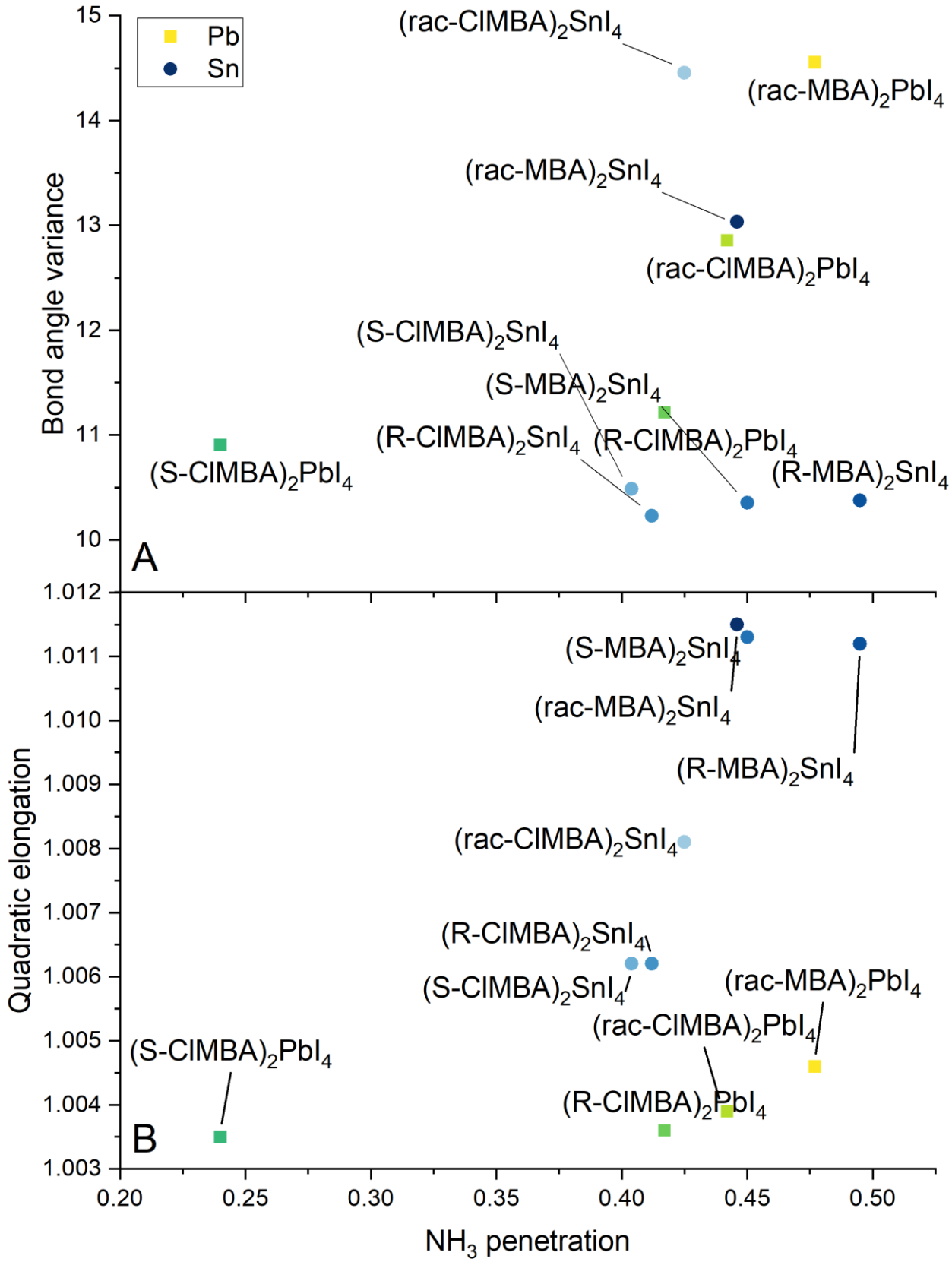

Figure S1. Distortion parameters for selected 2D chiral perovskites.

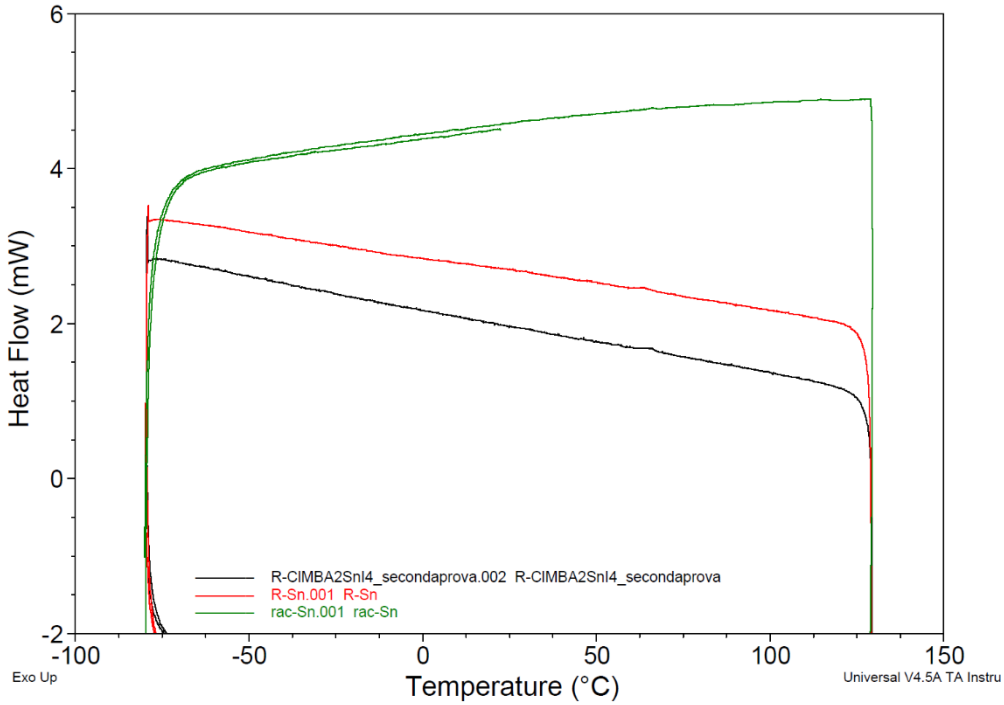

Figure S2. DSC traces from -80 to 140°C for (*R*-ClMBA)$_2$SnI$_4$ (black curve), (*S*-ClMBA)$_2$SnI$_4$ (red curve), and (*rac*-ClMBA)$_2$SnI$_4$ (green curve).

a)

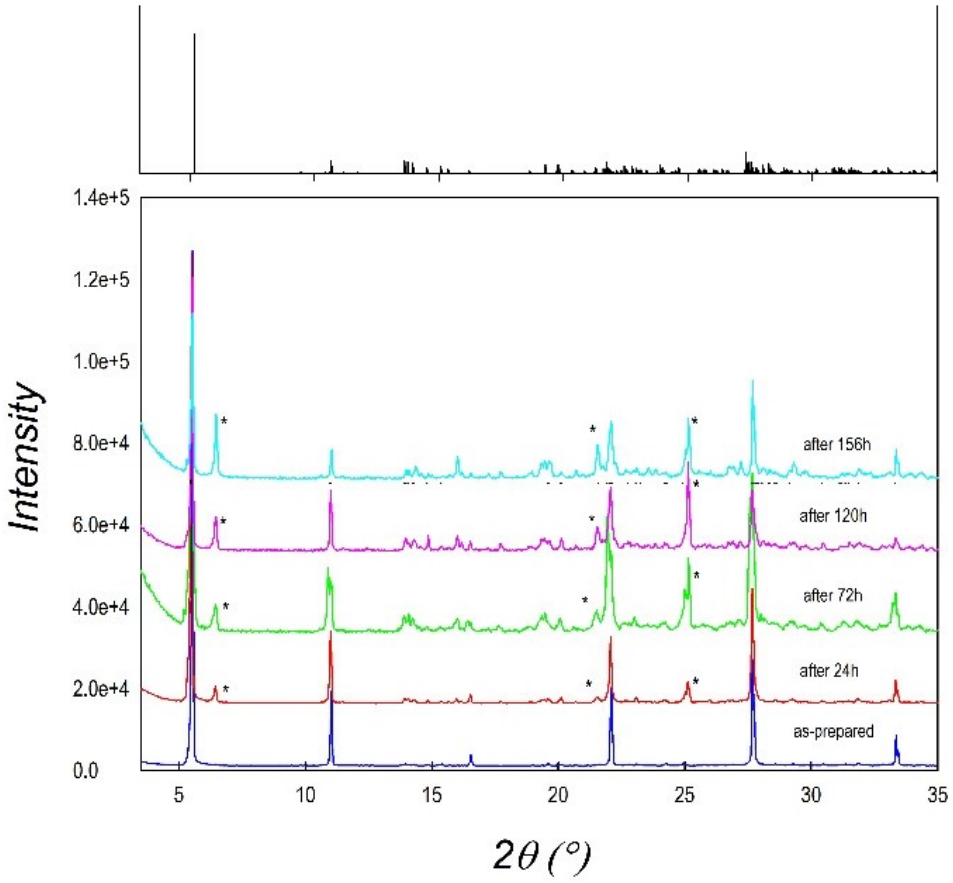

b)

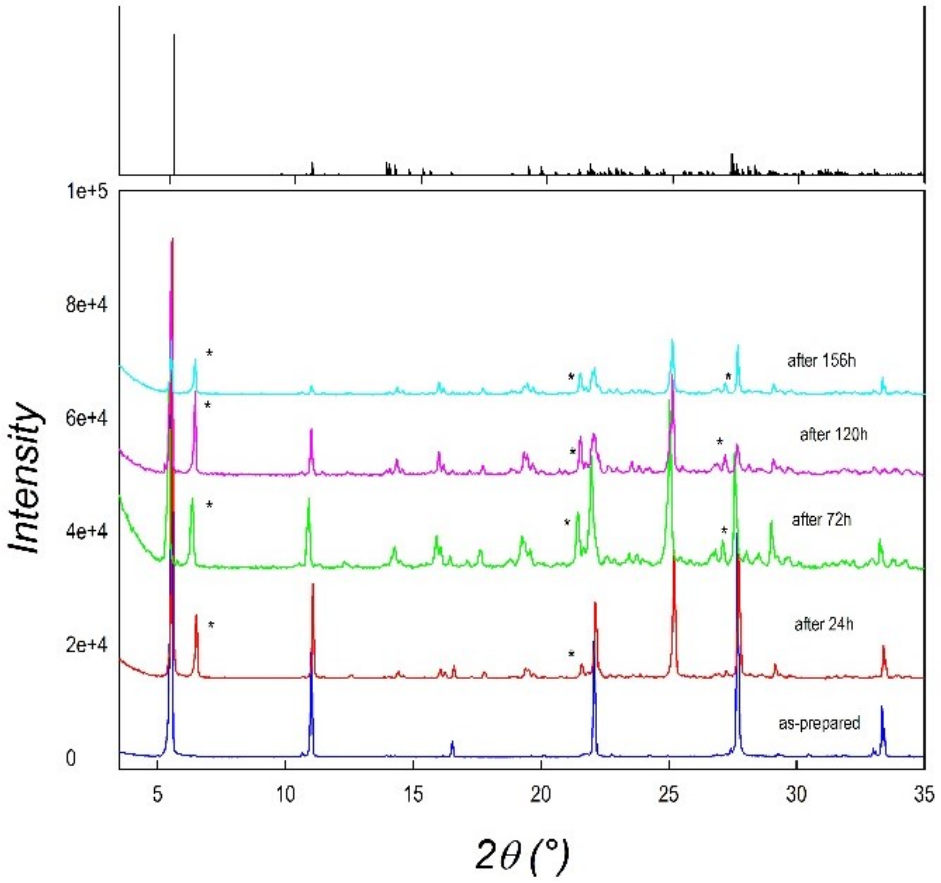

Figure S3. XRD data as a function of time for (a) (*R*-ClMBA)$_2$SnI$_4$ and (b) (*S*-ClMBA)$_2$SnI$_4$ after air exposure. For both figures the calculated pattern is reported at the top of the plots. Asterisks mark the novel peaks appeared.

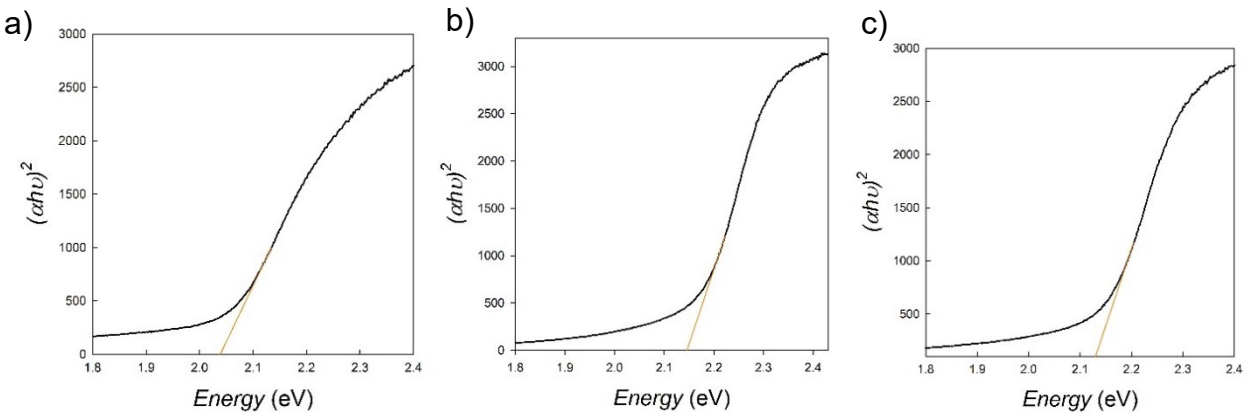

Figure S4. Tauc plots for a) (rac-ClMBA)$_2$SnI$_4$; b) (*R*-ClMBA)$_2$SnI$_4$, and c) (*S*-ClMBA)$_2$SnI$_4$.

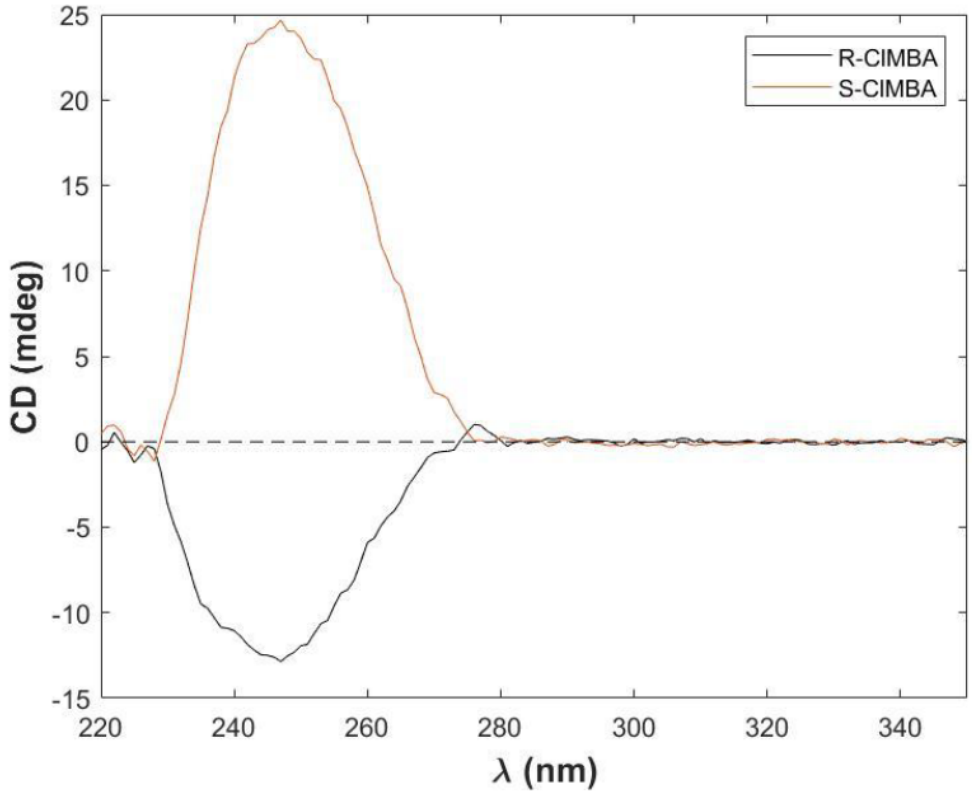

Figure S5. CD spectrum of *R*-ClMBA and *S*-ClMBA

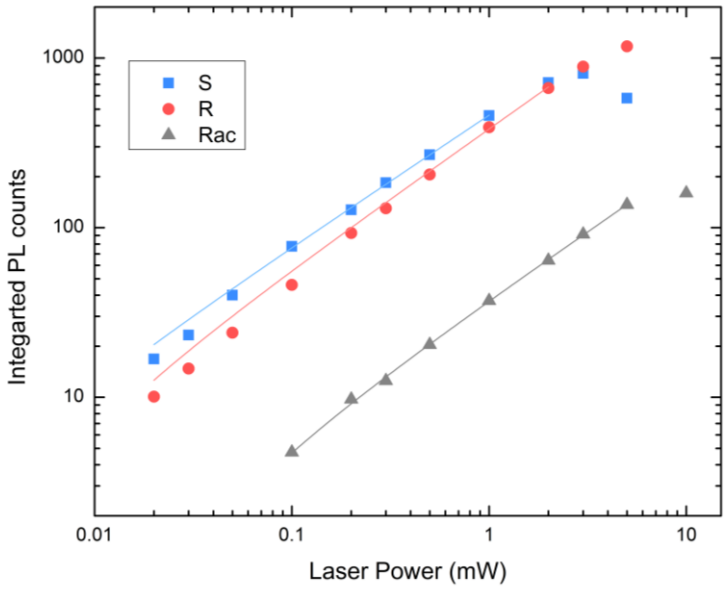

Sample	k
R	0.77 ± 0.02
S	0.82 ± 0.03
Rac	0.8 ± 0.02

Figure S6: Fluence dependence of the PL of *S*, *R*- and racemic $CIMBA_2SnI_4$, fit with the expression $I_{PL} = I_0 P_{laser}^{k}$.

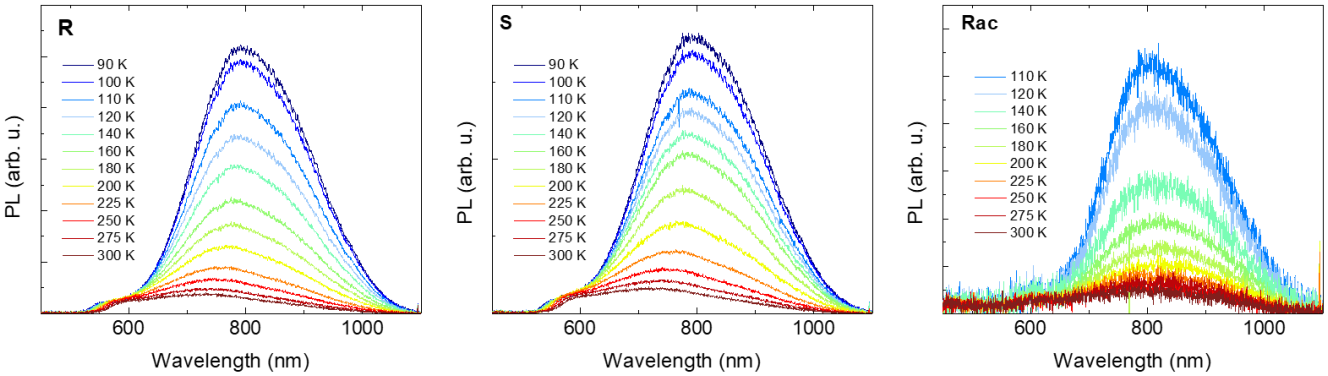

Figure S7*:* Temperature dependent photoluminescence spectra of *R*-, *S*- And racemic $CIMBA_2SnI_4$. As the temperature decreases, the intensity of the broadband emission component is increased, with its 800 nm peak gaining strength compared to the 500-600 nm spectral region closer to the absorption edge.

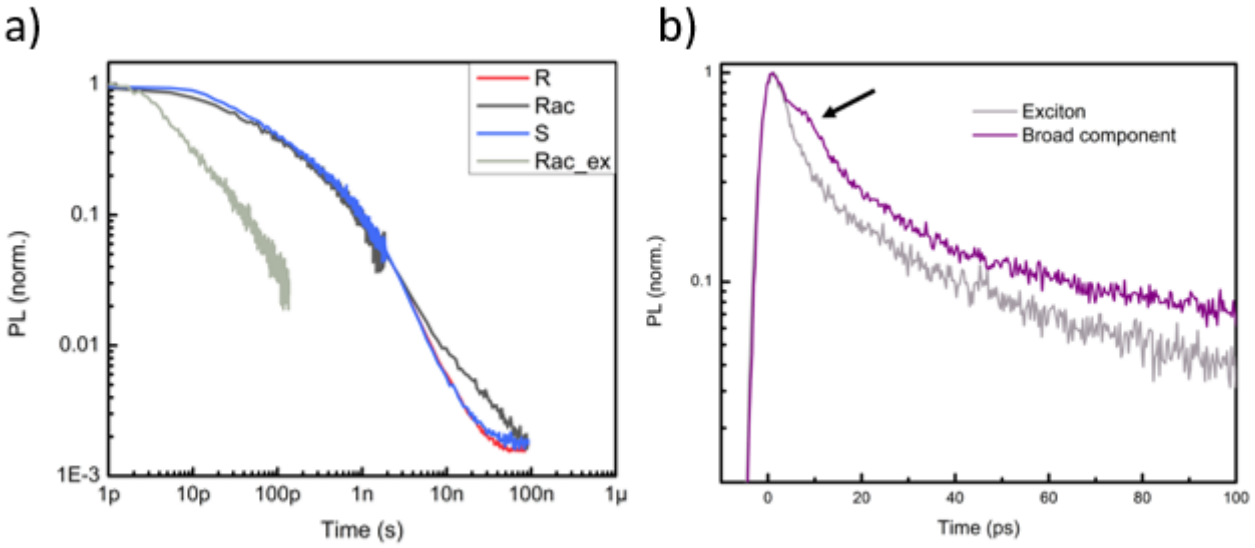

Figure S8: a) Time resolved normalized PL of *R*-, *S*- And racemic $ClMBA_2SnI_4$. In the racemic compound, excitonic emission can be observed in the first 100 ps of emission: as the excitonic component decays, a transfer to the broadband luminescence component can be observed (b).

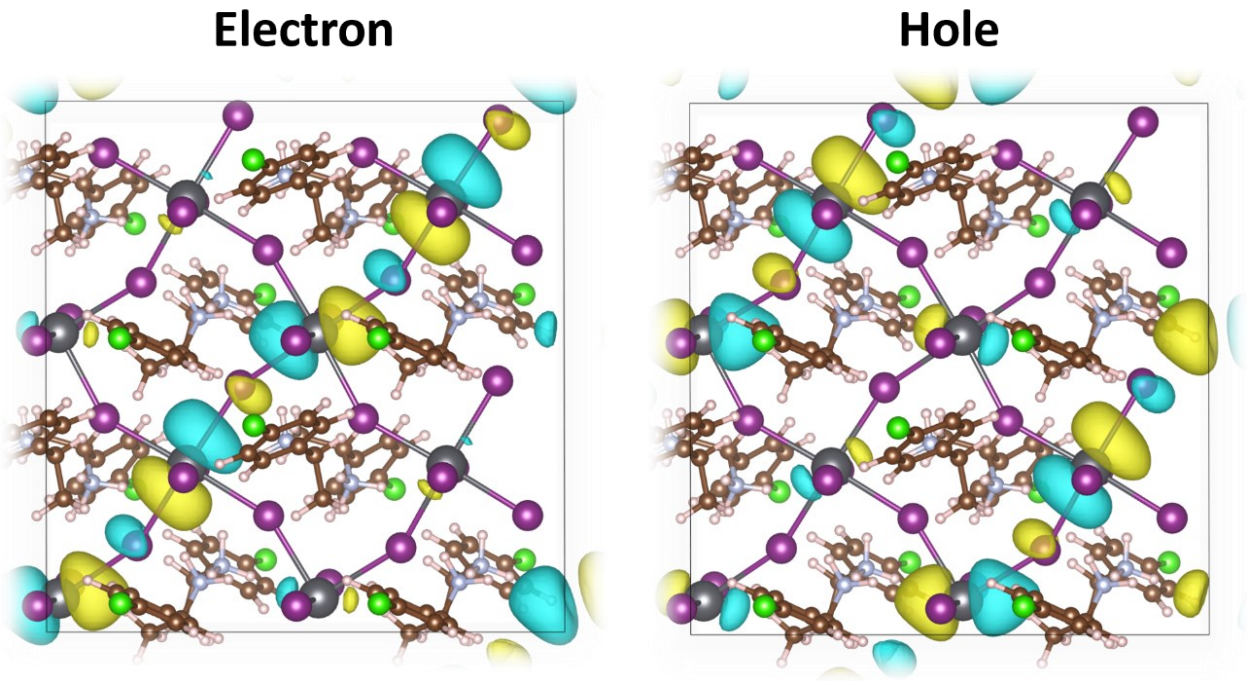

Figure S9. Kohn-Sham (KS) orbitals of the electron and hole in triplet state for $Cl\text{-}MBA_2PbI_4$

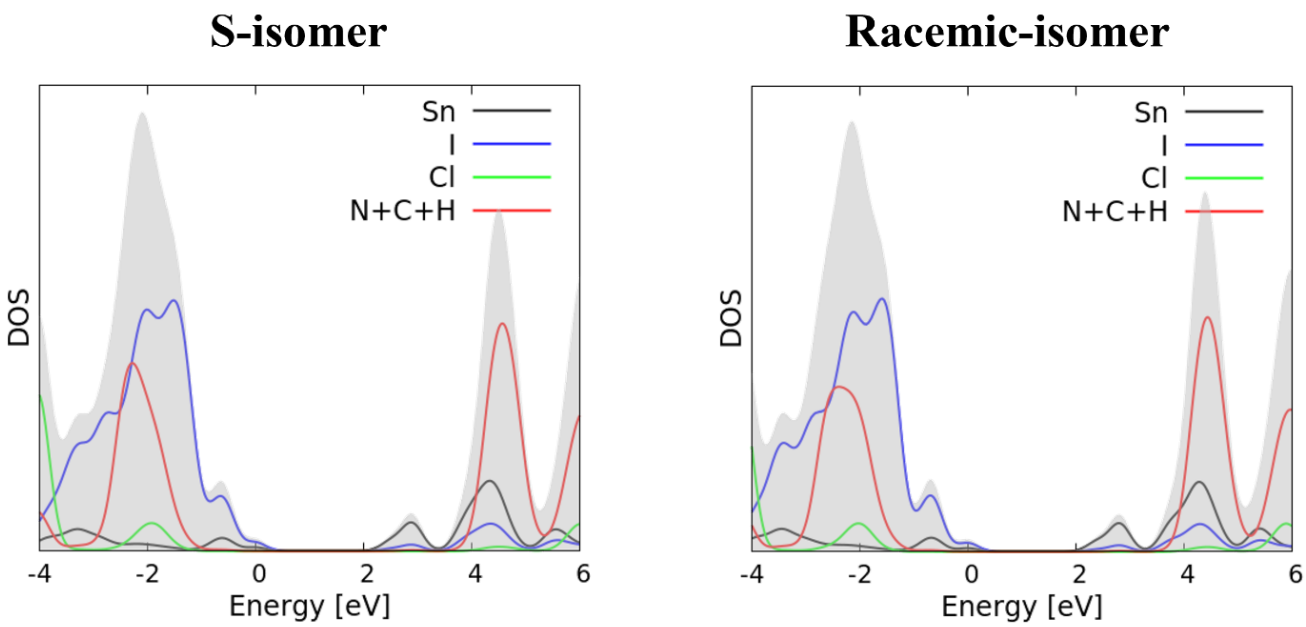

Figure S10. Projected density of states (HSE06-SOC level) of S-isomer and Racemic isomer. In both the figures the VBM has been set to zero.

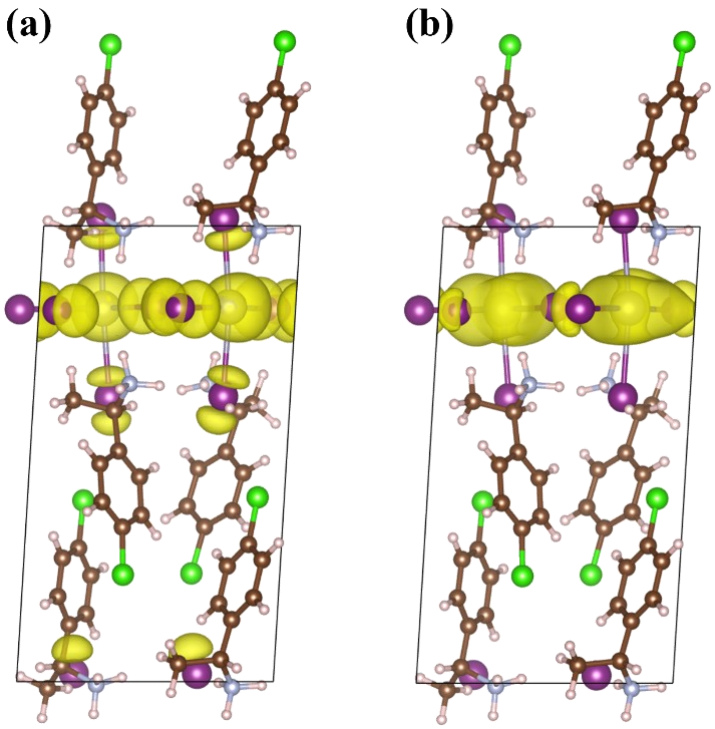

Figure S11. Isodensity plots of the band edge wave functions for the *R*-isomer; (a) HOMO and (b) LUMO

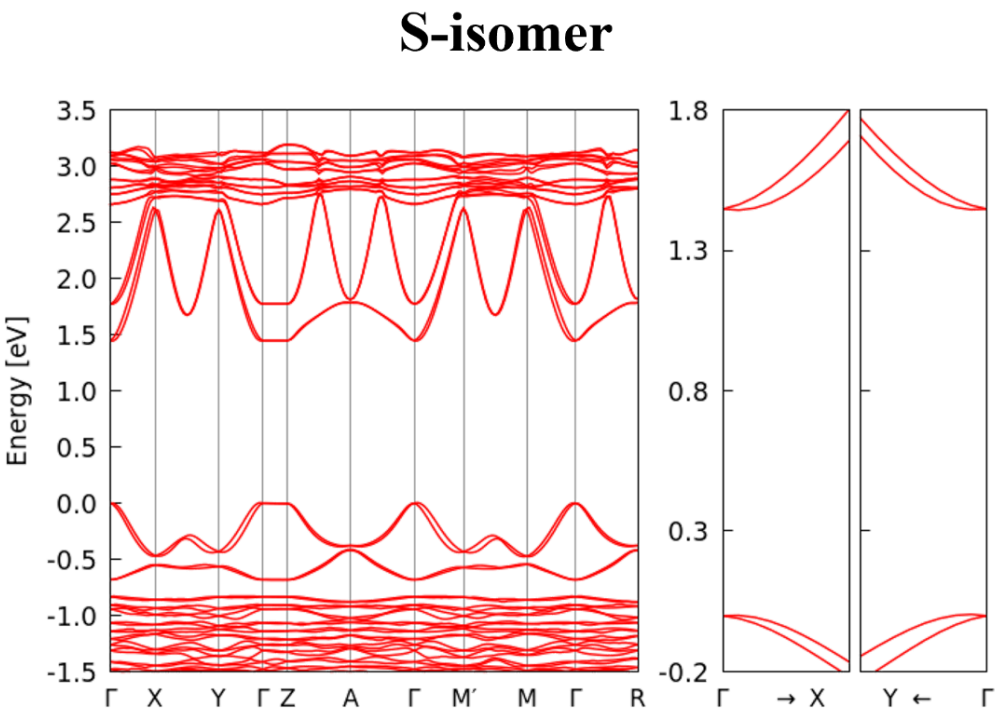

Figure S12. Band structure (PBE-SOC level) of S- isomer. The VBM has been set to zero.

Experimental

Synthesis of (R-ClMBA)$_2$SnI$_4$, (S-ClMBA)$_2$SnI$_4$, and (rac-ClMBA)$_2$SnI$_4$.
Single crystals of (*R*-ClMBA)$_2$SnI$_4$, (*S*-ClMBA)$_2$SnI$_4$ and (*rac*-ClMBA)$_2$SnI$_4$ were grown by dissolving a proper amount of tin(II) acetate powder in a large excess of 57% w/w aqueous HI and 50% w/w aqueous H_3PO_2, heating the mixture to 90°C. After the solid dissolution, the stoichiometric amount of the liquid amine *R*/*S*/*rac*-ClMBA was added. The crystals formation was obtained by a slow cooling down to room temperature at 1°C h^{-1}.

Thin films preparation. First, the glass substrates were washed using water, isopropanol and acetone in a sonicator for 20 min each. Then, the perovskites (powders or crystals) were dissolved in DMF:acetone (90:10) in order to obtain a final solution 0.08 M, and the thin films were prepared on substrates by dip coating method. The films were annealed at 10°C for 10 min on a hot plate.

Single Crystal X-ray Diffraction. Single crystal X-ray diffraction data were collected (λ = 0.71073 Å) on a Bruker D8 Venture, equipped with Cu and Mo microfocus X-ray sources, a PHOTON II detector, and Bruker APEX3 program. The Bruker SAINT[1] software was employed for integration and data reduction, and absorption correction was performed using SADABS-2016/22[2]. Crystal structures were solved and refined using SHELXT 2014/5 and SHELXL 2018/3[3,4].

UV-Vis spectroscopy. DRS spectra were acquired in the wavelength range 300- 800 nm directly on the powders by using a Jasco V-750 spectrophotometer, equipped with an integrating sphere (Jasco ISV-922).

Circular Dichroism. CD spectra were acquired in the wavelength range 350- 800 nm on thin films by using a Jasco J-1500 CD spectrophotometer.

Photoluminescence measurements: the PL of ClMBASnI$_4$ powders was measured under excitation with a 405 nm CW laser (Oxxius Laser Boxx) in vacuum conditions, The PL was measured using a visible spectrometer (Ocean Optics Maya2000). Fluence dependent measurements were conducted at room temperature, varying the incident laser power in a fluence range from 64 mW/cm^2 to 16 W/cm^2. The temperature dependent measurements were conducted in a Linkam cryostat stage in a temperature range between 90 K and 300 K, at afluence of 60 mW/cm^2. The circular dichroism of the photoluminescence was

measured at 90 K by selecting the left hand and right hand circular components of the luminescence by ensuring that the pump radiation had a well-defined (vertical) polarization using a Glen-Thomson polarizer and inserting a visible broadband quarter-wave plate and linear polarizer in the PL collection line. The g_{CPL} signal was then calculated by comparing the PL emission of the RH and LH component of the PL, obtained by rotating the wave plate by 90°, as $g_{CPL} = 2(I_{RH} - I_{LH})/I_{RH} + I_{LH}$.

Time-resolved PL: the time resolved photoluminescence has been measured using a high resolution (<3 ps) Hamamatsu streak camera in the temporal range below 2 ns, using a 400 nm pulsed laser (80 MHz, 800 mW/cm^2, 2nd harmonic of a Ti:Sapphire Coherent Chameleon oscillator tuned at 800 nm) as excitation. For delay times longer than 2 ns we used a gated iCCD (Andor iStar) with a 2 ns temporal resolution, using a 343 nm laser (3rd Harmonic of Light Conversion Pharos, Yb:KGW) at 1 kHz repetition rate at comparable excitation density.

Computational Details:

First-principles calculations based on density functional theory (DFT) were carried out as implemented in the PWSCF Quantum-Espresso package.[5] Geometry optimization is performed using GGA-PBE[6] level of theory and the electron-ion interactions were described by the ultrasoft pseudo-potentials with electrons from Cl 3s, 3p; I 5s, 5p; N, C 2s, 2p; H 1s; Sn 5s, 5p, 4d shells explicitly included in calculations, using a cutoff on the wavefunctions of 25 Ryd (200 Ryd on the charge density). Electronic structure calculations were performed by a single point spin polarized hybrid calculations including SOC using the modified version of the HSE06 functional[7] including 43% Hartree-Fock exchange proposed in ref 51 with scalar-relativistic norm-conserving pseudo potentials with electrons from Cl 3s, 3p; I 5s, 5p; N, C 2s, 2p; H 1s; Sn 4s, 4p, 5s, 5p, 4d 4s shells explicitly included in the calculations, using a cutoff on the wavefunctions of 40 Ryd (80 Ryd on the charge density). The experimental cell parameters were used in all the cases. A k-point sampling[8] of 4×4×2 and 4×1×4 were used for the geometry optimizations of chiral and Racemic isomers, respectively. For the electronic structure calculations, a k-point sampling[9] of 2×2×2 and 2×1×2 were used for the chiral and Racemic isomers, respectively. The z- and y-direction represent the stacking direction for the chiral and Racemic isomers, respectively. Triplet state geometry optimization have been performed using CP2K software package, using PBE0 hybrid exchange-correlation functional with 25% fraction of Fock exchange, including van der

Waals interactions with the DFT-D3 scheme with Becke-Johnson damping.[10-13] Kohn-Sham orbitals are expanded in a double-zeta basis set in combination with the Goedecker-Teter-Hutter pseudopotentials, and a cutoff of 300 Ry for expansion of the electron density in plane waves.[14,15] The auxiliary density matrix method with the cFIT auxiliary basis set was applied to accelerate the optimization of ionic positions within hybrid functional calculations.[16]

References

(1) Bruker. SAINT (version 8.37A) Bruker AXS Inc. **2015**

(2) Bruker. SADABS (version 2016/2) Bruker AXS Inc., Madison, WI, USA **2016**.

(3) G. M. Sheldrick, *Acta Cryst C*, **2015**, 71, 3–8.

(4) G. M. Sheldrick, *Acta Cryst A*, **2015**, 71, 3–8.

(5) Giannozzi, P.; Baroni, S.; Bonini, N.; Calandra, M.; Car, R.; Cavazzoni, C.; Ceresoli, D.; Chiarotti, G. L.; Cococcioni, M.; Dabo, I.; Corso, A. D.; de Gironcoli, S.; Fabris, S.; Fratesi, G.; Gebauer, R.; Gerstmann, U.; Gougoussis, C.; Kokalj, A.; Lazzeri, M.; Martin-Samos, L.; Marzari, N.; Mauri, F.; Mazzarello, R.; Paolini, S.; Pasquarello, A.; Paulatto, L.; Sbraccia, C.; Scandolo, S.; Sclauzero, G.; Seitsonen, A. P.; Smogunov, A.; Umari, P.; Wentzcovitch, R. M. QUANTUM ESPRESSO: A Modular and Open-Source Software Project for Quantum Simulations of Materials. *J. Phys.: Condens. Matter* **2009**, *21* (39), 395502.

(6) Perdew, J. P.; Burke, K.; Ernzerhof, M. Generalized Gradient Approximation Made Simple. *Phys. Rev. Lett.* **1996**, *77* (18), 3865–3868.

(7) Heyd, J.; Scuseria, G. E.; Ernzerhof, M. Hybrid Functionals Based on a Screened Coulomb Potential. *J. Chem. Phys.* **2003**, *118* (18), 8207–8215.

(8) Du, M.-H. Density Functional Calculations of Native Defects in CH3NH3PbI3: Effects of Spin–Orbit Coupling and Self-Interaction Error. *J. Phys. Chem. Lett* **2015**, *6* (8), 1461–1466.

(9) Monkhorst, H. J.; Pack, J. D. Special Points for Brillouin-Zone Integrations. *Phys. Rev. B* **1976**, *13* (12), 5188–5192.

(10) Grimme, S.; Antony, J.; Ehrlich, S.; Krieg, H. A Consistent and Accurate Ab Initio Parametrization of Density Functional Dispersion Correction (DFT-D) for the 94 Elements H-Pu. The Journal of Chemical Physics **2010**, 132 (15), 154104.

(11) (54) Kühne, T. D.; Iannuzzi, M.; Del Ben, M.; Rybkin, V. V.; Seewald, P.; Stein, F.; Laino, T.; Khaliullin, R. Z.; Schütt, O.; Schiffmann, F.; Golze, D.; Wilhelm, J.; Chulkov, S.; BaniHashemian, M. H.; Weber, V.; Borštnik, U.; Taillefumier, M.; Jakobovits, A. S.; Lazzaro, A.; Pabst, H.; Müller, T.; Schade, R.; Guidon, M.; Andermatt, S.; Holmberg, N.; Schenter, G. K.;Hehn, A.; Bussy, A.; Belleflamme, F.; Tabacchi, G.; Glöß, A.; Lass, M.; Bethune, I.; Mundy, C.J.; Plessl, C.; Watkins, M.;

VandeVondele, J.; Krack, M.; Hutter, J. CP2K: An Electronic Structure and Molecular Dynamics Software Package - Quickstep: Efficient and Accurate Electronic Structure Calculations. J. Chem. Phys. **2020**, 152 (19), 194103.

(12) Adamo, C.; Barone, V. Toward Reliable Density Functional Methods without Adjustable Parameters: The PBE0 Model. The Journal of Chemical Physics **1999**, 110 (13), 6158–6170.

(13) Grimme, S.; Ehrlich, S.; Goerigk, L. Effect of the Damping Function in Dispersion Corrected Density Functional Theory. J. Comput. Chem. **2011**, 32 (7), 1456–1465.

(14) VandeVondele, J.; Hutter, J. Gaussian Basis Sets for Accurate Calculations on Molecular Systems in Gas and Condensed Phases. The Journal of Chemical Physics **2007**, 127 (11), 114105.

(15) Goedecker, S.; Teter, M.; Hutter, J. Separable Dual-Space Gaussian Pseudopotentials. Phys. Rev. B **1996**, 54 (3), 1703–1710.

(16) Guidon, M.; Hutter, J.; VandeVondele, J. Auxiliary Density Matrix Methods for Hartree−Fock Exchange Calculations. J. Chem. Theory Comput. **2010**, 6 (8), 2348–2364.

CHAPTER 3

Unraveling the Role of Structural Topology on Chirality Transfer and Chiroptical Properties in Chiral Germanium Iodides

Clarissa Coccia,[a] Marco Moroni,[a] Antonella Treglia,[b] Massimo Boiocchi,[c] Yali Yang,*[d] Chiara Milanese,[a] Marta Morana,[e] Doretta Capsoni,[a] Alessio Porta,[a] Annamaria Petrozza,[b] Alessandro Stroppa,[f] and Lorenzo Malavasi*[a]

[a] Department of Chemistry and INSTM, University of pavia, Pavia 27100, Italy

[b] Center for Nano Science and Technology@Polimi, Istituto Italiano di Tecnologia, Milan 20133, Italy

[c] Centro Grandi Strumenti, University of Pavia, 27100 Pavia, Italy

[d] School of Mathematics and Physics, University of Science and Technology Beijing, Beijing 100083, China

[e] Department of Earth Science, Univeristy of Firenze, Firenze 50121, Italy

[f] CNR-SPIN c/o Department of Physical and Chemical Sciences, University of L'Aquila, I-67100 L'Aquila, Italy;

Corrisponding Authors

Lorenzo Malavasi, email: lorenzo.malavasi@unipv.it

Yali Yang, email: ylyang@estb.edu.cn

ToC

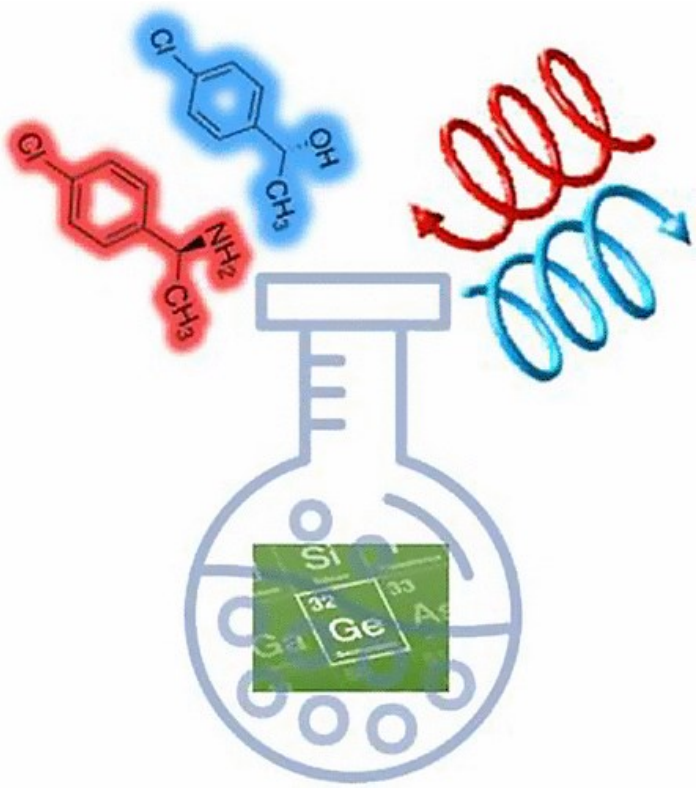

Abstract

Chiral hybrid organic-inorganic metal halides are highly promising chiroptoelectronic materials with potential applications in several fields such as circularly polarized photodetectors, second-order nonlinear optics, and spin-selective devices. However, the ability of manipulating the chiroptical response and the chirality transfer from the organic ligands requires to shed light on structure-property correlations. Herein, we devised and prepared two novel Ge-based chiral hybrid organic-inorganic metal halides showing a different structural topology, namely a 1D and a 2D arrangement, but composed of the same chemical building blocks: (*R*/*S*-ClMBA)$_3$GeI$_5$, and (*R*/*S*-ClMBA)$_2$GeI$_4$. Through a combined experimental and computational investigation on these samples, we discuss the impact of structural dimensionality on chiroptical properties, chirality transfer, and spin-splitting effects, also we highlight the impact of structural distortions. The approach presented here paves the way for a solid understanding of the factors affecting the properties of chiral metal halides thus allowing a future wise materials engineering.

1. Introduction

Chiral hybrid organic-inorganic metal halides, including low-dimensional perovskites, showing peculiar non-linear optical and spin-dependent properties, are triggering a huge interest for their potential use in different applicative areas such as chiroptoelectronics and spintronics.[1–3] In addition, their intrinsic non-centrosymmetric structure may be exploited in ferroelectric and piezoelectric devices.[4] To date, the number of chiral systems is growing very quickly and, among the different structures reported, 2D chiral perovskites represent the vast majority. Indeed, one of the first and still extensively explored compound is the *R*/*S*-MBA_2PbI_4 layered perovskite (MBA=methylbenzylammonium) reported by Billing in 2006 and deeply investigated for its chiroptical response in 2017.[5,6] Other early studies considered the analogous 2D systems with the para-halogenated (F, Cl, Br, and I) methylbenzylammonium cation to unveil the role of hydrogen bonding and halogen-halogen interaction on chiroptical properties such as circular dichroism (CD) and circularly polarized luminescence (CPL).[7,8] The structural family of chiral metal halides extends well beyond 2D perovskites and includes several 0D and 1D systems, as well as 3D and quasi-2D motifs, which have been prepared using the commercially available chiral amines. It is expected that for low-dimensional metal halides, the chirality degree would be higher due to the larger number of organic ligands per unit cell.[9] As a matter of fact, the anisotropy factors determined from CD, *i.e.* g_{CD}, tend to increase of about one order of magnitude moving from 2D to lower dimensional 1D and 0D structures. Such order of magnitude change in the g_{CD} value with a change in dimensionality can be attributed to the structural rigidity within the inorganic layer.[10] For 1D and 0D structures it is possible, for the inorganic units, to structurally follow the chirality dictated by the chiral organic components more effectively than in the case of the more rigid corner-shared 2D systems. A careful study on the effect of dimensionality on the CD response has been performed by Zhang and co-workers.[11] By combining experimental and computational modelling the authors could unveil the role of the organic cation and of the halide in a series of 1D systems, thus suggesting, for example, that the presence of the iodide would lead to higher CD values compared to bromide analogues due to smaller exciton binding energies.[11] On the same line, 1D systems with smaller interchain distances between the chiral ligands should provide higher CD values.[11] It should be noted, however, that the correlations

between dimensionality and chiroptical properties reported so far have been proposed on chemically different systems, *i.e.* with different organic cations. Since it has been shown that the chiral ligand induces a medium to large modulation of the anisotropy factors, to date, a genuine structure-property correlation on dimensional diverse chiral metal halides having the same organic cation, central metal, and halide is still missing. This applies also to the understanding of the role of chirality transfer, namely the symmetry-breaking effect induced by a chiral cation on the inorganic framework, which is at the basis of the insurgence of the chiroptical properties. Recently, attempts to quantify the degree of chirality of the organic cations have been considered. One of them, the Electronic Chirality Measure (ECM), has received special attention. ECM is a descriptor that measures the chirality of any (chiral) molecular system and was proposed by Bellarosa and Zerbetto in 2003.[12] In 2023, J. J. Aucar *et al*. showed a novel, strong, and positive correlation between the energy difference of the total electronic energies of two enantiomers and ECM, supporting a subtle interplay between the parity-violating weak-forces acting within the nuclei of a given molecule and its chirality.[13] However, if the ECM of a given cation can be used to determine the physical properties of a corresponding chiral metal-halides is still an open question.

Based on these considerations, our aim was to prepare and characterize a novel family of chiral metal halides having the same chemical nature in terms of organic cation, central metal, and halide, and modulating their structural dimensionality (represented by the dimensionality of the inorganic framework). For the design of these novel compounds, we selected ClMBA (ClMBA=4-chloro-methylbenzylamine) as the chiral ligand (in the *R*-/*S*- enantiopure isomers), germanium as central metal, and iodide as halide. The choice of ClMBA was based on the availability of the analogous Pb and Sn systems which could provide some insight into the role of central atom on the chiroptical properties.[7,14] Germanium was selected to overcome the concerns about the toxicity and environmental impact of lead which are prompting scientists to explore alternative metals that can offer comparable or even superior performance in any area where metal halides (specifically perovskites) are being used.[15–17] We believe that this point should be even more important for a recently developing research field as the one of chiral metal halides. The substitution of lead with alternative elements in hybrid metal halides structures presents an opportunity

to develop environmentally friendly and sustainable materials while retaining or enhancing their chiral properties.[18] This not only addresses the concerns associated with lead toxicity, but also opens up new avenues for exploring novel optoelectronic phenomena and expanding the scope of intended devices. To date, the number of lead-free chiral metal halides, including perovskites and double perovskites, where lead (Pb) has been primarily replaced by tin (Sn), germanium (Ge), copper (Cu), manganese (Mn), and bismuth (Bi), is very limited. To understand the fundamental mechanisms of chirality transfer in these compounds, uncover the role of the central metal atom, and develop new and advanced materials, it is essential to explore the synthesis and characterization of novel lead-free chiral metal halides.[14,19–31] Moreover, Ge, with respect to Sn and Pb, is known to modulate the distortion degree of the inorganic octahedra which in turn has an impact on chirality- and spin-related properties such as the Rashba splitting.[32–35] Finally, iodide halide was selected to potentially extend the optical properties in the visible region of the spectrum and for the expected higher asymmetry factor compared to bromide systems as suggested in Ref. 11.[11]

Using these three “ingredients”, namely, ClMBA and Ge cations and iodide anion, and by changing the experimental conditions, we were able to prepare the *R*/*S* chiral pairs of two novel systems showing, respectively, a 1D and a 2D topology of the inorganic sublattice, *i.e.* $(ClMBA)_3GeI_5$, and $(ClMBA)_2GeI_4$. The samples were grown as single crystals solving their structure and characterized by a combined experimental and computational modelling approach allowing to access a direct correlation between chiroptical properties and chirality transfer as a function of structural dimensionality.

2. Results and Discussion

Crystal Structure Determination

Light orange single crystals of (*R*-ClMBA)$_3$GeI$_5$ and (*S*-ClMBA)$_3$GeI$_5$ have been grown as described in the electronic Supplementary Information (SI) and subjected to single-crystal X-ray diffraction (SCXRD). A sketch of the two structures is reported in Figure 1(a)-(b) together with a picture of the (*R*-ClMBA)$_3$GeI$_5$ single crystals, while Table 1 reports selected crystallographic data.

Table 1. Crystal structure data for(*R/S*-ClMBA)$_3$GeI$_5$ and (*rac*/*R/S*-ClMBA)$_2$GeI$_4$

	(*R*-ClMBA)$_3$GeI$_5$	**(*S*-ClMBA)$_3$GeI$_5$**	**(*R*-ClMBA)$_2$GeI$_4$**	**(*S*-ClMBA)$_2$GeI$_4$**	**(*rac*-ClMBA)$_2$GeI$_4$**
Formula weight	2353.98	2353.98	893.47	893.47	893.47
Temperature (K)	298	298	298	298	298
Wavelength (Å)	0.7107	0.7107	0.7107	0.7107	0.7107
Crystal system	Monoclinic	Monoclinic	Monoclinic	Monoclinic	Monoclinic
Space group	$P2_1$	$P2_1$	C2	C2	$P2_1$
Lattice parameters (Å, °)	*a* = 18.7304(5)	*a* = 18.7271(6)	*a* = 33.7599(11)	*a* = 33.7679(9)	*a* = 8.621(10)
	b = 8.8918(2)	*b* = 8.8982(2)	*b* = 6.3359(2)	*b* = 6.3387(2)	*b* = 9.375(9)
	c = 23.0151(8)	*c* = 23.0211(8)	*c* = 12.5561(4)	*c* = 12.5611(4)	*c* = 16.193(17)
	β= 105.998(3)	*β* = 105.967(3)	*β*= 99.886(3)	*β* = 99.897(3)	*β* = 96.40(4)
Lattice Volume (Å^3)	3684.64(19)	3688.2(2)	2645.86(15)	2648.62(14)	1301(2)
Z	2	2	4	4	4
CCDC code	2283932	2283931	2311478	2311477	2311891

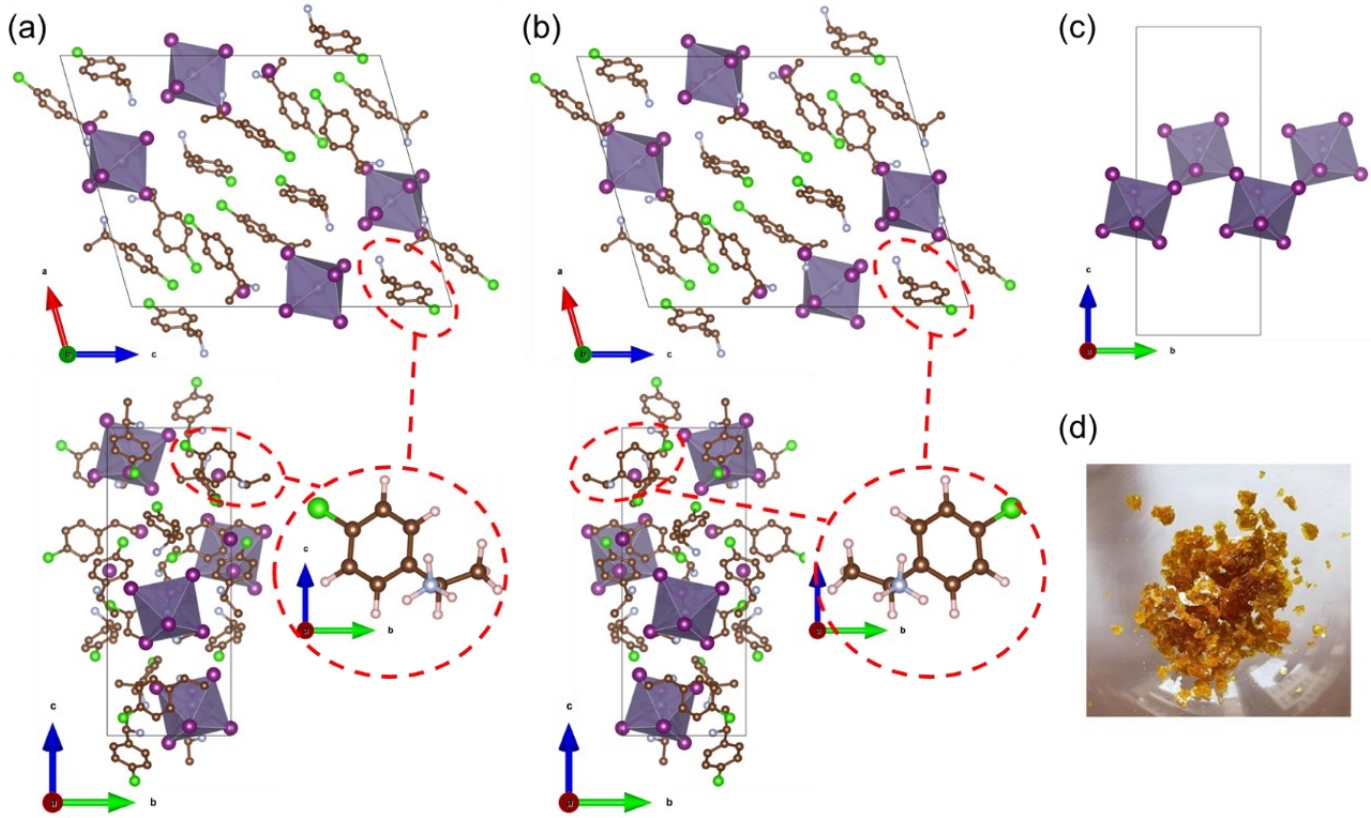

Figure 1. (a) and (b) represent sketches of the crystal structures of (*R*-ClMBA)$_3$GeI$_5$ and (*S*-ClMBA)$_3$GeI$_5$, respectively; (c) detail of the zig-zag linear chain arrangement along the *b*-axis; (d) appearance of the single crystals of (*R*-ClMBA)$_3$GeI$_5$. The hydrogen atoms in the unit cells are not shown for clarity. The organic cations have been highlighted with dashed curve lines.

As can be seen from Table 1, the two chiral samples (*R*-ClMBA)$_3$GeI$_5$ and (*S*-ClMBA)$_3$GeI$_5$ crystallize in the non-centrosymmetric $P2_1$ space group (n° 4), one of the 65 Sohncke space groups, and form two enantiomeric structures. The crystal structure is composed of GeI$_6$ octahedra arranged in linear zig-zag chains running along the *b*-axis (cfr. Fig 1c) with Ge-I-Ge bond angle in the range 155.93-157.70°, leading to a one-dimensional (1D) germanium iodide. The octahedra are distorted presenting six different Ge-I bond-lengths grouped in two sets of comparable lengths, *i.e.,* around 2.8 and 3.3 Å. A full list of octahedra parameters is reported in Table S1 of the SI. To the best of our knowledge, the only other example of such structural arrangement has been reported for the guanidinium lead iodide (C(NH$_2$)$_3$)$_3$PbI$_5$.[36] Concerning chiral 1D systems, few of them have been recently reported by including the *R*/*S*-2-aminomethylpyrrolidine (AMP) cation in lead bromide compositions (*R*/*S*-AMP)$_2$Pb$_3$Br$_{10}$), and N-ethyl-quinuclidine (EQ) in a lead iodide perovskite (EQPbI$_3$).[37,38] The only other chiral lead-free 1D metal halide, namely [(*R*/*S*)-β

MPA]$_4$AgBiI$_8$ (MPA= methylphenethylammonium), has been reported in 2021 by Liu and co-workers.[39] Another interesting feature of the present Ge-based chiral 1D system is related to the octahedral distortion parameters which can be quantified in terms of bond length distortion index (*D*) and bond angle variance (σ^2).[40,41] The larger the value of *D* and σ^2, the larger becomes the octahedral distortion. The *D* parameter for (*R*-ClMBA)$_3$GeI$_5$ and (*S*-ClMBA)$_3$GeI$_5$ is in the range 0.071-0.075 with bond angle variance in the range 12.59-15.70 deg^2, respectively.

Moving to the 2D system prepared by using the same starting building blocks, the crystal structure of (*R*-ClMBA)$_2$GeI$_4$ and (*S*-ClMBA)$_2$GeI$_4$ samples has been solved as well, and the main crystallographic data are reported in Table 1. A sketch of the crystal structure for both enantiomers is reported in Figure 2a-b together with a picture of the single crystals (2c).

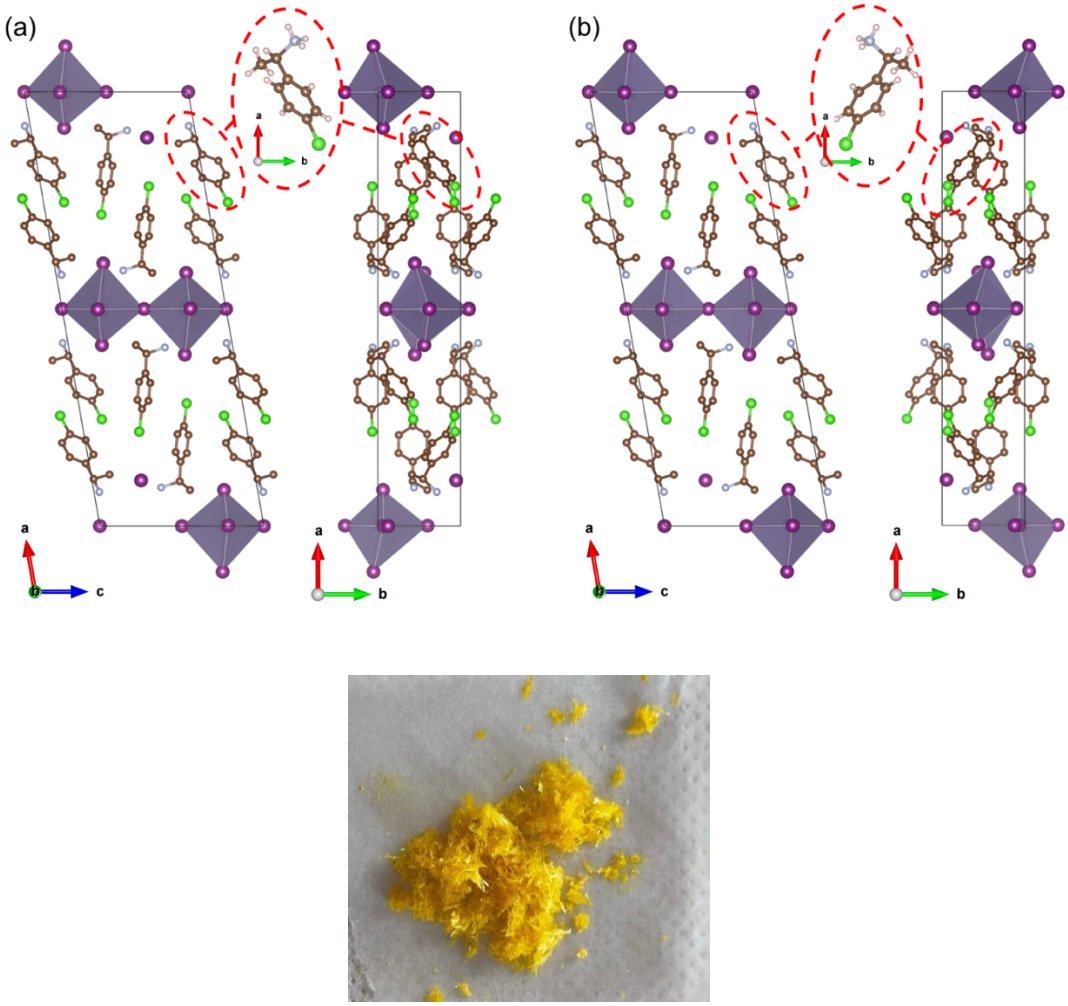

Figure 2. a) and b) represent sketches of the crystal structures of (*R*-ClMBA)$_2$GeI$_4$ and (*S*-ClMBA)$_2$GeI$_4$, respectively. The hydrogen atoms in the unit cells are not shown for clarity. The organic cations have been highlighted with dashed curve lines; c) reports the appearance of the single crystals of (*R*-ClMBA)$_2$GeI$_4$.

According to the SCXRD analysis, (*R*-ClMBA)$_2$GeI$_4$ and (*S*-ClMBA)$_2$GeI$_4$ crystallize in the non-centrosymmetric monoclinic *C*2 space group (n° 5) (a Sohncke space group) and display the typical arrangement of Ruddlesden-Popper 2D perovskites characterized by layers of corner-sharing GeI_6^{4-} octahedra separated by a bilayer of ClMBA cations penetrating into the perovskite sheets by about 0.47 Å. The two in-plane Ge-I-Ge bond angles are 171.6° and 166.7°, respectively, showing a moderate deviation from the ideal 180° of undistorted perovskites layer. On the other hand, the six Ge-I bond lengths of the octahedra show a significant distribution from 2.7236(10) to 3.6250(9) Å, with a maximum difference of about 0.9 Å (full list of bond lengths in Table S1). This is a huge distortion of the bond lengths, and, to the best of our knowledge, Ge-I bond distances greater than 3.6 Å have never been reported in the Cambridge Structural Database (CSD).[42] The octahedra distortion parameters for (*R*-ClMBA)$_2$GeI$_4$ and (*S*-ClMBA)$_2$GeI$_4$ are: *D*=0.093 (both enantiomers), and σ^2 54.59 (*S* enantiomer) and 55.16 (*R* enantiomer) deg^2. Such distortion parameters place (*R*-ClMBA)$_2$GeI$_4$ and (*S*-ClMBA)$_2$GeI$_4$ as the most distorted 2D chiral perovskites known to date. For comparison, the analogous systems with the same chiral ligand and halide but with Pb or Sn, have distortion *D* index of about 0.014 and 0.042, respectively, showing a progressive increase of octahedral distortion moving from Pb to Ge.[14] This is in line with previous reports on the role of central atom on the structural properties of 2D perovskites.[34] By incorporating structural data from lead and tin systems and introducing new germanium-containing 2D chiral perovskites, we try to elucidate, for the first time, the influence of the central metal and structural distortions on chiroptical properties (as discussed later).

For the 2D system we were also able to grow single crystal of the racemic compound (*rac*-ClMBA)$_2$GeI$_4$, which main crystallographic data are reported as well in Table 1. As in the case of (*R*-ClMBA)$_2$GeI$_4$ and (*S*-ClMBA)$_2$GeI$_4$, the material crystallizes as a Ruddlesden-Popper 2D perovskite, comprising layers of corner-sharing GeI_6-octahedra separated by a bilayer of organic cations. Compared to enantiopure phases, the NH_3 penetration is smaller, about 0.30 Å, as some difference can be envisaged in the structural distortions. The two in-plane Ge-I-Ge bond angles (146.8° and 166.2°) show a larger deviation from the ideal 180° angle than (*R*-ClMBA)$_2$GeI$_4$ and (*S*-ClMBA)$_2$GeI$_4$. The octahedral distortion parameter, *D*, reaches the record value (for a chiral 2D perovskite) of 111 and, impressively, the longest Ge-I bond

length reaches 3.774 Å. Quadratic elongation is in line with the enantiopure samples whereas the bond-angle variance is smaller (see Table S1).
Comparing the two series of samples reported here, showing a different dimensionality of the inorganic framework, we observe that 1D topology presents a reduced distortion level with respect to the 2D system which may be correlated to its higher lattice rigidity. Together with the *D* and σ^2 parameters discussed above, also the quadratic elongation (λ), measuring the degree of off-center displacement of Ge atom in the octahedron unit, shows an increase from about 1.01 for the 1D system to about 1.03 for the 2D system (see Table S1). As for the other two parameters, such high value of λ has not been reported before in chiral 2D perovskites. Therefore, moving from 1D to 2D dimensionality, keeping the same chiral ligand, central metal, and halide, provides a way to increase the inorganic framework distortion which is known to impact the electronic structure and optical properties of metal halides.

The thermal stability of all the four enantiopure samples has been checked by differential scanning calorimetry (DSC) and thermogravimetry (TGA). DSC measurements (Figure S1a and b) rule out the presence of structural phase transitions in the considered temperature range (from -65 to 100°C). TGA measurements (Figures S1c-S1f) show a similar trend for all the four samples with decomposition starting around 250°C and full sample degradation occurring around 300°C.

Optical properties of (*R/S*-ClMBA)$_3$GeI$_5$ and (*R*/*S*-ClMBA)$_2$GeI$_4$ have been measured by UV-Vis (on powdered single crystals) and CD spectroscopy (on dip-coated polycrystalline thin films of about 400 nm thickness). Details about thin films preparation are reported in the SI.
The linear absorption spectra of (*R/S*-ClMBA)$_3$GeI$_5$ (see Figure S2) show quite sharp edge around 420 nm without any indication of excitonic peak which could be related to the high level of structural distortion (see above).[25] The band-gap values extrapolated from the Tauc plots (Figure 3a) for indirect transitions are 2.69 and 2.71 eV, respectively, for (*R*-ClMBA)$_3$GeI$_5$ and (*S*-ClMBA)$_3$GeI$_5$. The CD spectra (Figure 3b) present two peaks in the range 350-460 nm, namely one cantered around 371 nm and the second one around 440 nm in good agreement with the absorption edge. The presence of opposite sign CD peaks for the two samples confirms the chirality transfer from the chiral ligand ClMBA to the

inorganic framework. As a matter of fact, the two chiral amines have CD spectra with a peak centred around 245 nm (see Figure S3) and g-values of +/- 4 × 10^{-4}. The chiral anisotropy factor, g_{CD}, has been calculated according to the following equation:

$$g_{CD} = \frac{A_L - A_R}{2(A_L + A_R)} \qquad \text{(eq. 1)}$$

where A_L and A_R are the absorbance of the sample for left- and right-handed circularly polarized light, respectively, and resulted to be -6 × 10^{-3} for the *R*- sample and 5 × 10^{-3} for the *S*-sample (measured at 430 nm), in line with values reported for 1D chiral metal halides (see Table S2).

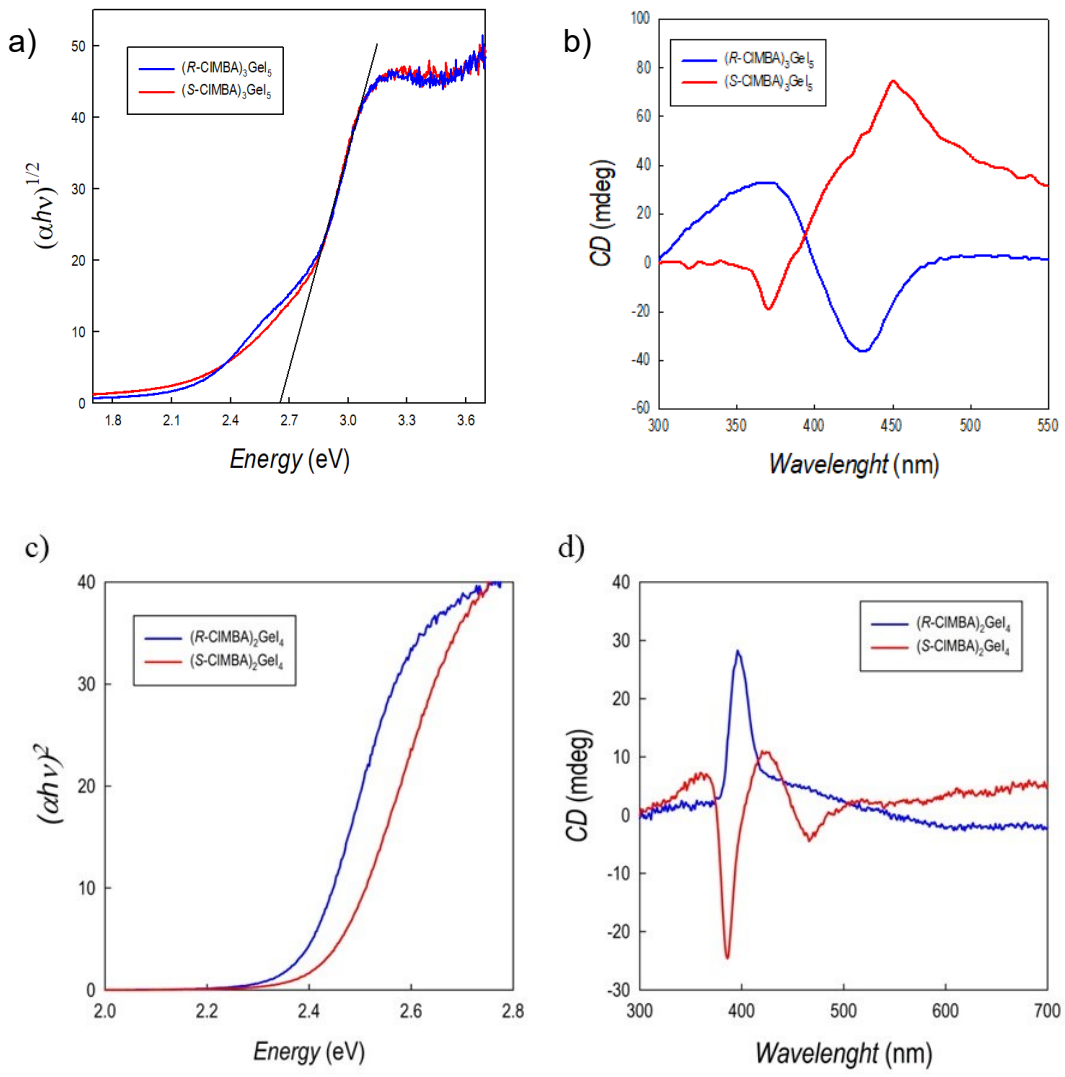

Figure 3. a) Tauc plot b) and CD spectra for (*R*-ClMBA)$_3$GeI$_5$ and (*S*-ClMBA)$_3$GeI$_5$; c) Tauc plot and d) CD spectra for (*R*-ClMBA)$_2$GeI$_4$ and (*S*-ClMBA)$_2$GeI$_4$.

The same characterization has been performed on (*R/S*-ClMBA)$_2$GeI$_4$ chiral pairs and the corresponding Tauc plots and CD spectra are reported in Figure 3c and Figure 3d while Figure S3 shows the absorbance data. There is a slight difference in the absorption spectra between the two samples with the *R* one showing a small red-shift with respect to the *S* sample. As a matter of fact, the two direct band-gap estimated from the Tauc plots are 2.34 eV for (*R*-ClMBA)$_2$GeI$_4$ and 2.42 eV for (*S*-ClMBA)$_2$GeI$_4$. The CD spectra show, as in the previous case, a symmetric trend with opposite sign and spectral features well corresponding to the onset of the absorption data. The g_{CD} for these two samples is +4 × 10^{-4} and -4 × 10^{-4} (measured at 395 nm) for the two enantiomers in line with Pb and Sn including ClMBA and iodide (see also Table S2).[14] Finally, Figures S2c-e report the absorption, Tauc plot and CD spectrum for (*rac*-ClMBA)$_2$GeI$_4$. The band-gap resulted to be in line with the (*S*, *R*) samples and around 2.3 eV while no CD response, as expected, has been observed (Fig. S2e).

Concerning the 1D samples it is not possible, at present, to make a direct comparison of the chiroptical properties of (*R/S*-ClMBA)$_3$GeI$_5$ with available data on chiral perovskites due to the fact that the structural motif of the present samples has not been found in any other chiral metal halide to date. However, we can compare the actual two series of chiral halides considering the evolution of the dimensionality from 1D to 2D. In terms of band-gap, the observed blue-shift passing from the 2D to the 1D samples may be related to the stronger deviation of the Ge-I-Ge bond angles from the ideal 180° (about 170° for 2D and about 156° for 1D) and recalling the impact of bond angle on the band-gap value.[43] On the other hand, there is a clear increase of about one order of magnitude of the g_{CD} moving from 2D to 1D systems, namely form ~4×10^{-4} to ~4×10^{-3}. As mentioned in the introduction, this might be an expected result considering the higher amount of chiral ligand in lower dimensional systems and the reduced lattice rigidity, however this is the first time such parameter is quantitatively and effectively demonstrated in two systems with the same building blocks (ClMBA, Ge and I) but with a different dimensionality. However, the observed increase of g_{CD} moving from 2D to 1D systems is correlated negatively with the other chirality transfer indicator such as the amplitude of the chiral distortion which increases from 1D to 2D. While this seems counterintuitive, it is not unexpected though, since the shape and magnitude of the chiroptical spectra depend critically on the electronic matrix elements, which have not been analysed in this work. In addition, it appears that the

extend of parameters such as the spin-splitting are more related to structural distortion effects while chiroptical properties might be more closely related to the enantiomeric fraction of the chiral ligands.[9] However, all these results clearly call for further studies in this direction.

For the (*R/S*-ClMBA)$_2$GeI$_4$ compositions, thanks to the availability of the analogous lead- and tin-based chiral 2D perovskites, it is further possible to provide a comparison of their optical and chiroptical properties by changing the central metal. In terms of optical data, the present samples are those with higher band-gap values with respect to Sn (~2.10 eV) and Pb (~2.30 eV) analogues, a result which can be related to the combined effects of the electronic contribution to the density of state of the atomic orbitals (in general the presence of tin and germanium induces a red-shift of absorption with respect to lead) and of the distortion level as confirmed by DFT calculations(see later in the text). However, another interesting point is related to the chiroptical response. For the three (*R/S*-ClMBA)$_2$BI$_4$ (B=Pb, Sn, and Ge) chiral 2D perovskites the average g_{CD} is around 4×10^{-4} (see Table S2).[14] This is roughly constant irrespective to the nature of central atom and structural distortion (increasing from Pb to Ge) and appears therefore related to the chemical nature of the chiral ligand. Such observation is of interest and may suggest an important role of the chiral cation in tuning the asymmetry factor in 2D perovskites. However, both present and available data do not yet represent and large enough data set to draw solid conclusions in this sense and more systematic studies as a function of the chiral amine, by keeping the central metal and the halide constant, are therefore urgent.

The photoluminescence (PL) spectra at 77 K of (*S/R*-ClMBA)$_3$GeI$_5$ (Figure 4a) and (S/*R*-ClMBA)$_2$GeI$_4$ (Figure 4b) present a broad emission with a significant Stokes shift, centered at 640-700 nm. The emission spectrum of the (rac-ClMBA)$_2$GeI$_4$ is shown in Figure S4. Notably, (*S*-ClMBA)$_3$GeI$_5$ shows an excitonic peak near the absorption onset, centered at 502 nm, which is otherwise not present in the other compositions where the broad emission dominates. The origin of such broad emission is attributed to defects and the distortion of the crystal lattice, which is calculated to be more significant for Ge compared to Pb an Sn.[44–48] This is and corroborated by the notable increase in luminescence at cryogenic temperatures (Figure S5-6).

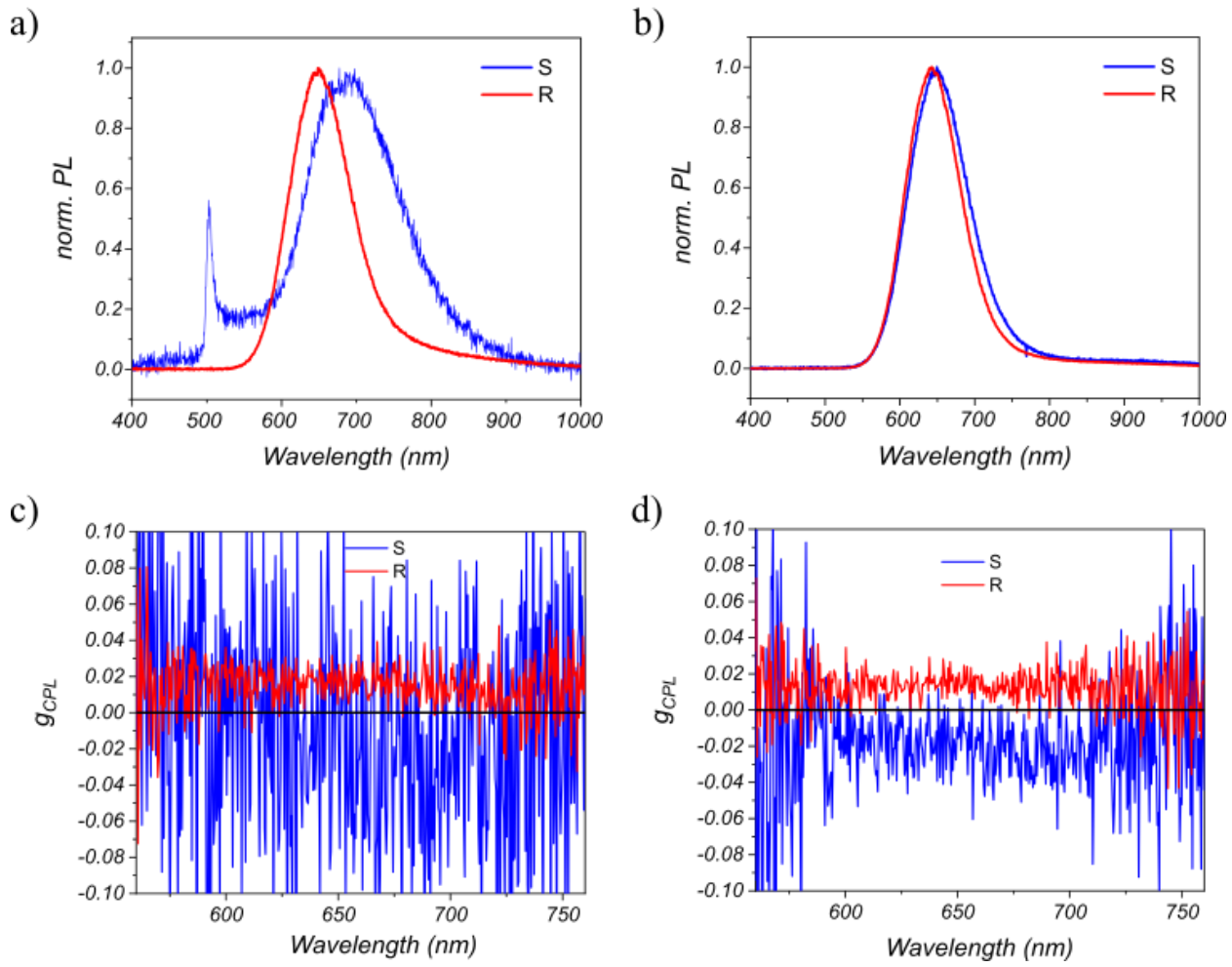

Figure 4. a-b) normalized PL and c-d) g_{CPL} for (S/*R*-ClMBA)$_3$GeI$_5$ and (S/*R*-ClMBA)$_2$GeI$_4$ respectively, measured at 77 K.

The PL lifetime of the broadband emission at 77K is shown in Figure S7 for all samples. (*S*-ClMBA)$_3$GeI$_5$ shows a rapid decay within the instrument response function (2 ns) and a slower component with a lifetime of about 2 µs, whereas the excitonic peak lifetime also falls within the instrument response function. The other samples exhibit an initial rise, indicating a slow transfer process, followed by a decay. For (*R*-ClMBA)$_3$GeI$_5$ the transfer occurs within 1 µs and then the photoluminescence decays with a 2 µs lifetime. In the case of the 2D structures, the transfer process is slowed down from *rac*- to *S*- to *R*- and also the lifetime of the decay increases from 1 µs to 2 µs to 2.5 µs, respectively.

We characterized the chirality of the PL emission at 77 K, as shown in Figure 4 c-d for (*S/R*-ClMBA)$_3$GeI$_5$ (Figure 4a) and (S/*R*-ClMBA)$_2$GeI$_4$ respectively. We calculate the

$g_{CPL} = 2(I_{RH} - I_{LH})/(I_{RH} + I_{LH})$ where I_{LH} and I_{RH} are respectively the left hand and right hand circularly polarized component of the photoluminescence. We obtain a PL dichroism of the order of 0.015-0.02 with opposite sign for the *R*- and S- enantiomers except for the (*S*-ClMBA)$_3$GeI$_5$ due to the lower PL intensity. Such values are in line with those reported previously for bulk lead-free chiral 2D perovskites.[14]

First-principles calculations are performed to further investigate the structural and electronic properties of the four samples reported in the present paper. The atomic positions of the structures are optimized with the lattice parameters being fixed to the experimental values. Additional calculations for optimizing both the atomic positions and the lattice parameters are also performed. The results show that the changes of the lattice parameters with respect to the experimental values are smaller than 3% (see Table S3 in the SI), thus we fix the lattice parameters to the experimental ones and we optimize the atomic positions. Starting from the 1D system, after optimization and taking (*R*-ClMBA)$_3$GeI$_5$ as example, the GeI$_6$ octahedra shows 14° tilting angle about the axis vertical to the inorganic GeI$_5$ layers, as shown in Figure 5a. Such tilting angle leads to the Ge-I-Ge bond angle of about 152.04° which is close to the experimental angle 157.70°. For the other two axes of the pseudo cubic of GeI$_6$, which lie in the GeI$_5$ layers, there are no obvious tilting. The Ge-I bond lengths are also shown in Figure 5a. The band structure of (*R*-ClMBA)$_3$GeI$_5$ is shown in Figure 5b in which an indirect band gap of about 2.65 eV is presented with the VBM at Γ (0 0 0) point and CBM at A (-0.5 0 0.5) point. The calculated band gap value is in good agreement with the experimental one, *i.e.*, 2.69 eV (see above in the text). The band structure considering the spin-orbit coupling (SOC) is also calculated (see Figure S8 in SI). However, it shows very small differences with the band structure without SOC. In Figure 5c, we show the projected density of states of (*R*-ClMBA)$_3$GeI$_5$. One can easily find that the VBM is mainly contributed by the atoms from the GeI$_5$ inorganic framework (specifically, the I atoms), while the CBM is mainly contributed by the C atoms of the organic molecules.

The structural and electronic properties of (*R*-ClMBA)$_2$GeI$_4$ are calculated for comparison and shown in Figure 6. Differently from the GeI$_6$ octahedra in (*R*-ClMBA)$_3$GeI$_5$, the GeI$_6$ framework shows no obvious octahedra tilting, but larger Ge-I bond length differences. Figure 6b and 6d report the band structure of (*R*-ClMBA)$_2$GeI$_4$ with and without SOC effect. It is nearly a direct band gap with the VBM

and CBM located around the high-symmetry point V_2 in the first Brillouin zone of its primitive cell structure. The band gap without and with SOC are around 1.7 and 1.6 eV, respectively, which are somewhat underestimated with respect to the experimental values of about 2.3 eV. This suggests that additional corrections may be required in this case. Therefore, the modified Becke-Johnsom (mBJ) meta-GGA functional is also adopted to calculate the band gap.[49,50] As shown in Figure S9b of SI, the band gap of (*R*-ClMBA)$_2$GeI$_4$ increases to about 2.1 eV, which is much closer to the experimental value. However, the bang gap of (*R*-ClMBA)$_3$GeI$_5$ using mBJ functional increases to 3.18 eV, as shown in Figure S9a, which is larger than the experimental 2.69 eV. These results suggest that a given functional may not be able to properly describe all the properties, e.g. the energy gap, for the different compounds, thus suggesting that the corrections may be system dependent. In Figure 6c, we see that the VBM of (*R*-ClMBA)$_2$GeI$_4$ is also mainly contributed by the atoms from the GeI$_5$ inorganic framework (specifically, the I atoms). On the other hand, in the CBM there is significant down-shift of the spectral weight of framework-like electronic states with respect to the molecular states, which significantly reduces the energy gap with respect to (*R*-ClMBA)$_3$GeI$_5$. Therefore, our calculations highlight important changes induced in the VBM and CBM orbital projected density of states mainly related to the different topology of the two compounds. The band structure for (*R*-ClMBA)$_2$SnI$_4$ and (*R*-ClMBA)$_2$PbI$_4$ without SOC are also calculated. As shown in Figure S10, the calculated band gaps for (*R*-ClMBA)$_2$SnI$_4$ and (*R*-ClMBA)$_2$PbI$_4$ compounds are 1.75 eV and 2.26 eV, respectively, and both the VBM and CBM of these two compounds are mainly contributed by the atoms from the inorganic framework which is similar to that of (*R*-ClMBA)$_2$GeI$_4$. As shown in Figure S9c and d, the band gap of (*R*-ClMBA)$_2$SnI$_4$ and (*R*-ClMBA)$_2$PbI$_4$ compound calculated using the mBJ functional is about 2.18 and 2.89 eV, respectively.

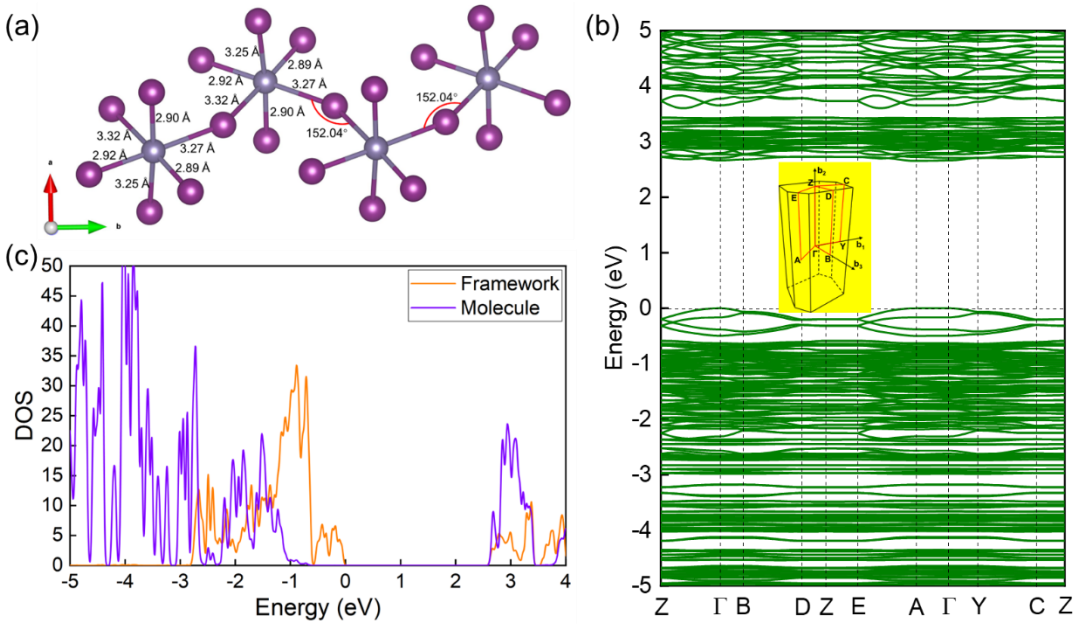

Figure 5. Structural and electronic properties (without SOC) of (*R*-ClMBA)$_3$GeI$_5$. (a) Structural details of relaxed (*R*-ClMBA)$_3$GeI$_5$. (b) Band structure of (*R*-ClMBA)$_3$GeI$_5$. (c) Projected density of states of (*R*-ClMBA)$_3$GeI$_5$. Here and in the following figures, the zero-energy level has been aligned to the VBM.

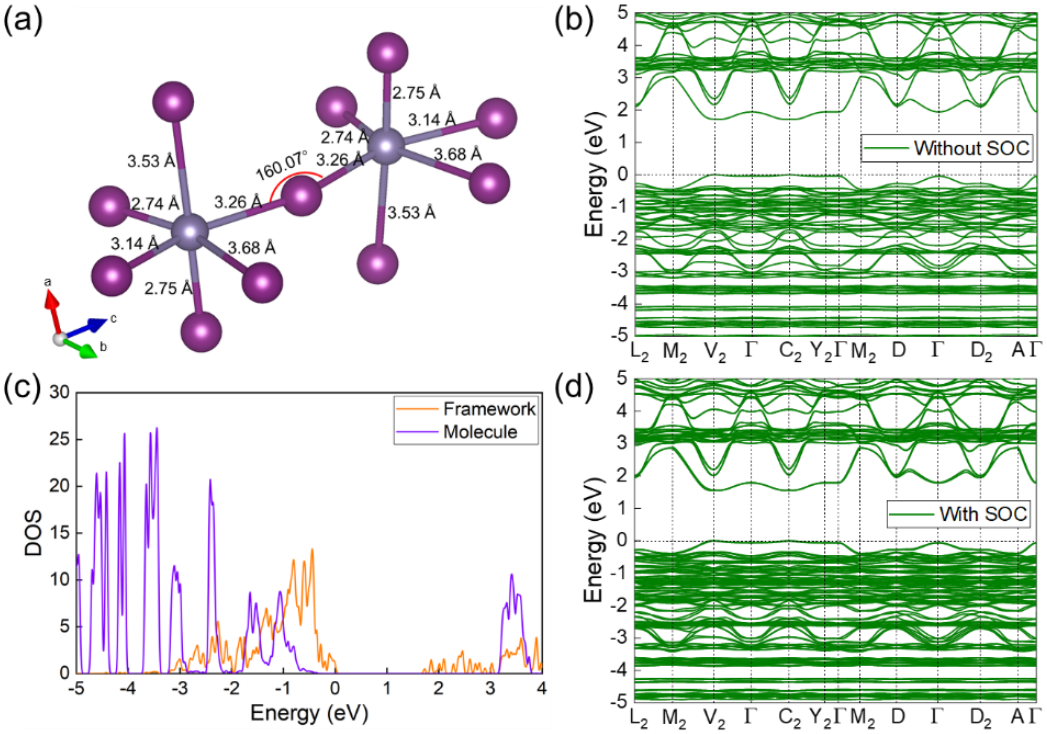

Figure 6. Structural and electronic properties of (*R*-ClMBA)$_2$GeI$_4$. (a) Structural details of relaxed (*R*-ClMBA)$_2$GeI$_4$. (b) Band structure of (*R*-ClMBA)$_2$GeI$_4$ without SOC effect. (c) Projected density of states of (*R*-ClMBA)$_2$GeI$_4$ without SOC effect. (d) Band structure of (*R*-ClMBA)$_2$GeI$_4$ with SOC effect.

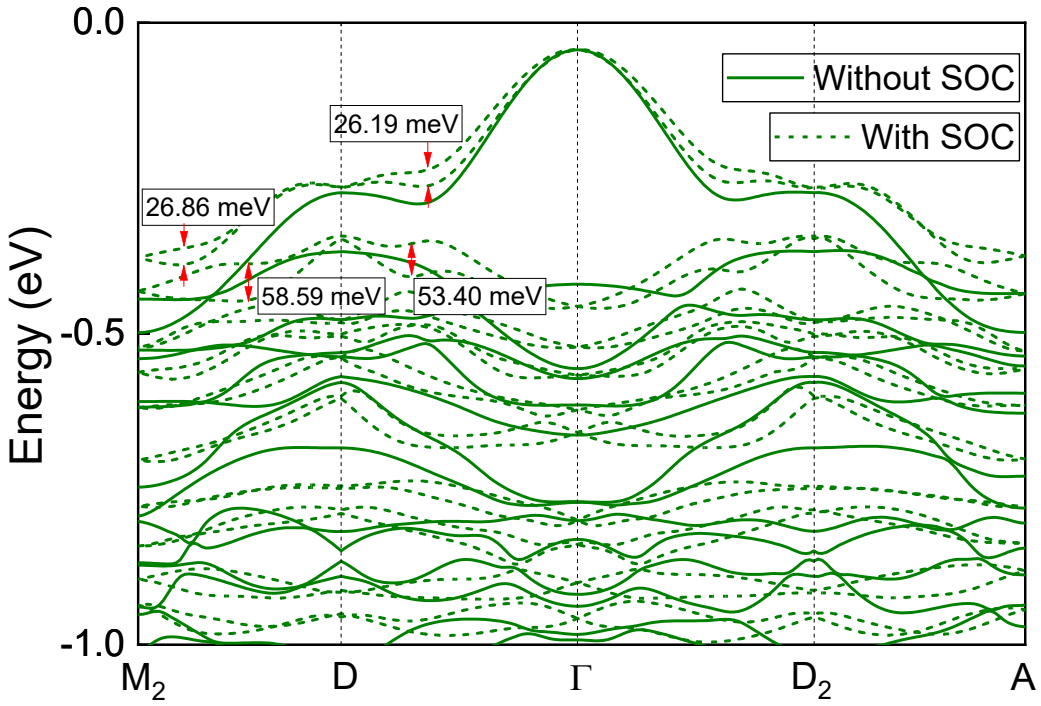

Figure 7. Superpositions of the bands in 2D (R-ClMBA)$_2$GeI$_4$ without SOC (continuous lines) with SOC (dashed lines). The highest band-eigenvalues at Gamma has been aligned.

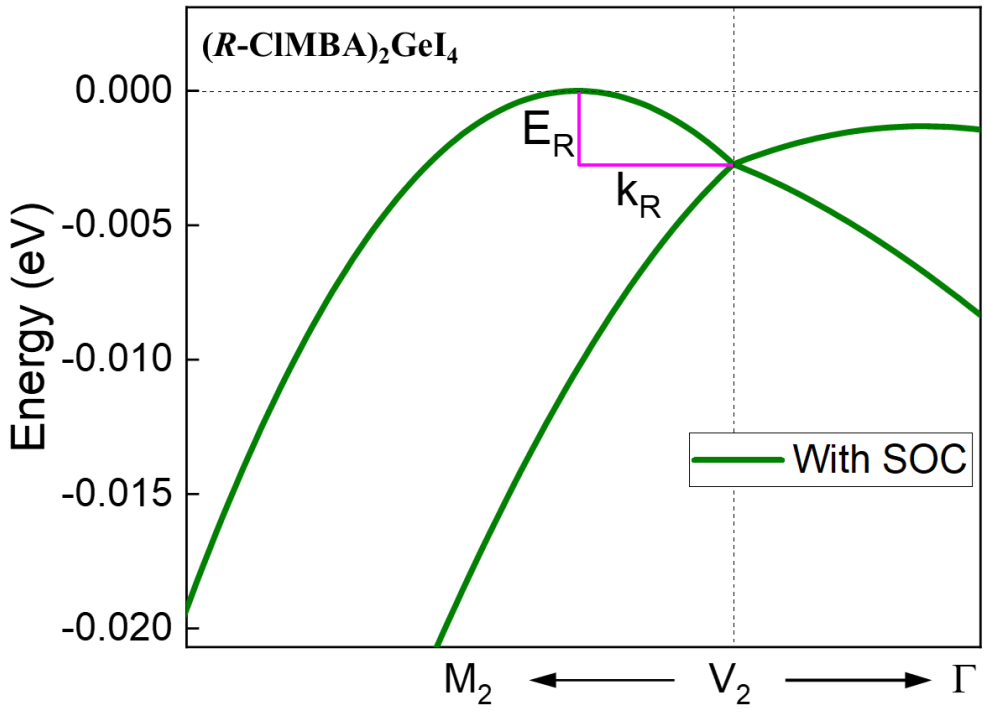

Figure 8. The Rashba splitting around the high-symmetry point V_2 in the first Brillouin zone of (*R*-ClMBA)$_2$GeI$_4$. The Rashba parameter, $\alpha_R = \frac{2E_R}{k_R}$, is estimated to be 227 meV/Å.

Many interesting phenomena, *e.g.*, the Rashba splitting of the band structure, can be induced by the SOC interaction. Therefore, to further reveal the SOC induced effects on the band structure of the two compounds, *i.e.*, (*R*-/S-CIMBA)$_3$GeI$_5$ and (*R*-/S-CIMBA)$_2$GeI$_4$, a comparative discussion is given in the Supporting Information (Figure S11 and S12). Furthermore, in Figure 7, we superimpose the valence bands of (*R*-CIMBA)$_2$GeI$_4$ without SOC (continuous lines) with SOC (dashed lines) in the energy windows between -1 and 0 eV, along a reduced region along the symmetry lines. The effect of SOC is now evident, which induces splittings as large as 20-60 meV. Finally, in Figure 8, we estimate the Rashba parameter as 227 meV/Å, which is comparable with the estimate for other 2D organic-inorganic hybrid perovskites such as [S-4-NH$_3$-MBA]PbI$_4$, [S-4-Cl-MBA]$_2$PbI$_4$ and [S-MHA]$_2$PbI$_4$ (see Supplementary Table 2 of Ref. 51).[51] However, for the 1D case, the Rashba parameter is negligible. For the 2D (*R*-CIMBA)$_2$GeI$_4$ perovskite it could be of interest to correlate the calculated Rashba parameter with structural descriptors proposed in the current literature, specifically the $\Delta\beta_{in}$, suggested by Mitzi an co-workers correlating octahedral distortion with the spin-splitting in 2D MHPs.[51] $\Delta\beta_{in}$ for the (*R*-CIMBA)$_2$GeI$_4$ samples is practically 0 (0.021) which would correlate to an almost zero Rashba parameter, while, in the present case, α parameter is around 227 meV/Å. Such limited level of correlation was already demonstrated by us for the analogous Sn-based system suggesting that the general trend of intra-octahedral distortion along with the spin-splitting proposed in Ref. 51 is most probably limited to Pb-based 2D MHPs. The results of this work on (*R*-CIMBA)$_2$GeI$_4$ strongly calls for an urgent extension of the family of lead-free chiral 2D perovskites in order to be able to formulate more solid and general structure-property correlations for future materials engineering.

We now focus on the comparative structural symmetry mode analysis of the two compounds. We will consider only on the framework atomic positions of the representative R-enantiomer for both structures, i.e. 1D (*R*-ClMBA)$_3$GeI$_5$ and 2D (*R*-ClMBA)$_2$GeI$_4$. First, we make use of the COMPSTRU software, provided by the Bilbao Crystallographic Server [https://www.cryst.ehu.es/][52] which permits a quantitative comparison of two structure descriptions of the same phase, where one structure description is given by the experimental atomic positions (*i.e*. CIF files), and the other is given by the relaxed atomic positions based on DFT calculations. The difference between the two descriptions is quantified by evaluation of the global distortion given in terms of atomic displacement field representing the differences in the positions of the matching atoms of the two structure descriptions. In this way, one can quantify the agreement between experimental and theoretical atomic

positions. The comparison is described by the following descriptors: the parameter $d_{max.}$ corresponds to the maximum difference between the atomic positions of the matching atoms; the arithmetic mean (d_{av}) of the differences between the atomic positions of the matching atoms; the measure of similarity (δ) is a function of the differences in atomic positions (weighted by the multiplicities of the sites) and the ratios of the corresponding lattice parameters of the structures. For more details about the definitions of the parameters we refer to Ref. 32. For the 1D (R-ClMBA)$_3$GeI$_5$ structure, we otbain d_{max}= 0.0861 Å, d_{av}= 0.0583 Å and the measure of δ calculated for this case is 0.124. For the 2D (R-ClMBA)$_2$GeI$_4$ structure we obtain d_{max}= 0.0903Å, d_{av}= 0.0567Å and the measure of δ calculated for this case is 0.006. In both cases, the theoretical description of the framework is very close to the experimental atomic positions. Therefore, for simplicity, we will refer to the theoretical atomic positions for further analysis. It may be instructive to quantify the symmetry breaking atomic distortions of the framework with respect to a parent phase. Since the organic cations are the same in both 1D and 2D structures, the degree of cation chirality, quantified in terms of ECM, is the same in both structures.[13] Therefore, any difference of the *chiral distortion* of the framework should be related to the different topology of the two structures. After atomic relaxations, one can analyze the induced framework distortions in terms of an appropriate reference centric pseudosymmetric parent structure. Here pseudosymmetric means that the positions of the atoms of the framework of the 2D or 1D structure can be obtained from the atomic positions of the parent structure with symmetry adapted atomic displacements. In order to define the centrosymmetric parent structure for our systems we used the tool PSEUDOSYMMETRY of the Bilbao Crystallographic Server.[53] For the 1D system, we started from the full atomic structure, and, after removing all the atoms of the organic cations, we considered the framework-only structure in space group $P2_1$ (n° 4) symmetry. This allows us to focus only on the distortions of the framework and remove additional computational complexity due to the presence of the organic cations. We can find a suitable parent phase in space group $C2/m$ (n. 12) defined by an appropriate transformation matrix and including additional shift of the origin. By considering the Symmetry Mode Analysis with AMPLIMODES, one can quantify the induced symmetry breaking distortion[54,55] connecting the high-symmetry (n. 12) to the low-symmetry (n. 4) structure. For convenience, the mode belonging to the trivial Irreducible Representation (irrep) GM1+ has been removed (i.e. its amplitude is zero) since it always appears as possible symmetry of secondary variables that are allowed to have non-zero values both at the distorted phase and at the parent phase. The additional modes involved besides the trivial GM1+ mode are: Y2- and Y2+, whose

isotropy subgroups are $P2_1/m$ (n. 11) and $P2_1/c$ (n. 14) respectively. In both cases, the modes do not break inversion symmetry since the isotropy subgroups are centric, and, therefore, not chiral. Interestingly, a third mode is present, namely GM1-, with isotropy subgroup $C2$ (n. 5), which is clearly chiral. Its amplitude with respect to the primitive unit cell of the high-symmetry structure is 0.1329 A. When performing the same type of analysis for the 2D $(R\text{-}ClMBA)_2GeI_4$, *i.e.* by relating the low-symmetry structure with space group $C2$ (n. 5) to the same space group as before, *i.e*. $C2/m$ (n. 12), for the parent structure, and by considering the trivial GM1+ set to zero amplitude, one finds two modes, M1+ and M1- with centric isotropy subgroups $C2/m$ (n. 12) and $C2/c$ (n. 15), and a chiral mode GM1- with chiral isotropy subgroup, $C2$ (n. 5). In this case, the amplitude of the chiral mode is significantly increased to 0.6665 A. Note that, since the primitive unit cells of the two parent structures in $C2/m$ (n. 12), have a different number of atoms, the mode amplitudes of the two cases are not directly comparable. But considering that in the case of the $P2_1$ structure the parent primitive unit cell has 24 atoms and that the other case has 10 atoms, the average (i.e. per atom) amplitude of the chiral distortion in the $P2_1$ structure, that would be comparable to that of the other structure, would be even smaller by a factor of the order of sqrt (2.4). Therefore, one can say that this average (i.e. per atom) distortion amplitude is much smaller in the $P2_1$ structure. This analysis further confirms and quantifies, on solid symmetry based-approach, the increased chirality transfer to the framework from 1D to 2D structure, due to structural topology change. We note that the qualitative analysis of the chiral transfer from organic ligand to the inorganic framework could also be performed in the future based on the method proposed in Ref. 56 that a set of descriptors were identified to effectively characterize the chirality of the halide systems in combination with the machine-learning technics.[56]

3. Conclusions

We report here two novel series of chiral ClMBA-containing germanium iodides, (*R*/*S*-ClMBA)$_3$GeI$_5$, and (*R*/*S*-ClMBA)$_2$GeI$_4$, presenting the same chemical building blocks but a different dimensionality, namely a 1D structural motif for the first and a typical 2D arrangement of RP perovskites for the second system. The experimental and computational investigation allows to highlight some important points related to the change in dimensionality. First of all, from the structural data, the 1D topology presents a reduced distortion level of the octahedra with respect to the 2D system which may be correlated to its higher lattice rigidity providing a clue to tune distortion parameters which are known to affect the electronic and optical properties. DFT calculations predict stronger effect of SOC on relevant electronic states passing from a 1D to a 2D structure, which correlates with the increase of the amplitude of the chiral distortions induced into the framework. The optical properties indicate a change from indirect to direct bandgap passing from 1D to 2D dimensionality with a slight red-shift in the same direction. In terms of chiroptical properties, the CD results clearly indicate a one order of magnitude increase of the g_{CD} from ~4×10^{-4} to ~4×10^{-3} when dimensionality reduces passing from a 2D layered perovskite to a 1D system. The origin of such trend can be interpreted as an “increase” of the chirality transfer to the inorganic framework when changing the structural dimensionality as demonstrated by the analysis of the symmetry breaking distortions. For the novel 2D (*R*/*S*-Cl-MBA)$_2$GeI$_4$ system, a comparison with the analogous Pb- and Sn-based chiral perovskites may suggest a minor role of central metal and distortion level on the extent of chiroptical response in terms of asymmetry factor.[14] To conclude, our study reveals an active role of the dimensionality change keeping the same chemical building blocks, *i.e*. the organic cation, metal-atom and halide. In this case, the chirality transfer from the organic cations to the framework is more effective in the transition from 1D to 2D structure topology which also impact the chiroptical properties. It is clear that the novel strategy tuning presented in this work should be further extended to other chiral systems to provide solid structure-property correlations for future materials engineering.

Acknowledgement

L.M. acknowledges support from the Ministero dell'Università e della Ricerca (MUR) and the University of Pavia through the program "Dipartimenti di Eccellenza 2023–2027. We acknowledge support from the Italian Ministry of Research under the PRIN 2022 Grant No 2022F2K7J5 with title "Two-dimensional chiral hybrid organic−inorganic perovskites for chiroptoelectronics" PE 3 funded by PNRR Mission 4 Istruzione e Ricerca - Component C2 - Investimento 1.1, Fondo per il Programma Nazionale di Ricerca e Progetti di Rilevante Interesse Nazionale PRIN 2022 - CUP B53D23004130006. A.S. acknowledges Prof. M. Perez-Mato for useful discussions. Y.Y. acknowledges the support by National Natural Science Foundation of China (Grant No. 12304115) and the support by the Fundamental Research Funds for the Central Universities (Grant No. FRF-TP-24-039A).

The first-author Clarissa Coccia, author of the present Ph.D. work, carried out the synthesis of all the materials and part of the optical characterization: Absorption spectra, CD Spectra and the connected part of the revision of the paper.

References

(1) Dang, Y.; Liu, X.; Cao, B.; Tao, X. Chiral Halide Perovskite Crystals for Optoelectronic Applications. *Matter* **2021**, *4* (3), 794–820.

(2) Dong, Y.; Zhang, Y.; Li, X.; Feng, Y.; Zhang, H.; Xu, J. Chiral Perovskites: Promising Materials toward Next-Generation Optoelectronics. *Small* **2019**, *15* (39), 1902237.

(3) Long, G.; Sabatini, R.; Saidaminov, M. I.; Lakhwani, G.; Rasmita, A.; Liu, X.; Sargent, E. H.; Gao, W. Chiral-Perovskite Optoelectronics. *Nat Rev Mater* **2020**, *5* (6), 423–439.

(4) Ma, J.; Wang, H.; Li, D. Recent Progress of Chiral Perovskites: Materials, Synthesis, and Properties. *Adv. Mater.* **2021**, *33* (26), 2008785.

(5) Billing, D. G.; Lemmerer, A. Synthesis and Crystal Structures of Inorganic–Organic Hybrids Incorporating an Aromatic Amine with a Chiral Functional Group. *CrystEngComm* **2006**, *8* (9), 686–695.

(6) Ahn, J.; Lee, E.; Tan, J.; Yang, W.; Kim, B.; Moon, J. A New Class of Chiral Semiconductors: Chiral-Organic-Molecule-Incorporating Organic–Inorganic Hybrid Perovskites. *Mater. Horiz.* **2017**, *4* (5), 851–856.

(7) Lin, J.; Chen, D.; Yang, L.; Lin, T.; Liu, Y.; Chao, Y.; Chou, P.; Chiu, C. Tuning the Circular Dichroism and Circular Polarized Luminescence Intensities of Chiral 2D Hybrid Organic–Inorganic Perovskites through Halogenation of the Organic Ions. *Angew Chem Int Ed* **2021**, *60* (39), 21434–21440.

(8) Dibenedetto, A.; Coccia, C.; Boiocchi, M.; Moroni, M.; Milanese, C.; Malavasi, L. Synthesis and Characterization of Cu-Containing Chiral Metal Halides and Role of Halogenation of the Organic Ligand. *J. Phys. Chem. C* **2024**, acs.jpcc.4c00150.

(9) Fan, C.-C.; Liu, C.-D.; Liang, B.-D.; Wang, W.; Jin, M.-L.; Chai, C.-Y.; Jing, C.-Q.; Ju, T.-Y.; Han, X.-B.; Zhang, W. Tuning Ferroelectric Phase Transition Temperature by Enantiomer Fraction. *Nat Commun* **2024**, *15* (1), 1464.

(10) Das, R.; Hossain, M.; Mahata, A.; Swain, D.; De Angelis, F.; Santra, P. K.; Sarma, D. D. Unique Chiro-Optical Properties of the Weakly-2D (R-/S-MBA) $_2$ CuBr $_4$ Hybrid Material. *ACS Materials Lett.* **2023**, 1556–1564.

(11) Zhang, Z.; Wang, Z.; Sung, H. H.-Y.; Williams, I. D.; Yu, Z.-G.; Lu, H. Revealing the Intrinsic Chiroptical Activity in Chiral Metal-Halide Semiconductors. *J. Am. Chem. Soc.* **2022**, *144* (48), 22242–22250.

(12) Bellarosa, L.; Zerbetto, F. Enantiomeric Excesses and Electronic Chirality Measure. *J. Am. Chem. Soc.* **2003**, *125* (7), 1975–1979.

(13) Aucar, J. J.; Stroppa, A.; Aucar, G. A. A Relationship between the Molecular Parity-Violation Energy and the Electronic Chirality Measure. *J. Phys. Chem. Lett.* **2024**, *15* (1), 234–240.

(14) Coccia, C.; Morana, M.; Mahata, A.; Kaiser, W.; Moroni, M.; Albini, B.; Galinetto, P.; Folpini, G.; Milanese, C.; Porta, A.; Mosconi, E.; Petrozza, A.; De Angelis, F.; Malavasi, L. Ligand-Induced Chirality in ClMBA $_2$ SnI $_4$ 2D Perovskite**. *Angew Chem Int Ed* **2024**, e202318557.

(15) Abate, A. Perovskite Solar Cells Go Lead Free. *Joule* **2017**, *1* (4), 659–664.

(16) Abate, A. Stable Tin-Based Perovskite Solar Cells. *ACS Energy Lett.* **2023**, *8* (4), 1896–1899.

(17) Li, J.; Cao, H.-L.; Jiao, W.-B.; Wang, Q.; Wei, M.; Cantone, I.; Lü, J.; Abate, A. Biological Impact of Lead from Halide Perovskites Reveals the Risk of Introducing a Safe Threshold. *Nat Commun* **2020**, *11* (1), 310.

(18) Noel, N. K.; Stranks, S. D.; Abate, A.; Wehrenfennig, C.; Guarnera, S.; Haghighirad, A.-A.; Sadhanala, A.; Eperon, G. E.; Pathak, S. K.; Johnston, M. B.; Petrozza, A.; Herz, L. M.; Snaith, H. J. Lead-Free Organic–Inorganic Tin Halide Perovskites for Photovoltaic Applications. *Energy Environ. Sci.* **2014**, *7* (9), 3061–3068.

(19) Coccia, C.; Moroni, M.; Malavasi, L. Chiral Metal Halide Perovskites: Focus on Lead-Free Materials and Structure-Property Correlations. *Molecules* **2023**, *28* (16), 6166.

(20) Hu, J.; Wen, X.; Yang, D.; Chen, Y.; Liu, Z.; Li, D. Lead-Free Chiral Perovskite for High Degree of Circularly Polarized Light Emission and Spin Injection. *Nano Lett.* **2024**, *24* (3), 1001–1008.

(21) Zhu, T.; Li, X.; Yu, P.; Zhu, Z.; Li, M.; Li, R.; Han, S.; Ye, H.; Ji, C.; Luo, J. Rational Design of Enantiomeric Lead-Free Double Perovskites by Achiral-Chiral Cation Intercalation. *Chem* **2024**, *10* (3), 882–890.

(22) Peng, H.; Liu, Q.; Lu, Y.-Z.; Yang, S.-J.; Qi, J.-C.; Chen, X.-G.; Liao, W.-Q. A Chiral Two-Dimensional Perovskite-like Lead-Free Bismuth(III) Iodide Hybrid with High Phase Transition Temperature. *Chem. Commun.* **2023**, *59* (68), 10295–10298.

(23) Maiti, A.; Pal, A. J. Spin-Selective Charge Transport in Lead-Free Chiral Perovskites: The Key towards High-Anisotropy in Circularly-Polarized Light Detection. *Angew Chem Int Ed* **2022**, *61* (52), e202214161.

(24) Dong, X.; Chen, T.; Liang, J.; Wang, L.; Wu, H.; Xu, Z.; Luo, J.; Li, L.-N. Structure Design of Lead-Free Chiral-Polar Perovskites for Sensitive Self-Powered X-Ray Detection. *Chinese Journal of Structural Chemistry* **2024**, *43* (6), 100256.

(25) Lu, H.; Xiao, C.; Song, R.; Li, T.; Maughan, A. E.; Levin, A.; Brunecky, R.; Berry, J. J.; Mitzi, D. B.; Blum, V.; Beard, M. C. Highly Distorted Chiral Two-Dimensional Tin Iodide Perovskites for Spin Polarized Charge Transport. *J. Am. Chem. Soc.* **2020**, *142* (30), 13030–13040.

(26) Wang, H.; Li, J.; Lu, H.; Gull, S.; Shao, T.; Zhang, Y.; He, T.; Chen, Y.; He, T.; Long, G. Chiral Hybrid Germanium(II) Halide with Strong Nonlinear Chiroptical Properties. *Angew Chem Int Ed* **2023**, *62* (41), e202309600.

(27) Song, Z.; Yu, B.; Liu, G.; Meng, L.; Dang, Y. Chiral Hybrid Copper(I) Iodide Single Crystals Enable Highly Selective Ultraviolet-Pumped Circularly Polarized Luminescence Applications. *J. Phys. Chem. Lett.* **2022**, *13* (11), 2567–2575.

(28) Guo, Z.; Li, J.; Wang, C.; Liu, R.; Liang, J.; Gao, Y.; Cheng, J.; Zhang, W.; Zhu, X.; Pan, R.; He, T. Giant Optical Activity and Second Harmonic Generation in 2D Hybrid Copper Halides. *Angew. Chem. Int. Ed.* **2021**, *60* (15), 8441–8445.

(29) Hao, J.; Lu, H.; Mao, L.; Chen, X.; Beard, M. C.; Blackburn, J. L. Direct Detection of Circularly Polarized Light Using Chiral Copper Chloride–Carbon Nanotube Heterostructures. *ACS Nano* **2021**, *15* (4), 7608–7617.

(30) Wang, M.; Wang, X.; Zhang, B.; Li, F.; Meng, H.; Liu, S.; Zhao, Q. Chiral Hybrid Manganese(II) Halide Clusters with Circularly Polarized Luminescence for X-Ray Imaging. *J. Mater. Chem. C* **2023**, *11* (9), 3206–3212.

(31) Asensio, Y.; Bahmani Jalali, H.; Marras, S.; Gobbi, M.; Casanova, F.; Mateo-Alonso, A.; Di Stasio, F.; Rivilla, I.; Hueso, L. E.; Martín-García, B. Circularly Polarized Photoluminescence in Chiral Hybrid Organic–Inorganic Manganese Halide Perovskites: From Bulk Materials to Exfoliated Flakes. *Advanced Optical Materials* **2024**, 2400554.

(32) Malavasi, L.; Morana, M.; Chiara, R. Germanium-based Halide Perovskites: Materials, Properties, and Applications. *ChemPlusChem* **2021**, cplu.202100191.

(33) Malavasi, L.; Bindi, L.; Coduri, M.; De Angelis, F.; Fracassi, F.; Gaboardi, M.; Listorti, A.; Mahata, A.; Milanese, C.; Morana, M.; Quadrelli, P.; boiocchi, massimo; Striccoli, M.; Chiara, R. Role of Spacer Cations and Structural Distortion in Two-Dimensional Germanium Halide Perovskites. *J. Mater. Chem. C* **2021**.

(34) Chiara, R.; Accorsi, G.; Listorti, A.; Coduri, M.; Coccia, C.; Tedesco, C.; Morana, M.; Malavasi, L. Halide Alloying and Role of Central Atom on the Structural and Optical Properties of Decylammonium Germanium 2D Perovskites. *APL Energy* **2023**, *1* (1), 016101.

(35) Jana, M. K.; Song, R.; Liu, H.; Khanal, D. R.; Janke, S. M.; Zhao, R.; Liu, C.; Valy Vardeny, Z.; Blum, V.; Mitzi, D. B. Organic-to-Inorganic Structural Chirality Transfer in a 2D Hybrid Perovskite and Impact on Rashba-Dresselhaus Spin-Orbit Coupling. *Nat Commun* **2020**, *11* (1), 4699.

(36) Wilke, M.; Casati, N. Insight into the Mechanochemical Synthesis and Structural Evolution of Hybrid Organic-Inorganic Guanidinium Lead(II) Iodides. *Chem. Eur. J.* **2018**, *24* (67), 17701–17711.

(37) Liu, H.-L.; Ru, H.-Y.; Sun, M.-E.; Wang, Z.-Y.; Zang, S.-Q. Mixed-Cation Chiral Perovskites Displaying Warm-White Circularly Polarized Luminescence. *Sci. China Chem.* **2023**, *66* (5), 1425–1434.

(38) Fu, D.; Hou, Z.; He, Y.; Liu, J.-C.; Lv, H.-P.; Tang, Y.-Y. Multiaxial Ferroelectricity and Ferroelasticity in a Chiral Perovskite. *Chem. Mater.* **2022**, *34* (7), 3518–3524.

(39) Li, D.; Liu, X.; Wu, W.; Peng, Y.; Zhao, S.; Li, L.; Hong, M.; Luo, J. Chiral Lead-Free Hybrid Perovskites for Self-Powered Circularly Polarized Light Detection. *Angew. Chem. Int. Ed.* **2021**, *60* (15), 8415–8418.

(40) Baur, W. H. The Geometry of Polyhedral Distortions. Predictive Relationships for the Phosphate Group. *Acta Crystallogr B Struct Sci* **1974**, *30* (5), 1195–1215.

(41) Robinson, K.; Gibbs, G. V.; Ribbe, P. H. Quadratic Elongation: A Quantitative Measure of Distortion in Coordination Polyhedra. *Science* **1971**, *172* (3983), 567–570.

(42) Groom, C. R.; Bruno, I. J.; Lightfoot, M. P.; Ward, S. C. The Cambridge Structural Database. *Acta Crystallogr B Struct Sci Cryst Eng Mater* **2016**, *72* (2), 171–179.

(43) Filip, M. R.; Eperon, G. E.; Snaith, H. J.; Giustino, F. Steric Engineering of Metal-Halide Perovskites with Tunable Optical Band Gaps. *Nat Commun* **2014**, *5* (1), 5757.

(44) Smith, M. D.; Connor, B. A.; Karunadasa, H. I. Tuning the Luminescence of Layered Halide Perovskites. *Chem. Rev.* **2019**, *119* (5), 3104–3139.

(45) Koegel, A. A.; Mozur, E. M.; Oswald, I. W. H.; Jalarvo, N. H.; Prisk, T. R.; Tyagi, M.; Neilson, J. R. Correlating Broadband Photoluminescence with Structural Dynamics in Layered Hybrid Halide Perovskites. *J. Am. Chem. Soc.* **2022**, *144* (3), 1313–1322.

(46) Han, X.-B.; Jing, C.-Q.; Zu, H.-Y.; Zhang, W. Structural Descriptors to Correlate Pb Ion Displacement and Broadband Emission in 2D Halide Perovskites. *J. Am. Chem. Soc.* **2022**, *144* (40), 18595–18606.

(47) Kahmann, S.; Meggiolaro, D.; Gregori, L.; Tekelenburg, E. K.; Pitaro, M.; Stranks, S. D.; De Angelis, F.; Loi, M. A. The Origin of Broad Emission in ⟨100⟩ Two-Dimensional Perovskites: Extrinsic vs Intrinsic Processes. *ACS Energy Lett.* **2022**, *7* (12), 4232–4241.

(48) Paritmongkol, W.; Powers, E. R.; Dahod, N. S.; Tisdale, W. A. Two Origins of Broadband Emission in Multilayered 2D Lead Iodide Perovskites. *J. Phys. Chem. Lett.* **2020**, *11* (20), 8565–8572.

(49) Becke, A. D.; Johnson, E. R. A Simple Effective Potential for Exchange. *The Journal of Chemical Physics* **2006**, *124* (22), 221101.

(50) Tran, F.; Blaha, P. Accurate Band Gaps of Semiconductors and Insulators with a Semilocal Exchange-Correlation Potential. *Phys. Rev. Lett.* **2009**, *102* (22), 226401.

(51) Jana, M. K.; Song, R.; Xie, Y.; Zhao, R.; Sercel, P. C.; Blum, V.; Mitzi, D. B. Structural Descriptor for Enhanced Spin-Splitting in 2D Hybrid Perovskites. *Nat Commun* **2021**, *12* (1), 4982.

(52) De La Flor, G.; Orobengoa, D.; Tasci, E.; Perez-Mato, J. M.; Aroyo, M. I. Comparison of Structures Applying the Tools Available at the Bilbao Crystallographic Server. *J Appl Crystallogr* **2016**, *49* (2), 653–664.

(53) Aroyo, M. I.; Perez-Mato, J. M.; Capillas, C.; Kroumova, E.; Ivantchev, S.; Madariaga, G.; Kirov, A.; Wondratschek, H. Bilbao Crystallographic Server: I. Databases and Crystallographic Computing Programs. *Zeitschrift für Kristallographie - Crystalline Materials* **2006**, *221* (1), 15–27.

(54) Orobengoa, D.; Capillas, C.; Aroyo, M. I.; Perez-Mato, J. M. *AMPLIMODES*: Symmetry-Mode Analysis on the Bilbao Crystallographic Server. *J Appl Crystallogr* **2009**, *42* (5), 820–833.

(55) Perez-Mato, J. M.; Orobengoa, D.; Aroyo, M. I. Mode Crystallography of Distorted Structures. *Acta Crystallogr A Found Crystallogr* **2010**, *66* (5), 558–590.

(56) Pols, M.; Brocks, G.; Calero, S.; Tao, S. Temperature-Dependent Chirality in Halide Perovskites. *J. Phys. Chem. Lett.* **2024**, 8057–8064.

SUPPLEMENTARY INFORMATION

Unraveling the Role of Structural Topology on Chirality Transfer and Chiroptical Properties in Chiral Germanium Iodides

Clarissa Coccia,[a] Marco Moroni,[a] Antonella Treglia,[b] Massimo Boiocchi,[c] Yali Yang,*[d] Chiara Milanese,[a] Marta Morana,[e] Doretta Capsoni,[a] Alessio Porta,[a] Annamaria Petrozza,[b] Alessandro Stroppa,[f] and Lorenzo Malavasi*[a]

[a] Department of Chemistry and INSTM, University of pavia, Pavia 27100, Italy

[b] Center for Nano Science and Technology@Polimi, Istituto Italiano di Tecnologia, Milan 20133, Italy

[c] Centro Grandi Strumenti, University of Pavia, 27100 Pavia, Italy

[d] School of Mathematics and Physics, University of Science and Technology Beijing, Beijing 100083, China

[e] Department of Earth Science, Univeristy of Firenze, Firenze 50121, Italy

[f] CNR-SPIN c/o Department of Physical and Chemical Sciences, University of L'Aquila, I-67100 L'Aquila, Italy;

Corrisponding Authors

Lorenzo Malavasi, email: lorenzo.malavasi@unipv.it

Yali Yang, email: ylyang@estb.edu.cn

Experimental

Synthesis of (R-ClMBA)$_3$GeI$_5$, (S-ClMBA)$_3$GeI$_5$, (R-ClMBA)$_2$GeI$_4$, (S-ClMBA)$_2$GeI$_4$ and (rac-ClMBA)$_2$GeI$_4$. To prepare 1.5 g of (*R*-ClMBA)$_3$GeI$_5$ and (*S*-ClMBA)$_3$GeI$_5$ 133,3 mg of GeO_2 (Merck 99.9%) were dissolved in a large excess of 57% w/w aqueous HI (ThermoScientific, stabilized with 1.5% hypophosphorous acid) and 50% w/w aqueous H_3PO_2 (Merck) equivalent to 2 mL and heating the mixture to 90°C. After the dissolution of the solid, the stoichiometric amount of the liquid amine *R*-/*S*-ClMBA (ThermoScientific, 97%, ee 98%), which corresponds to 0.54 mL, was added. To obtain the formation of single crystals the solution has been cooled down to room temperature at 1°C h^{-1}. The (*rac*/*R*/*S*-ClMBA)$_2$GeI$_4$ samples were synthesized in a similar manner by varying the molar ration between the amine and the metal. In this case, 176 mg of GeO_2 were weighed and dissolved in 2.5 mL of HI and H_3PO_2. Once the germanium oxide was dissolved, an amount of amine (*S*, *R* of a 50% mixture of *S* and *R* for racemic compound) equal to 0.47 ml was added. Both syntheses were carried out under a nitrogen flow.

Thin films preparation. First, the glass substrates were washed using water, isopropanol and acetone in a sonicator for 20 min each. Then, the perovskites were dissolved in DMF:acetone (90:10) in order to obtain a final solution 0.08 M, and the thin films were prepared on substrates by dip coating method. The films were annealed at 90°C for 10 min on a hot plate.

Single Crystal X-ray Diffraction. Measurements on selected crystal were collected on Rigaku XtaLab SuperNova (Rigaku Europe SE, Neu-Isenburg, Germany) four-circle diffractometer equipped by a microfocus X-ray source (λ = 0.7107 Å) and a Dectris Pilatus 200K hybrid pixel array detector (DECTRIS AG, Baden-Daettwil, Switzerland). Data collection, data reduction and accurate measurements of the unit cell parameters were performed by means of the CrysAlisPro software suite, ver. 1.171.41.[1] Absorption effects were empirically evaluated based on a multi-scan approach using spherical harmonics by the SCALE3 ABSPACK scaling algorithm implemented in the CrysAlisPro crystallographic suite. Crystal structures were solved by direct methods (SIR 97)[2] and refined by full-matrix least-square procedures on F^2 using all reflections (SHELXL 2018/3).[3]

UV-Vis spectroscopy. DRS spectra were acquired in the wavelength range 300- 800 nm directly on the powders by using a Jasco V-750 spectrophotometer, equipped with an integrating sphere (Jasco ISV-922).

Circular Dichroism. CD spectra were acquired in the wavelength range 350- 800 nm on thin films by using a Jasco J-1500 CD spectrophotometer.

Photoluminescence. Temperature-dependent photoluminescence was measured from bulk crystals under vacuum using a Linkam Stage cooled with liquid nitrogen. The sample was excited with CW laser (375 nm - TOPTICA) linearly polarized. PL was detected using a Maya2000 visible spectrometer. CD PL was acquired using with a quarter-wave plate set to ±45° relative to a linear polarizer. The samples were excited at a fluence of 100 mW/cm^2.

Time-resolved photoluminescence. The sample was excited with the third harmonic (355 nm) from a Nd:YAG Picolo-AOT laser (pulse length of approximately 900 ps, 1 kHz repetition rate). An Andor spectrometer paired with an iStar iCCD is used for the detection. The camera acquisition is synchronized with the 1 kHz trigger signal from the laser. We track the photoemission dynamics by gating the camera's acquisition over a temporal window of 50 ns collected at increasing delay from the trigger reference (50 ns steps). The overall time resolution of the system is 2-4 ns. Kinetics are obtained by integrating the whole PL spectrum recorded at each delay. The samples were excited at a fluence of 100 mW/cm^2.

Computational Details

All density functional theory (DFT) calculations are performed with the VASP package.[4] The generalized gradient approximation (GGA)[5] in the form of the Perdew-Burke-Ernzerhof (PBE) functional and the projector augmented wave (PAW)[6] method are applied to describe the exchange-correlation and the core electrons, respectively. The plane-wave cutoff and convergence criteria for energy and force are set to be 520 eV, 10^{-6} eV, and 0.01 eV/Å, respectively. The PBE-D3 method with Becke-Jonson damping[7] is used to describe the van der Waals interactions. The atomic positions of the structures are optimized while with the lattice parameters being fixed to the experimental values. The k-mesh is set to 2×2×2 when optimizing the structures. The high-symmetry points in the irreducible Brillouin zone are obtained through VASPKIT package[8] for calculating the band structures.

Table S1. Octahedral distortion parameters and bond lengths for (*R*-ClMBA)$_3$GeI$_5$, (*S*-ClMBA)$_3$GeI$_5$, (*R*-ClMBA)$_2$GeI$_4$ and (*S*-ClMBA)$_2$GeI$_4$.

Compound	Polyhedron	Distortion Index (x10^3)	Bond angle variance (deg^2)	Quadratic elongation	Bond lengths (Å)	M-X-M (deg)
(*R*-ClMBA)$_3$GeI$_5$	GeI_6	71	12.61	1.0094	2.9513(9) 2.8072(9) 2.8571(8) 3.2041(9) 3.4285(9) 3.3066(8)	155.93(2)
	GeI_6	75	15.70	1.0105	2.8292(8) 2.8572(8) 2.8857(9) 3.3598(8) 3.2236(9) 3.3756(8)	157.70(2)
(*S*-ClMBA)$_3$GeI$_5$	GeI_6	72	12.59	1.0094	2.9523(9) 2.8079(8) 2.8568(7) 3.2066(9) 3.4294(8) 3.3085(8)	155.94(2)
	GeI_6	75	15.56	1.0104	2.8294(8) 2.8588(7) 2.8870(8) 3.3589(8) 3.2259(9) 3.3780(8)	157.70(2)
(*R*-ClMBA)$_2$GeI$_4$		94	55.16	1.0291	2.7231(10) 2.7545(8) 3.147(4) 3.1941(13) 3.5914(10) 3.6236(8)	171.6° 166.7°
(*S*-ClMBA)$_2$GeI$_4$		94	54.59	1.0290	2.7236(10) 2.7560(9) 3.147(3) 3.1954(13) 3.5917(10) 3.6250(9)	171.3(5)° 166.7(4)°
(*rac*-ClMBA)$_2$GeI$_4$		111	34.52	1.0289	2.781(3) Å 2.796(3) Å 3.030(4) Å 3.088(4) Å 3.700(4) Å 3.774(4) Å	146.8(4)° 166.2(5)°

a)

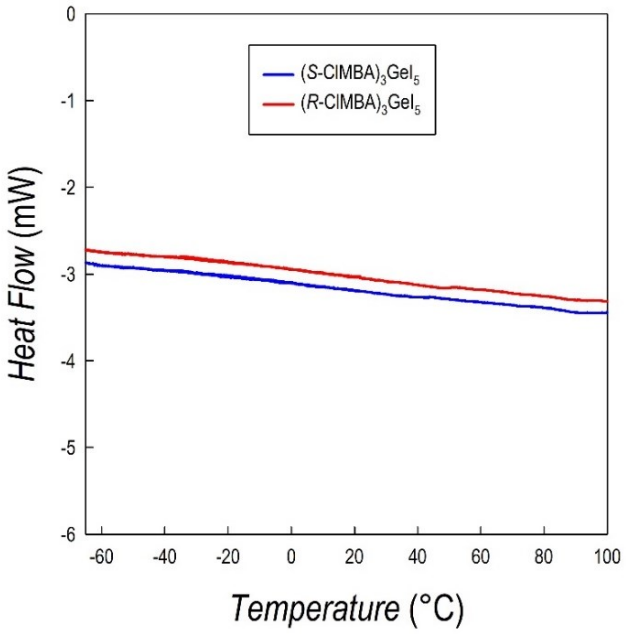
(S-ClMBA)3GeI5
(R-ClMBA)3GeI5
Heat Flow (mW)
Temperature (°C)

b)

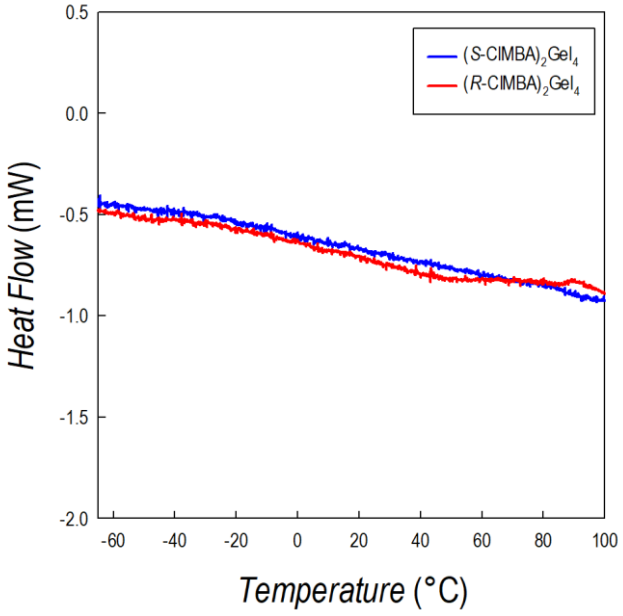
(S-ClMBA)2GeI4
(R-ClMBA)2GeI4
Heat Flow (mW)
Temperature (°C)

c)

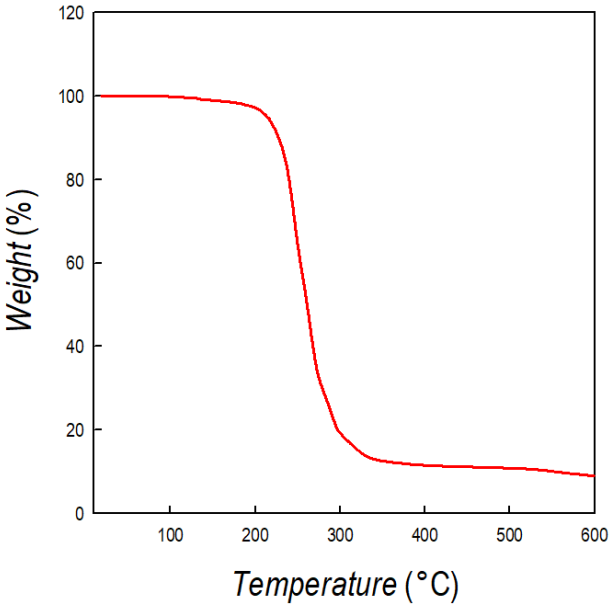
Weight (%)
Temperature (°C)

d)

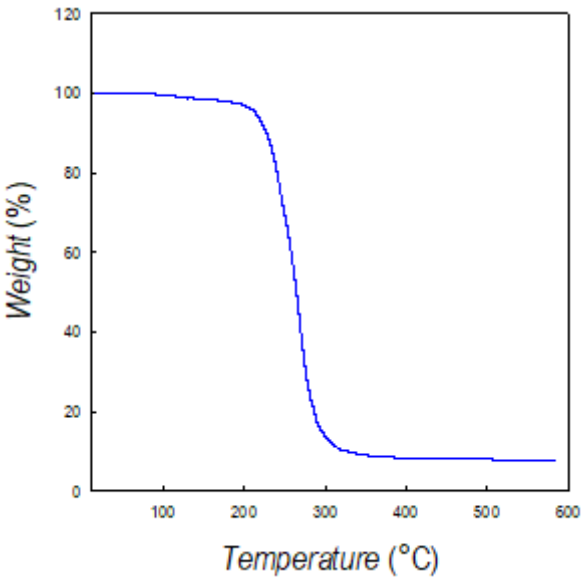
Weight (%)
Temperature (°C)

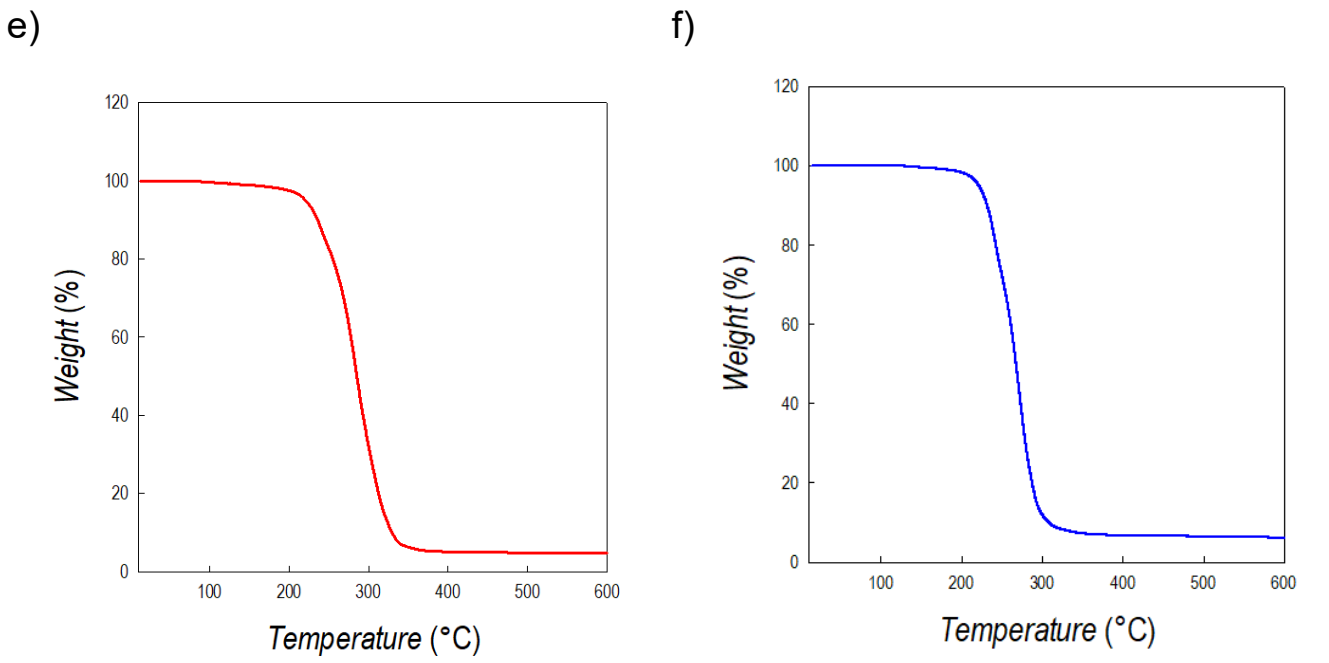

Figure S1. DSC traces a) of $(R\text{-}ClMBA)_3GeI_5$ (red curve) and $(S\text{-}ClMBA)_3GeI_5$ (blue curve) and b) of $(R\text{-}ClMBA)_2GeI_4$ (red curve) and $(S\text{-}ClMBA)_2GeI_4$; TGA curves of c) $(R\text{-}ClMBA)_2GeI_4$, d) $(S\text{-}ClMBA)_2GeI_4$, e) $(R\text{-}ClMBA)_3GeI_5$, and f) of $(S\text{-}ClMBA)_3GeI_5$.

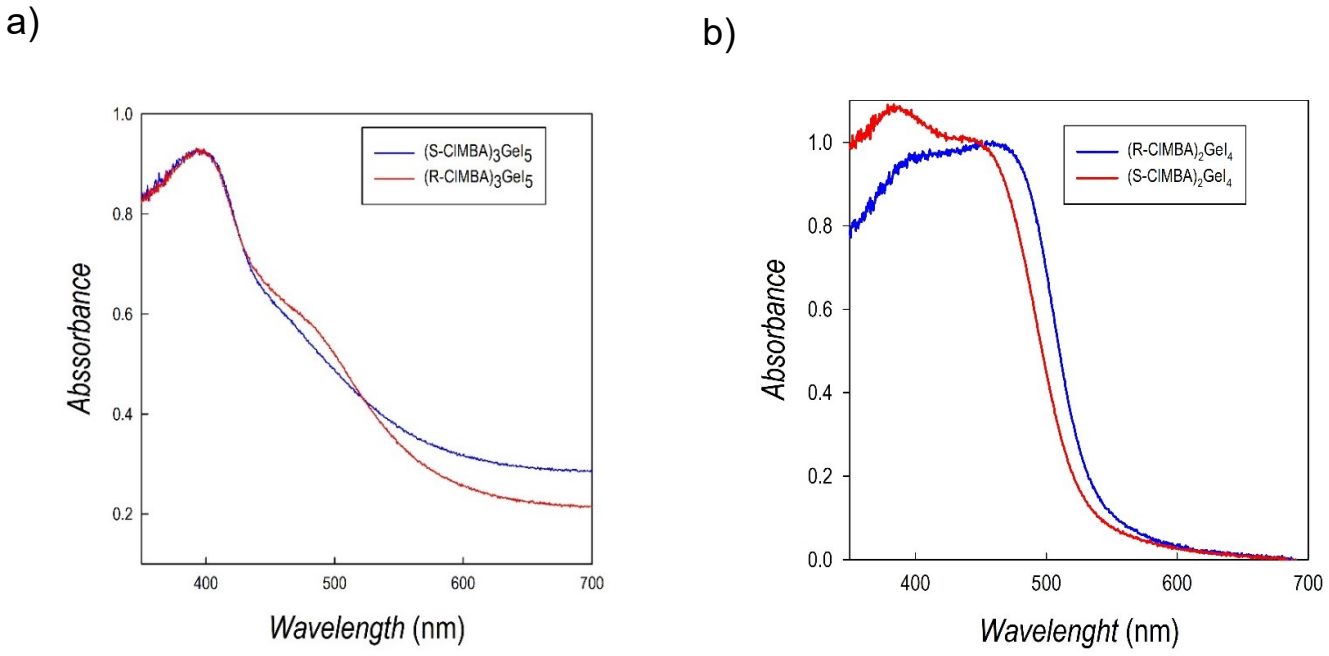

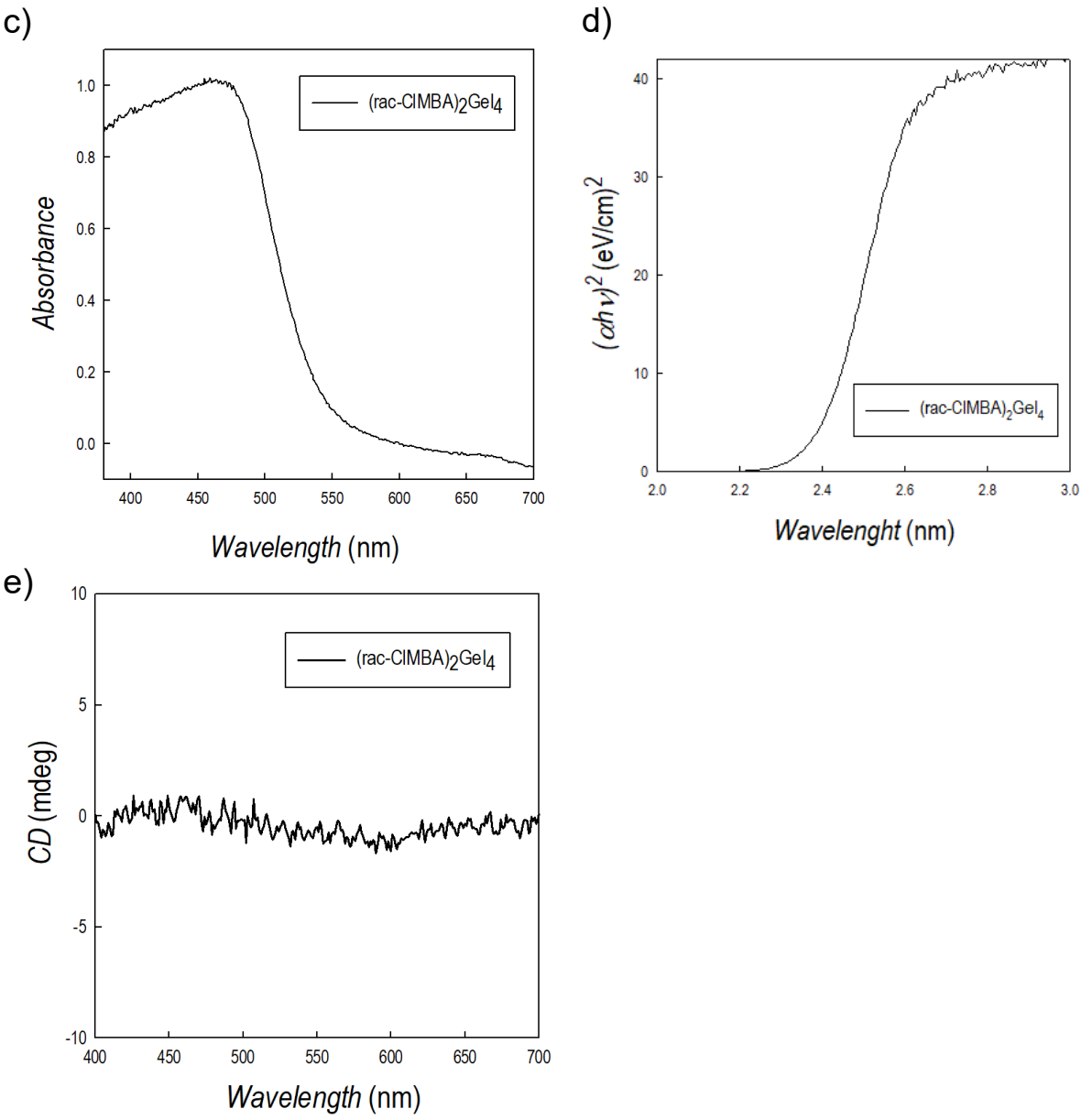

Figure S2. a) Absorption spectra of (*S*/*R*-ClMBA)$_3$GeI$_5$ and b) of (*S*/*R*-ClMBA)$_2$GeI$_4$. Figures c) and d) show the absorption spectrum and the Tauc plot for (*rac*-ClMBA)$_2$GeI$_4$ while in e) is shown its CD spectrum.

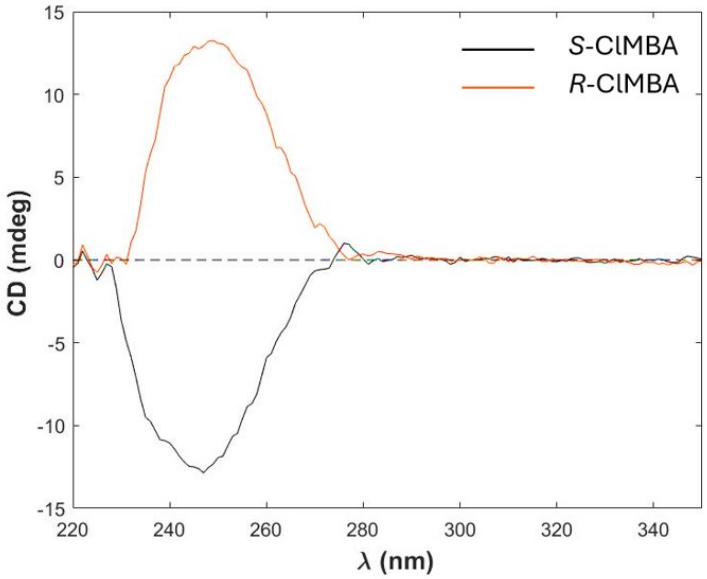

Figure S3. CD spectrum of *R*-ClMBA and *S*-ClMBA

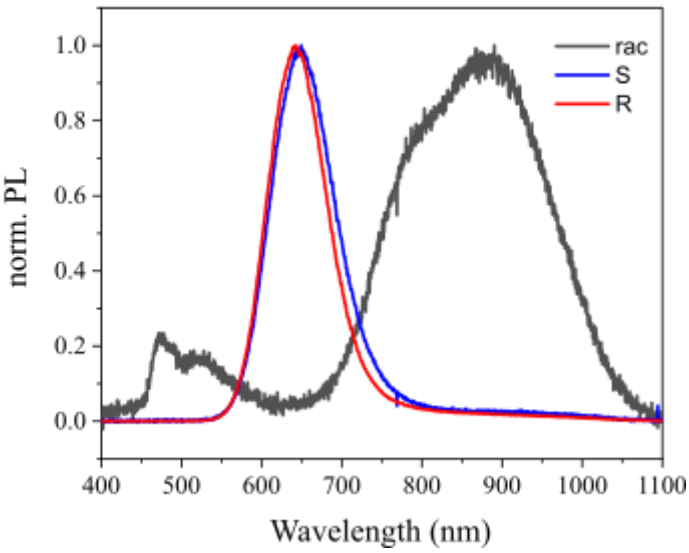

Figure S4. Normalized photoluminescence spectra of (*R*-ClMBA)$_2$GeI$_4$, (*S*-ClMBA)$_2$GeI$_4$ and (*rac*-ClMBA)$_2$GeI$_4$ measured at 77 K.

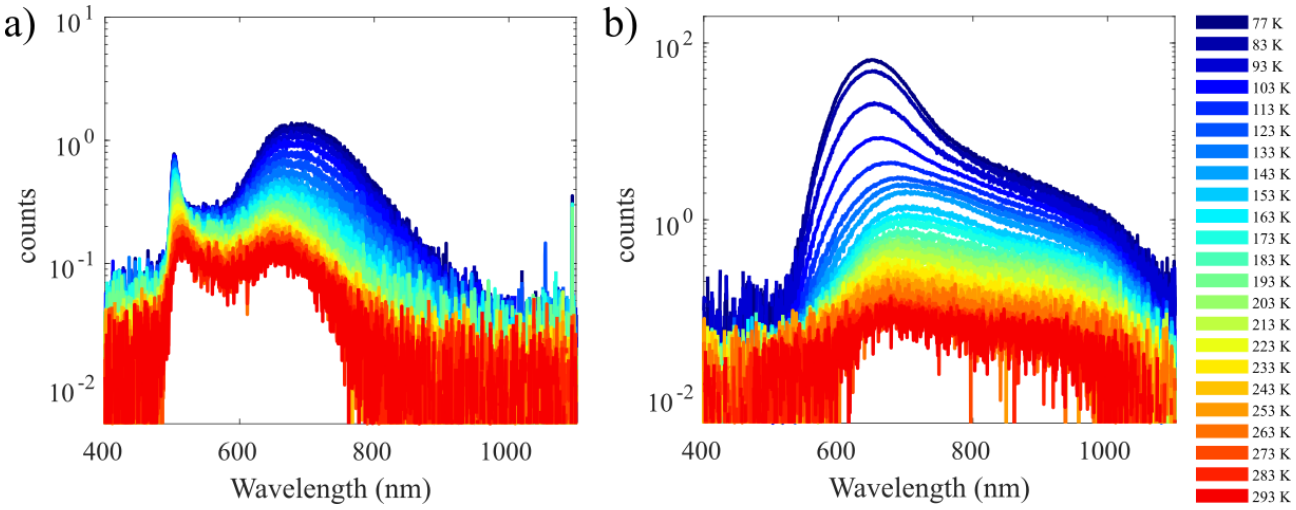

Figure S5. Temperature dependence of the photoluminescence of a) (*S*-ClMBA)$_3$GeI$_5$ and b) (*R*-ClMBA)$_3$GeI$_5$. All measurements were conducted in CW excitation conditions using a 375 nm laser pump.

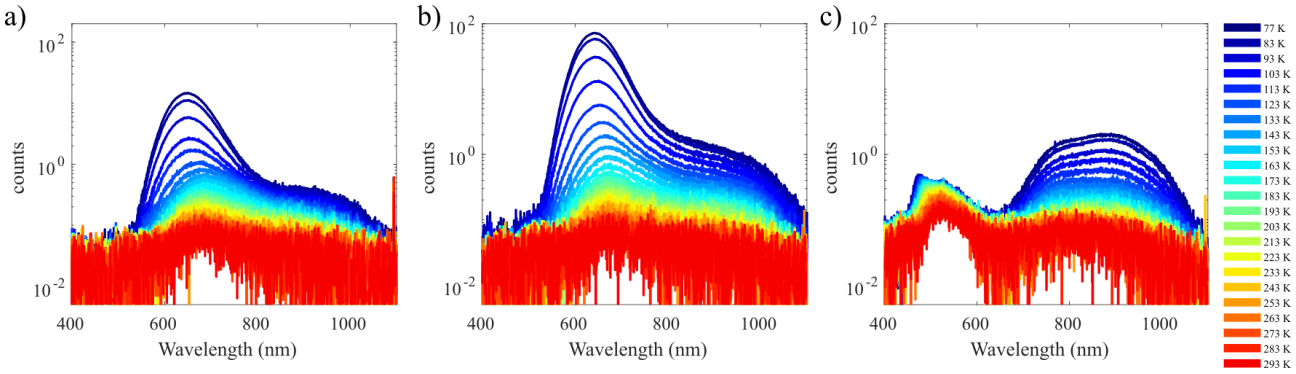

Figure S6. Temperature dependence of the photoluminescence of a) (*S*-ClMBA)$_2$GeI$_4$, b) (*R*-ClMBA)$_2$GeI$_4$ and c) (*rac*-ClMBA)$_2$GeI$_4$. All measurements were conducted in CW excitation conditions using a 375 nm laser pump.

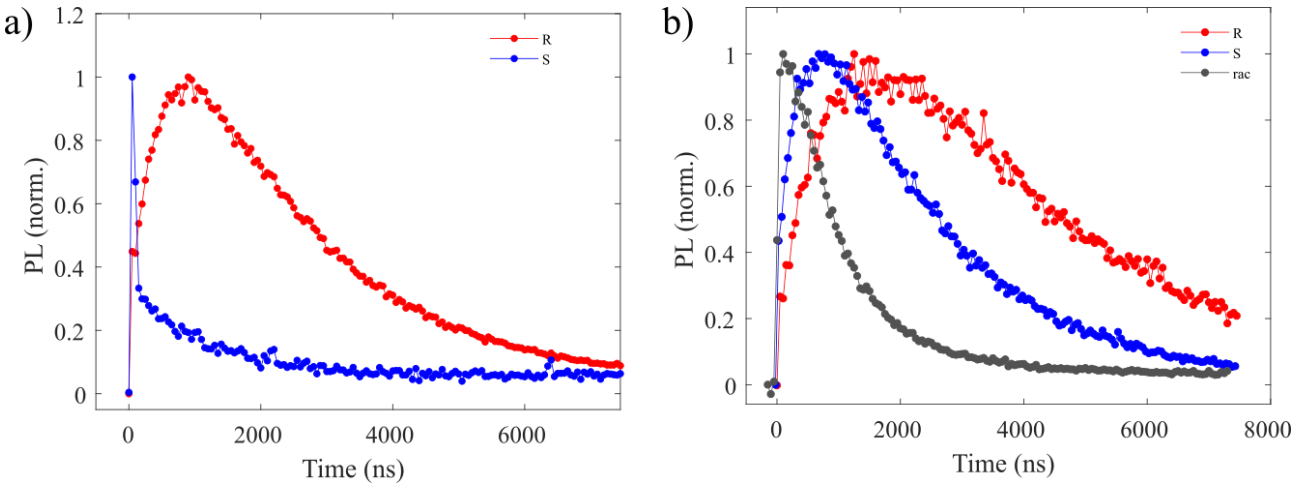

Figure S7. PL luminescence decays of the broadband emission above 600 nm of a) (*S*-ClMBA)$_3$GeI$_5$ and (*R*-ClMBA)$_3$GeI$_5$ and b) (*S*-ClMBA)$_2$GeI$_4$, (*R*-ClMBA)$_2$GeI$_4$ and c) (*rac*-ClMBA)$_2$GeI$_4$.

Table S2. List of anisotropy factors from the CD spectra for a series of 2D and 1D metal halides.

2D perovskites	Anisotropy Factor (g_{CD})	Ref	1D perovskites	Anisotropy Factor (g_{CD})	Ref
$(Cl\text{-}MBA)_2SnI_4$	$\pm1\times10^{-4}$	11	$(MPA)_4AgBiI_8$	$\pm10^{-3}$	15
$(MBA)_2SnI_4$	$\pm2\times10^{-4}$	11	$(NEA)PbI_3$	$\pm10^{-3}$	16
$(Cl\text{-}MBA)_2PbI_4$	$\pm8\times10^{-3}$	11	$(MPA)_2BiBr_5$	$\pm6\times10^{-4}$	17
$(MBA)_2PbI_4$	$\pm1\times10^{-3}$	11	$(ClPEA)_4Bi_2I_{10}$	$\pm5.3\times10^{-4}$	18
$(Br\text{-}MBA)_2PbI_4$	$\pm2.2\times10^{-3}$	12	$(Pro)PbI_3\cdot H_2O$	$\pm3\times10^{-4}$	19
$(F\text{-}MBA)_2PbI_4$	$\pm3\times10^{-4}$	12	$(PEA)PbI_3$	$\pm10^{-3}$	20
$(MePEA)_2PbBr_4$	$\pm1.2\times10^{-4}$	13	$(PEA)SnCl_3$	$\pm1\times10^{-4}$	21
$(MPEA)_2CuCl_4$	$\pm10^{-4}$	14	$(PEA)SnBr_3$	$\pm2\times10^{-4}$	21

Table S3. Lattice constants of the full optimized structure of $(R\text{-}ClMBA)_3GeI_5$ and $(R\text{-}ClMBA)_2GeI_4$.

Compounds	*a* (Å)	*b* (Å)	*c* (Å)	*β* (°)
$(R\text{-}ClMBA)_3GeI_5$	18.5837	8.6727	22.6620	106.7835
$(R\text{-}ClMBA)_2GeI_4$	33.3590	6.2716	12.1941	99.7400

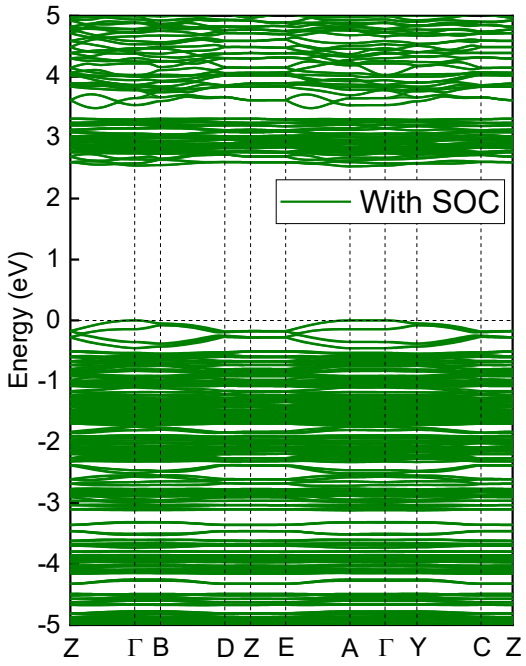

Figure S8. Band structure of (*R*-ClMBA)$_3$GeI$_5$ with SOC effect.

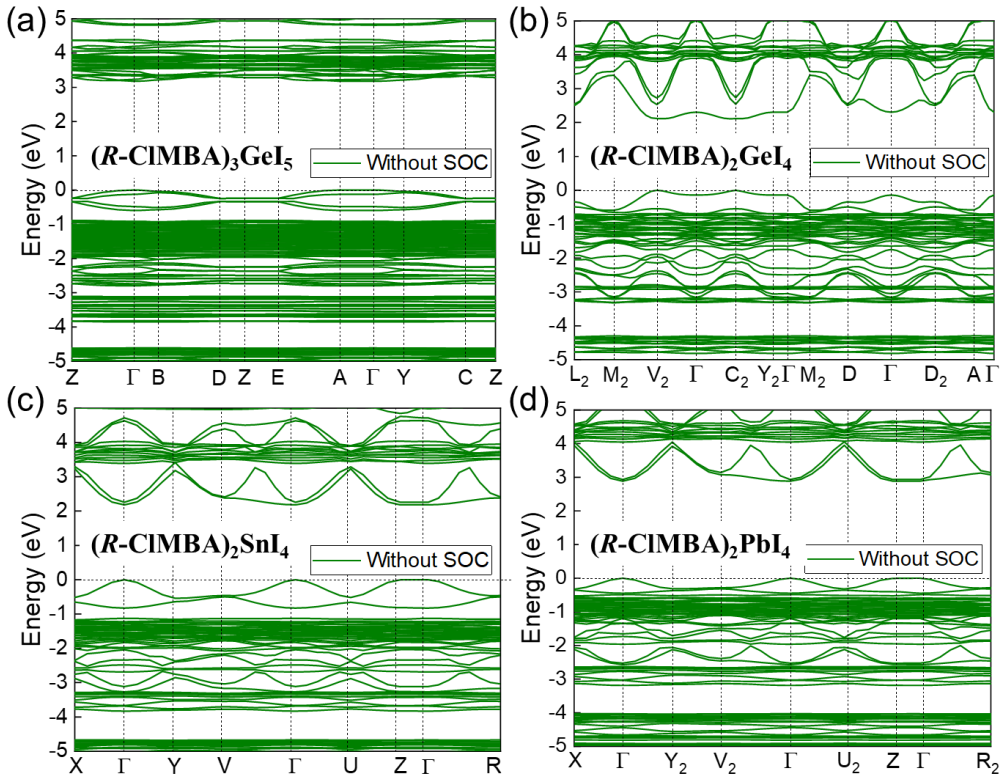

Figure S9. Band structure of (*R*-ClMBA)$_3$GeI$_5$, (*R*-ClMBA)$_2$GeI$_4$, (*R*-ClMBA)$_2$SnI$_4$ and (*R*-ClMBA)$_2$PbI$_4$ compound with using the modified Becke-Johnson (mBJ)[9,10] metaGGA functional. Here, the spin-orbital coupling is not included in the calculations.

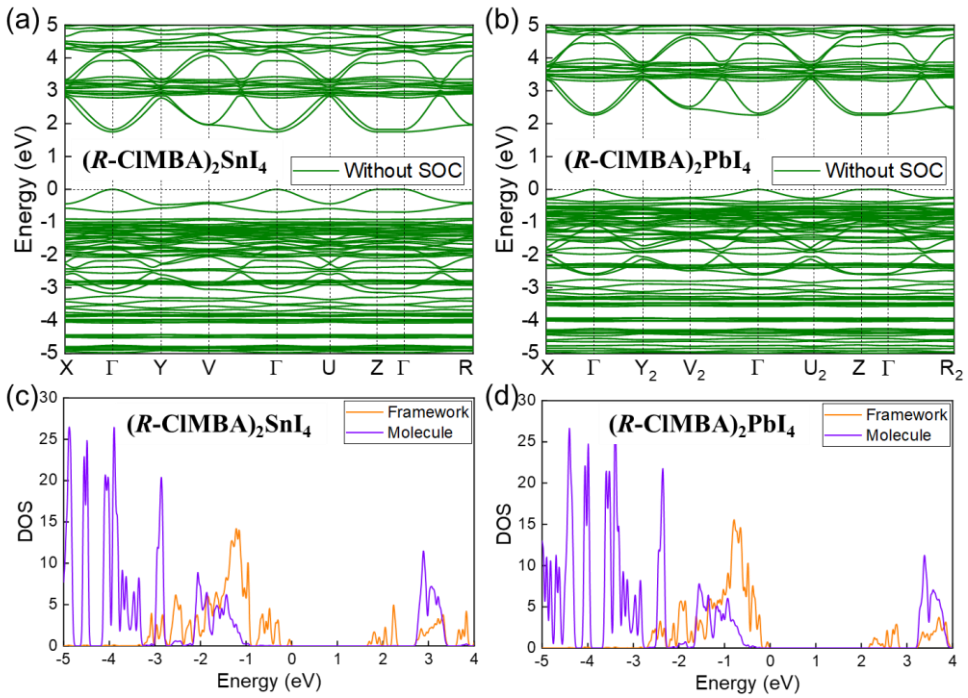

Figure S10. Band structure and density of state of (*R*-ClMBA)$_2$SnI$_4$ and (*R*-ClMBA)$_2$PbI$_4$ compounds. Here, the spin-orbital coupling is not included in the calculations. The calculated band gap for (*R*-ClMBA)$_2$SnI$_4$ and (*R*-ClMBA)$_2$PbI$_4$ compounds are 1.75 eV and 2.26 eV, respectively.

SOC effects on band structures

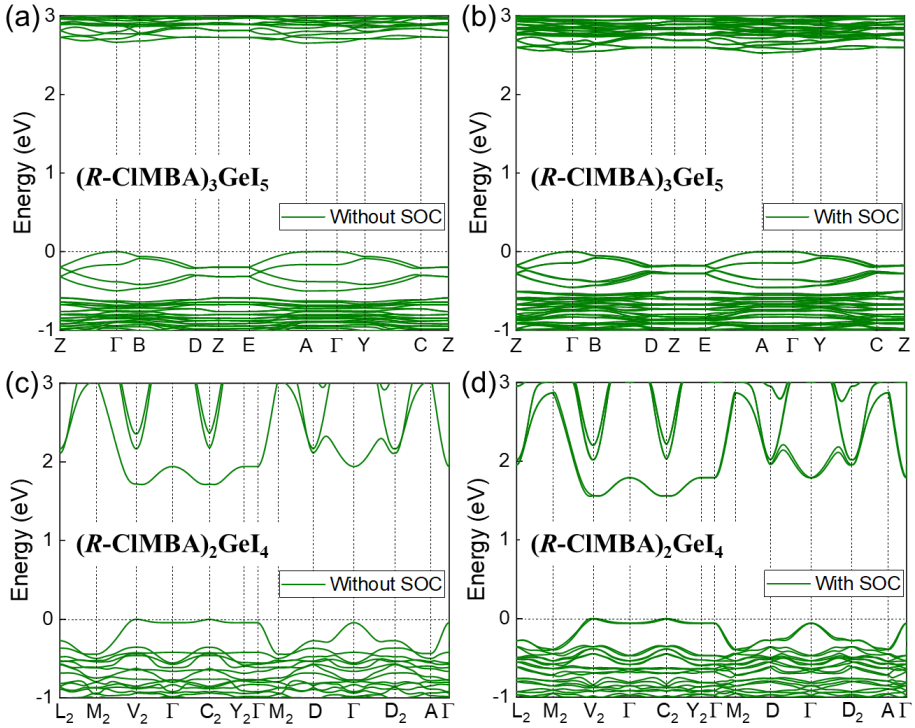

Figure S11. Zoom of the electronic bands along the symmetry lines in the energy region between -1 and 3 eV. Significant changes in the band dispersions and effect of SOC are seen from 1D to 2D topology.

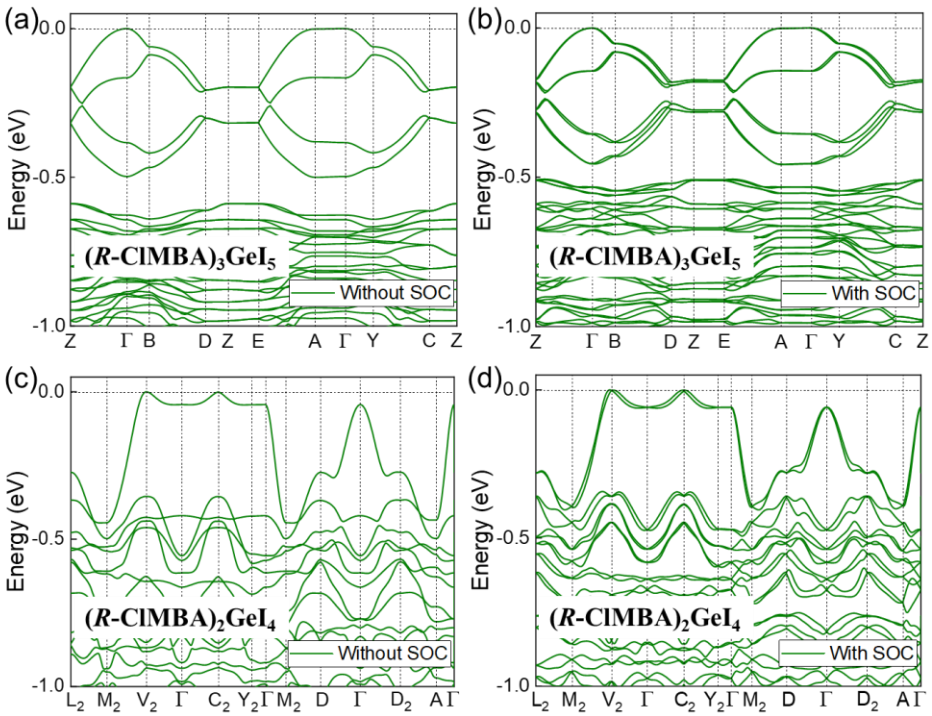

Figure S12. Details of the valence bands in the energy region between -1 and 0 eV. The SOC induced spitting appears more significant in the 2D cases: compare (a) with (b) and (c) with (d).

In order to get more insights in the comparative study of the electronic structure of the two compounds, with and without SOC, in Figure S11 we consider a zoom for the relevant valence band states: in the top panel, we show the band structure of the 1D (*R*-ClMBA)$_3$GeI$_5$ without SOC (a) and with SOC (b) respectively, and in the bottom panel, we show the band structure of 2D (*R*-ClMBA)$_2$GeI$_4$ without SOC (c) and with SOC (d) respectively. Clearly the effect of SOC in (b) is negligible if we compare to (a), while it appears significant if we compare (d) to (c). This appears counterintuitive, since the organic cations, metal and halogen atoms are the same, while only the network topology changes. This highlights again the important role of the dimensionality in hybrid metal-halides as a possible further source for tuning the electronic features. As we noted before from structural analysis, from 1D to 2D structure, the metal-iodide framework becomes progressively more distorted thus correlating with an increased spin-splitting of the relevant electronic states. The stronger effect of SOC coupling is highlighted in Figure S12, where we show a zoom of the valence bands in the energy region between -1 and 0 eV along the symmetry lines.

References

(1) Rigaku Oxford Diffraction **2021**. CrysAlisPro Software system, version 1.171.41.104a, Rigaku Corporation, Wroclaw, Poland.

(2) A. Altomare, M.C. Burla, M. Camalli, G.L. Cascarano, C. Giacovazzo, A. Guagliardi, A.G.G. Moliterni, G. Polidori, R. Spagna. SIR97: a new tool for crystal structure determination and refinement. J. Appl. Crystallogr. **1999**, 32, 115.

(3) G. M. Sheldrick. Crystal structure refinement with SHELXL. Acta Crystallogr. **2015**, C71, 3.

(4) G. Kresse and D. Joubert. From ultrasoft pseudopotentials to the projector augmented-wave method. Phys. Rev. B. **1999**, 59, 1758.

(5) J. P. Perdew, K. Burke, and M. Ernzerhof. Generalized Gradient Approximation Made Simple. Phys. Rev. Lett. **1996**, 77, 3865.

(6) P. E. Blochl, Projector augmented-wave method. Phys. Rev. B Condens Matter**.** **1994**, 50, 17953.

(7) S. Grimme, S. Ehrlich, L. Goerigk. Effect of the damping function in dispersion corrected density functional theory. J. Comput. Chem. **2011,** 32, 1456-65.

(8) V. Wang, N. Xu, J.C. Liu, G. Tang, W.T. Geng. VASPKIT: A user-friendly interface facilitating high-throughput computing and analysis using VASP code. Comput. Phys. Commun. **2021,** 267, 108033.

(9) A. D. Becke and E. R. Johnson. A simple effective potential for exchange. J. Chem. Phys. **2006**, 124, 221101.

(10) F. Tran and P. Blaha. Accurate Band Gaps of Semiconductors and Insulators with a Semilocal Exchange-Correlation Potential. Phys. Rev. Lett. **2009**, 102, 226401.

(11) Clarissa, C.; Marta, M.; Arup, M.; Waldemar, K.; Marco, M.; Benedetta, A.; Pietro, G.; Giulia. F.; Chiara, M.; Alessio, P.; Edoardo, M.; Annamaria, P.; Filippo, D. A.; Lorenzo, M.; Ligand-Induced Chirality in ClMBA$_2$SnI$_4$ 2D Perovskite. Angew. Chem. Int. Ed. **2024**, 63, e202318557.

(12) Jin-Tai, L.; Deng-Gao, C.; Lan-Sheng, Y.; Tai-Chun, L.; Yi-Hung, L.; Yu-Chiang, C.; Pi-Tai, C.; Ching-Wen, C.; Tuning the Circular Dichroism and Circular Polarized

Luminescence Intensities of Chiral 2D Hybrid Organic-Inorganic Perovskites through Halogenation of the Organic Ions. Angew. Chem. Int. Ed. **2021**, 60, 21434-21440.

(13) Liang, Y.; Manoj, K. J.; Peter C. S.; David B. M.; Wei. Y.; Alkyl-Aryl Cation Mixing in Chiral 2D Perovskites. J. Am. Chem. Soc. **2021**, 143, 43, 18114-18120.

(14) Bing, S.; Xiao-Fei, L.; Xiang-Yang, L.; Yamin, Z.; Xiangfeng, S.; Dezheng, Y.; Hao-Li, Z.; Two-Dimenzional Perovskite Chiral Ferromagnets. Chem. Mater. **2020**, 32, 8914-8920.

(15) Dong, L.; Xitao, L.; Wentao, W.; Yu, P.; Sangen, Z.; Lina, L.; Maochun, H.; Junhua, L.; Chiral Lead-Free Hybrid Perovskites for Self-Powered Circularly Polarized Light Detection. Angew. Chem. Int. Ed. **2021**, 60, 8415-8418.

(16) Maoxin, L.; Feier, F.; Xiao, H.; Guangyou, L.; Zheng, L.; Zhihao, C.; Jiahao, H.; Yu, C.; Rong-jia, W.; Guo-Hong, N.; Kai, L.; Yumeng, S.; Bingbing, T.; Chiral Ligand-Induced Structural Transformation of Low-Dimensional Hybrid Perovskite for Circularly Polarized Photodetection. Chem. Mater. **2022**, 34, 7, 2955–2962.

(17) Shuang, J.; Peisheng, Z.; Guoxiang, X.; Huimin, K.; Xiaolei, L.; Tianzhe, Z.; Bin, L.; Tianyong, Z.; Bismuth-Based Chiral Perovskites with Different Dimensions for Second-Order Nonlinear Optical Properties. Adv. Optical Mater. **2023**, 11, 2203078.

(18) Jinjin, Z.; Hao, H.; Yingjie, Z.; Yangwu, G.; Meiqiu, D.; Yue, F.; Jingyuan, Z.; Zhixiang, G.; Lei, K.; Chiral Hybrid Perovskites (R-/S-CLPEA)$_4$Bi$_2$I$_{10}$ with EnhancedChirality and Spin−Orbit Coupling Splitting for Strong NonlinearOptical Circular Dichroism and Spin Selectivity Effects. Chem. Mater. **2023**, 35, 4347−4354.

(19) Mingyang, X.; Puxin, C.; Xiao, H.; Rongchao, S.; Yongshen, Z.; Junjie, G.; Hexuan, C.; Chao, W.; Yuhan, L.; Jialiang, X.; Xian-He, B.; Resonant Second Harmonic Generation in Proline Hybrid Lead Halide Perovskites. Adv. Optical Mater. **2023**, 11, 2202700.

(20) Chao, C.; Liang, G.; Wanru, G.; Cong, G.; Xinyuan, D.; Zha, L.; Ying, Y.; Guangda, N.; Jiang, T.; Circularly polarized light detection using chiral hybrid perovskite. Nature Communications, **2019**.

(21) Kezheng, T.; Qiang, L.; Qingfeng, Y.; 1D Tin(II)-Based Chiral Hybrid Perovskite Single Crystals with Extremely Distorted Inorganic Chains for Second Harmonic Generation. Adv. Optical Mater. **2024**, 12, 2400018.

CHAPTER 4

Engineering the Electronic Structure and Optoelectronic Properties of Chiral Metal Halides through Cation Design

Clarissa Coccia,[a] Marco Moroni,[a.*] Massimo Boiocchi,[b] Marta Morana,[d] Maddalena Patrini,[e] Doretta Capsoni,[a] Alessio Porta,[a] Andera Olivati[c], Giulia Folpini,[c,d] Annamaria Petrozza,[c] Luca Gregori,[f,g] Edoardo Mosconi,[g,h] , Filippo De Angelis,[f,g,i] and Lorenzo Malavasi,[a,*]

[a]University of Pavia, Department of Chemistry and INSTM, Via Taramelli 12, 27100, Pavia, Italy

[b]University of Pavia, Centro Grandi Strumenti, Via Bassi 21, 27100, Pavia, Italy

[c]Center for Nano Science and Technology@PoliMi, Istituto Italiano di Tecnologia 20134 Milan (Italy)

[d]Institute for Photonics and Nanotechnology, CNR – IFN, 20133 Milano

[e]University of Pavia, Department of Physics, Via Bassi 6, 27100, Pavia, Italy

[f]University of Perugia, Department of Chemistry, Biology and Biotechnology, Via Elce di Sotto 8, 06123, Perugia, Italy

[g]Computational Laboratory for Hybrid/Organic Photovoltaics (CLHYO), Istituto CNR di Scienze e Tecnologie Chimiche “Giulio Natta” (CNR-SCITEC), Via Elce di Sotto 8, 06123 Perugia, Italy

[h] Chemistry Department, College of Science, King Saud University, 11451, Riyadh, Saudi Arabia

[i]SKKU Institute of Energy Science and Technology (SIEST), Sungkyunkwan University, Suwon 440-746, South Korea

Corresponding Authors

Lorenzo Malavasi, email: lorenzo.malavasi@unipv.it

Marco Moroni, email: marco.moroni@unipv.it

ToC

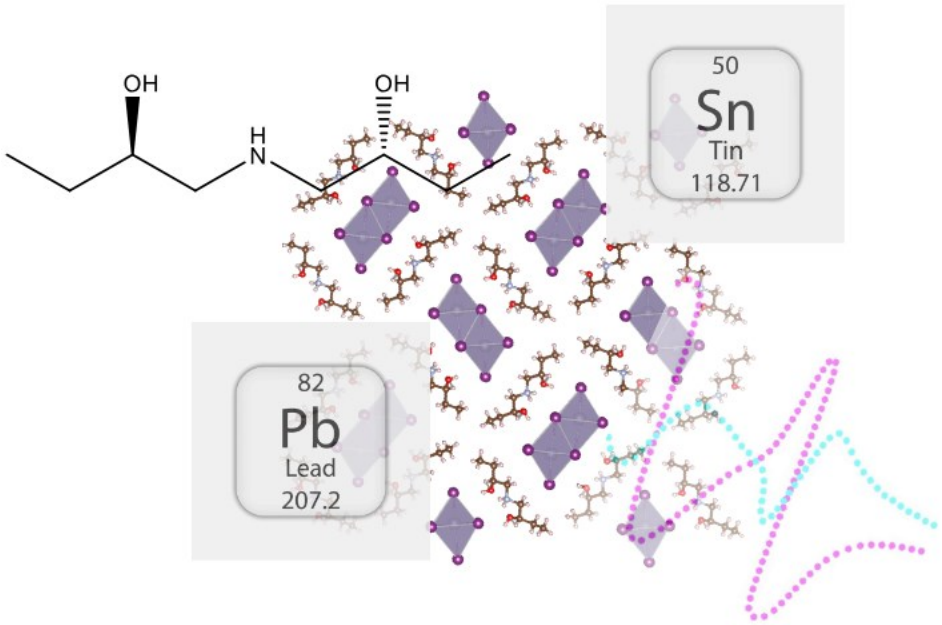

Abstract

The ability of tuning the properties of hybrid organic-inorganic metal halides through chemical design represents one of their most fascinating aspects with key implications for potential applications. When dealing with chiral metal halides, where chirality is imparted by the presence of chiral amines, the limitations of available cations strongly limit such tuning ability. We present here a class of lead- and tin-based 1D hybrid organic-inorganic metal halides including an *ad hoc* synthesized cation containing aminic and hydroxyl functional groups which have been used to prepare the enantiopure (*S*/*R*-AMOL)SnI_3 and (*S*/*R*-AMOL)PbI_3 (*S*/*R*-AMOL=(2*R*,2'*R*)-1,1'-azanediylbis(butan-2-ol) and (2*S*,2'*S*)-1,1'-azanediylbis(butan-2-ol)). The chiral metal halides feature a distinctive structural arrangement and bonding interaction between the organic ligand and inorganic framework demonstrating that chirality transfer may occur also through chiral carbons bearing a hydroxyl group. A strong modulation of the electronic structure and chiroptical properties has been observed between the Pb and Sn-containing samples, as a result of the peculiar and different bonding environments, leading to changes in the emission properties, exciton binding energy, and nature of the orbital contributions to the electronic structure.

1. Introduction

The emergence of chiral metal halides perovskites and related structures, generally defined as chiral metal halides, as an exciting field of research stems from both their inherent structural complexity and their remarkable potential for innovative technological applications.[1–4] By introducing chirality into the inorganic framework, researchers have unlocked novel functionalities, such as circular dichroism (CD), circularly polarized luminescence (CPL), second harmonic generation (SHG), and topological quantum states. In addition, the potential applications of chiral metal halides extend well beyond conventional optoelectronics. Their unique properties may also find use in spintronics, quantum computing, and emerging fields such as topological photonics.[3,5] Understanding the underlying principles of chiral metal halides and their interactions with external stimuli will be vital in harnessing their full potential for future technologies.[5]

To date, all the chiral perovskites and perovskite-derivatives reported are based on the few commercially available chiral amines, with methylbenzylamine, MBA, and its halogenated derivatives (X-MBA; X=F, Cl, Br), as the most widely used ligands.[2,6–9] Based on these chiral cations, several 2D chiral perovskites have been prepared and investigated, helping in clarifying, for example, the role of the nature of halogen substituent and its position on the aromatic ring on the CD and CPL response due to the different extent of hydrogen bonding with the halide of the inorganic framework and the local distortion induced on the octahedra.[9–12] Other common monoammonium chiral cations employed to date for 2D chiral perovskites involve 1-(2-naphthyl)ethylammonium (NEA), β-methylphenethylammonium (MPA), and 1-(1-naphthyl)ethylammonium (NPB), as well as samples with alloyed cations on the A-site of the perovskite.[13–16] All these studies provided a set of tuning strategies of the chiroptical and of spin-based properties of chiral perovskites shedding light on the role of short-range and noncovalent intermolecular interactions, structural distortions and Rashba splitting and build also the bases for device engineering and computational modelling.[17]

To widen the understanding of chirality in metal halide perovskites, unraveling unexplored properties, advance the optoelectronic devices including chiral metal halides, as well as to gain a deeper comprehension of the chirality transfer mechanism and structure-property correlations in this emerging area, it is important to extend the set of available chiral cations

and therefore of novel compositions and structural topologies. Such extension could also involve the design of multi-functional ligands where, in addition to the amine moiety, other functional groups are present. This is of particular interest in the field of chiral metal halides where the structural framework, and in turn the optoelectronic properties, are strongly connected to the ability of the organic cation of short-range bonding (hydrogen and Van der Waals) to the inorganic framework.[18–21] Therefore, the design and use of chiral bifunctional ligands could widen the scope of chiral perovskite and perovskite derivatives engineering. In addition, the comprehension of the role of central metal nature on the chiroptical properties, together with the need of moving towards lead-free compositions, is another urgent issue in the field of chiral metal halides. To date, few reports explored metals other than Pb, and 2D perovskites or low-dimensional chiral metal halides incorporating Sn, Bi, Cu or Ge have been reported in the last few years.[8,22–31] The substitution of Pb with other metals allowed to focus on the role of spin-orbit coupling on chiroptical properties and showed, in most of the cases, an increased octahedral distortion leading to enhanced CD and second-order nonlinear responses.

2. Results and Discussion

To try to add an additional piece of information on both the role of chiral cation and metal nature, we performed the synthesis of a dimeric bifunctional chiral ligands, namely (2*R*,2'*R*)-1,1'-azanediylbis(butan-2-ol) and (2*S*,2'*S*)-1,1'-azanediylbis(butan-2-ol), which structure is reported in the bottom part of Figure 1 for both the enantiomers. As can be seen, the chiral ligands contain one amino and two hydroxyl functional groups, with the chiral carbons being those bearing the -OH groups. For sake of brevity, in the following, the chiral ligands will be defined as "(*S*-/*R*-)AMOL", indicating the fact that, from a chemical point of view, such bifunctional molecules are amino alcohols (or amino diols). In agreement with reaction conditions, starting from (*R*) epoxide the (*R,R*) amino-diols with the same enantiomeric excess (e.e.) of starting material (> 99%) are obtained and, analogously, if the epoxide is (*S*), the (*S,S*) amino-diols will be obtained. On the other hand, the situation was more complicated if the starting material was a racemic mixture since two different diastereoisomers in racemic mixture are obtained. For this reason, we focused our attention on an

enantiopure starting material for the preparation of (*R,R*) or (*S,S*) amino-diols. The representative structures of AMOL monomers and dimers were reported in Figure 1.

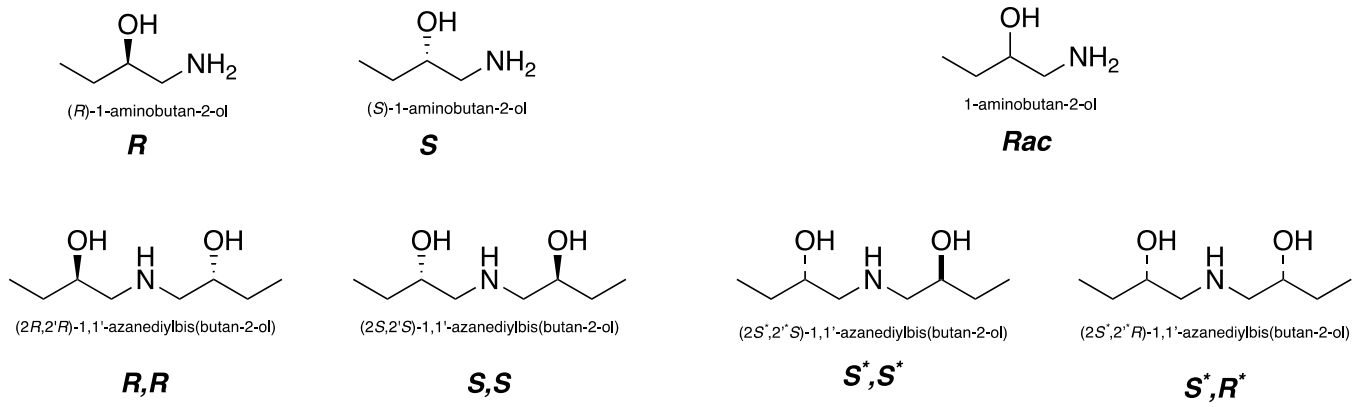

Figure 1. Structures of monomeric (top) and dimeric form (bottom) of amino alcohols. *S**,*S** and *S**, *R** are the IUPAC notation for the two pairs of diastereoisomers.

The synthesis of dimeric and/or monomeric amino-alcohols was carried out starting from epoxides which are readily available versatile building blocks for the synthesis of many structural motifs. These compounds were easily prepared from racemic mixtures and the reactivity towards the regiospecific oxirane ring opening with soft nucleophiles is well known.[32–35] The two AMOL-monomers in enantiopure form were prepared following the literature procedures starting from the corresponding epoxide.[36] From a synthetic point of view, it was possible to prepare monomeric AMOLs and dimeric AMOLs by changing some reaction conditions. It should be emphasized that the preparation of the two enantiomers of dimeric AMOLs has been subjected of an extensive optimization work to maximize the amount of what is usually an undesired by-product. A detailed description of the synthetic procedure is reported in the Supporting Information (SI), together with spectroscopic data, including the optical rotation power. From the stereochemical point of view, the absolute configuration of starting material is the same of amino alcohol obtained following the protocols described in the literature.

The two enantiopure dimeric AMOL ligands, namely (2*R*,2'*R*)-1,1'-azanediylbis(butan-2-ol) and (2*S*,2'*S*)-1,1'-azanediylbis(butan-2-ol), have been used to prepare lead and tin iodide samples by means of solution chemistry as reported in the Experimental Section (see SI). For the tin-containing compositions we could

achieve the growth of high-quality single crystals of the *S*-enantiomer and of lower quality for the *R*-enantiomer which have been used to solve the structure through single crystal X-ray diffraction (SC-XRD). Table 1 reports the main crystallographic data of the two enantiopure chiral tin iodides of formula (*S*/*R*-AMOL)SnI_3.

Table 1. Crystallographic data of (*S*/*R*-AMOL)BI_3 (B=Sn and Pb) and octahedral distortion parameters. CCDC Code for (*S*-AMOL)SnI_3: 2365047

	(*S*-AMOL)SnI_3	**(*R*-AMOL)SnI_3**	**(*S*-AMOL)PbI_3**	**(*R*-AMOL)PbI_3**
Crystal system	Orthorhombic	Orthorhombic	Orthorhombic	Orthorhombic
Space group	$P2_12_12_1$	$P2_12_12_1$	$P2_12_12_1$	$P2_12_12_1$
a (Å)	4.5687(2)	4.573(2)	4.5935(4)	4.5936(5)
b (Å)	18.3063(6)	18.307(8)	18.263(1)	18.2644(8)
c (Å)	20.4374(6)	20.444(9)	20.629(1)	20.6146(8)
V (Å^3)	1709.30(11)	1711.11(13)	1730.7(2)	1729.6(2)
Z	4	4	4	4
λ_{oct}	1.0047	1.0047	1.0073	1.0067
D	0.0333	0.0337	0.037	0.0315
σ^2	8.54	8.33	19.24	18.69
B-I lengths (Å)	2.9376(6) 3.1562(6) 3.1964(6) 3.2057(6) 3.2604(6) 3.4642(6)	2.939(3) 3.156(4) 3.195(4) 3.211(4) 3.261(4) 3.466(4)	3.01866(0) 3.21214(0) 3.23187(0) 3.33235(0) 3.40022(0) 3.46515(0)	3.05647 3.17738 3.26298 3.31022 3.37109 3.43379

From a structural point of view, the material consists of 1D double chains running along the crystallographic *a*-axis built up by face-sharing $[SnI_6]^{4-}$ octahedra, generating the structural motif reported in Figures 2a and 2b (referring to (*S*-AMOL)SnI_3). This is a quite rare structural arrangement in halide perovskites and perovskite-derivatives and, to the best of our knowledge, has been previously observed only in one hybrid iodoplumbate containing protonated urea as the organic cation[37]. One crystallographically independent (*S*-)AMOL molecule interacts with the iodide anions of the metal-halide chains through four short-distance bonds. In particular, the hydrogens of the protonated -NH_2^+ moiety display two bonds at 3.109(4) and 3.170(5) Å, while even shorter bonds are established between the H atoms of the -OH groups and the I of the octahedra: 3.001(4) and 2.831(4) Å (see Figure 2c). This is a complex bonding pattern involving both the amino and hydroxyl functional

groups which, through this peculiar framework, gives origin to the structural arrangement shown in Figure 2.

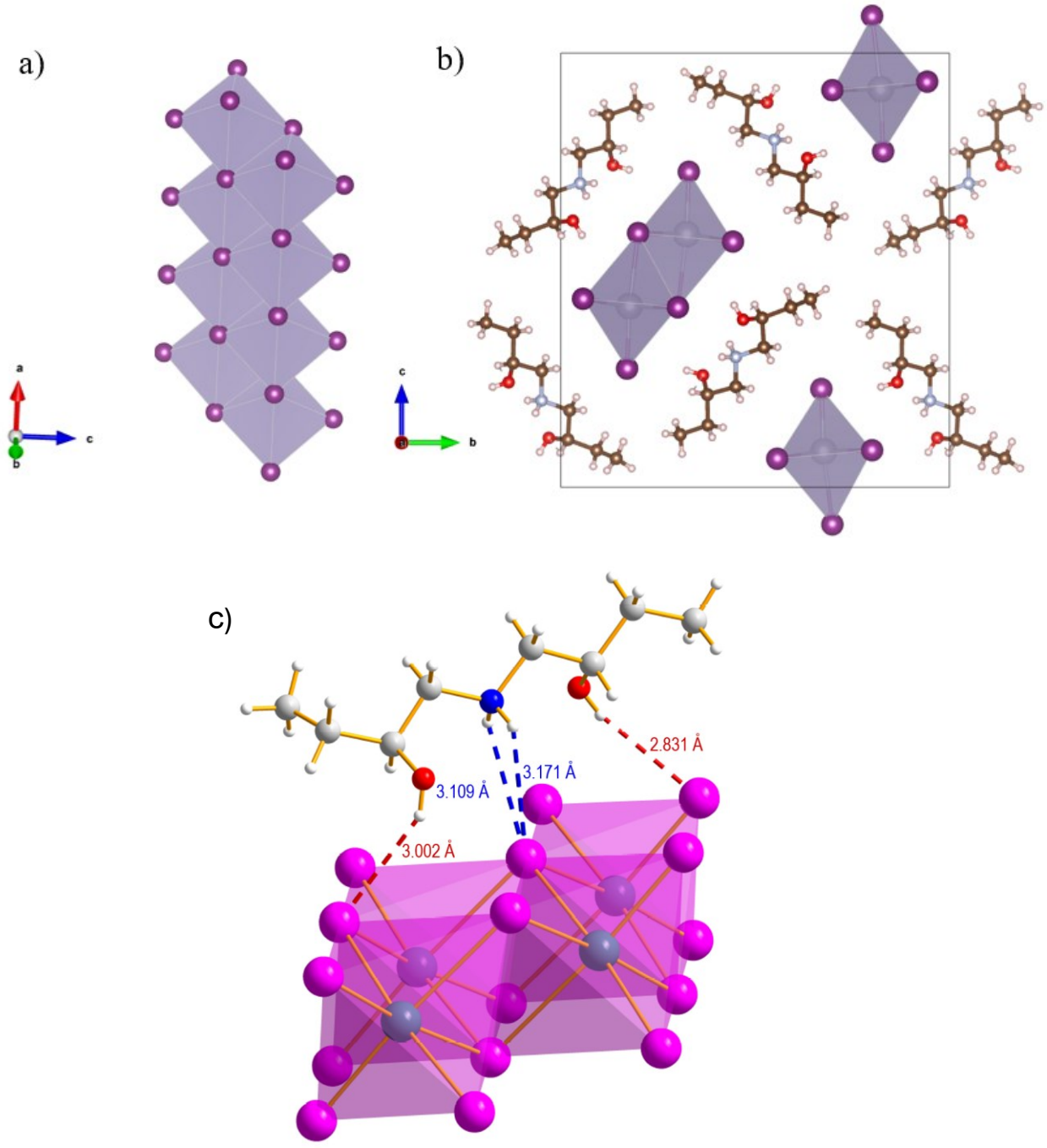

Figure 2. a) Representation of the 1D inorganic double chains of (*S*-AMOL)SnI_3 along the *a*-axis; b) sketch of the unit cell along the *c*-axis; c) detail of the crystal structure highlighting the interaction between the chiral cation and the inorganic framework.

There are few examples of perovskites or perovskite derivatives containing bifunctional organic spacers with -NH_2 and -OH, namely [$(HOC_nH_{2n}NH_3)_2PbI_4$] with n = 2[19,20] and 3[19]. Noteworthy, in these examples, the linkers are achiral linear molecules, with the two functional groups at the opposite sides of the chain, generating 2D layered structures. The present ligand is a novel molecular entity not yet used in any hybrid metal halide, and clearly in any chiral system, and resulted in a novel structural arrangement and polar interaction network. In addition, it is interesting to observe that this is the first chiral ligand where the chiral carbon does not bear an amine group but a hydroxyl group. The crystal structure of (*R*-AMOL)SnI_3 is in agreement with that of the *S* enantiomer but, as expected, showing the opposite arrangement in space (cfr. Table 1). Attempts to grow single crystals of the Pb-analogues were not successful. However, by looking at the powder XRD patterns of the four samples reported here and shown in Figure 3a, it can be observed that the main characteristics peaks of the (*R/S*-AMOL)SnI_3 are also found for the lead samples.

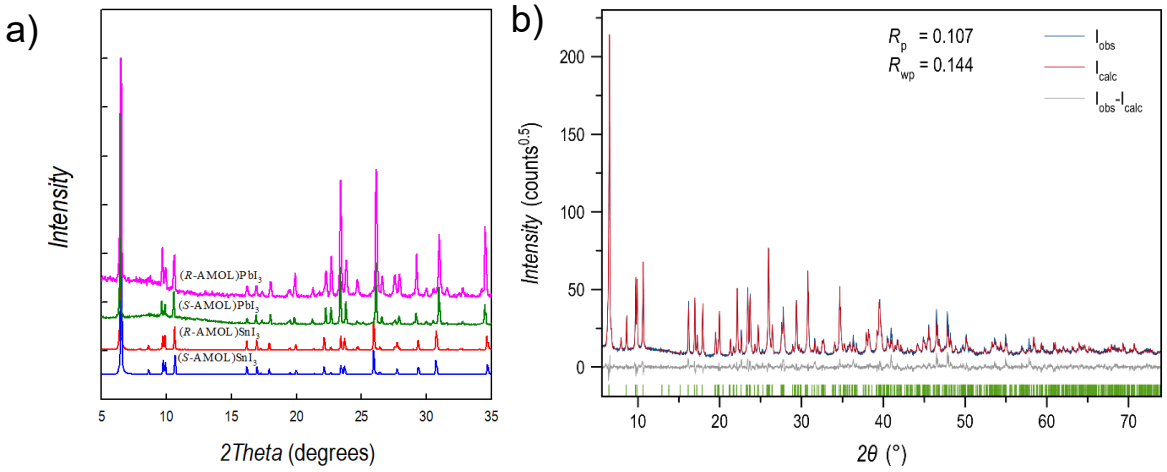

Figure 3. a) Powder x-ray diffraction patterns of (*R/S*-AMOL)SnI_3 and (*R/S*-AMOL)PbI_3; b) Rietveld refinement plot of the (*R*-AMOL)PbI_3 PXRD pattern in terms of experimental, calculated and difference traces (blue, red and grey, respectively). The green ticks indicate the positions of the Bragg reflections.

Accordingly, the powder patterns for (*R/S*-AMOL)PbI_3 were refined starting from the single crystal data of the Sn-containing counterparts providing a very good fit as shown, as a representative example, in Figure 3b for (*R*-AMOL)PbI_3. The analogous result for (*S*-AMOL)PbI_3 is reported in Figure S1. By looking at Table 1 it can be seen that the Pb-containing samples have a bigger lattice volume than the chiral tin iodides with an expansion of the *a* and *c* axes and a slight contraction of the *b* axis. The

general increase of the volume could be anticipated based on the ionic radii difference between Pb(II) and Sn(II).

The level of octahedral distortion for the 4 samples has been quantified in terms of the octahedral quadratic elongation (λ_{oct}) and bond angle variance (σ^2), as defined by Robison *et al.*, as well as by calculating the distortion index, *D*.[38,39] The distortion parameter is of the order of 0.03 for all the samples which places the present materials as intermediate distorted compounds even though such comparison is based on available data on 2D chiral perovskites, being the structure reported in this work not common.[8] Interestingly, the impact of the variation of central metal on the distortion index is modest for these chiral 1D metal iodides, which is a different trend with respect to what has been observed in 2D chiral perovskites. As for the latter, recent works on MBA_2PbI_4 and MBA_2SnI_4 have associated the distortion increase moving from Pb to Sn to their different hard/soft behaviour, recalling the Pearson's HSAB theory.[40] Indeed, the coordination between the hard Sn cation and the soft I anion results in weaker bonds favouring octahedra distortion and stabilizing CH-π interaction in the organic part, enhancing the overall chirality of the system. In the present compounds, however, the presence of face-sharing octahedra limits the structural degrees of freedom and could be a key factor for the similar distortion index in the two series.[23] Moreover, the different chiral cation nature, not displaying aromatic moieties allowing for CH-π interactions, probably behaves as another factor not stabilizing a highly distorted structure. Average B-I (B=Sn and Pb) bond length increases, as expected, moving from Sn samples (~3.20 Å) to Pb samples (~3.27 Å). The only significant difference in the octahedral distortion parameters is related to the bond angle variance, which is more than doubled in the (*R/S*-AMOL)PbI_3, indicating a greater distortion in terms of bond angles in these last samples.

Optical properties of (*R/S*-AMOL)SnI_3 and (*R/S*-AMOL)PbI_3 have been determined by UV-vis and CD spectroscopies. The spectra are reported in Figures 4a-d (and Figs. S2-S3).

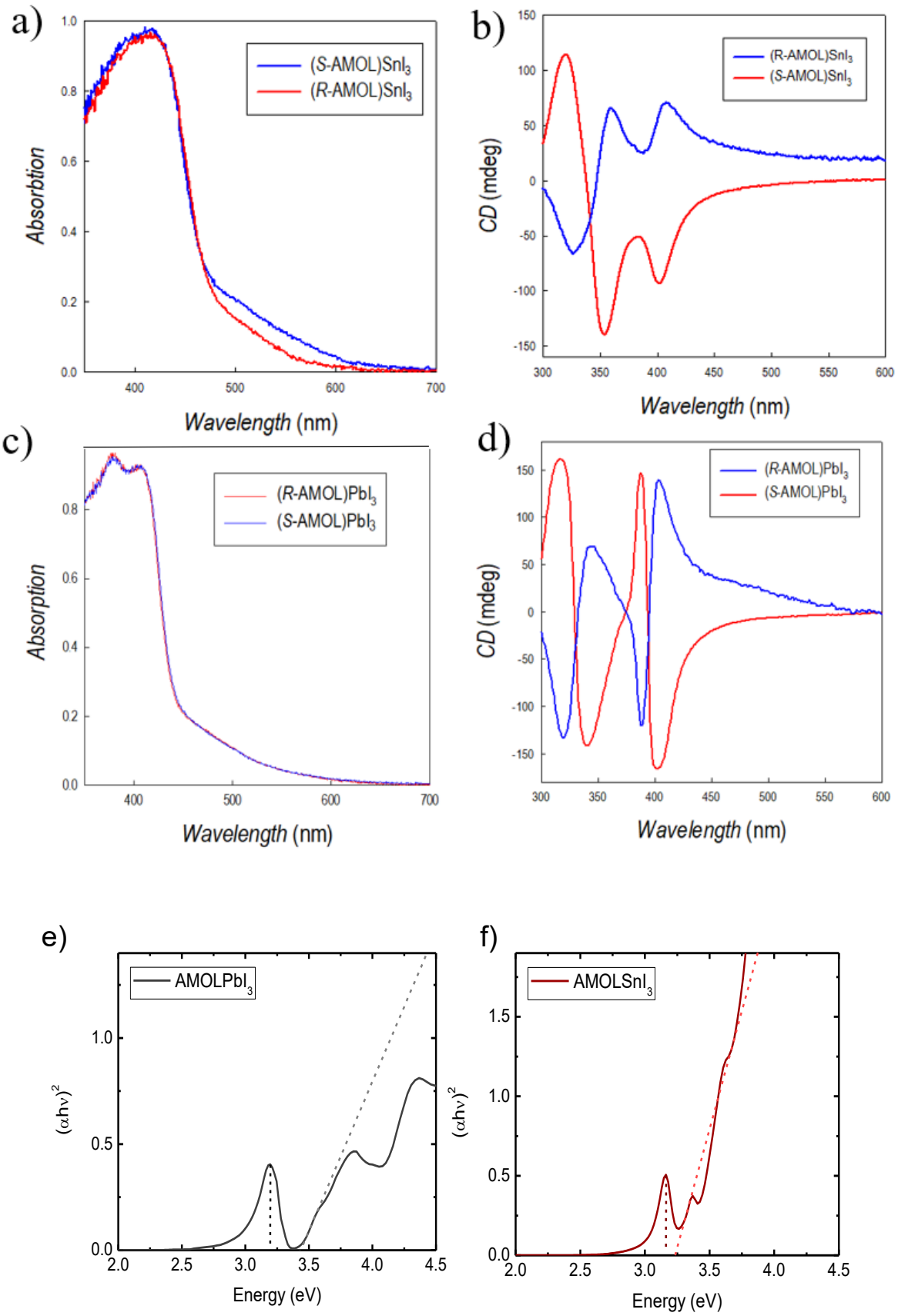

Figure 4. a) absorption and b) CD spectra of (*R/S*-AMOL)SnI_3 and c) absorption and d) CD spectra of (*R/S*-AMOL)PbI_3; f) Tauc plot of respectively (*R*-AMOL)PbI_3 and (*R*-AMOL)AMOLSnI_3 at 77 K. The dashed lines indicate the centre of the excitonic absorption peak and the bandgap energy emerging from a linear fit of the absorption edge.

The absorption spectra for (*R/S*-AMOL)SnI_3, calculated from the reflectivity of powdered samples, show an absorption edge for the two chiral systems around 440 nm while the Tauc plot are reported in Figure S2. The band gap at room temperature was determined by the Kubelka-Munk method from diffuse reflectance spectra on drop casted films (see Figure S3) and is estimated to be ~2.83 eV for the direct transition. Figure 4b shows the CD spectra for the two enantiomers which have opposite features confirming their chirality. Three intense CD peaks with opposite sign are clearly visible in the range 300-430 nm, with this last one well corresponding to the absorption edge. For (*R/S*-AMOL)PbI_3 the analogous characterization provides an absorption edge around 420 nm with an extrapolated band gap energy of 3.17 eV (see Figure S3), indicating a slight blue-shift when replacing Pb for Sn, as already observed in other metal halides even though with a smaller impact with respect to 3D and 2D metal halide perovskites.[41]

To more precisely assess the contribution of bound excitonic states on the absorption edge of these materials, we performed absorption measurements at cryogenic temperatures (77 K) on drop casted thin films of (*R*-AMOL)PbI_3 and (*R*-AMOL)SnI_3 (Fig. 4e,f): both materials exhibit clear excitonic absorption peaks at low temperature, respectively at 3.2 and 3.16 eV for Pb- and Sn-containing samples. The bandgap absorption edge, retrieved by a Tauc fit of the absorption rise, is found at 3.44 and 3.23 eV, respectively. This corresponds to an estimated excitonic binding energy of 73 meV for (*R*-AMOL)SnI_3, consistent with no discernible excitonic absorption at room temperature as confirmed by diffuse reflectance measurements (see Figure S3). Conversely, for (*R*-AMOL)PbI_3, the excitonic binding energy is 240 meV, which result in a stable excitonic population at room temperature, as corroborated by the reflectance spectrum at room temperature shown in Fig S3, where a clear excitonic peak is evident at 3.05 eV.

The CD spectra (Figure 4d) present in this case four intense and opposite peaks with the one placed at the highest wavelength again well corresponding to the absorption edge (cfr. Figure 4c). While we recognize that the mdeg value is not an absolute scale since it has a dependence with the sample amount, the present films, for both samples, of thickness around 400 nm, present one of the highest values of CD response reported to date, indicating their potential use in efficient circular polarized

light photodetection. The respective chiral ligands do not show any relevant CD in the UV-Vis region, as anticipated based on their molecular structure and our measurements not showing any peak. Therefore, all the chiroptically active transitions derive from a chirality transfer from the chiral bifunctional ligand to the inorganic network. It is interesting to note that an effective chirality transfer occurs also when an interaction network is established by means of -OH groups, while all the previous examples of chirality transfer to the inorganic framework were based on the hydrogen bonding through the protonated amine group. The peculiar derivative-like features of the CD signal around the band edge for all the samples suggest a lifting of the spin degeneracy within the electronic states at the edge induced by the chiral molecules defined as the Cotton effect.[42] The chiral anisotropy factor, g_{CD}, has been calculated from the CD measurements and resulted to be around 2×10^{-3} for both series of samples. Since no other chiral systems possessing the structural motif of the present samples or including a similar ligand are present in the current literature, a direct comparison of the chiroptical properties with available data is not straightforward. However, these values are higher with respect to data reported for some 2D chiral perovskites.[43] Moreover, for 2D perovskites excitonic coupling is usually not observed in lead-based perovskites encapsulating MBA or 1-(1-naphthyl)ethylammonium while it appears in MBA_2SnI_4.[8,44] This could be ascribed to an enhanced interaction between the organic and the inorganic moieties in the tin-based systems due to higher electronic coupling.[26] In our 1D compounds, however, the comparable distortion and the aliphatic nature of the cation, not allowing for interactions such as the CH-π one mentioned in the literature, could induce a different behavior. It can be hypothesized that the concomitant presence of two hydroxyl group and the aminogroup on the cation induces strong interactions with the I atoms of the octahedra, being beneficial for the chirality transfer for both systems and resulting in their enhanced CD response displaying in all cases excitonic coupling. Overall, this complex short-range bonding pattern is capable of effectively promote a chirality transfer to the inorganic framework as well as to impact on the charge localization (see later in the text).

We also measured the photoluminescence (PL) at room temperature. Both the Pb and Sn based samples showed only weak PL response: the observed PL spectra (figure S4) show a very broadband, if weak, PL signal for all samples, with FWHM of

the order of hundreds of nanometres. The PL from Pb based samples shows two main components, centred around 500 nm and 700 nm. On the other hand, the Sn-based materials show a significant shift from their absorption edge, with a main peak centred around 780 nm and a broad shoulder extending to 450 nm. Such shift in chiral Sn-based metal halides has been reported only in a previous case in literature by our group on 2D chiral perovskites where the origin of such phenomenon was accounted for by the presence of self-trapped excitons (STEs).[23]

To gain insight into the electronic properties of these novel 1D hybrid materials, we performed DFT electronic structure analysis, see Computational Details in SI. From the density of states (DOS) simulation, we can notice that the main contribution of the valence band (VB) is associated to the halogen and the conduction band (CB) shows a predominant contribution of the central metal (Sn or Pb), while the contribution of the organic molecules is deep in the VB and CB, see Figure 5. From a more detailed analysis of the band structure and isodensity plot of VB and CB edges, Figure 5, we can notice that the Sn-based 1D metal halides exhibit a quasi-direct band gap, showing a band edge placed off from an high symmetry point in the Brillouin Zone: the conduction band minimum (CBM) is located at the Γ high-symmetry point, while the valence band maximum (VBM) is slightly shifted toward the X point.[45] The band structure reveals a distinctly one-dimensional electronic character, with noticeable dispersion only along the direction of the inorganic moiety's growth axis, see effective masses in Table S1. In the perpendicular directions, the electronic momentum is completely flat, reflecting a lack of interaction and confirming the quasi-1D nature of the material; see band structure in Figure S6 in SI. For the Pb-based counterpart, the band gap is found to be direct at the Γ point.

An interesting distinction from the Sn-based material is the emergence of a different character of the VBM. As we can see from the crystal structure reported in Figure 2, these novel systems have two different types of iodide anions: (i) the bi-coordinated and (ii) the undercoordinated species. By analyzing the isodensity plots of the charge distribution associated with the VB edges state of the Sn-based material, we found a quite homogeneous contribution from all iodide atoms, while for the Pb-based species, the VB edge contribution comes from only the undercoordinated iodide, see Figure 5a and 5c.

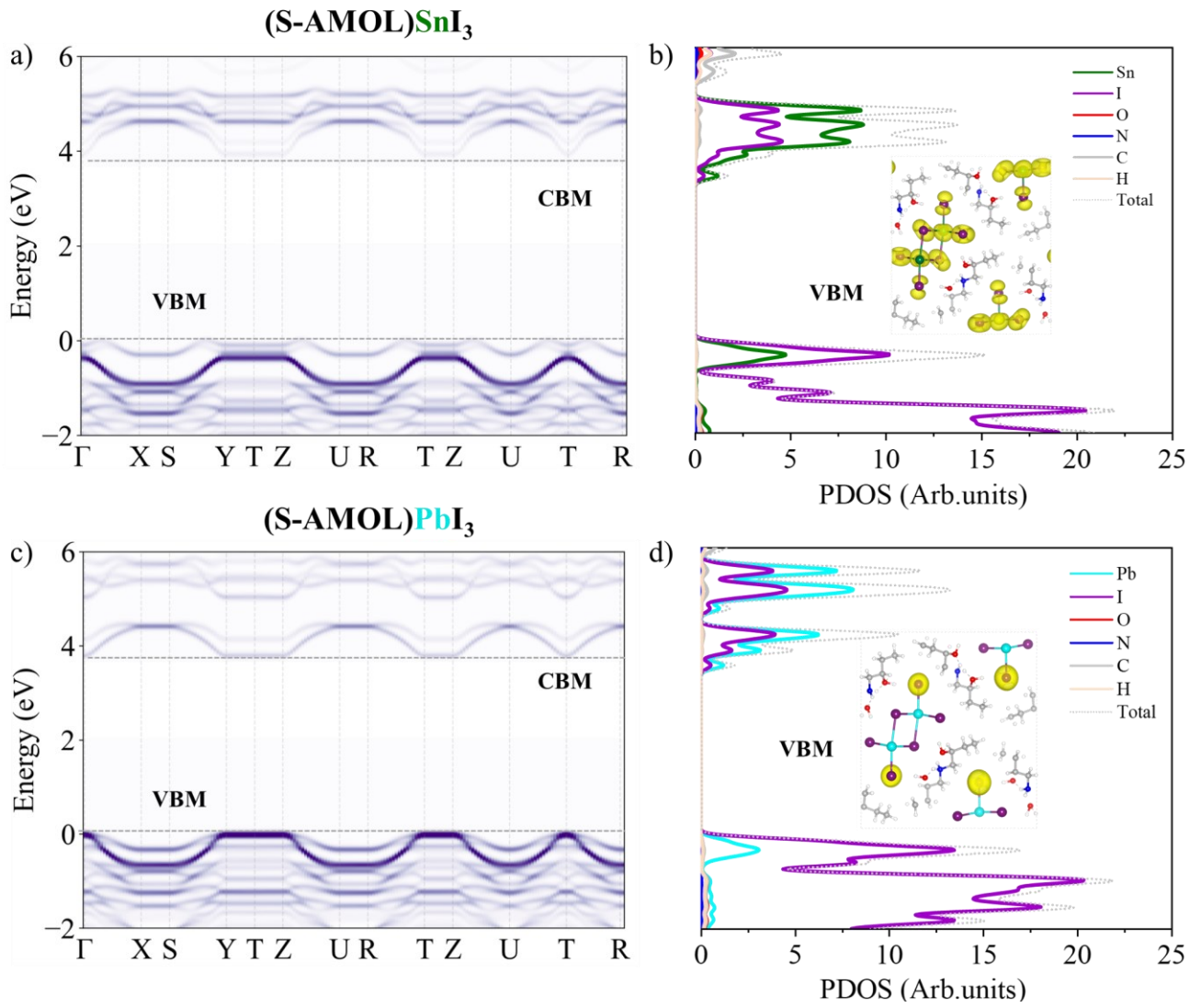

Figure 5: Projected Band structure of the undercoordinated iodine moiety for the (a) Sn-based and (b) Pb-based chiral metal halides (*S*-enantiomer) along with the respective Density of State and isodensity plot (c) and (d) of the VBM.

To clearly visualize along the band structure the role of the different types of iodide, in Figure 5a and c we illustrated the projected contributions of the undercoordinated iodine atoms to the band structure, highlighting their roles in the valence and conduction bands for the (*S*-AMOL)SnI_3 and (*S*-AMOL)PbI_3, as selected examples. In the Sn-based system (Figure 5a), both coordinated and uncoordinated iodine contribute to the valence band, emphasizing their critical role in shaping the electronic states near the Fermi level. Conversely, for the Pb-based system (Figure 5c), the valence band is primarily localized on the uncoordinated iodine, indicating a clear localization of the charge on the Iodine that could in principle also lead to a shift in the electronic structure following the effect of having different metal centers. These

projections provide a detailed visualization of the orbital contributions and demonstrate how iodine coordination geometry (coordinated *vs*. uncoordinated) governs the electronic properties of these materials. Lastly, the more localized form of the charge of the valence band isodensity described in Figure 5d may be associated with the greater exciton binding energy obtained for the Pb-based system. According to Wu et al., it is well known that the E_b rises as valence electron localization increases because of the decreased electronic screening.[46] This distinction further underscores the differing bonding environments and electronic interactions in Sn- and Pb-based chiral low-dimensional metal halides, with potential implications for their optoelectronic performance.

3. Conclusions

The novel (2*R*,2'*R*)-1,1'-azanediylbis(butan-2-ol) and (2*S*,2'*S*)-1,1'-azanediylbis(butan-2-ol) bifunctional chiral ligands have been synthesized for the first time and used to prepare the 1D chiral metal halides (*R/S*-AMOL)PbI_3 and (*R/S*-AMOL)SnI_3. The presence of aminic and hydroxyl functional groups, these last on the chiral carbon, leads to the formation of an unprecedented structural arrangement in low-dimensional chiral metal halides. While this structure is found for both the Sn- and Pb-based systems, relevant differences are found in the optical response and electronic structure. While both samples show a strong CD response, centred around the absorption edge, the PL, while weak for both, is strongly red-shifted for (*R/S*-AMOL)SnI_3, which also displays an exciton binding energy three times lower than the Pb-counterpart. The calculation of the electronic structure of the samples shows some similarities in terms of atom contribution to VB and CB but a significant difference arising from the nature of the iodide atoms participating to the density of states. Specifically, both bi-coordinated and undercoordinated iodides contribute to the VB in the case of (*R/S*-AMOL)SnI_3 while for (*R/S*-AMOL)PbI_3 the VB is mostly localized on the axial atoms causing a shift of the electronic structure which can be correlated to the observed optoelectronic properties.

The present results, reporting an *ad hoc* synthesized difunctional chiral ligand leading to a novel structural family of 1D chiral metal halides, highlight the importance of

extending the actual library of hybrid chiral systems in order to widen the properties tuning of the chiroptical and electronic properties.

Acknowledgement

L.M. acknowledges support from the Ministero dell'Università e della Ricerca (MUR) and the University of Pavia through the program "Dipartimenti di Eccellenza 2023–2027. LM and MM acknowledge Fondazione Cariplo through the program ''Young Researchers'', Grant No. 2023-1246. We acknowledge support from the Italian Ministry of Research under the PRIN 2022 Grant No 2022F2K7J5 with title "Two-dimensional chiral hybrid organic−inorganic perovskites for chiroptoelectronics" PE 3 funded by PNRR Mission 4 Istruzione e Ricerca - Component C2 - Investimento 1.1, Fondo per il Programma Nazionale di Ricerca e Progetti di Rilevante Interesse Nazionale PRIN 2022 - CUP B53D23004130006. E.M. acknowledges financial support under the National Recovery and Resilience Plan (NRRP), Mission 4, Component 2, Investment 1.1, Call for tender No. 104 published on 2.2.2022 by the Italian Ministry of University and Research (MUR), funded by the European Unisia - NextGenerationEU - Project Title 2022HRZH7P - Re-evolutionary solar fuel production envisioning water stable lead-free perovskite exploitation - REVOLUTION - CUP B53D23015350006 - Grant Assignment Decree No. 1064 adopted on 18.7.2022 by the Italian Ministry of University and Research (MUR). Centro Grandi Strumenti of University of Pavia is acknowledged for the access to single crystal x-ray diffraction facility. L.G., and F.D.A. acknowledge funding by the Italian Ministry of Environment and Energy Security in the framework of the Project GoPV (CSEAA_00011) for Research on the Electric System.

The first-author Clarissa Coccia, author of the present Ph.D. work, carried out the synthesis of all the materials and part of the optical characterization: Absorption spectra, CD Spectra and the connected part of the revision of the paper.

References

(1) Dang, Y.; Liu, X.; Cao, B.; Tao, X. Chiral Halide Perovskite Crystals for Optoelectronic Applications. *Matter* **2021**, *4* (3), 794–820.

(2) Dang, Y.; Liu, X.; Sun, Y.; Song, J.; Hu, W.; Tao, X. Bulk Chiral Halide Perovskite Single Crystals for Active Circular Dichroism and Circularly Polarized Luminescence. *J. Phys. Chem. Lett.* **2020**, *11* (5), 1689–1696.

(3) Long, G.; Sabatini, R.; Saidaminov, M. I.; Lakhwani, G.; Rasmita, A.; Liu, X.; Sargent, E. H.; Gao, W. Chiral-Perovskite Optoelectronics. *Nat Rev Mater* **2020**, *5* (6), 423–439.

(4) Malavasi, L.; Moroni, M.; Coccia, C. *Chiral Metal Halide Perovskites: Focus on Lead-Free Materials and Structure-Property Correlations*; preprint; Chemistry and Materials Science, 2023.

(5) Wei, Q.; Ning, Z. Chiral Perovskite Spin-Optoelectronics and Spintronics: Toward Judicious Design and Application. *ACS Materials Lett.* **2021**, *3* (9), 1266–1275.

(6) Lu, H.; Wang, J.; Xiao, C.; Pan, X.; Chen, X.; Brunecky, R.; Berry, J. J.; Zhu, K.; Beard, M. C.; Vardeny, Z. V. Spin-Dependent Charge Transport through 2D Chiral Hybrid Lead-Iodide Perovskites. *Sci. Adv.* **2019**, *5* (12), eaay0571.

(7) Yao, L.; Niu, G.; Li, J.; Gao, L.; Luo, X.; Xia, B.; Liu, Y.; Du, P.; Li, D.; Chen, C.; Zheng, Y.; Xiao, Z.; Tang, J. Circularly Polarized Luminescence from Chiral Tetranuclear Copper(I) Iodide Clusters. *J. Phys. Chem. Lett.* **2020**, *11* (4), 1255–1260.

(8) Lu, H.; Xiao, C.; Song, R.; Li, T.; Maughan, A. E.; Levin, A.; Brunecky, R.; Berry, J. J.; Mitzi, D. B.; Blum, V.; Beard, M. C. Highly Distorted Chiral Two-Dimensional Tin Iodide Perovskites for Spin Polarized Charge Transport. *J. Am. Chem. Soc.* **2020**, *142* (30), 13030–13040.

(9) Lin, J.; Chen, D.; Yang, L.; Lin, T.; Liu, Y.; Chao, Y.; Chou, P.; Chiu, C. Tuning the Circular Dichroism and Circular Polarized Luminescence Intensities of Chiral 2D Hybrid Organic–Inorganic Perovskites through Halogenation of the Organic Ions. *Angew Chem Int Ed* **2021**, *60* (39), 21434–21440.

(10) Zhou, C.; Chu, Y.; Ma, L.; Zhong, Y.; Wang, C.; Liu, Y.; Zhang, H.; Wang, B.; Feng, X.; Yu, X.; Zhang, X.; Sun, Y.; Li, X.; Zhao, G. Photoluminescence Spectral Broadening, Chirality Transfer and Amplification of Chiral Perovskite Materials (R-X- *p* -mBZA)$_2$ PbBr$_4$ (X = H, F, Cl, Br) Regulated by van Der Waals and Halogen Atoms Interactions. *Phys. Chem. Chem. Phys.* **2020**, *22* (30), 17299–17305.

(11) Ma, S.; Jung, Y.-K.; Ahn, J.; Kyhm, J.; Tan, J.; Lee, H.; Jang, G.; Lee, C. U.; Walsh, A.; Moon, J. Elucidating the Origin of Chiroptical Activity in Chiral 2D Perovskites through Nano-Confined Growth. *Nat Commun* **2022**, *13* (1), 3259.

(12) Liu, S.; Kepenekian, M.; Bodnar, S.; Feldmann, S.; Heindl, M. W.; Fehn, N.; Zerhoch, J.; Shcherbakov, A.; Pöthig, A.; Li, Y.; Paetzold, U. W.; Kartouzian, A.; Sharp, I. D.; Katan, C.; Even, J.; Deschler, F. Bright Circularly Polarized Photoluminescence in Chiral Layered Hybrid Lead-Halide Perovskites. *Sci. Adv.* **2023**, *9* (35), eadh5083.

(13) Yuan, C.; Li, X.; Semin, S.; Feng, Y.; Rasing, T.; Xu, J. Chiral Lead Halide Perovskite Nanowires for Second-Order Nonlinear Optics. *Nano Lett.* **2018**, *18* (9), 5411–5417.

(14) Trujillo-Hernández, K.; Rodríguez-López, G.; Espinosa-Roa, A.; González-Roque, J.; Gómora-Figueroa, A. P.; Zhang, W.; Halasyamani, P. S.; Jancik, V.; Gembicky, M.; Pirruccio, G.; Solis-Ibarra, D. Chirality Control in White-Light Emitting 2D Perovskites. *J. Mater. Chem. C* **2020**, *8* (28), 9602–9607.

(15) Ren, H.; Wu, Y.; Wang, C.; Yan, Y. 2D Perovskite Nanosheets with Intrinsic Chirality. *J. Phys. Chem. Lett.* **2021**, *12* (10), 2676–2681.

(16) Yan, L.; Jana, M. K.; Sercel, P. C.; Mitzi, D. B.; You, W. Alkyl–Aryl Cation Mixing in Chiral 2D Perovskites. *J. Am. Chem. Soc.* **2021**, *143* (43), 18114–18120.

(17) Moroni, M.; Coccia, C.; Malavasi, L. Chiral 2D and Quasi-2D Hybrid Organic Inorganic Perovskites: From Fundamentals to Applications. *Chem. Commun.* **2024**, 10.1039.D4CC03314K.

(18) Li, X.; Hoffman, J. M.; Kanatzidis, M. G. The 2D Halide Perovskite Rulebook: How the Spacer Influences Everything from the Structure to Optoelectronic Device Efficiency. *Chem. Rev.* **2021**, *121* (4), 2230–2291.

(19) Lemmerer, A.; Billing, D. G. Effect of Heteroatoms in the Inorganic–Organic Layered Perovskite-Type Hybrids [(ZC $_n$ H $_{2n}$ NH $_3$) $_2$ PbI $_4$], n = 2, 3, 4, 5, 6; Z = OH, Br and I; and [(H $_3$ NC $_2$ H $_4$ S $_2$ C $_2$ H $_4$ NH $_3$)PbI $_4$]. *CrystEngComm* **2010**, *12* (4), 1290–1301.

(20) Mercier, N.; Poiroux, S.; Riou, A.; Batail, P. Unique Hydrogen Bonding Correlating with a Reduced Band Gap and Phase Transition in the Hybrid Perovskites (HO(CH $_2$) $_2$ NH $_3$) $_2$ PbX $_4$ (X = I, Br). *Inorg. Chem.* **2004**, *43* (26), 8361–8366.

(21) Bouguima, S.; Ouahrani, T.; Bouheddadj, A.; Roux, M. L.; Errandonea, D.; Badawi, M. Understanding the Optical and Bonding Properties of Hybrid Metal-Halide (C5H16NP) PbX4 (X = Cl, Br, I) Perovskite: A Density-Functional Theory Study. *Inorganic Chemistry Communications* **2021**, *130*, 108721.

(22) Zhao, L.; Han, X.; Zheng, Y.; Yu, M.-H.; Xu, J. Tin-Based Chiral Perovskites with Second-Order Nonlinear Optical Properties. *Advanced Photonics Research* **2021**, *2* (11), 2100056.

(23) Coccia, C.; Morana, M.; Mahata, A.; Kaiser, W.; Moroni, M.; Albini, B.; Galinetto, P.; Folpini, G.; Milanese, C.; Porta, A.; Mosconi, E.; Petrozza, A.; De Angelis, F.; Malavasi, L. Ligand-Induced Chirality in ClMBA $_2$ SnI $_4$ 2D Perovskite**. *Angew Chem Int Ed* **2024**, e202318557.

(24) Coccia, C.; Moroni, M.; Malavasi, L. Chiral Metal Halide Perovskites: Focus on Lead-Free Materials and Structure-Property Correlations. *Molecules* **2023**, *28* (16), 6166.

(25) Tao, K.; Li, Q.; Yan, Q. 1D Tin(II)-Based Chiral Hybrid Perovskite Single Crystals with Extremely Distorted Inorganic Chains for Second Harmonic Generation. *Advanced Optical Materials* **2024**, *12* (17), 2400018.

(26) Fortino, M.; Mattoni, A.; Pietropaolo, A. Atomistic Modeling of Metal–Ligand Chirality Transfer and Chiroptical Properties of Lead and Tin Hybrid Perovskites. *J. Mater. Chem. C* **2023**, *11* (27), 9135–9143.

(27) Wang, H.; Li, J.; Lu, H.; Gull, S.; Shao, T.; Zhang, Y.; He, T.; Chen, Y.; He, T.; Long, G. Chiral Hybrid Germanium(II) Halide with Strong Nonlinear Chiroptical Properties. *Angewandte Chemie* **2023**, *135* (41), e202309600.

(28) Coccia, C.; Moroni, M.; Treglia, A.; Boiocchi, M.; Yang, Y.; Milanese, C.; Morana, M.; Capsoni, D.; Porta, A.; Petrozza, A.; Stroppa, A.; Malavasi, L. Unraveling the Role of Structural Topology on Chirality Transfer and Chiroptical Properties in Chiral Germanium Iodides. *J. Am. Chem. Soc.* **2024**, *146* (35), 24377–24388.

(29) Jiang, S.; Zhao, P.; Xing, G.; Kang, H.; Li, X.; Zhao, T.; Li, B.; Zhang, T. Bismuth-Based Chiral Perovskite with Different Dimensions for Second-Order Nonlinear Optical Properties. *Advanced Optical Materials* **2023**, *11* (18), 2203078.

(30) Peng, H.; Liu, Q.; Lu, Y.-Z.; Yang, S.-J.; Qi, J.-C.; Chen, X.-G.; Liao, W.-Q. A Chiral Two-Dimensional Perovskite-like Lead-Free Bismuth(III) Iodide Hybrid with High Phase Transition Temperature. *Chem. Commun.* **2023**, *59* (68), 10295–10298.

(31) Rajput, P. K.; Poonia, A. K.; Mukherjee, S.; Sheikh, T.; Shrivastava, M.; Adarsh, K. V.; Nag, A. Chiral Methylbenzylammonium Bismuth Iodide with Zero-Dimensional Perovskite Derivative Structure. *J. Phys. Chem. C* **2022**, *126* (23), 9889–9897.

(32) Tokunaga, M.; Larrow, J. F.; Kakiuchi, F.; Jacobsen, E. N. Asymmetric Catalysis with Water: Efficient Kinetic Resolution of Terminal Epoxides by Means of Catalytic Hydrolysis. *Science* **1997**, *277* (5328), 936–938.

(33) Jacobsen, E. N. Asymmetric Catalysis of Epoxide Ring-Opening Reactions. *Acc. Chem. Res.* **2000**, *33* (6), 421–431.

(34) Saddique, F. A.; Zahoor, A. F.; Faiz, S.; Naqvi, S. A. R.; Usman, M.; Ahmad, M. Recent Trends in Ring Opening of Epoxides by Amines as Nucleophiles. *Synthetic Communications* **2016**, *46* (10), 831–868.

(35) Shivani; Pujala, B.; Chakraborti, A. K. Zinc(II) Perchlorate Hexahydrate Catalyzed Opening of Epoxide Ring by Amines: Applications to Synthesis of (*RS*)/(*R*)-Propranolols and (*RS*)/(*R*)/(*S*)-Naftopidils. *J. Org. Chem.* **2007**, *72* (10), 3713–3722

(36) Hodgson, D. M.; Humphreys, P. G.; Xu, Z.; Ward, J. G. Lithiation-Induced Migrations from Nitrogen to Carbon in Terminal Aziridines. *Angew. Chem. Int. Ed.* **2007**, *46* (13), 2245–2248.

(37) Eppel, S.; Fridman, N.; Frey, G. Amide-Templated Iodoplumbates: Extending Lead-Iodide Based Hybrid Semiconductors. *Crystal Growth & Design* **2015**, *15* (9), 4363–4371.

(38) Robinson, K.; Gibbs, G. V.; Ribbe, P. H. Quadratic Elongation: A Quantitative Measure of Distortion in Coordination Polyhedra. *Science* **1971**, *172* (3983), 567–570.

(39) Baur, W. H. The Geometry of Polyhedral Distortions. Predictive Relationships for the Phosphate Group. *Acta Crystallogr B Struct Sci* **1974**, *30* (5), 1195–1215.

(40) Fortino, M.; Mattoni, A.; Pietropaolo, A. The Role of Metal-Halide Bond in the Distortions and Asymmetric Non-Covalent Interactions in Chiral Hybrid Perovskites. *J. Phys. Mater.* **2024**, *7* (4), 045009.

(41) Chiara, R.; Accorsi, G.; Listorti, A.; Coduri, M.; Coccia, C.; Tedesco, C.; Morana, M.; Malavasi, L. Halide Alloying and Role of Central Atom on the Structural and Optical Properties of Decylammonium Germanium 2D Perovskites. *APL Energy* **2023**, *1* (1), 016101.

(42) Ben-Moshe, A.; Teitelboim, A.; Oron, D.; Markovich, G. Probing the Interaction of Quantum Dots with Chiral Capping Molecules Using Circular Dichroism Spectroscopy. *Nano Lett.* **2016**, *16* (12), 7467–7473.

(43) Das, R.; Hossain, M.; Mahata, A.; Swain, D.; De Angelis, F.; Santra, P. K.; Sarma, D. D. Unique Chiro-Optical Properties of the Weakly-2D (R-/S-MBA) $_2$ CuBr $_4$ Hybrid Material. *ACS Materials Lett.* **2023**, 1556–1564.

(44) Jana, M. K.; Song, R.; Liu, H.; Khanal, D. R.; Janke, S. M.; Zhao, R.; Liu, C.; Valy Vardeny, Z.; Blum, V.; Mitzi, D. B. Organic-to-Inorganic Structural Chirality Transfer in a 2D Hybrid Perovskite and Impact on Rashba-Dresselhaus Spin-Orbit Coupling. *Nat Commun* **2020**, *11* (1), 4699.

(45) He, C.; Zhang, C.; Li, J.; Peng, X.; Meng, L.; Tang, C.; Zhong, J. Direct and Quasi-Direct Band Gap Silicon Allotropes with Remarkable Stability. *Phys. Chem. Chem. Phys.* **2016**, *18* (14), 9682–9686.

(46) Dvorak, M.; Wei, S.-H.; Wu, Z. Origin of the Variation of Exciton Binding Energy in Semiconductors. *Phys. Rev. Lett.* **2013**, *110* (1), 016402.

SUPPLEMENTARY INFORMATION

Engineering the Electronic Structure and Optoelectronic Properties of Chiral Metal Halides through Cation Design

Clarissa Coccia,[a] Marco Moroni,[a.*] Massimo Boiocchi,[b] Marta Morana,[d] Maddalena Patrini,[e] Doretta Capsoni,[a] Alessio Porta,[a] Andera Olivati[c], Giulia Folpini,[c,d] Annamaria Petrozza,[c] Luca Gregori,[f,g] Edoardo Mosconi,[g,h] , Filippo De Angelis,[f,g,i] and Lorenzo Malavasi,[a,*]

[a]University of Pavia, Department of Chemistry and INSTM, Via Taramelli 12, 27100, Pavia, Italy

[b]University of Pavia, Centro Grandi Strumenti, Via Bassi 21, 27100, Pavia, Italy

[c]Center for Nano Science and Technology@PoliMi, Istituto Italiano di Tecnologia 20134 Milan (Italy)

[d]Institute for Photonics and Nanotechnology, CNR – IFN, 20133 Milano

[e]University of Pavia, Department of Physics, Via Bassi 6, 27100, Pavia, Italy

[f]University of Perugia, Department of Chemistry, Biology and Biotechnology, Via Elce di Sotto 8, 06123, Perugia, Italy

[g]Computational Laboratory for Hybrid/Organic Photovoltaics (CLHYO), Istituto CNR di Scienze e Tecnologie Chimiche “Giulio Natta” (CNR-SCITEC), Via Elce di Sotto 8, 06123 Perugia, Italy

[h] Chemistry Department, College of Science, King Saud University, 11451, Riyadh, Saudi Arabia

[i]SKKU Institute of Energy Science and Technology (SIEST), Sungkyunkwan University, Suwon 440-746, South Korea

Corresponding Authors

Lorenzo Malavasi, email: lorenzo.malavasi@unipv.it

Marco Moroni, email: marco.moroni@unipv.it

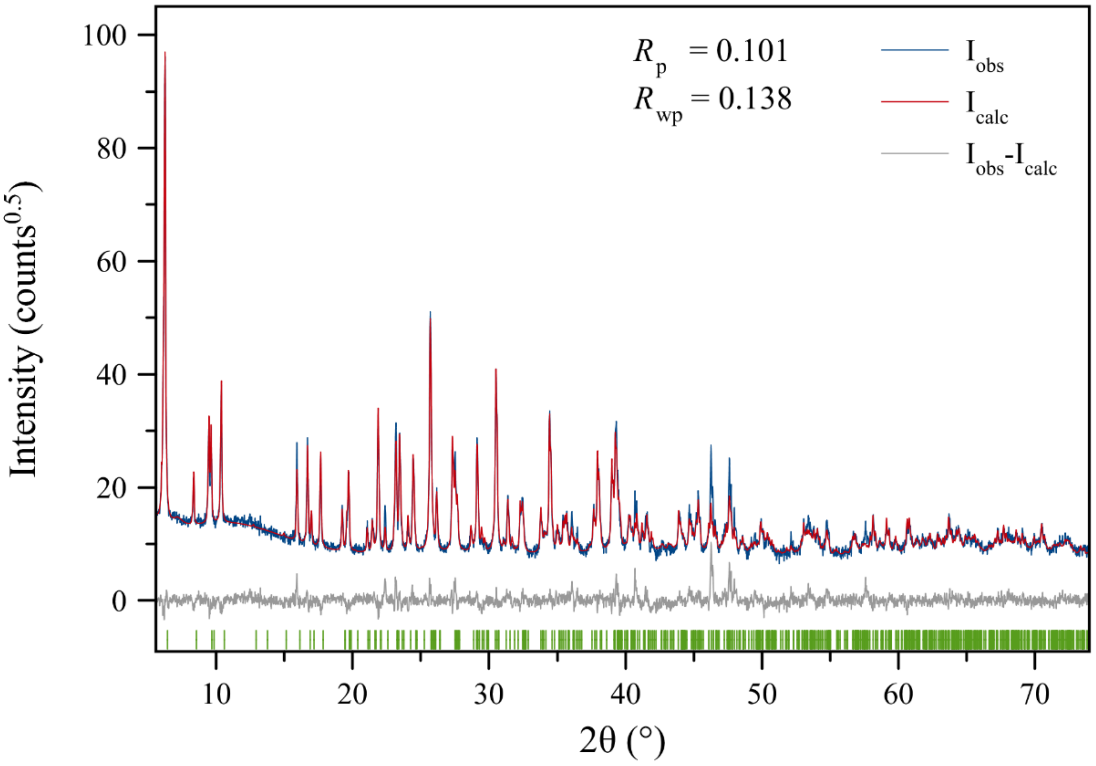

Figure S1. Rietveld refinement of (*S*-AMOL)PbI_3.

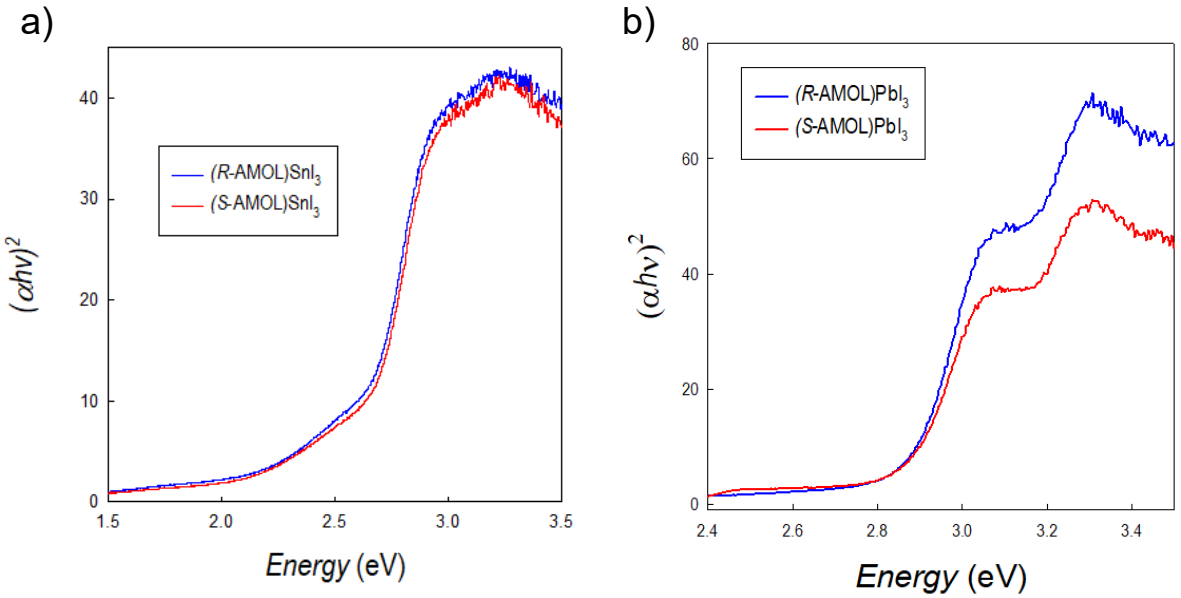

Figure S2. Tauc plots of a) (*R/S*-AMOL)SnI_3 and b) (*R/S*-AMOL)PbI_3.

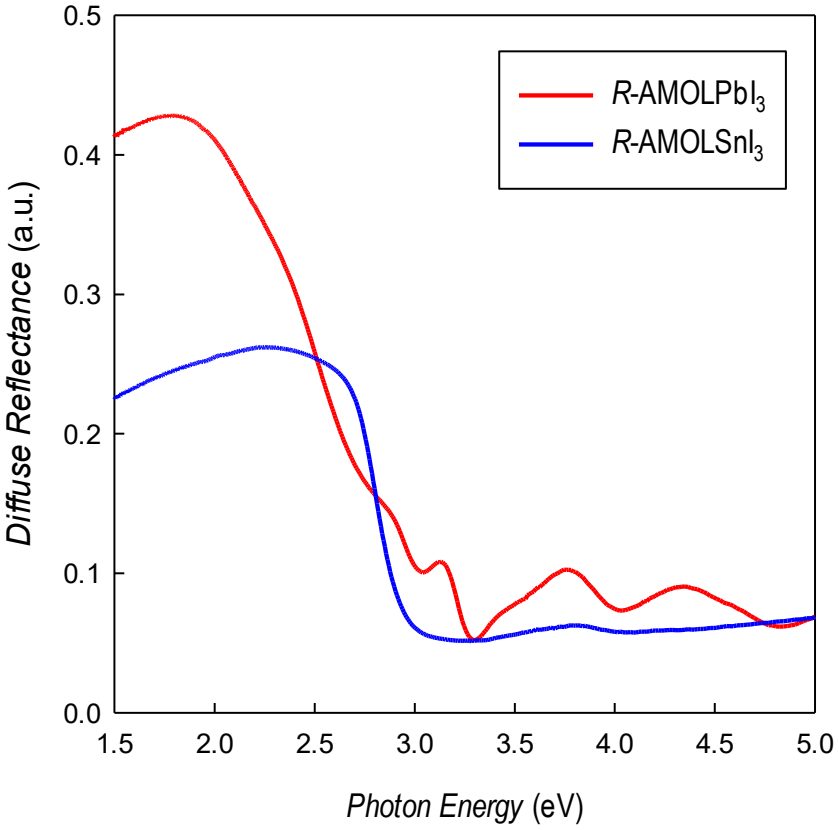

Figure S3 Diffuse Reflectance spectra on thin films of (*R*-AMOL)SnI_3 and (*R*-AMOL)PbI_3 carried out at room temperature.

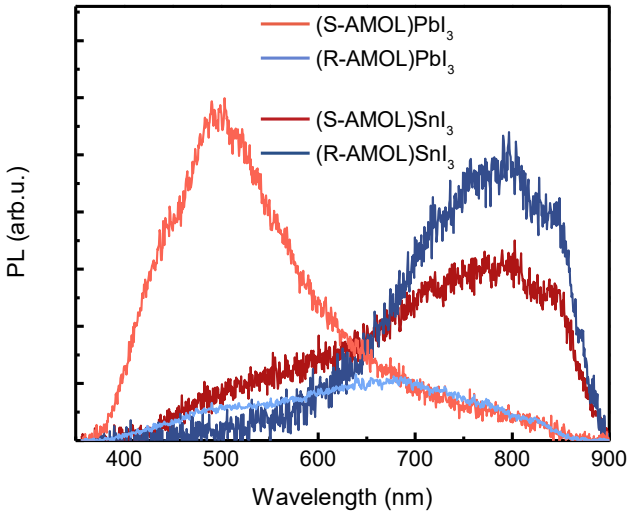

Figure S4 PL spectra of the samples at room temperature.

Experimental

Synthesis of (2R,2'R)-1,1'-azanediylbis(butan-2-ol) and (2S,2'S)-1,1'-azanediylbis(butan-2-ol) (AMOL-monomer)

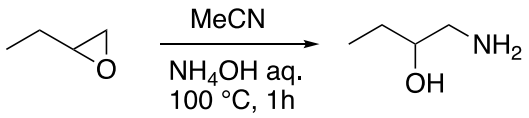

To a stirred solution of *(R/S)*-1,2-epoxybutane (1.72 mL, 20 mmol) in MeCN (4 mL) Aqueous NH_3 solution (10 mL, 30% w/w) was added dropwise. The resulting clear solution was heated at 100°C in a pressure tube apparatus for 1h. Volatiles were removed from the crude compound with rotary evaporator without heating the bath. The residue was then distilled bulb-to-bulb (7 mmHg, 127 °C) gave to give the two enantiomers of 1-amminobutan-2-ol as a colourless oil.

IR (liquid film): 3355 (br, NH and OH), 2931, 2861, 1579, 1076.
^{1}H NMR (400 MHz, $CDCl_3$) 3.45-3.41 (m, 1H), 2.80 (dt, *J* =13, 4, 3 Hz, 1H, CH(*H*)N), 2.51 (dt, *J* = 10, 5, 4 Hz, 1H, CH(H)N), 2.24 (br, 3H, NH_2, OH overlapped), 1.47-1.39 (m, 2H, CH_2CH_3), 0.94 (t, J = 7.9Hz, 3H, CH_3);
^{13}C NMR (100 MHz, $CDCl_3$) 73.4 d, 46.8 t, 27.6 t, 10.1 q.
MS-ESI: 90.09 $[M+H]^+$.
The data were the same for (*R*) and (*S*) enantiomer, ORP were reported below:
$[\alpha]^{20}_D$ = +7.6 (c 1.0, CH_2Cl_2) for (*R*)-1-aminobutan-2-ol.
$[\alpha]^{20}_D$ = -7.5 (c 1.1, CH_2Cl_2) for (*S*)-1-aminobutan-2-ol.

Synthesis of (2R,2'R)-1,1'-azanediylbis(butan-2-ol) and (2S,2'S)-1,1'-azanediylbis(butan-2-ol) (AMOL-dimer)

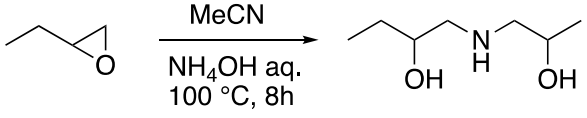

To a stirred solution of *(R/S)*-1,2-epoxybutane (1.72 mL, 20 mmol) in MeCN (4 mL) Aqueous NH_3 solution (1.6 Equiv., 2 mL, 30% w/w) was added dropwise. The resulting clear solution

was heated at 100°C in a pressure tube apparatus for 8h. Volatiles were removed from the crude compound with rotary evaporator without heating the bath. The residue was then distilled bulb-to-bulb (7 mmHg, 127 °C) gave to remove residue of 1-amminobutan-2-ol as a colourless oil. The residue contains AMOL-dimer with more than 93% grade of purity (HESI-LC/MS).

^{1}H NMR (400 MHz, $CDCl_3$) δ 3.64 – 3.48 (m, 2H), 3.47 – 2.94 (m, 4H), 2.81 – 2.35 (m, 4H), 1.40 (tdd, *J* = 13.9, 10.2, 7.7 Hz, 4H), 0.91 (dd, *J* = 8.3, 6.8 Hz, 6H).

^{13}C NMR (101 MHz, $CDCl_3$) δ 70.9 d, 47.1 t, 28.2 t, 10.1 q.

$[\alpha]^{20}_D$ = +3.6 (c 1.0, CH_2Cl_2) for (*R*)-Dimer.
$[\alpha]^{20}_D$ = -3.5 (c 1.1, CH_2Cl_2) for (*S*)-Dimer.

Synthesis of (R/S-AMOL)SnI_3 and (R/S-AMOL)PbI_3

Powdered samples of (*R/S*-AMOL)PbI_3 and (*R/S*-AMOL)SnI_3 were prepared by dissolving proper amounts of $Pb(CH_3COO)_2$ or $Sn(CH_3COO)_2$ in HI at 90°C. Once the powder was dissolved in the solution, the proper amount of (*R*/*S*- AMOL) was added. After the dissolution of the latter the solution was cooled down at room temperature (25°C), favouring the precipitation of the final compounds. The synthesis of the Sn-based perovskite was carried out under an N_2 atmosphere, with the addition of H_3PO_2 as reductive reagent for the Sn(IV), while the Pb compound has been synthesised in an ambient atmosphere.

Thin films preparation. First, the glass substrates were washed using water, isopropanol and acetone in a sonicator for 20 min each. Then, the proper amount of perovskites were dissolved in DMF:acetone (90:10) in order to obtain a final solution 0.08 M, and the thin films were prepared on substrates by drop casting method. The films were annealed at 100°C for 10 min on a hot plate. Film thickness was measured with a mechanical profilometer (AP06 KLA Tencor).

UV-vis-NIR spectroscopy. Absorption and Diffuse Reflectance measurements were performed under ambient conditions by using a Varian Cary 6000i spectrophotometer equipped with a double monochromator, a 110 mm diameter integrating sphere, Si photomultiplier and InGaAs photodiode detectors. Spectral range was 190-1800 nm, in steps of 1 nm.

UV-Vis spectroscopy. DRS spectra were acquired in the wavelength range 300- 800 nm directly on the powders by using a Jasco V-750 spectrophotometer, equipped with an

integrating sphere (Jasco ISV-922). For each spectrum, one accumulation was performed with a scan speed of 50 nm/min. The low temperature absorption measurements were acquired putting drop casted thin films samples in a nitrogen-cooled cryostat stage (Linkam) in a UV/VIS/NIR spectrophotometer Lambda 1050, Perkin Elmer.

Circular Dichroism. CD spectra were acquired in the wavelength range 350- 800 nm on thin films by using a Jasco J-1500 CD spectrophotometer. For each spectrum, three accumulations were performed with a scale of 200 mdeg/0.1 dOD, a bandwidth of 1 nm, and a scan speed of 50 nm/min. The g_{CD} value for both samples has been calculated after normalizing the absorptions using the following formula:

$$g_{cd} = \frac{\Delta A}{A} = \left(\frac{Ellipticity}{32980}\right)/Abs$$

Where Ellipticity is expressed in millidegrees (mdeg). The effect of Linear Dichroism (LD) was eliminated by performing measurements on the thin films tilted by 90° and then rotated by 180°.

Photoluminescence spectroscopy. The PL spectra were acquired under excitation from the 3rd harmonic of a Nd:YVO_4 laser (Innolas Picolo, 900 ps, 1 kHz, 355 nm) keeping the samples under vacuum condition in a Linkam stage (P = 6e-3 mbar). The pump was focused on the sample with a 25 cm focal lens, to achieve a fluence of 2.2 W/cm^2. The PL was measured using a cooled iCCD (Andor iStar) coupled to a Shamrock monochromator, offering enhanced spectral and detection sensitivity by synchronizing the PL acquisition with the optical excitation via electronic gating (measurement window: 4 ns, integration time 10s).

Structural determination. Powder X-ray diffraction (PXRD) data were acquired employing a Bruker D8 Advance θ:θ diffractometer and a Si zero-background sample-holder, in the 2θ range 3.0-74.0°, with steps of 0.02° and a time *per* step of 10 s and treated taking advantage of the TOPAS-6 software. Suitable unit cell parameters were retrieved upon indexing the PXRD pattern through the Singular Value Decomposition algorithm, then performing a whole powder pattern refinement with the Le Bail method[2] (Figure S5a).[1,2] The structure was solved with the Simulated Annealing approach[3] and refined with the Rietveld method (Figure 1b of main text), describing the (*S*-/*R*-)AMOL as rigid bodies through the *z*-matrix

formalism.[3,4] The background was described by means of a Chebyshev type polynomial function, and the instrumental contribution to the peak profile through the Fundamental Parameters Approach.[5] The crystallographic data are reported in table S1.

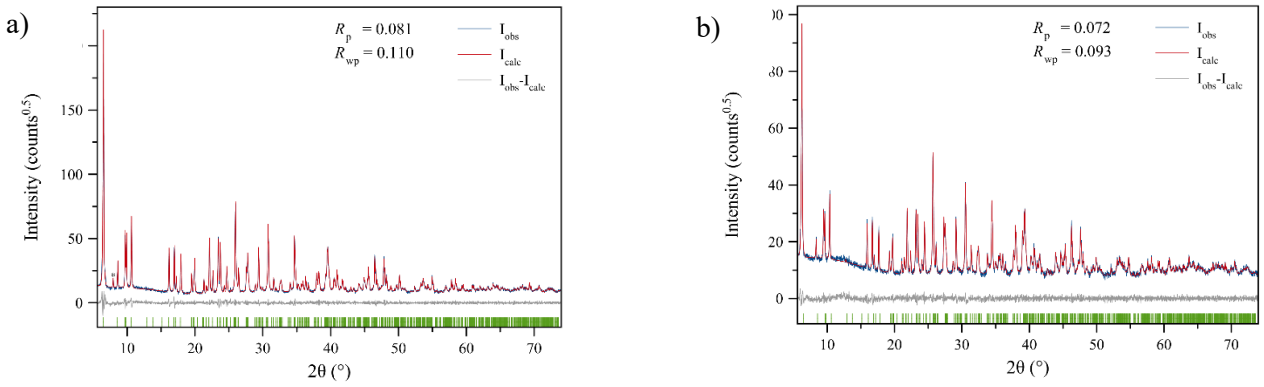

Figure S5. Whole powder pattern Le Bail refinement of the (R-AMOL)PbI_3 (a) and (S-AMOL)PbI_3 (b) PXRD patterns in terms of experimental, calculated and difference traces (blue, red and grey, respectively). The green ticks indicate the positions of the Bragg reflections.

Computational Details

Density Functional Theory (DFT) calculations were performed using the Quantum ESPRESSO suite of programs and with VASP.[6–9] Initial structures for both Sn- and Pb-based perovskite models were derived from experimentally determined CIF data (CCDC Code for (*S*-AMOL)SnI_3: 2365047) and subsequently optimized to achieve relaxed ionic configurations. To accurately account for van der Waals interactions, we employed the PBE exchange-correlation functional augmented with DFT-D3 dispersion corrections. All the structural optimizations were carried out using QE, while VASP was used for more accurate calculations of the fine electronic properties of both materials.

Structural optimizations utilized norm-conserving pseudopotentials, explicitly including the following electronic states: I (5s, 5p), N and C (2s, 2p), H (1s), and Pb/Sn (6s, 6p, 5d).[10] A plane-wave cutoff energy of 60 Ry was applied for the wavefunctions, with a charge density cutoff of 240 Ry to ensure computational accuracy. Spin-orbit coupling (SOC) effects were incorporated post-optimization to accurately capture Rashba-type spin splitting, which is particularly significant for heavy elements such as lead. Finally, both Quantum ESPRESSO and VASP were employed for fine electronic structure calculations. Specifically, the Heyd,

Scuseria, and Ernzerhof (HSE06) hybrid functional with spin-orbit coupling (SOC) addition was used, with a 6 × 1 × 1 Γ-centered grid and a plane wave cut-off of 60/120 Ry for QE with 500 eV. The calculated band gaps for Sn-based perovskites were 2.64 eV using PBE, 2.31 eV with PBE-SOC, and 3.52 eV with HSE06-SOC. For Pb-based perovskites, the band gaps were slightly higher, with values of 2.85 eV (PBE), 2.16 eV (PBE-SOC), and 3.67 eV (HSE06-SOC). These results highlight the significant impact of SOC and hybrid functionals on the electronic structure, demonstrating the need for advanced methods to accurately capture the material properties.

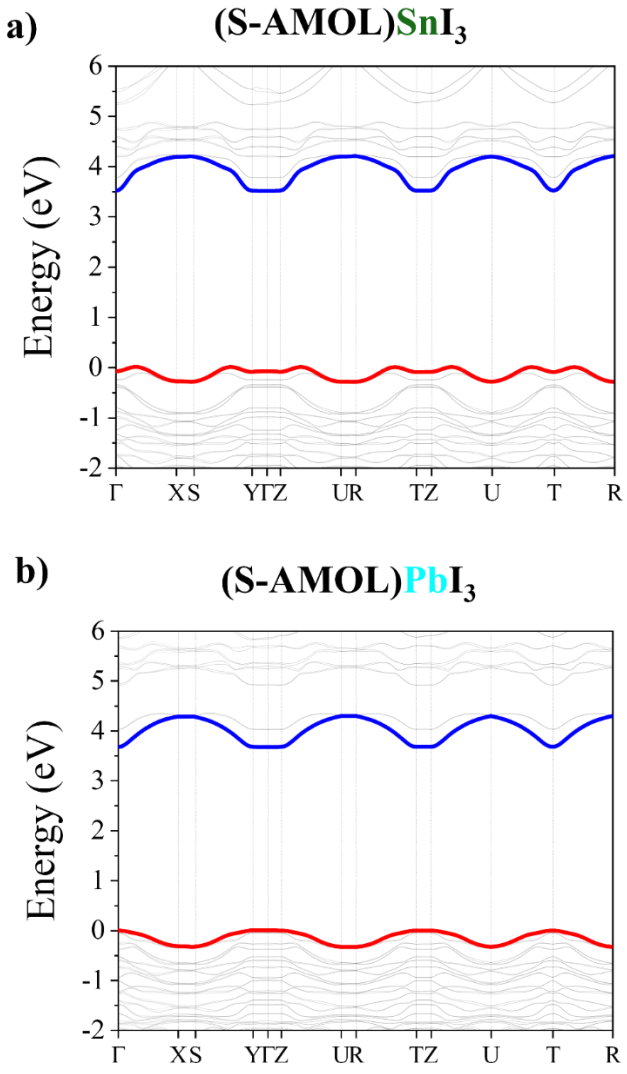

Figure S6: Electronic band structures of Sn-based (a) and Pb-based (b) perovskites computed using the PBE+D3 with spin-orbit coupling (SOC) and rigidly shifted to match the HSE06-SOC calculated band gap of both materials. The conduction band minimum (CBM) and valence band maximum (VBM) are highlighted in blue and red, respectively. The band structures reveal the direct band gap nature of Pb-based materials, while for Sn the valence band is found to be off the point of high symmetry leading to a quasi-indirect band gap.

Table S1. Hole, electron and effective masses for the investigated systems.

	m_h^*	m_e^*	μ
Sn (Γ → X)	0.59	0.17	0.13
Pb (Γ → X)	0.93	0.25	0.19
Pb and Sn (Γ → Z)	∞	∞	/

References

(1) Coelho, A. A. Indexing of Powder Diffraction Patterns by Iterative Use of Singular Value Decomposition. *J Appl Crystallogr* **2003**, *36* (1), 86–95.

(2) Le Bail, A.; Duroy, H.; Fourquet, J. L. Ab-Initio Structure Determination of LiSbWO6 by X-Ray Powder Diffraction. *Materials Research Bulletin* **1988**, *23* (3), 447–452.

(3) Coelho, A. A. Whole-Profile Structure Solution from Powder Diffraction Data Using Simulated Annealing. *J Appl Crystallogr* **2000**, *33* (3), 899–908.

(4) Rietveld, H. M. A Profile Refinement Method for Nuclear and Magnetic Structures. *J Appl Crystallogr* **1969**, *2* (2), 65–71.

(5) Cheary, R. W.; Coelho, A. A Fundamental Parameters Approach to X-Ray Line-Profile Fitting. *J Appl Crystallogr* **1992**, *25* (2), 109–121.

(6) Giannozzi, et al, R. M. QUANTUM ESPRESSO: A Modular and Open-Source Software Project for Quantum Simulations of Materials. *Journal of Physics: Condensed Matter* **2009**, *21* (39), 395502.

(7) Kresse, G.; Hafner, J. *Ab Initio* Molecular Dynamics for Liquid Metals. *Phys. Rev. B* **1993**, *47* (1), 558–561.

(8) Kresse, G.; Furthmüller, J. Efficiency of Ab-Initio Total Energy Calculations for Metals and Semiconductors Using a Plane-Wave Basis Set. *Computational Materials Science* **1996**, *6* (1), 15–50.

(9) Kresse, G.; Furthmüller, J. Efficient Iterative Schemes for *Ab Initio* Total-Energy Calculations Using a Plane-Wave Basis Set. *Phys. Rev. B* **1996**, *54* (16), 11169–11186.

(10) Van Setten, M. J.; Giantomassi, M.; Bousquet, E.; Verstraete, M. J.; Hamann, D. R.; Gonze, X.; Rignanese, G.-M. The PseudoDojo: Training and Grading a 85 Element Optimized Norm-Conserving Pseudopotential Table. *Computer Physics Communications* **2018**, *226*, 39–54.

CHAPTER 5

3D Chiral Metal Halide Semiconductors

Marco Moroni,[a] Luca Gregori,[b,i] Clarissa Coccia,[a] Massimo Boiocchi,[c] Marta Morana,[d] Doretta Capsoni,[a] Andrea Olivati,[e,f] Antonella Treglia,[e] Giulia Folpini,[e,g] Maddalena Patrini,[h] Isabel Pinto Goncalves,[e] Heyong Wang,[e] Chiara Milanese,[a] Annamaria Petrozza,[e] Edoardo Mosconi,[i,*] Filippo De Angelis,[b,i,l] and Lorenzo Malavasi,[a,*]

[a] University of Pavia, Department of Chemistry and INSTM, Via Taramelli 16, 27100, Pavia, Italy.

[b] University of Perugia, Department of Chemistry, Biology and Biotechnology, Via Elce di Sotto 8, 06123, Perugia, Italy.

[c] University of Pavia, Centro Grandi Strumenti, Via Bassi 21, 27100, Pavia, Italy.

[d] Dipartimento di Scienze della Terra, Università di Firenze, Via La Pira 4, 50121 Florence, Italy

[e] Center for Nano Science and Technology@PoliMi, Istituto Italiano di Tecnologia 20134 Milan, Italy.

[f] Physics Department, Politecnico di Milano, Piazza L. da Vinci, 32, 20133 Milano, Italy.

[g] Istituto di Fotonica e Nanotecnologie, CNR-IFN, 20133 Milan, Italy.

[h] University of Pavia, Department of Physics, Via Bassi 6, 27100, Pavia, Italy.

[i] Computational Laboratory for Hybrid/Organic Photovoltaics (CLHYO), Istituto CNR di Scienze e Tecnologie Chimiche “Giulio Natta” (CNR-SCITEC), Via Elce di Sotto 8, 06123 Perugia, Italy

[l] SKKU Institute of Energy Science and Technology (SIEST), Sungkyunkwan University, Suwon 440-746, South Korea

Corresponding Authors

Lorenzo Malavasi, email: lorenzo.malavasi@unipv.it

Edoardo Mosconi, email: edoardo@thch.unipg.it

ToC

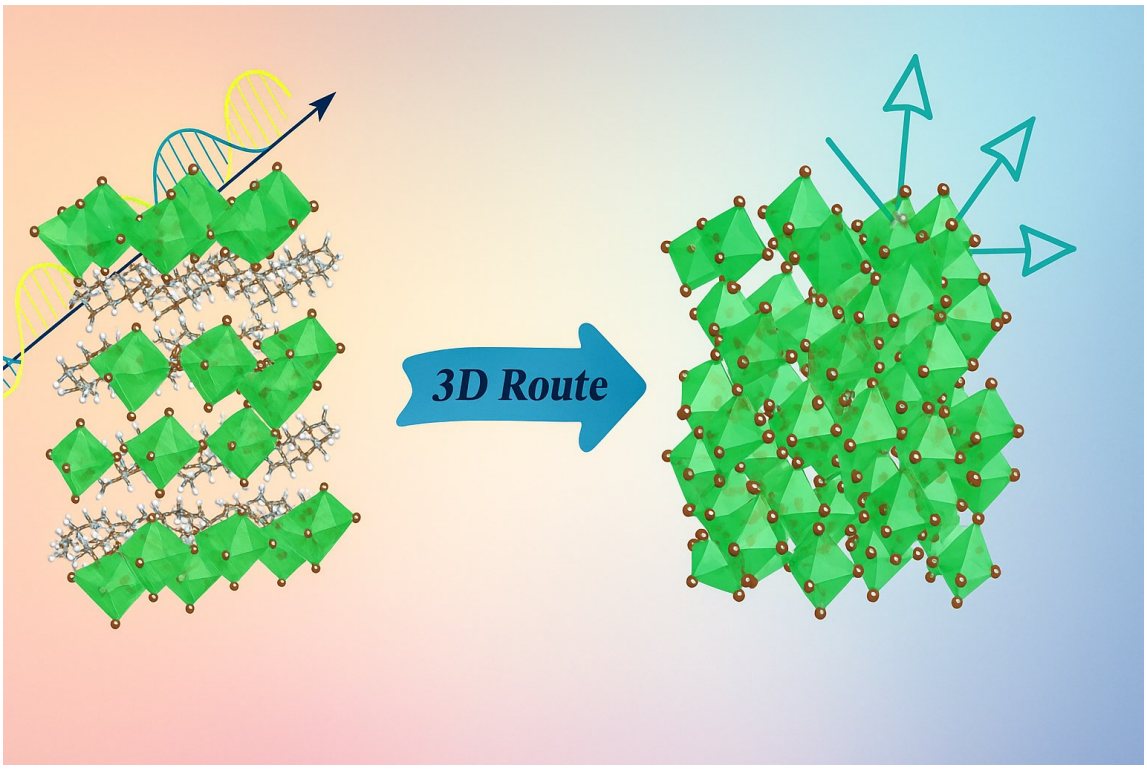

Abstract

Chiral metal halides offer a rich library of materials for non-linear optics and spin selective devices. Chirality is usually transferred from chiral organic cations to the inorganic sublattice and this strategy, so far, has targeted low-dimensional materials, given the size of available cations, posing limitations due to quantum and dielectric confinement. Despite the elegant design, their embodiment in devices would benefit from efficient three-dimensional charge transport. To this end, we have designed a family of chiral metal halides closely related to the 3D corner-sharing octahedral network of prototypical perovskites through the relatively small ditopic *R*/*S*-3-aminoquinuclidine (3-AQ) cation, leading to an arrangement of corner-sharing octahedra of formula (*R*/*S*-3AQ)Pb_2Br_6. Direct bandgap and isotropic band structure provide a 3D delocalized photoexcitation, with a chiral anisotropy factor consistent with the theoretically calculated value for such a system. As expected for a chiral semiconductor, Rashba effect occurs in the conduction band due to the combination of spin-orbit coupling and non-centrosymmetry. This 3D system, offering rich chemical tunability, will facilitate future materials engineering for non-linear optoelectronic devices.

1. Introduction

Metal halide perovskites constitute a class of wonder materials, characterized by huge structural diversity associated to variations in both the inorganic (metal, halide) and organic (A-site cations) sublattices. Besides their success in solar cells and LEDs, such chemical richness can be exploited to engineer a variety of chiral compounds with associated spin-dependent chiroptical electronic properties.[1–8] Potential technological applications of chiral perovskites are in circularly polarized light emission and detection, chiral sensing, chiral-induced spin selectivity, up to enantioselective synthesis and photocatalysis.[9–11] Thus, the broad tunability of these materials arises by the interplay of organic and inorganic moieties through the chirality transfer mechanism, whereby chiral A-site organic cations impart chiroptical response to the optically active inorganic framework.[12] The family of chiral 2D perovskites and low-dimensional metal halides (0D and 1D systems), first reported from 2003,[13,14] has grown impressively by exploring various organic cations and different metals.[15–21] These low-dimensional structures were demonstrated to exhibit chiroptical properties as well as spin-polarized absorption, spin-polarized photoluminescence, and second harmonic generation. [22–25] The inherent carrier and excitonic confinement of such low-dimensional materials and the associated anisotropic transport remains a challenge for their effective integration in devices.

The synthesis of 3D chiral perovskites would represent a significant advancement, lifting the above-mentioned limitations. It is now clear, however, that only small organic cations, such as methylammonium ($CH_3NH_3^+$) or formamidinium ($NH_2CHNH_2^+$)), can give rise to 3D perovskites which clearly have no chiral-templating nature.[26,27] A different approach was proposed by Chen and co-workers through the growth of $MAPbBr_3$ single crystals with the addition of micro- or nanoparticles as nucleating agents.[28] Chirality, in this case, emerges from chiral orientation patterns of the incorporated A-site cations through the formation of chiral supercells inducing chiroptical activity. The heterogeneous chiral nucleation proposed, however, assures only a partial enantiomeric excess (*i.e.* the ratio of the two chiral enantiomers) so that control over the handedness (*R*/*L*) selectivity remains a major isssue. In addition, this synthetic process is limited to single crystals whereby thin films are the optimal choice for their embodiment in devices.[28]

Here we face the challenge of achieving 3D chiral metal halide materials by making use of enantiopure cage-like ditopic amines, specifically exploiting *R*/*S*-3-aminoquinuclidine (3-AQ), Figure 1a. The peculiar steric hindrance of this amine and its relatively small size allows the formation of a 3D chiral metal halide of formula (*R*/*S*-3AQ)Pb_2Br_6 composed exclusively of $PbBr_6$ corner-sharing octahedral, similar to the 3D connectivity of prototypical perovskite structures. The new compound presents a direct band gap with chiroptical properties in the circular dichroism response, while clearly maintaining signatures typical of 3D semiconductors, as shown by its band dispersion and reduced exciton binding energy and band gap compared to its 2D perovskite counterpart, (*R/S*-3-AQ)$_2PbBr_4$·2Br. In line with such properties coupled to the non-centrosymmetric crystal structure, the 3D (*R*/*S*-3AQ)Pb_2Br_6 chiral system is predicted to show a significant Rashba conduction band splitting that makes it potentially amenable for spintronics.[29]

2. Results and Discussion

Samples of (*R*/*S*-3AQ)Pb_2Br_6 and of (*R/S*-3-AQ)$_2PbBr_4$·2Br have been synthesized as reported in the Methods Section (see Supplementary Information, SI). For (*R*-3AQ)Pb_2Br_6 we grow high-quality single crystals which were used to solve the crystal structure by X-ray diffraction and the main crystallographic data are reported in Table 1. For the *S*-enantiomer, however, this was hardly possible and therefore the crystal structure was Rietveld-refined starting from the single-crystal data of the *R*-enantiomer.

Table 1. Crystal structure data for [(*R*/*S*-3AQ)$_2PbBr_4$]·2Br and (*R*/*S*-3AQ)Pb_2Br_6. For (*S*-3AQ)Pb_2Br_6 we report the Rietveld refinement of powder diffraction pattern.

	[(*R*-3AQ)$_2$PbBr$_4$]·2Br	**[(*S*-3AQ)$_2$PbBr$_4$]·2Br**	**(*R*-3AQ)Pb$_2$Br$_6$**	**(*S*-3AQ)Pb$_2$Br$_6$**
Empirical formula	$C_{14}H_{32}N_4Br_6Pb$	$C_{14}H_{32}N_4Br_6Pb$	$C_7H_{16}N_2Br_6Pb_2$	$C_7H_{16}N_2Br_6Pb_2$
Formula weight	943.05	943.05	1022.04	1022.04
Temperature (K)	298	298	298	298
Wavelength (Å)	0.7107	0.7107	0.7107	1.5406
Crystal system	Tetragonal	Tetragonal	Orthorhombic	Orthorhombic
Space group	$P4_12_12$	$P4_32_12$	$P2_12_12_1$	$P2_12_12_1$
Lattice parameters (Å)	*a* = 6.58258(8)	*a* = 6.58253(5)	*a* = 10.9133(2)	*a* = 10.9184(2)
	b = 6.58258(8)	*b* = 6.58253(5)	*b* = 11.0771(2)	*b* = 11.0820(2)
	c = 56.6268(14)	*c* = 56.6576(8)	*c* = 15.5426(3)	*c* = 15.5470(3)
Lattice Volume (Å^3)	2453.66(9)	2454.96(5)	1878.91(6)	1881.14(6)
Z	4	4	4	4
CCDC code	2416647	2416648	2416219	-

(*R*/*S*-3AQ)Pb_2Br_6 crystallizes in the orthorhombic chiral space group $P2_12_12_1$ (No. 19) at 293 K. The crystal structure of (*R*/*S*-3AQ)Pb_2Br_6 is peculiar and, to our knowledge, not yet reported in the literature for any other metal halide: it is composed of two independent Pb sites (Pb1 and Pb2) forming two distinct types of octahedra with Br ions, see Figure 1b-d. Notably, the reported crystal structure presents a AB_2X_6, chemical formula analog to that of typical perovskitoids.

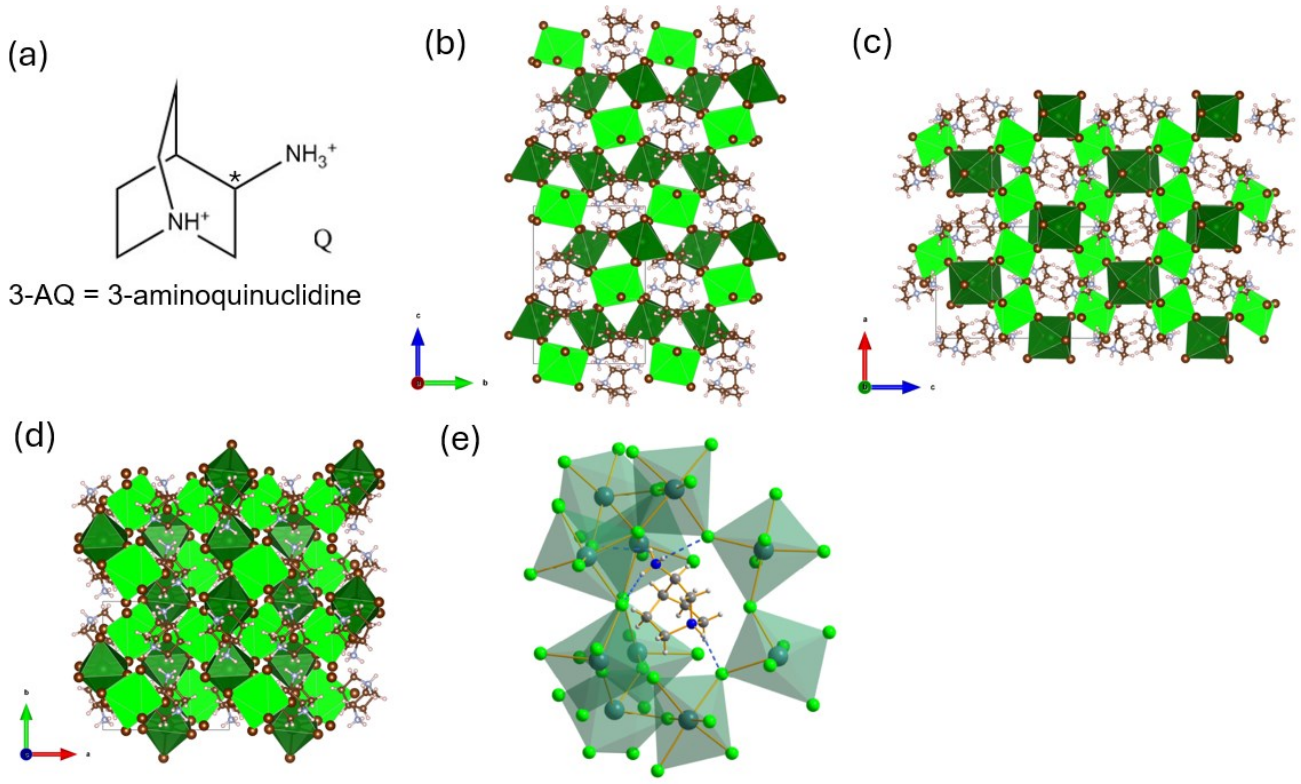

Figure 1. (a) Chemical formula of 3-aminoquinuclidine (3-AQ), the asterisk marks the chiral center; (b-d) sketches of the crystal structures of (*R*/*S*-3-AQ)Pb_2Br_6 along the *a*, *c* and *b* axes, respectively; the two crystallographically independent Pb ions are represented with their coordination octahedra in dark green (Pb1) and light green (Pb2), respectively; (e) Highlight of the (*R*-3-AQ)Pb_2Br_6 N-H···Br hydrogen bonds interactions, represented as blue dashed lines.

From Figure 1 one may notice the peculiar arrangement of the $PbBr_6$ octahedra: [Pb1Br_6] octahedra are corner-sharing arranged along the *b*-direction while [Pb2Br_6] octahedra form an analogous corner-sharing pattern along the *a*-direction. These two perpendicular rows are then again corner-sharing bonded along the *c*-direction creating central voids along the *a* and *b* directions which host the 3-AQ moieties. N-H···Br hydrogen bond interactions are established for both N atoms of 3-AQ, namely the tertiary amine of the quinuclidine ring and

the primary amine in position 3 of the ring, with H···Br distances in the range 2.36-2.99 Å, Figure 1e.

The $PbBr_6$ octahedra present six different Pb-Br bond-lengths; these are, however, very close to each other for both [$Pb1Br_6$] and [$Pb2Br_6$], lying in the range 2.93-3.09 Å. Interestingly, the average bond length for [$Pb1Br_6$] is 3.0103 Å and 3.0077 Å for [$Pb2Br_6$] octahedra which are only slightly longer than the Pb-Br bond length found in cubic $MAPbBr_3$ (2.964 Å).[30] Indeed, the Robinson distortion parameter, *D*,[31] is very low for both octahedra type, 0.019, while the bond angle variance (σ^2) is 42.7 and 51.9 deg^2 for [$Pb1Br_6$] and [$Pb2Br_6$], respectively, see list of structural parameters in Table S1, Supporting Information.

To remark the difference between the (*R*-3-AQ)Pb_2Br_6 3D compound and the typical chiral 2D perovskites we synthesized also the (*R/S*-3-AQ)$_2PbBr_4$·2Br compound and solved the crystal structure by SC-XRD, Table 1. The crystal symmetry of both *R*/*S* enantiomers is tetragonal and belongs to the two chiral Sohncke space groups $P4_12_12$ and $P4_32_12$, for the *R* and *S* sample, respectively. A sketch of the crystal structure for the two samples is reported in Figure S1, Supporting Information. Both enantiomers present the typical arrangement of Ruddlesden-Popper 2D perovskites characterized by layers of corner-sharing $PbBr_6$ octahedra separated by a bilayer of 3-AQ molecules including and additional layer of bromide anions to ensure electroneutrality. The six Pb-Br bond lengths show a significant distribution from ~2.78 to ~3.81 Å for both samples, with an average bond length of about 3.20 Å (see also Table S1). The octahedra distortion parameters for (*R*-3-AQ)$_2PbBr_4$·2Br and (*S*-3-AQ)$_2PbBr_4$·2Br are *D*=0.128 and σ^2 40.77 deg^2, thus an increased octahedra distortion is found compared to the 3D system (0.019 *vs.* 0.128).

For both systems we also afforded the preparation of the racemic samples in form of powders. The X-ray diffraction patterns have been indexed and refined showing an analogous structural arrangement as the chiral compounds but with centrosymmetric space groups, namely *Pmma* for (*rac*-3-AQ)$_2PbBr_4$·2Br and *C*2 (*rac*-3-AQ)$_2PbBr_4$·2Br. The refined patterns are reported in Figure S2 while Table S2 lists the corresponding lattice parameters.

Thermal stability of the *R*-samples has been determined by thermogravimetric analysis in the 30-750°C temperature range and by differential scanning calorimetry (DSC) in the range from -165 to 65°C. The results, reported in Figure S3, show good stability of the samples up to 300°C when the first weight loss occurs. Notably, DSC shows the absence of phase transitions in the considered temperature range, at variance with the typical 3D metal-halide perovskites showing the formation of high-temperature cubic phases.[32] The phase stability

of (*R*-3-AQ)$_2$PbBr$_4$·2Br and (*R*-3-AQ)Pb$_2$Br$_6$ has been further explored by collecting XRD patterns of thin films prepared by spin coating (see methods in Supporting Information) left at open air in the laboratory environment (*T*≈22°C, RH≈40%) as a function of time for up to 47 days, showing significant air and moisture stability, see Figure S4.

To gain insight into the electronic structure of the 3D and 2D samples we have performed Density Functional Theory (DFT) calculations, see Supporting Information for computational details. The structures were optimized starting from the crystallographic data at the scalar relativistic PBE level, followed by higher level HSE06 (α = 0.43) calculations including spin-orbit coupling (SOC). Direct band gap values of 3.46 eV for (*R/S*-3-AQ)Pb$_2$Br$_6$ and 3.82 eV for (*R/S*-3-AQ)$_2$PbBr$_4$·2Br are calculated, at Γ and M points, respectively, see Figure 2 and Table S3.[33–35]

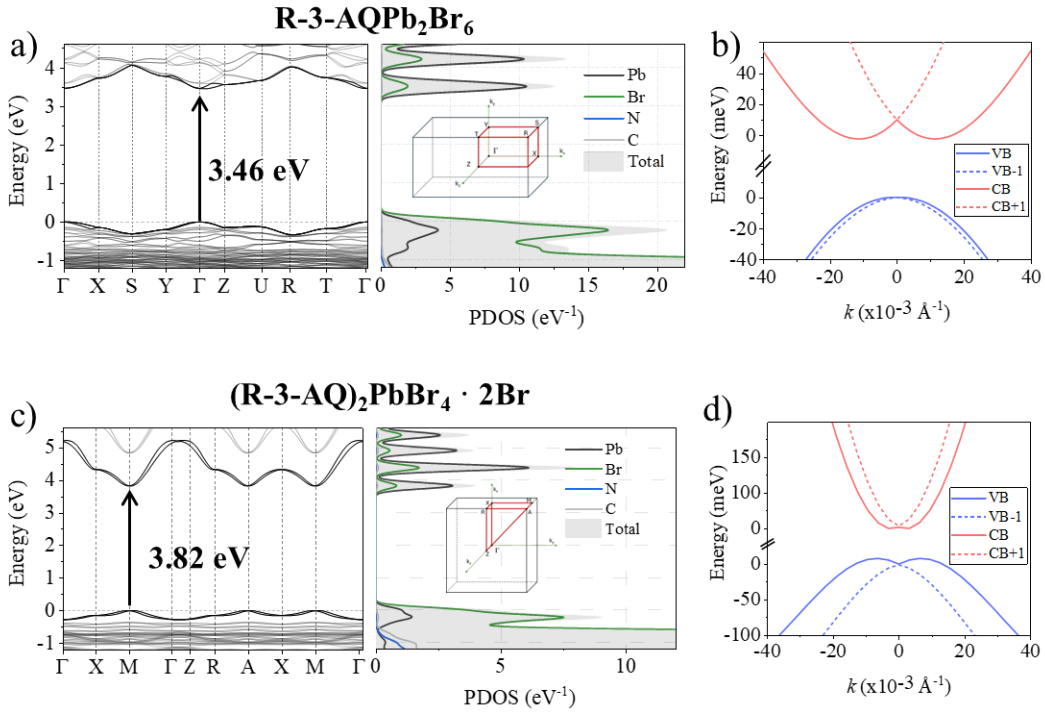

Figure 2. (a, c) Electronic band structures and projected density of states (PDOS) for the 3D and 2D materials, respectively. The PDOS was computed using the HSE06-SOC level of theory, whereas the band structures were initially obtained with PBE-SOC and subsequently corrected to align with the HSE06-SOC band gap. The insets in the PDOS panels illustrate the corresponding Brillouin zone representations. (b, d) Rashba splitting of the valence and conduction bands for the respective materials, highlighting spin-orbit coupling effects. The energy zero reference is set to the valence band maximum (VBM) and conduction band minimum (CBM) to enhance the visualization of the splitting

The projected density of states (PDOS) of the *R*-isomers, Figure 2a-c, shows that the band edges in both 3D and 2D materials are dominated by Pb and Br contributions, while the C, N and H atoms from the organic molecules contribute to states far away from the band

edges, similar to typical lead-halide perovskites.[36] The calculated band structure, Figure 2a-c, shows a direct band gap for both structural arrangements. Importantly, the 2D band structure shows a flat band dispersion along the direction perpendicular to the inorganic perovskite layers, *i.e.* Γ → Z (see Figure S11), while the (*R/S*-3-AQ)Pb_2Br_6 system has a clearly isotropic band structure, indicating that the charge carriers can be transported along the 3D octahedra network. Carrier effective masses for (*R/S*-3-AQ)Pb_2Br_6 were determined by parabolic fitting along the Γ → Y / Γ → Z in the band gap region, finding m_h* and m_e* values of 0.54/0.66 and 0.34/0.53 m_0, respectively, where m_0 is the electron mass. Effective masses along other crystallographic directions are provided in Table S4. An exciton reduced mass of 0.21/0.29 m_0 is thus estimated. It is interesting to compare calculated effective masses for (*R/S*-3-AQ)Pb_2Br_6 to those of typical 3D perovskites, *e.g.* $MAPbBr_3$.[37] Although the values obtained for our system are a factor ~1.5 times higher than those for $MAPbBr_3$ (m_h* and m_e* =0.31 and 0.27 m_0, respectively), a similar trend is observed, with electrons being more mobile than holes.

Notably, both 3D and 2D systems display a Rashba/Dresselhaus spin splitting of the electronic band structure, Figure 2b-d,[38–40] a characteristic that can be exploited in spintronic applications. The Rashba splitting parameters including the energy splitting $\varepsilon_{c/v}^{\neq}$, moment offset (Δk) and Rashba coefficient (α) are reported in Table S4-S5. For (*R/S*-3-AQ)Pb_2Br_6 a significant Rashba effect is observed in the conduction band with α = 2.22 eV Å. In contrast, the valence band shows weaker Rashba splitting indicating minimal spin-orbit interactions in this band. On the other hand, high values of α were found for the 2D (*R/S*-3-AQ)$_2PbBr_4$·2Br (7.12 and 8.19 for the valence and conduction band, respectively) in line with a higher octahedra distortion for the 2D species with respect to the 3D, see Table S1.

Structural and electronic structure calculations confirm a 3D character for the novel (*R/S*-3-AQ)Pb_2Br_6 chiral compound. The optical properties of the 3D and 2D systems have thus been measured by UV-vis and PL spectroscopy; and by circular dichroism (CD). The absorption measurements at 300 K are shown in Figure 3a-b for the four samples as Tauc plots, while Figure S5-S6 reports a comparison of room temperature data with those recorded at 77 K. We observe absorption features at 3.39 eV and 3.64 eV for (*R/S*-3-AQ)Pb_2Br_6 and for (*R/S*-3-AQ)$_2PbBr_4$·2Br, respectively, compatible with excitonic absorption. The band gap, as identified by fitting the subsequent absorption rise, is found at 3.72 and 4.05 eV for the 3D and 2D structures, respectively. Both data are in good agreement with calculated values, in particular the band gap increase moving from 3D to 2D

structures (0.33 vs. 0.36 eV). Thus, for both the excitonic peak and band gap a noticeable blue shift is observed when moving to the 2D structural arrangement, consistent with a more delocalized excited state and band dispersion in the 3D case. For the (*R/S*-3-AQ)Pb_2Br_6 the exciton binding energy, E_b, is 480 meV, consistent with the presence of a stable excitonic population at room temperature, Figure 3a. For (*R/S*-3-AQ)$_2$$PbBr_4$·2Br the exciton binding energy is 500-540 meV for the *R* and *S* enantiomers, respectively, consistent with a higher degree of confinement in the 2D arrangement.

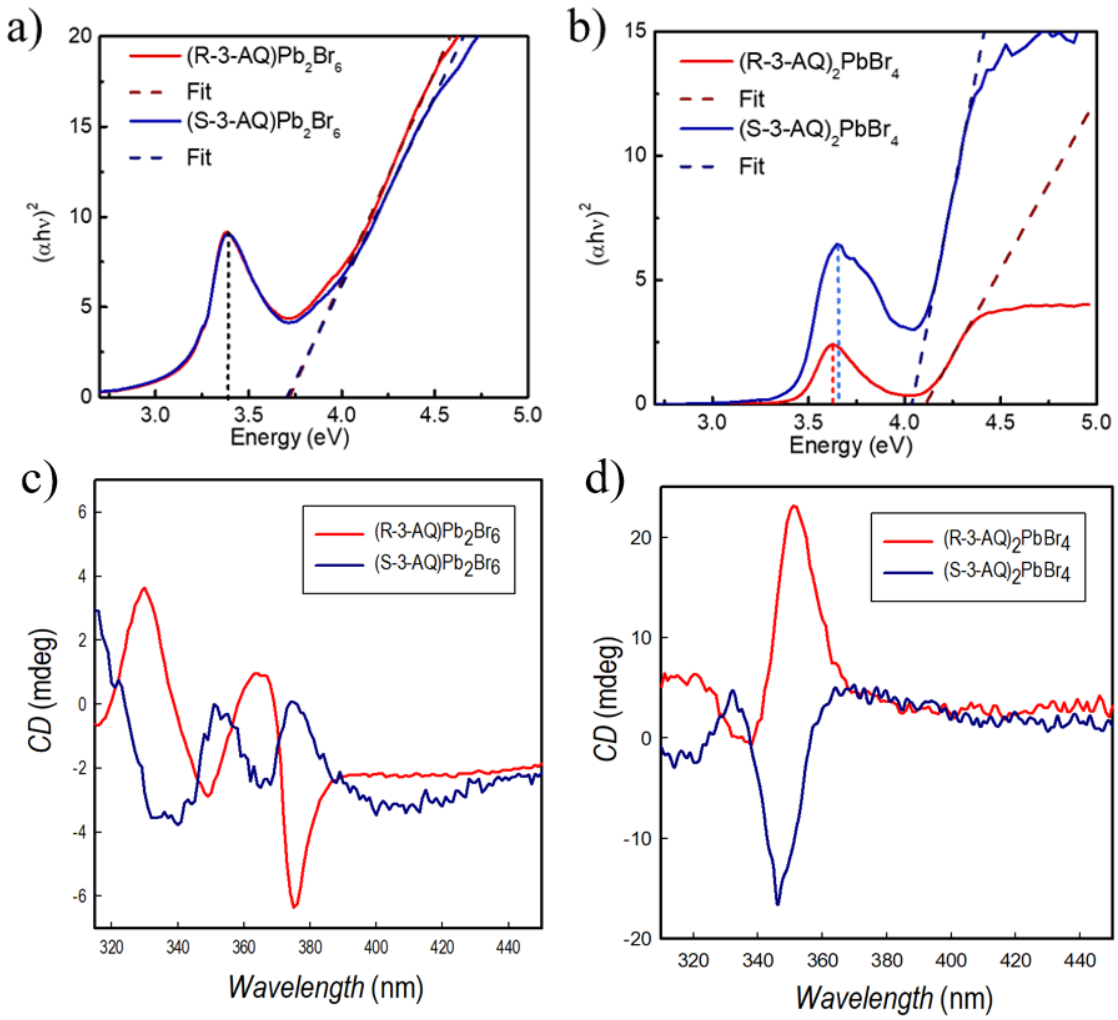

Figure 3. Tauc plot for (a) (*R*/*S*-3AQ)Pb_2Br_6 and (b) (*R/S*-3-AQ)$_2$$PbBr_4$·2Br at 300 K; CD spectra for (c) (*R*/*S*-3AQ)Pb_2Br_6 and (d) (*R/S*-3-AQ)$_2$$PbBr_4$·2Br.

The PL emission of (*R*/*S*-3AQ)Pb_2Br_6, Figure S7, is centered at 1.7 eV, with a significant Stokes shift and a bandwidth of about 500 meV. For the 2D system the photoluminescence spectra are even more broadband, peaking at about 2.3 eV, with a bandwidth up to 800

meV, consistent with the high distortion of the octahedral layers, see Figure S7 and Table S1.

Lastly, we characterized the CD response of thin films of average thickness 300 nm, see methods in Supporting Information. The XRD patterns of the thin films are shown in Figure S8 indicating a single-phase nature. Their morphology has been investigated by Atomic Force Microscopy and representative images are reported in Figure S9. The CD spectra of (*R*/*S*-3-AQ)Pb_2Br_6, Figure 3c, present distinct peaks in the range 315-400 nm, with the one centered at higher wavelength corresponding to the absorption edge. The presence of opposite sign in the CD peaks for the *R* and *S* samples confirms the chirality transfer from the ditopic 3-AQ chiral cation to the Pb-Br inorganic framework. The chiral anisotropy factor, g_{CD}, has been calculated according to the following equation:

$$g_{CD} = \frac{A_L - A_R}{2(A_L + A_R)} \qquad \text{(eq. 1)}$$

where A_L and A_R are the absorbance of the sample for left- and right-handed circularly polarized light, respectively, and resulted to be 6×10^{-5} for the of (*R*-3-AQ)Pb_2Br_6 and -9×10^{-5} for (*S*-3-AQ)Pb_2Br_6. The CD spectra for the 2D perovskites are instead shown in Figure 3d. A single peak, with opposite sign around 345-350 nm (again in line with the absorption edge, cfr. Figure S6) can be observed, with a slight blue-shift with respect to the 3D systems. g_{CD} values are 4×10^{-4} (*R*-3-AQ)$_2PbBr_4 \cdot 2Br$ and -3×10^{-4} for (*S*-3-AQ)$_2PbBr_4 \cdot 2Br$. Interestingly, the chiral anisotropy factor is one order of magnitude larger for the 2D perovskite with respect to the 3D compound. Such a result further supports the correlation between structural dimensionality and g_{CD} values. Indeed, it has been recently shown that there is a progressive reduction of roughly one order of magnitude of the anisotropy factor passing from 0D to 1D to 2D chiral systems.[15,41,42] Thus, the first chiral 3D system characterized by only corner-sharing octahedra allows to extend the correlation further confirming such a progressive reduction which seems closely related to the higher amount of chiral ligand in lower dimensional systems and the reduced lattice rigidity.[43,44] CPL measurements at 77K (Figure S10) further confirms the trend of dimensionality also on emission properties. The 2D system has a detectable CPL with g_{CPL} of about 0.2% while, on the other hand, the 3D system does not show appreciable CPL.

3. Conclusion

In summary, a new chiral metal halide semiconductor with a 3D structure, namely (*R/S*-3-AQ)Pb_2Br_6, has been synthesized by using a small and steric hindered ditopic cation, providing the first chiral halide structural network composed of corner-shared octahedra only. The calculation of the electronic band structure for (*R/S*-3-AQ)Pb_2Br_6 demonstrates an improved isotropic carrier mobility with respect to the (*R/S*-3-AQ)$_2PbBr_4$·2Br 2D system, which, on the other hand, shows a transport confined in the plane of the inorganic layers. These findings are corroborated by the photophysical properties of the semiconductor which shows a lower degree of localization of the photoexcitation, and of excitation nature, with respect to its 2D counterpart. The novel 3D system reported has a clear chiroptical response in the CD spectra which scales with the structural dimensionality and shows a sizable Rashba splitting in the conduction band.

Overall, this novel family of chiral 3D hybrid metal halides semiconductors has the potential to overcome the limitation of anisotropic transport of actual chiral systems paving the way for the development of chiroptical and spintronic devices. Moreover, the well-recognized properties tunability of hybrid metal halides through chemical alloying could be applied to (*R/S*-3-AQ)Pb_2Br_6 to further manipulate its chiroptical and transport properties thus creating a library of novel chiral 3D systems.

Acknowledgement

L.M. acknowledges support from the Ministero dell'Università e della Ricerca (MUR) and the University of Pavia through the program "Dipartimenti di Eccellenza 2023–2027. We acknowledge support from the Italian Ministry of Research under the PRIN 2022 Grant No 2022F2K7J5 with title "Two-dimensional chiral hybrid organic−inorganic perovskites for chiroptoelectronics" PE 3 funded by PNRR Mission 4 Istruzione e Ricerca - Component C2 - Investimento 1.1, Fondo per il Programma Nazionale di Ricerca e Progetti di Rilevante Interesse Nazionale PRIN 2022 - CUP B53D23004130006. G. F acknowledges financial support by the European Union's NextGenerationEU Programme with the I-PHOQS Infrastructure [IR0000016, ID D2B8D520, CUP B53C22001750006]. We acknowledge Mireille Thimon of KEP Technologies EMEA for DSC measurements. H.W. is a Marie Skłodowska-Curie Fellow (No. 101105123). LM and MM acknowledge Fondazione Cariplo through the program ‘‘Young Researchers’’, Grant No. 2023-1246.

The third-author Clarissa Coccia, author of the present Ph.D. work, carried out the synthesis of some materials and part of the optical characterization.

References

(1) Dang, Y.; Liu, X.; Cao, B.; Tao, X. Chiral Halide Perovskite Crystals for Optoelectronic Applications. *Matter* **2021**, *4* (3), 794–820.

(2) Long, G.; Sabatini, R.; Saidaminov, M. I.; Lakhwani, G.; Rasmita, A.; Liu, X.; Sargent, E. H.; Gao, W. Chiral-Perovskite Optoelectronics. *Nat Rev Mater* **2020**, *5* (6), 423–439.

(3) Malavasi, L.; Moroni, M.; Coccia, C. *Chiral Metal Halide Perovskites: Focus on Lead-Free Materials and Structure-Property Correlations*; preprint; Chemistry and Materials Science, **2023**.

(4) Min, J.; Choi, Y.; Kim, D.; Park, T. Beyond Imperfections: Exploring Defects for Breakthroughs in Perovskite Solar Cell Research. *Advanced Energy Materials* **2024**, *14* (6), 2302659.

(5) Wang, H.; Treglia, A.; Albaqami, M. D.; Gao, F.; Petrozza, A. Tin-Halide Perovskites for Near-Infrared Light-Emitting Diodes. *ACS Energy Lett.* **2024**, *9* (6), 2500–2507.

(6) Yuan, F.; Folpini, G.; Liu, T.; Singh, U.; Treglia, A.; Lim, J. W. M.; Klarbring, J.; Simak, S. I.; Abrikosov, I. A.; Sum, T. C.; Petrozza, A.; Gao, F. Bright and Stable Near-Infrared Lead-Free Perovskite Light-Emitting Diodes. *Nat. Photon.* **2024**, *18* (2), 170–176.

(7) Luo, X.; Liu, X.; Lin, X.; Wu, T.; Wang, Y.; Han, Q.; Wu, Y.; Segawa, H.; Han, L. Recent Advances of Inverted Perovskite Solar Cells. *ACS Energy Lett.* **2024**, *9* (4), 1487–1506.

(8) Xing, S.; Yuan, Y.; Zhang, G.; Zhang, S.; Lian, Y.; Tang, W.; Zhou, K.; Liu, S.; Gao, Y.; Ren, Z.; Zhang, G.; Sun, T.; Zhao, B.; Di, D. Energy-Efficient Perovskite LEDs with Rec. 2020 Compliance. *ACS Energy Lett.* **2024**, *9* (8), 3643–3651.

(9) Chen, C.; Gao, L.; Gao, W.; Ge, C.; Du, X.; Li, Z.; Yang, Y.; Niu, G.; Tang, J. Circularly Polarized Light Detection Using Chiral Hybrid Perovskite. *Nat Commun* **2019**, *10* (1), 1927.

(10) Lee, C. U.; Lee, H.; Jeong, C.-S.; Ma, S.; Jang, G.; Park, Y. S.; Yun, J.; Lee, J.; Son, J.; Jeong, W.; Yang, S.; Park, J. H.; Woo, K.; Moon, J. Enhanced Stability of Spin-

Dependent Chiral 2D Perovskite Embedded PV-Biased Anode via Cross-Linking Strategy. *ACS Energy Lett.* **2024**, *9* (8), 4032–4043.

(11) Chen, D.; Tang, B.; Sergeev, A. A.; Wu, Y.; Liu, H.; Zhu, D.; Hu, S.; Wong, K. S.; Yip, H.-L.; Rogach, A. L. Green Spin Light-Emitting Diodes Enabled by Perovskite Nanocrystals *in Situ* Modified with Chiral Ligands. *ACS Energy Lett.* **2025**, *10* (2), 815–821.

(12) Ma, S.; Ahn, J.; Moon, J. Chiral Perovskites for Next-Generation Photonics: From Chirality Transfer to Chiroptical Activity. *Advanced Materials* **2021**, *33* (47), 2005760.

(13) Billing, D. G.; Lemmerer, A. Bis[(*S*)-β-Phenethylammonium] Tribromoplumbate(II). *Acta Crystallogr E Struct Rep Online* **2003**, *59* (6), m381–m383.

(14) Billing, D. G.; Lemmerer, A. Synthesis, Characterization and Phase Transitions in the Inorganic–Organic Layered Perovskite-Type Hybrids [$(C_nH_{2n+1}NH_3)_2PbI_4$], *n* = 4, 5 and 6. *Acta Crystallogr B Struct Sci* **2007**, *63* (5), 735–747.

(15) Coccia, C.; Morana, M.; Mahata, A.; Kaiser, W.; Moroni, M.; Albini, B.; Galinetto, P.; Folpini, G.; Milanese, C.; Porta, A.; Mosconi, E.; Petrozza, A.; De Angelis, F.; Malavasi, L. Ligand-Induced Chirality in ClMBA$_2$SnI$_4$ 2D Perovskite**. *Angew Chem Int Ed* **2024**, e202318557.

(16) Wang, H.; Li, J.; Lu, H.; Gull, S.; Shao, T.; Zhang, Y.; He, T.; Chen, Y.; He, T.; Long, G. Chiral Hybrid Germanium(II) Halide with Strong Nonlinear Chiroptical Properties. *Angew Chem Int Ed* **2023**, *62* (41), e202309600.

(17) Asensio, Y.; Bahmani Jalali, H.; Marras, S.; Gobbi, M.; Casanova, F.; Mateo-Alonso, A.; Di Stasio, F.; Rivilla, I.; Hueso, L. E.; Martín-García, B. Circularly Polarized Photoluminescence in Chiral Hybrid Organic–Inorganic Manganese Halide Perovskites: From Bulk Materials to Exfoliated Flakes. *Advanced Optical Materials* **2024**, 2400554.

(18) Dibenedetto, A.; Coccia, C.; Boiocchi, M.; Moroni, M.; Milanese, C.; Malavasi, L. Synthesis and Characterization of Cu-Containing Chiral Metal Halides and Role of Halogenation of the Organic Ligand. *J. Phys. Chem. C* **2024**, acs.jpcc.4c00150.

(19) Hao, J.; Lu, H.; Mao, L.; Chen, X.; Beard, M. C.; Blackburn, J. L. Direct Detection of Circularly Polarized Light Using Chiral Copper Chloride–Carbon Nanotube Heterostructures. *ACS Nano* **2021**, *15* (4), 7608–7617.

(20) Peng, H.; Liu, Q.; Lu, Y.-Z.; Yang, S.-J.; Qi, J.-C.; Chen, X.-G.; Liao, W.-Q. A Chiral Two-Dimensional Perovskite-like Lead-Free Bismuth(III) Iodide Hybrid with High Phase Transition Temperature. *Chem. Commun.* **2023**, *59* (68), 10295–10298.

(21) Wu, P.; Pietropaolo, A.; Fortino, M.; Bando, M.; Maeda, K.; Nishimura, T.; Shimoda, S.; Sato, H.; Naga, N.; Nakano, T. Amplified Chirality Transfer to Aromatic Molecules through Non-specific Inclusion by Amorphous, Hyperbranched Poly(Fluorenevinylene) Derivatives. *Angew Chem Int Ed* **2023**, *62* (29),

(22) Moroni, M.; Coccia, C.; Malavasi, L. Chiral 2D and Quasi-2D Hybrid Organic Inorganic Perovskites: From Fundamentals to Applications. *Chem. Commun.* **2024**,

(23) Long, G.; Jiang, C.; Sabatini, R.; Yang, Z.; Wei, M.; Quan, L. N.; Liang, Q.; Rasmita, A.; Askerka, M.; Walters, G.; Gong, X.; Xing, J.; Wen, X.; Quintero-Bermudez, R.; Yuan, H.; Xing, G.; Wang, X. R.; Song, D.; Voznyy, O.; Zhang, M.; Hoogland, S.; Gao, W.; Xiong, Q.; Sargent, E. H. Spin Control in Reduced-Dimensional Chiral Perovskites. *Nature Photon* **2018**, *12* (9), 528–533.

(24) Ma, J.; Fang, C.; Chen, C.; Jin, L.; Wang, J.; Wang, S.; Tang, J.; Li, D. Chiral 2D Perovskites with a High Degree of Circularly Polarized Photoluminescence. *ACS Nano* **2019**, *13* (3), 3659–3665.

(25) Li, Z.; Hong, E.; Zhang, X.; Deng, M.; Fang, X. Perovskite-Type 2D Materials for High-Performance Photodetectors. *J. Phys. Chem. Lett.* **2022**, *13* (5), 1215–1225.

(26) Saparov, B.; Mitzi, D. B. Organic–Inorganic Perovskites: Structural Versatility for Functional Materials Design. *Chem. Rev.* **2016**, *116* (7), 4558–4596.

(27) Mao, L.; Stoumpos, C. C.; Kanatzidis, M. G. Two-Dimensional Hybrid Halide Perovskites: Principles and Promises. *J. Am. Chem. Soc.* **2019**, *141* (3), 1171–1190.

(28) Chen, G.; Liu, X.; An, J.; Wang, S.; Zhao, X.; Gu, Z.; Yuan, C.; Xu, X.; Bao, J.; Hu, H.-S.; Li, J.; Wang, X. Nucleation-Mediated Growth of Chiral 3D Organic–Inorganic Perovskite Single Crystals. *Nat. Chem.* **2023**, *15* (11), 1581–1590.

(29) Lesne, E.; Fu, Y.; Oyarzun, S.; Rojas-Sánchez, J. C.; Vaz, D. C.; Naganuma, H.; Sicoli, G.; Attané, J.-P.; Jamet, M.; Jacquet, E.; George, J.-M.; Barthélémy, A.; Jaffrès, H.; Fert, A.; Bibes, M.; Vila, L. Highly Efficient and Tunable Spin-to-Charge Conversion through Rashba Coupling at Oxide Interfaces. *Nature Mater* **2016**, *15* (12), 1261–1266.

(30) Liang, A.; Gonzalez-Platas, J.; Turnbull, R.; Popescu, C.; Fernandez-Guillen, I.; Abargues, R.; Boix, P. P.; Shi, L.-T.; Errandonea, D. Reassigning the Pressure-Induced Phase Transitions of Methylammonium Lead Bromide Perovskite. *J. Am. Chem. Soc.* **2022**, *144* (43), 20099–20108.

(31) Robinson, K.; Gibbs, G. V.; Ribbe, P. H. Quadratic Elongation: A Quantitative Measure of Distortion in Coordination Polyhedra. *Science* **1971**, *172* (3983), 567–570.

(32) Poglitsch, A.; Weber, D. Dynamic Disorder in Methylammoniumtrihalogenoplumbates (II) Observed by Millimeter-Wave Spectroscopy. *The Journal of Chemical Physics* **1987**, *87* (11), 6373–6378.

(33) Gregori, L.; Meggiolaro, D.; De Angelis, F. Quantifying the Effect of Interfacial Dipoles on the Energy Level Alignment of Metal-Halide Perovskites. *ACS Energy Lett.* **2024**, *9* (11), 5329–5333.

(34) Marchal, N.; Mosconi, E.; García-Espejo, G.; Almutairi, T. M.; Quarti, C.; Beljonne, D.; De Angelis, F. Cation Engineering for Resonant Energy Level Alignment in Two-Dimensional Lead Halide Perovskites. *J. Phys. Chem. Lett.* **2021**, *12* (10), 2528–2535

(35) Meggiolaro, D.; Mosconi, E.; Proppe, A. H.; Quintero-Bermudez, R.; Kelley, S. O.; Sargent, E. H.; De Angelis, F. Energy Level Tuning at the $MAPbI_3$ Perovskite/Contact Interface Using Chemical Treatment. *ACS Energy Lett.* **2019**, *4* (9), 2181–2184.

(36) Umari, P.; Mosconi, E.; De Angelis, F. Relativistic GW Calculations on CH3NH3PbI3 and CH3NH3SnI3 Perovskites for Solar Cell Applications. *Sci Rep* **2014**, *4* (1), 4467.

(37) Mosconi, E.; Umari, P.; De Angelis, F. Electronic and Optical Properties of $MAPbX_3$ Perovskites (X = I, Br, Cl): A Unified DFT and GW Theoretical Analysis. *Phys. Chem. Chem. Phys.* **2016**, *18* (39), 27158–27164.

(38) Mosconi, E.; Etienne, T.; De Angelis, F. Rashba Band Splitting in Organohalide Lead Perovskites: Bulk and Surface Effects. *J. Phys. Chem. Lett.* **2017**, *8* (10), 2247–2252.

(39) Etienne, T.; Mosconi, E.; De Angelis, F. Dynamical Origin of the Rashba Effect in Organohalide Lead Perovskites: A Key to Suppressed Carrier Recombination in Perovskite Solar Cells? *J. Phys. Chem. Lett.* **2016**, *7* (9), 1638–1645.

(40) Jana, M. K.; Song, R.; Liu, H.; Khanal, D. R.; Janke, S. M.; Zhao, R.; Liu, C.; Valy Vardeny, Z.; Blum, V.; Mitzi, D. B. Organic-to-Inorganic Structural Chirality Transfer in a 2D Hybrid Perovskite and Impact on Rashba-Dresselhaus Spin-Orbit Coupling. *Nat Commun* **2020**, *11* (1), 4699.

(41) Coccia, C.; Moroni, M.; Treglia, A.; Boiocchi, M.; Yang, Y.; Milanese, C.; Morana, M.; Capsoni, D.; Porta, A.; Petrozza, A.; Stroppa, A.; Malavasi, L. Unraveling the Role of Structural Topology on Chirality Transfer and Chiroptical Properties in Chiral Germanium Iodides. *J. Am. Chem. Soc.* **2024**, *146* (35), 24377–24388.

(42) Moroni, M.; Coccia, C.; Malavasi, L. Chiral 2D and Quasi-2D Hybrid Organic Inorganic Perovskites: From Fundamentals to Applications. *Chem. Commun.* **2024**, *60* (70), 9310–9327.

(43) Das, R.; Hossain, M.; Mahata, A.; Swain, D.; De Angelis, F.; Santra, P. K.; Sarma, D. D. Unique Chiro-Optical Properties of the Weakly-2D (R-/S-MBA) $_2$ CuBr $_4$ Hybrid Material. *ACS Materials Lett.* **2023**, 1556–1564.

(44) Zhang, Z.; Wang, Z.; Sung, H. H.-Y.; Williams, I. D.; Yu, Z.-G.; Lu, H. Revealing the Intrinsic Chiroptical Activity in Chiral Metal-Halide Semiconductors. *J. Am. Chem. Soc.* **2022**, *144* (48), 22242–22250.

SUPPLEMENTARY INFORMATION

3D Chiral Metal Halide Semiconductors

Marco Moroni,[a] Luca Gregori,[b,i] Clarissa Coccia,[a] Massimo Boiocchi,[c] Marta Morana,[d] Doretta Capsoni,[a] Andrea Olivati,[e,f] Antonella Treglia,[e] Giulia Folpini,[e,g] Maddalena Patrini,[h] Isabel Pinto Goncalves,[e] Heyong Wang,[e] Chiara Milanese,[a] Annamaria Petrozza,[e] Edoardo Mosconi,[i,*] Filippo De Angelis,[b,i,l] and Lorenzo Malavasi,[a,*]

[a] University of Pavia, Department of Chemistry and INSTM, Via Taramelli 16, 27100, Pavia, Italy.

[b] University of Perugia, Department of Chemistry, Biology and Biotechnology, Via Elce di Sotto 8, 06123, Perugia, Italy.

[c] University of Pavia, Centro Grandi Strumenti, Via Bassi 21, 27100, Pavia, Italy.

[d] Dipartimento di Scienze della Terra, Università di Firenze, Via La Pira 4, 50121 Florence, Italy

[e] Center for Nano Science and Technology@PoliMi, Istituto Italiano di Tecnologia 20134 Milan, Italy.

[f] Physics Department, Politecnico di Milano, Piazza L. da Vinci, 32, 20133 Milano, Italy.

[g] Istituto di Fotonica e Nanotecnologie, CNR-IFN, 20133 Milan, Italy.

[h] University of Pavia, Department of Physics, Via Bassi 6, 27100, Pavia, Italy.

[i] Computational Laboratory for Hybrid/Organic Photovoltaics (CLHYO), Istituto CNR di Scienze e Tecnologie Chimiche “Giulio Natta” (CNR-SCITEC), Via Elce di Sotto 8, 06123 Perugia, Italy

[l] SKKU Institute of Energy Science and Technology (SIEST), Sungkyunkwan University, Suwon 440-746, South Korea

Corresponding Authors

Lorenzo Malavasi, email: lorenzo.malavasi@unipv.it

Edoardo Mosconi, email: edoardo@thch.unipg.it

Table S1. Octahedral distortion parameters and bond lengths for (R/S-3-AQ)Pb_2Br_6 and (R/S-3-AQ)$_2PbBr_4 \cdot 2Br$.

Compound	Polyhedron	Distortion Index (x10^3)	Bond angle variance (deg^2)	Quadratic elongation	Bond lengths (Å)	M-X-M (deg)
(*R*-3AQ)Pb_2Br_6	$Pb1Br_6$	19.4	42.7683	1.0127	2.9309(11) 2.9568(11) 2.9678(13) 3.0545(12) 3.0618(13) 3.0901(11)	120.10(4) 130.98(4) 132.00(4) 136.24(4) 136.52(4) 146.50(4)
	$Pb2Br_6$	18.9	51.9884	1.0158	2.9349(13) 2.9485(13) 2.9694(10) 3.0298(10) 3.0703(14) 3.0933(13)	
(*S*-3AQ)Pb_2Br_6	$Pb1Br_6$	19.9	50.2638	1.0150	2.939(10) 2.95(2) 3.00(3) 3.085(17) 3.085(16) 3.086(10)	118.0(5) 129.2(5) 130.0(5) 136.0(4) 137.2(7) 143.1(7)
	$Pb2Br_6$	14.0	65.4779	1.0201	2.950(19) 2.991(15) 3.02(3) 3.03(3) 3.05(3) 3.139(16)	
[(*R*-3AQ)$_2PbBr_4$]·2Br		129.0	40.6743	1.0350	2.7824(8) 3.0003(12) 3.8207(8)	170.84(4)
[(*S*-3AQ)$_2PbBr_4$]·2Br		128.8	40.7754	1.0349	2.7827(8) 3.0024(12) 3.8206(8)	170.79(4)

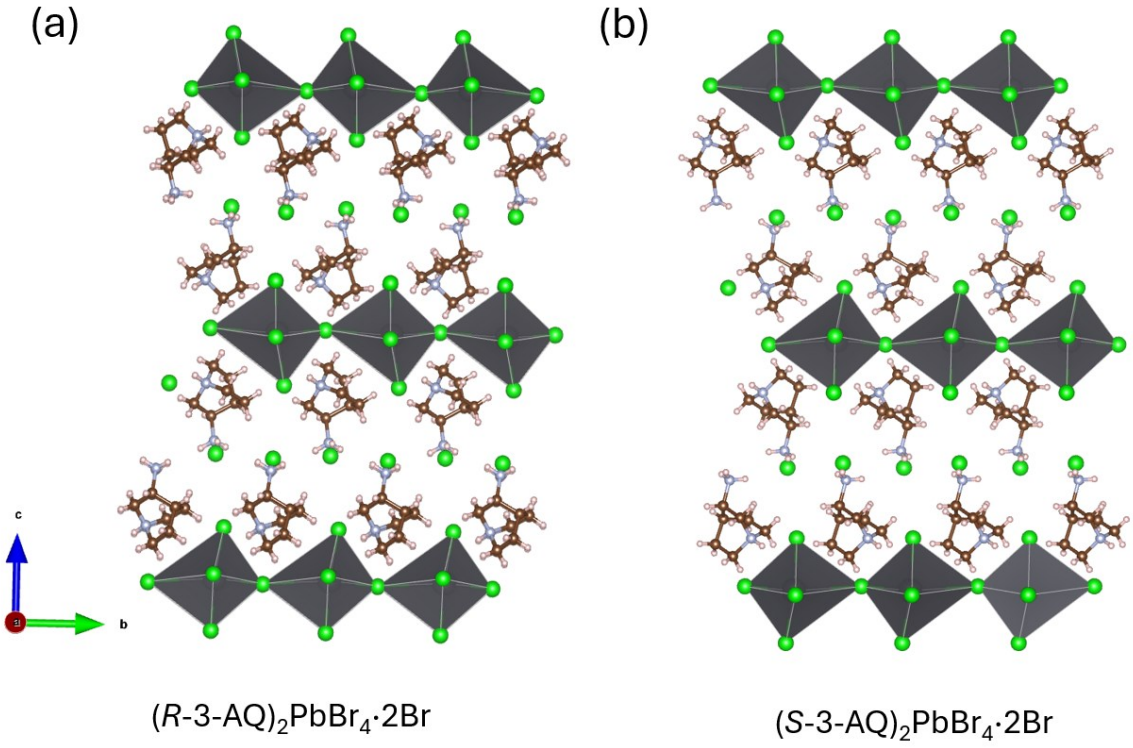

Figure S1. (a-b) Sketches of the crystal structures of (*R/S*-3-AQ)$_2$PbBr$_4$·2Br along the *c*-axis; green spheres represent Br ions.

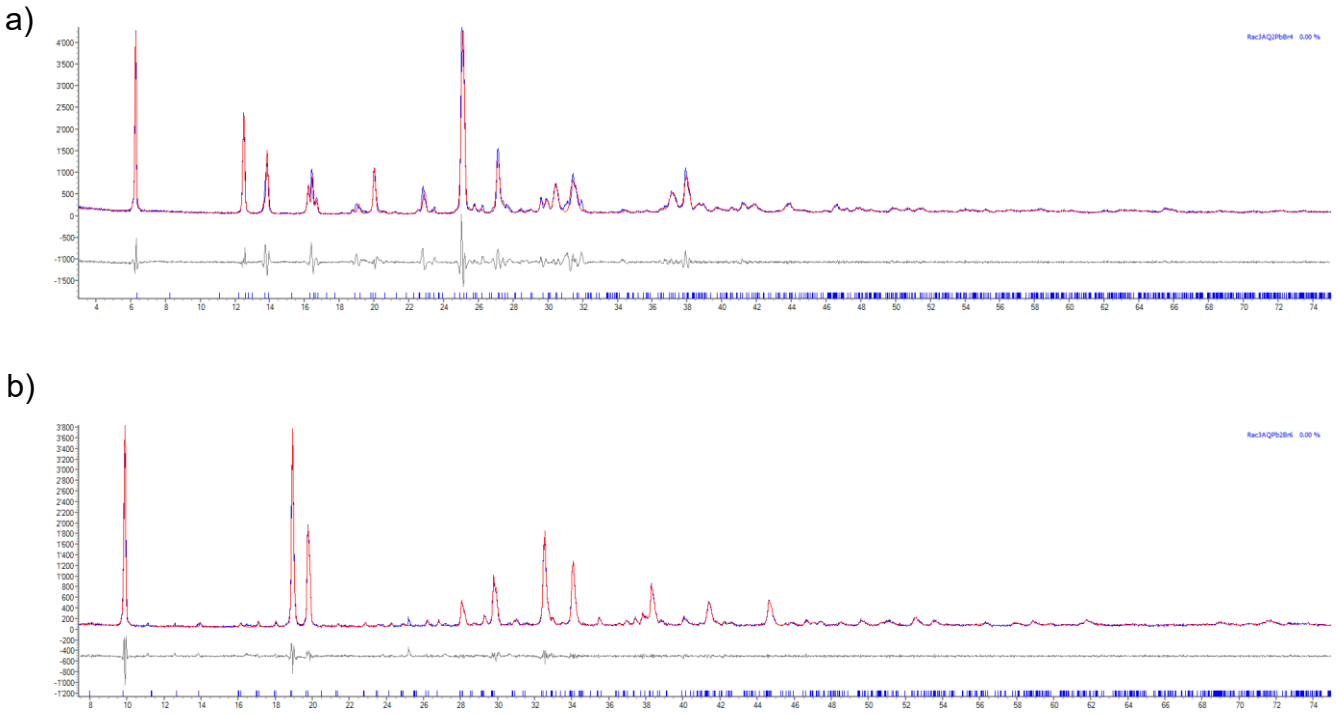

Figure S2. Whole powder pattern Le Bail refinement of (a) (*rac*-3-AQ)$_2$PbBr$_4$·2Br and (b) (*rac*-3-AQ)Pb$_2$Br$_6$ PXRD patterns in terms of experimental, calculated and difference traces (blue, red and grey, respectively). The green ticks indicate the positions of the Bragg reflections.

Table S2. Crystal structure data for (*rac*-3AQ)$_2$PbBr$_4$·2Br and (*rac*-3AQ)Pb$_2$Br$_6$

.

	(*rac*-3AQ)$_2$PbBr$_4$·2Br	**(*rac*-3AQ)Pb$_2$Br$_6$**
Empirical formula	$C_{14}H_{32}N_4Br_6Pb$	$C_7H_{16}N_2Br_6Pb_2$
Crystal system	Monoclinic	Orthorhombic
Space group	*C*2	*Pmma*
Lattice parameters (Å)	*a* = 27.717(3)	*a* = 10.9730(5)
	b = 11.6081(8)	*b* = 15.6188(6)
	c = 7.9741(6)	*c* = 11.0562(4)
β Angle (°)	92.163(6)	-
Lattice Volume (Å^3)	2463.163(6)	1894.9(1)

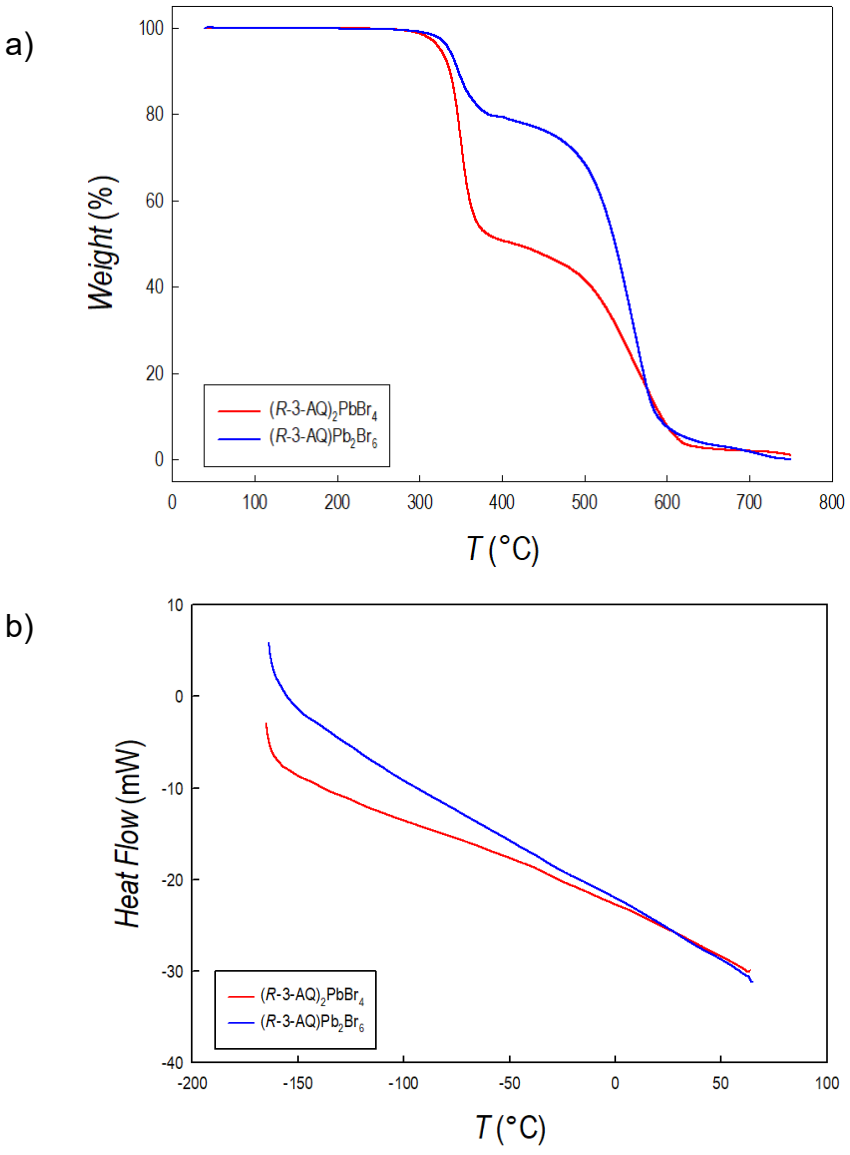

Figure S3. a) TGA curves for (*R*-3-AQ)$_2$PbBr$_4$·2Br (red line) and (*R*-3-AQ)Pb$_2$Br$_6$ (blue line); b) DSC curves for the same compounds.

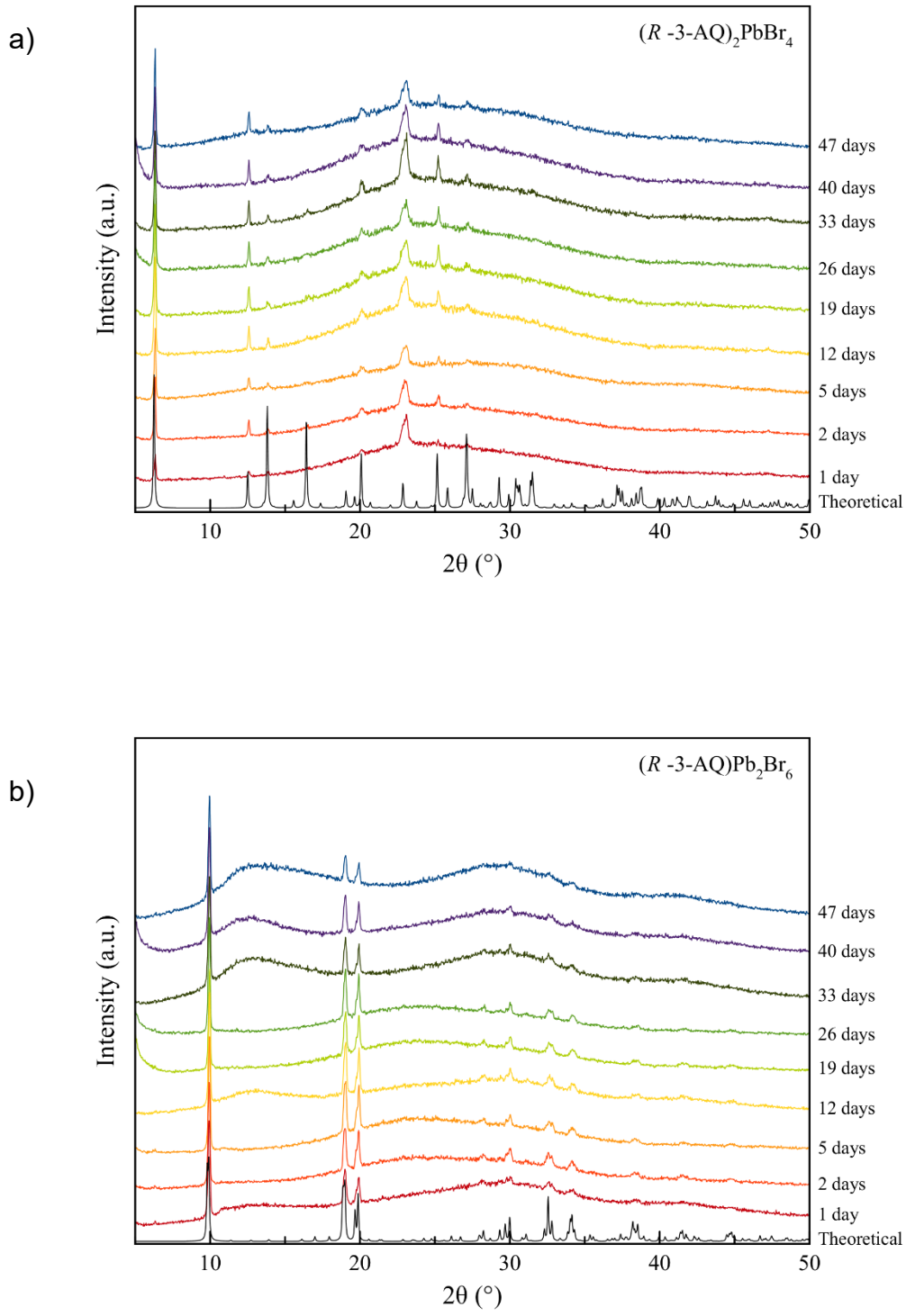

Figure S4. XRD patterns of a) (*R*-3-AQ)$_2$PbBr$_4$·2Br and (b) (*R*-3-AQ)Pb$_2$Br$_6$ as a function of time. Samples were left in the open air in the laboratory environment (*T*=22°C, RH=40%).

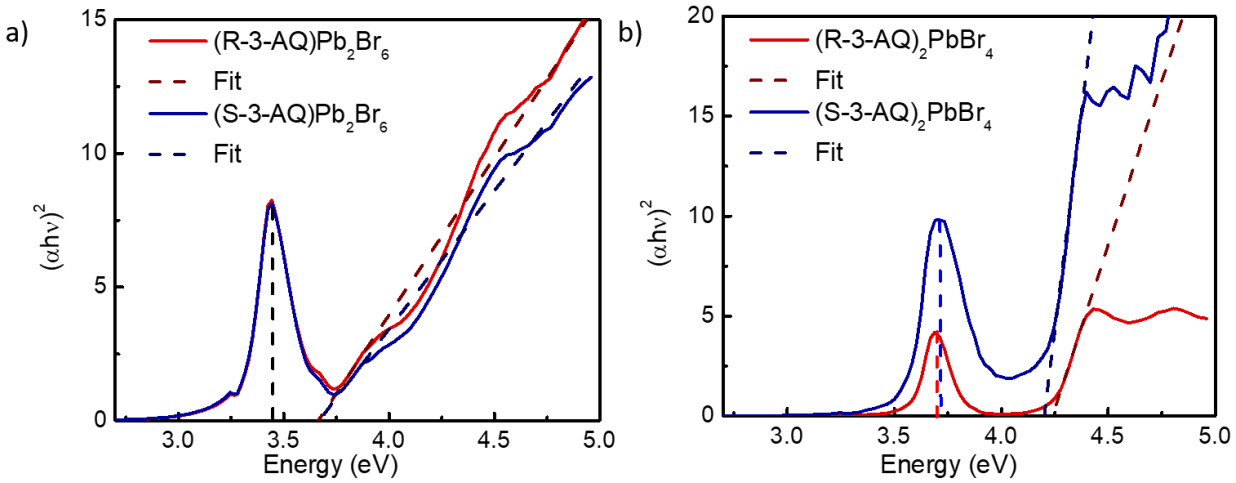

Figure S5. Tauc plot for (a) (*R*/*S*-3AQ)Pb_2Br_6 and (b) (*R*/*S*-3-AQ)$_2PbBr_4$·2Br at 77 K.

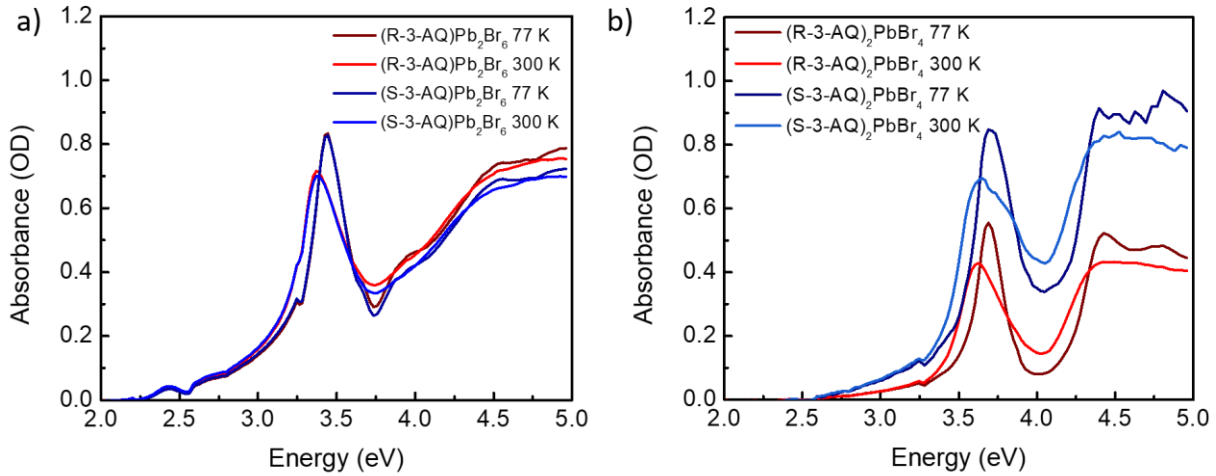

Figure S7. Photoluminescence spectra of, respectively, (*R*/*S*-3AQ)Pb_2Br_6 and (*R*/*S*-3-AQ)$_2PbBr_4$·2Br acquired at 300 K. In the inset, the room temperature PL lifetimes are shown.

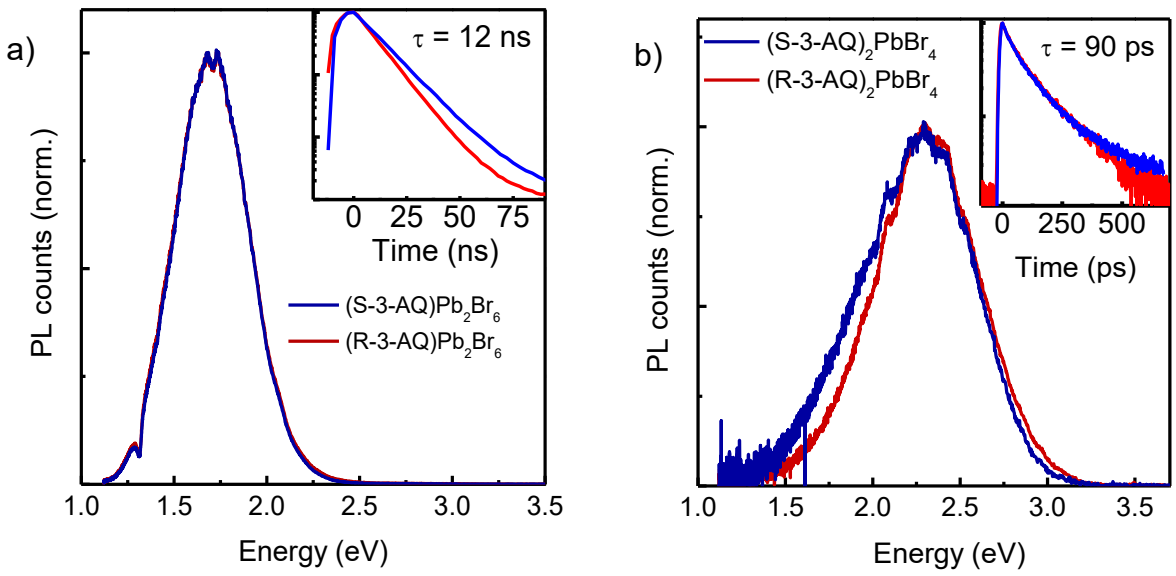

Figure S7. Photoluminescence spectra of, respectively, (*R*/*S*-3AQ)Pb_2Br_6 and (*R*/*S*-3-AQ)$_2PbBr_4$·2Br acquired at 300 K. In the inset, the room temperature PL lifetimes are shown.

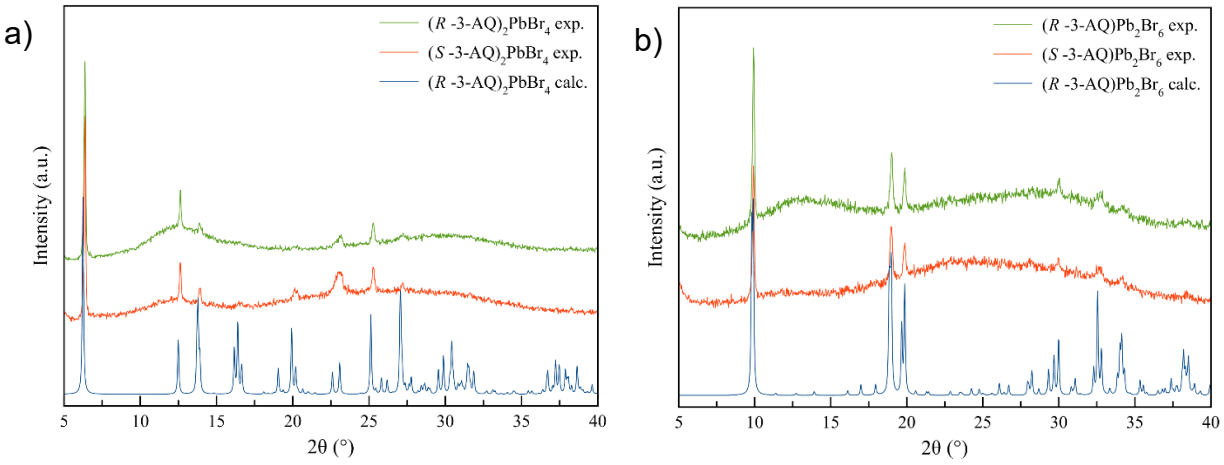

Figure S8. (a) XRD pattern of thin films of (a) (*R*/*S*-3-AQ)$_2PbBr_4$·2Br and (b) of (*R*/*S*-3-AQ)Pb_2Br_6 compared to the calculated pattern from single crystal data (blue pattern at the bottom).

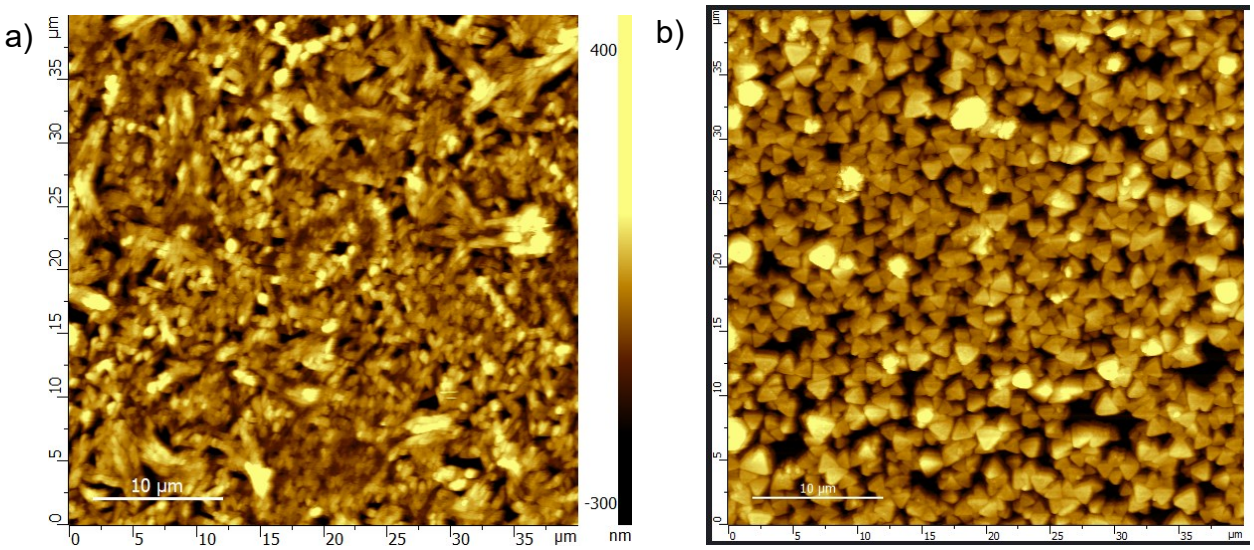

Figure S9. Representative AFM images of (a) (R-3-AQ)Pb_2Br_6 and (b) of (R-3-AQ)$_2PbBr_4$·2Br thin films

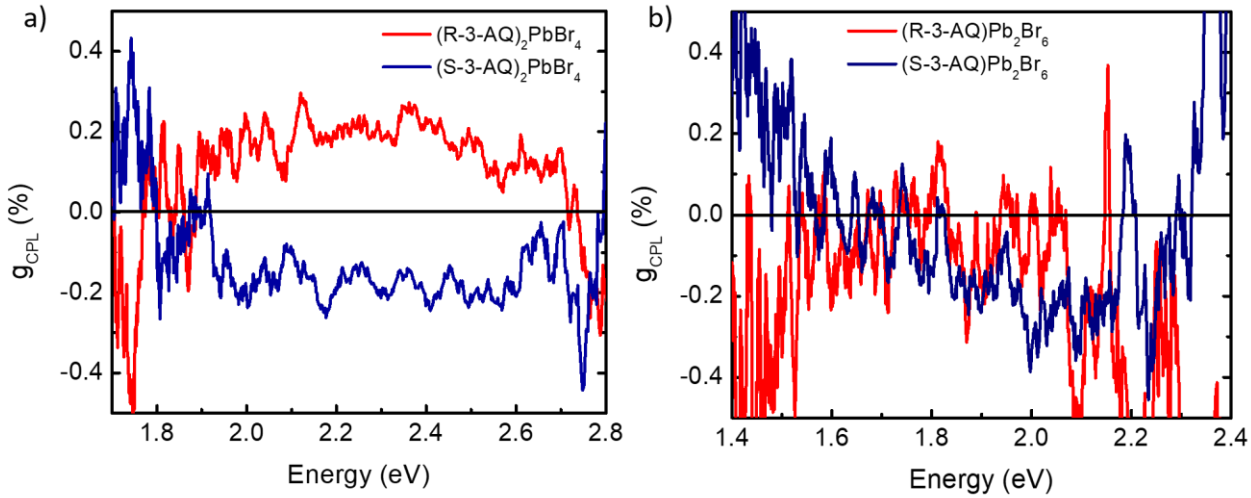

Figure S10. (a) CPL spectra of (a) (*R/S*-3-AQ)$_2PbBr_4$·2Br and (b) (*R/S*-3-AQ)Pb_2Br_6 at 77 K.

Experimental

Synthesis of (R/S-3AQ)Pb_2Br_6 and (R/S-3-AQ)$_2PbBr_4$·2Br.

To prepare (*R*/*S*-3AQ)Pb_2Br_6 and (*R/S*-3-AQ)$_2PbBr_4$·2Br, $PbOAc_2$ (Sigma-Aldrich 99.9%) was first dissolved in a large excess of 48% w/w aqueous HBr (Sigma-Aldrich) equivalent to 2 mL and the mixture was heated to 90°C. After the dissolution of the solid, the dihydrochloride salt of *R/S*-3-AQ (ApolloScientific, 97%, ee 98%) was added, with a diamine to metal molar ratio of 1:4 for (*R*/*S*-3AQ)Pb_2Br_6 and of 2:1 for (*R/S*-3-AQ)$_2PbBr_4$·2Br. To obtain the formation of single crystals the solution has been cooled down to room temperature at 1°C h^{-1}, then it was washed with anhydrous diethyl ether (Sigma-Aldrich 99.7%) and dried in vacuum at 65°C for 3 hours.

Thin films preparation. First, the glass substrates were washed using water, isopropanol and acetone in a sonicator for 20 min each and treated with oxygen plasma for 15 minutes. Then, the starting materials, prepared as indicated above, were dissolved in DMSO to obtain a 0.16 M final solution, and the thin films were prepared by spin coating method with the following program: 10 s, 150 rpm; 20 s, 350 rpm; 30 s, 1850 rpm. The films were annealed at 160°C for 2 min on a hot plate. Thin film thickness was determined by mechanical profilometer and resulted to be around 300 nm.

Single Crystal X-ray Diffraction. Measurements on selected crystal were collected on Rigaku XtaLab SuperNova (Rigaku Europe SE, Neu-Isenburg, Germany) four-circle diffractometer equipped by a microfocus X-ray source (λ = 0.7107 Å) and a Dectris Pilatus 200K hybrid pixel array detector (DECTRIS AG, Baden-Daettwil, Switzerland). Data collection, data reduction and accurate measurements of the unit cell parameters were performed by means of the CrysAlisPro software suite, ver. 1.171.41.[1] Absorption effects were empirically evaluated based on a multi-scan approach using spherical ha<monics by the SCALE3 ABSPACK scaling algorithm implemented in the CrysAlisPro crystallographic suite. Crystal structures were solved by direct methods (SIR 97) and refined by full-matrix least-square procedures on F^2 using all reflections (SHELXL 2018/3).[2,3]

Powder X-ray Diffraction. Powder X-ray diffraction (PXRD) data were acquired employing a Bruker D8 Advance θ:θ diffractometer and a Si zero-background sample-holder, in the 2θ range 3.0-105.0°, with steps of 0.02° and a time *per* step of 10 s and treated taking

advantage of the TOPAS-6 software. Suitable unit cell parameters were retrieved upon indexing the PXRD pattern through the Singular Value Decomposition algorithm[4], then performing a whole powder pattern refinement with the Le Bail method[5]. The structure of (*S*-3AQ)Pb_2Br_6 was refined with the Rietveld method[6], generating the enantiomer by taking advantage of the atomic coordinates of (*R*-3AQ)Pb_2Br_6, solved by SC-XRD, and refining the atomic coordinates of the Pb and Br atoms. The background was described by means of a Chebyshev type polynomial function, and the instrumental contribution to the peak profile through the Fundamental Parameters Approach[7].

Atomic force microscopy (AFM). images were obtained with a SmartSPM microscope (Horiba Scientific) on the spin-coated thin films. Topographic imaging was performed in tapping mode with MikroMash NSC14 tips, with an amplitude of 120-140 nm and scan rate ranging from 1 to 0.5Hz.

UV-Vis spectroscopy. DRS spectra were acquired in the wavelength range 300- 800 nm directly on the powders by using a Jasco V-750 spectrophotometer, equipped with an integrating sphere (Jasco ISV-922).

Circular Dichroism. CD spectra were acquired in the wavelength range 350- 800 nm on thin films by using a Jasco J-1500 CD spectrophotometer. The g_{CD} value for both samples has been calculated after normalizing the absorptions using the following formula:

$$g_{cd} = \frac{\Delta A}{A}$$

where ΔA is the value obtained by dividing the mdeg by the constant (~32000) and A represents the absorption difference, calculated as:

$$A_L - A_R /_2$$

where A_L and A_R are the left and right absorptions.

The effect of Linear Dichroism (LD) was eliminated by performing measurements on the thin films tilted by 90° and then rotated by 180°.

Low Temperature absorbance: The materials' absorbance at 77 K was measured in a spectrophotometer on thin films drop casted on fused silica substrates. The samples were mounted in a Linkam stage cryostat and cooled to 77 K with liquid nitrogen in vacuum condition. The excitonic energy level was identified as the central peak of a Gaussian feature, while the band gap energy was identified with a tauc fit.

Photoluminescence. Temperature-dependent photoluminescence was measured from bulk crystals under vacuum using a Linkam Stage cooled with liquid nitrogen. The sample was excited with CW laser (375 nm - TOPTICA) linearly polarized. PL was detected using a Maya2000 visible spectrometer. CD PL was acquired using with a quarter-wave plate set to ±45° relative to a linear polarizer. The samples were excited at a fluence of 100 mW/cm^2.
Time-resolved photoluminescence. For measurements with ns resolution, the 3d material was excited with the third harmonic (355 nm) from a Nd:YAG Picolo-AOT laser (pulse length of approximately 900 ps, 1 kHz repetition rate). An Andor spectrometer paired with an iStar iCCD is used for the detection. The camera acquisition is synchronized with the 1 kHz trigger signal from the laser. We track the photoemission dynamics by gating the camera's acquisition over a temporal window of 50 ns collected at increasing delay from the trigger reference (50 ns steps). The overall time resolution of the system is 2-4 ns. Kinetics are obtained by integrating the whole PL spectrum recorded at each delay. The samples were excited at a fluence of 100 mW/cm^2.
On the other hand to measure the shorter lifetime of the 2D material a shorter temporal resolution was required: we employed a Hamamatsu streak camera in Synchroscan mode, with a temporal resolution of 10 ps in the relevant measurement window (800 ps in total). The sample was excited at 350 nm using the second harmonic of a tunable Ti:Sapphire oscillator (Coherent Chameleon, 78 MHz, 150 ps).

Computational Details

Density functional theory (DFT) calculations were performed using the Quantum Espresso software package.[8] Structural optimizations for both two-dimensional (2D) and three-dimensional (3D) models were initiated from experimental CIF data. To account for van der Waals interactions, the Perdew–Burke–Ernzerhof (PBE) functional was employed with DFT-D3 dispersion corrections.[9] Norm-conserving pseudopotentials were used for all structural optimizations, and electronic shells for Br (5s, 5p), N and C (2s, 2p), H (1s), and Pb (6s, 6p, 5d) were explicitly included.[10] The wavefunction cutoff and charge density cutoff were set at 60 Ry and 240 Ry, respectively. The Brillouin zone was sampled using a 2×2×2 k-point grid centered at the Gamma point for the 3D system and a 4×4×1 grid for the 2D system. Following structural relaxation, spin-orbit coupling (SOC) was introduced to accurately capture Rashba-type spin splitting, particularly significant for lead-containing systems. To refine electronic structure predictions and enhance the accuracy of band gap estimations,

hybrid exchange-correlation functionals with varying fractions of exact exchange were subsequently applied. These results, presented in Table S2, highlight the impact of SOC and hybrid functional parameters on the electronic properties of both 2D and 3D configurations.

Table S3: Calculated band gap at different level of theory for the (*R*-3-AQ)Pb_2Br_6 and (*R*-3-AQ)$_2PbBr_4$·2Br.

	(*R*-3-AQ)Pb_2Br_6	(*R*-3-AQ)$_2PbBr_4$·2Br
PBE	2.81	3.01
PBE-SOC	2.06	2.38
HSE06-SOC α= 0.43	3.46	3.82
HSE06-SOC α= 0.25	2.84	3.19

Table S4: Calculated effective masses for different directions for the (*R*-3-AQ)Pb_2Br_6 compound at the PBE-D3 + SOC level of theory along with the Rashba data.

	m_e*	m_h*	μ		ε (meV)	Δk (x10^{-3} Å^{-1})	α (eV Å)
Γ → X	0.75	1.01	0.43				
Γ → Y	0.34	0.54	0.21				
				VB	0.70	2.80	0.12
Γ → Z	0.53	0.66	0.29				
				CB	50.30	11.31	2.22
Γ → T	0.54	0.85	0.33				

Table S5: Calculated effective masses for different directions for the (*R*-3-AQ)$PbBr_4$ x 2Br compound at the PBE-D3 + SOC level of theory along with the Rashba data.

	m_e^*	m_h^*	μ		ε (meV)	Δk (x10^{-3} Å^{-1})	α (eV Å)
R → A	0.55	1.14	0.37				
X → A	0.57	1.14	0.38				
Γ → M	0.42	0.55	0.24	VB	22.40	6.29	7.12
				CB	12.90	3.15	8.19
X → M	0.42	0.55	0.24				
Γ → Z	∞	∞	-				

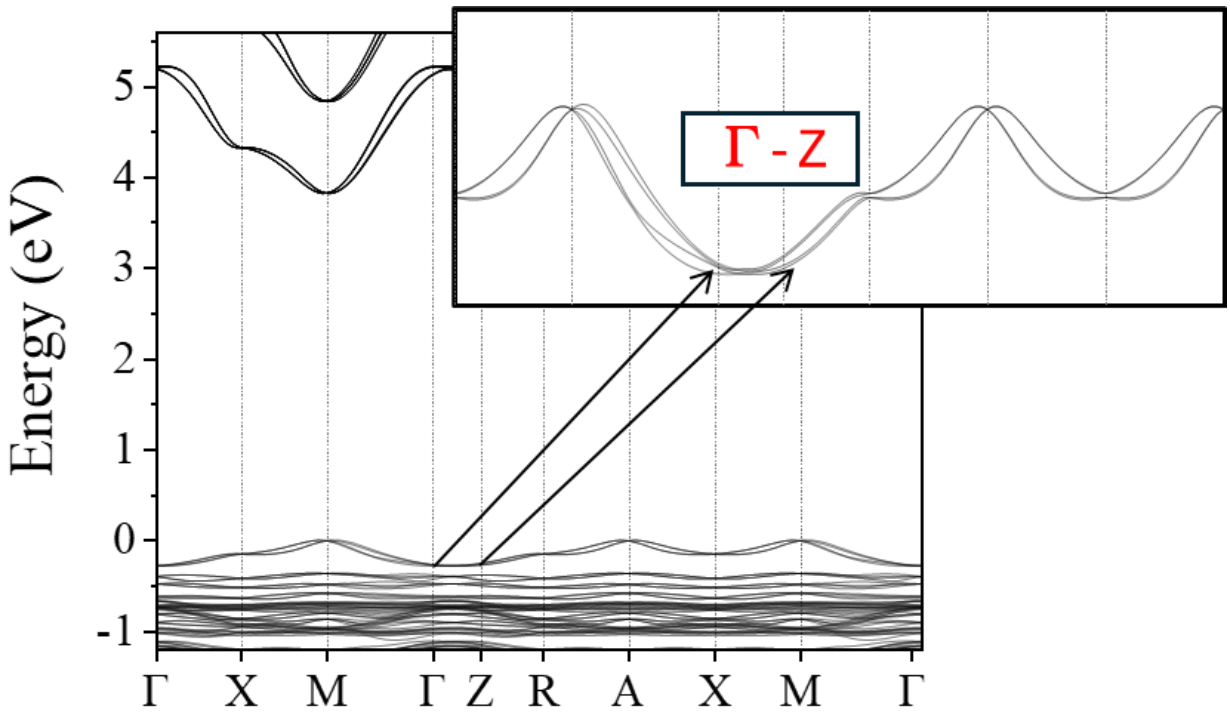

Figure S11: Close up on the flat Γ-> Z branch from the total band structure reported in the main text.

References

(1) Rigaku Oxford Diffraction **2021**. CrysAlisPro Software system, version 1.171.41.104a, Rigaku Corporation, Wroclaw, Poland.

(2) Altomare, A.; Burla, M. C.; Camalli, M.; Cascarano, G. L.; Giacovazzo, C.; Guagliardi, A.; Moliterni, A. G. G.; Polidori, G.; Spagna, R. It SIR97: A New Tool for Crystal Structure Determination and Refinement. *Journal of Applied Crystallography* **1999**, *32* (1), 115–119.

(3) Sheldrick, G. M. Crystal Structure Refinement with It SHELXL. *Acta Crystallographica Section C* **2015**, *71* (1), 3–8.

(4) Coelho, A. A. Indexing of Powder Diffraction Patterns by Iterative Use of Singular Value Decomposition. **2003**.

(5) Le Bail, A.; Duroy, H.; Fourquet, J. L. Ab-Initio Structure Determination of LiSbWO6 by X-Ray Powder Diffraction. *Materials Research Bulletin* **1988**, *23* (3), 447–452.

(6) Young, R. A. *The Rietveld Method*; IUCr Monograph on Crystallography-5; Oxford University Press, 1981.

(7) Cheary, R. W.; Coelho, A. A Fundamental Parameters Approach to X-Ray Line-Profile Fitting. *J Appl Crystallogr* **1992**, *25* (2), 109–121.

(8) Giannozzi, P., et al., R. M. QUANTUM ESPRESSO: A Modular and Open-Source Software Project for Quantum Simulations of Materials. *J. Phys.: Condens. Matter* **2009**, *21* (39), 395502.

(9) Grimme, S.; Antony, J.; Ehrlich, S.; Krieg, H. A Consistent and Accurate *Ab Initio* Parametrization of Density Functional Dispersion Correction (DFT-D) for the 94 Elements H-Pu. *The Journal of Chemical Physics* **2010**, *132* (15), 154104.

(10) Van Setten, M. J.; Giantomassi, M.; Bousquet, E.; Verstraete, M. J.; Hamann, D. R.; Gonze, X.; Rignanese, G.-M. The PseudoDojo: Training and Grading a 85 Element Optimized Norm-Conserving Pseudopotential Table. *Computer Physics Communications* **2018**, *226*, 39–54.

CHAPTER 6

Conclusion and Outlook

In the light of the results emerged from the previous chapters, the tuning of structural properties turned out to be a good strategy to exploit the optical and chiroptical properties. This Ph.D. thesis has demonstrated, across four different systems, the optimization of structure-properties correlation, the increasing of the significant values for the NLO properties and the possibility of obtaining interesting phases without the toxicity of the lead. The experimental results indicate new systems of different dimensionality, which lead to different improvement, from the increasing of the chirality transfer to higher isotropic carrier mobility, but also the implementation of new chiral cations which can create new interaction with the inorganic framework, developing new structural phases which, since now, were no longer present in the state of the art.

Chapter 2, "Ligand-Induced Chirality in Cl-MBA$_2$SnI$_4$ 2D Perovskites" was dedicated to the study of a novel low band gap Sn-based 2D chiral. The crystal structure of the novel lead-free perovskite (*R*/*S*-ClMBA)$_2$SnI$_4$. investigation confirmed that the *R*- and *S*- compound crystallized in non-centrosymmetric space groups while the racemic compound behaves as opposite. The presence of chiral ligands effectively induces the emergence of chiroptical properties, as demonstrated by the CD spectra and confirms by the presence of a Rasbha band splitting for the isomer compound, while absent for the racemic one. The phase has been characterized also by UV-vis spectroscopy and PL spectroscopy. The overall characterization confirms the structural distortion induced by chiral organic cations. Such structural distortions eventually lead to the formation of STEs and concomitant, red-shifted emission highlighting the impact of local environment on the electronic properties. Finally the compound has been compared with the analogue Pb-based compositions, namely (*R*/*S*-ClMBA)$_2$PbI$_4$, it can be seen that replacing lead with tin lead to a further reduction of the crystal symmetry, to a variation of the octahedral distortion parameters, to a reduction of the band gap from 2.55 eV (Pb) to 2.12 eV (Sn) and a strong variation from a narrow emission to a broad emission centered in the red region of the visible spectrum.

Chapter 3, “Unraveling the Role of Structural Topology on Chirality Transfer and Chiroptical Properties in Chiral Germanium Iodides” introduced two novel series of chiral ClMBA-containing germanium iodides, (*R*/*S*-ClMBA)$_3$GeI$_5$, and (*R*/*S*-ClMBA)$_2$GeI$_4$, presenting the same chemical building blocks but a different dimensionality, namely a 1D structural motif for the first and a typical 2D perovskite arrangement for the second system. The experimental and computational investigation highlight first, from the structural data, the 1D topology presents a reduced distortion level of the octahedra with respect to the 2D system. This provides an insight to tune distortion parameters which are known to affect the electronic and optical properties. DFT calculations predict stronger effect of SOC on relevant electronic states passing from a 1D to a 2D structure, which correlates with the increase of the amplitude of the chiral distortions induced into the framework. Indeed, the optical properties indicate a change from indirect to direct bandgap passing from 1D to 2D dimensionality with a slight red-shift in the same direction and from the CD results clearly the increasing of one order of magnitude of the g_{CD} from ~4×10^{-4} to ~4×10^{-3} when dimensionality reduces The origin of such trend can be interpreted as an “increase” of the chirality transfer to the inorganic framework when changing the structural dimensionality as demonstrated by the analysis of the symmetry breaking distortions To conclude, our study reveals an active role of the dimensionality change keeping the same chemical building blocks.

Chapter 4, “Engineering the Electronic Structure and Optoelectronic Properties of Chiral Metal Halides through Ligand Design” introduce the importance of extending the actual library of hybrid chiral systems in order to widen the properties tuning of the chiroptical and electronic properties. In here, we present the implementation of the novel (2*R*,2'*R*)-1,1'-azanediylbis(butan-2-ol) and (2*S*,2'*S*)-1,1'-azanediylbis(butan-2-ol) bifunctional chiral ligands, which have been synthesized for the first time and used to prepare the 1D chiral metal halides (*R/S*-AMOL)PbI$_3$ and (*R/S*-AMOL)SnI$_3$. This work highlights how the presence of aminic and hydroxyl functional groups, these last on the chiral carbon, leads to the formation of an unprecedented structural arrangement in low-dimensional chiral metal halides. This new structure has been found for both the Sn- and Pb- system and for this reason, both systems has been characterised, and relevant differences are found in the optical response and electronic structure. While both samples show a strong CD response, centred around the absorption edge, the PL, while weak for both, is strongly red-shifted for (*R/S*-AMOL)SnI$_3$. The calculation of the electronic structure of the samples shows some similarities in terms of atom contribution to VB and CB but a significant difference arising

from the nature of the iodide atoms participating to the density of states. Specifically, both bi-coordinated and undercoordinated iodides contribute to the VB in the case of (*R/S*-AMOL)SnI_3 while for (*R/S*-AMOL)PbI_3 the VB is mostly localized on the axial atoms causing a shift of the electronic structure which can be correlated to the observed optoelectronic properties.

Chapter 5, "3D Metal Halide Semiconductor" presents a new chiral metal halide semiconductor with a 3D structure, namely (*R/S*-3-AQ)Pb_2Br_6, which has been synthesized by using a small and steric hindered ditopic cation, providing the first chiral halide structural network composed of corner-shared octahedra only. The calculation of the electronic band structure for (*R/S*-3-AQ)Pb_2Br_6 demonstrates an improved isotropic carrier mobility with respect to the (*R/S*-3-AQ)$_2PbBr_4$·2Br 2D system, which, on the other hand, shows a transport confined in the plane of the inorganic layers. These findings are undelined by the photophysical properties of the semiconductor which shows a lower degree of localization of the photoexcitation, and of excitation nature, with respect to its 2D counterpart. Moreover, the well-recognized properties tunability of hybrid metal halides through chemical alloying could be applied to (*R/S*-3-AQ)Pb_2Br_6 to further manipulate its chiroptical and transport properties thus creating a library of novel chiral 3D systems.

These improvements have led to discover new interesting phases and structures which show how many possibilities of implementation exist in this field. The importance of the investigation in structure properties correlations leads to the discovery and the improvement of these materials, hopefully in some device that could be a future technology.

Acknowledgments

Arrivata a questo momento finale, che onestamente sembrava non arrivasse mai più, è giunto il momento di lasciare l'UniPV, fedele compagna negli ultimi otto anni della mia vita e praticamente la mia seconda casa in questi ultimi tre anni di Dottorato. Per cui, ritengo doveroso esprimere alcuni ringraziamenti.

Il primo ed il più grande ringraziamento va al Professor Lorenzo Malavasi, mio mentore di scienza e di vita. In questi quattro anni lei è stato il mio punto di riferimento lavorativo, mi ha guidata permettendomi di crescere come scienziata ma anche, e forse soprattutto, come persona. Grazie per essere sempre stato disponibile al dialogo scientifico e allo scherzo, ha reso il luogo di lavoro un posto bello dove venire ogni giorno. Grazie per avermi insegnato che l'umiltà paga sempre e soprattutto che nella scienza, come nella vita "un non risultato è sempre un risultato." Grazie Prof!

In secondo luogo, ci tengo a ringraziare il Professor Alessio Porta, per avermi accolto nel Laboratorio B2 e avermi fatto apprezzare la chimica organica. Collaborare insieme a lei è stato sempre stimolante e divertente.

Grazie a tutte le persone che hanno collaborato insieme a me a questo progetto di tesi, in particolare la Dott.ssa Annamaria Petrozza ed il suo gruppo: la Dott.ssa Giulia Folpini, il Dott. Andrea Olivati e la Dott.ssa Antonella Treglia. Il gruppo di Perugia, il Dott. Edoardo Mosconi e il Dott. Luca Gregori. Un ringraziamento particolare va anche alla Professoressa Maddalena Patrini e alla Professoressa Chiara Milanese. Ed infine alla Dott.ssa Marta Morana ed al Centro Grandi Strumenti, in particolare il Dott. Massimiliano Boiocchi.